Identification and Modeling of Sea Level Change Contributors

Identification and Modeling of Sea Level Change Contributors

On GRACE Satellite Gravity Data and their Applications to Sea Level Change Monitoring

B. Wouters

Contents

Summary

Recently, the Intergovernmental Panel on Climate Change named sea level rise as one of the major challenges of the 21st century. Given the high population density of coastal regions, a small rise of the sea level will have a substantial impact on human society. However, the Earth's climate system is a complex matter and model predictions of the sea level changes likely to be expected in the coming century currently show a wide spread. Clearly, a thorough understanding of present-day climate variability is imperative narrow this uncertainty band, which on its turn depends on the availability of accurate and detailed observations of our climate.

A valuable contribution to the expanding array of satellites dedicated to observations of the Earth System, are the *Gravity Recovery and Climate Experiment* (GRACE) satellites, launched in March 2002. This mission is dedicated to observing changes of the Earth's gravity field at (sub-)monthly intervals. At time-scales of a few years, these changes are mostly related to the redistribution of water on the Earth's surface. For example, a thinning of the Greenland ice sheet will manifest itself as a local negative anomaly in the gravity field, whereas the water that is added to the ocean will show up as a predominantly positive anomaly. The main objective of this dissertation is to study how the GRACE observations can be used to improve our knowledge of changes in the Earth's climate systems, and how the data should be processed in order to optimize quality and spatial resolution.

The GRACE data provided by the science teams consist of spherical harmonic coefficients. They show particular correlations between coefficients of identical order and even and odd degree, respectively, due to the mission's architecture and deficiencies in the background models used throughout the processing of the satellite measurements. These noise artifacts show up as striping patterns along the north-south direction in the monthly maps of surface mass changes, hampering the interpretation of the observations. In this dissertation, it is shown that empirical orthogonal function (EOF) analysis is an effective method to reduce the noise in the GRACE data. This statistical tool separates a data set into a number of characteristic (eigen)modes of variance, in combination with an index

describing the amplitude of the mode in time, i.e. the principal components. The EOF analysis can be applied to the maps of surface mass changes, in which case the first few modes are related to the annual and long-term trend components. The fourth mode appears to be related to the El Niño/Southern Oscillation. The noise signals are absorbed by the higher modes, which makes the leading modes largely stripe-free up to a resolution of approximately 400 kilometers.

A further reduction of the noise can be obtained by applying the EOF decomposition directly to the spherical harmonic coefficients, after grouping them following order. The principal components are compared to a random process and, if the two are statistically sufficiently alike, not used in the further data processing. A series of tests shows that this approach reduces the noise by 60–80%, compared to the non-filtered case. An important feature of this filter is that it does not alter the shape of the signal and causes less reduction its power, compared to other commonly used filter methods based on the approach of Swenson and Wahr (2006).

Using the filtered data, changes in the mass content of the ocean have been studied. The GRACE satellites are capable of capturing seasonal changes in the ocean mass content accurately on a global scale. In combination with sea surface height observations made by satellite altimeter, the steric sea level component (related to changes in the heat and salinity content of the ocean) can be separated as well. A comparison with reference data sets shows that locally a coherent signal can be obtained at a (Gaussian) resolution of approximately 500 km over the oceans. These steric changes dominate the sea level in most of the oceans, but strong ocean bottom pressure fluctuations are observed in several areas, e.g., the Gulf of Carpentaria and the Gulf of Thailand. Estimates of long-term changes in the ocean mass and heat content are a more challenging problem, and require a longer observation period and a better modeling of mass redistribution in the solid earth and the position of the center of mass of the Earth, two components to which the GRACE observations are particularly sensitive.

It is found that the global spherical harmonic coefficients contain more information than previously acknowledged. This is demonstrated by using the GRACE data to obtain a picture of the mass balance of the Greenland ice sheet at a regional scale. From the research in this dissertations, it shows that Greenland lost 179 Gigaton each year on average between 2003 and 2008, causing a global mean rise of sea level by 0.5 mm/yr. Comparing the trend in the first few to that in the last few years shows a speed-up of the thinning, which corroborates the picture of an increasingly negative mass balance of the ice sheet since the mid 1990's as indicated by, for example, regional climate models and radar altimetry observations. The majority of the losses occur in the coastal regions in the southeastern sector. The northwestern coastal zones were approximately in balance up to the summer of 2005, but show strong negative trends since. Large year-to-year differences in the mass balance of the ice sheet are observed, with a record loss in the warm summer of 2007. A strong correlation between the GRACE observations in summer and satellite measurements of surface melt area extent is demonstrated.

Also, good agreement is found with regional climate modeling data, highlighting the potential of the GRACE observations to validate and improve the numerical models.

A mass redistribution on land will cause a change in the shape of the global geoid. Sea level, when not acted upon by any other forcings, will adjust to this equipotential surface. Therefore, when water is exchanged between ocean and continents (and changes due to ocean dynamics are disregarded), sea level will not rise or fall uniformly, which is known as the so-called selfgravitation effect. Due to their global coverage, the GRACE observations of continental mass distribution are an excellent input to model this phenomenon. Strongest deviations from a uniform distribution are found off the coast of Alaska and in the Bay of Bengal, where differences of more than 100% are found on seasonal time-scales. In these regions, inclusion of the selfgravitation effect into numerical ocean model would result in a better agreement between modeled and observational data.

From the work presented in this dissertation, it shows that the GRACE satellites are an invaluable tool for the monitoring of our climate system. Statistically filtering of the data reveals a wealth of information. In combination with altimetry observations, the GRACE data allows the separation of mass and steric components in sea level on seasonal time scales. Given a longer observational period and an improved understanding of the processes in the solid earth, expected to come available soon thanks to ESA's GOCE missions, long-term trends in these components will be identifiable. Furthermore, the GRACE mission allows us to put a constraint on the contribution of the Greenland ice sheet to present-day sea level rise. The technique to recover these changes can easily be expanded to other regions, such as the Antarctic or the Alaskan glacier fields. The synergy between GRACE data, future missions such as Cryosat-2, which will map height variations of the cryosphere with an unprecedented accuracy, and regional climate models, uncovering the physical processes behind the observed changes, promises a leap forward in our understanding of the mass balance of the ice sheets. Finally, comparing the modeled deviations from uniform sea level changes with in-situ data such as from tide-gauges, may lead to a direct validation of the aforementioned selfgravitation theory with present-day data.

Samenvatting

Identificatie en modellering van zeespiegelveranderingscomponenten: over GRACE satellietzwaartekrachtwaarnemingen en hun toepassingen op het gebied van klimaatmonitoring

Het *Intergovernmental Panel on Climate Change* noemde zeespiegelstijging onlangs als een van de grootste uitdagingen van de 21$^{\text{ste}}$ eeuw. Aangezien kustgebieden vaak dichtbevolkt zijn, zal een kleine stijging van de zeespiegel al snel een grote impact hebben op onze samenleving. Het aardse klimaatsysteem is echter een complexe materie en de modelvoorspellingen van de te verwachten zeespiegelveranderingen in de komende eeuw vertonen nog een grote marge. Vanzelfsprekend is een goed begrip van het hedendaags klimaat een voorwaarde voor het maken van betrouwbare voorspellingen, wat op zijn beurt weer afhangt van de beschikbaarheid van nauwkeurige en gedetailleerde observaties.

Een belangrijke bijdrage hiertoe wordt sinds maart 2002 geleverd door de *Gravity Recovery and Climate Experiment* (GRACE) satellieten. Het doel van deze missie is het in kaart brengen van veranderingen in het aardse zwaartekrachtsveld. Op tijdschalen van enkele jaren zijn deze veranderingen grotendeels gekoppeld aan de verplaatsing van watermassa's op het aardoppervlak. Een afname van de hoeveelheid ijs op Groenland zal zich bijvoorbeeld manifesteren als een plaatselijke negatieve afwijking in het zwaartekrachtsveld, terwijl het smeltwater dat zich in de oceaan verspreidt een voornamelijk positieve afwijking veroorzaakt. Het hoofddoel van dit proefschrift is te onderzoeken hoe de GRACE waarnemingen kunnen worden gebruikt om onze kennis van het klimaatsysteem te verbeteren, en hoe de data verwerkt dient te worden om de kwaliteit en resolutie te optimaliseren.

De GRACE data wordt door de missieteams aangeleverd in de vorm van sferische harmonische coëfficienten. Deze vertonen kenmerkende correlaties tussen coëfficienten van eenzelfde orde en even of oneven graad, wat een gevolg is van het missieconcept en tekortkomingen in de correctiemodellen die gebruikt worden in het verwerken van de satellietmetingen. Deze ruissignalen uiten zich als een Noord-Zuid streeppatroon in de maandelijkse watermassa-verdelingobservaties, wat de interpretatie ervan ernstig bemoeilijkt. In dit proefschrift wordt aangetoond dat empirische orthogonale functie (EOF) analyse een geschikte methode

is om het ruissignaal te verminderen. Deze statistische methode deelt een data set op in een aantal eigenmodes die de variantie in het systeem weergeven, tezamen met een index die het gewicht van de mode in de tijd beschrijft (de 'principal component'). Als de EOF analyse wordt toegepast op de maandelijkse watermassa-verdelingsobservaties, zullen de eerste modes de jaarlijkse cyclus en een langetermijnstrend vertegenwoordigen. De vierde mode is waarschijnlijk gerelateerd aan het El Niño verschijnsel. De ruissignalen worden geabsorbeerd in de hogere modes, waardoor de eerste modes relatief ruisvrij blijven.

Een verdere reductie van de ruissignalen kan worden verkregen door de EOF analyse direct toe te passen op de sferische harmonische coëfficiënten, na ze te groeperen volgens orde. De tijd-gewichtsindex van elke mode wordt dan vergeleken met een randomproces, en, indien de twee statistisch gezien voldoende gelijkenis vertonen, niet meer verder gebruikt in de verwerking van de data. Een reeks van tests toont aan dat de ruis hierdoor met 60 tot 80% vermindert. Een belangrijk kenmerk van de filtermethode is dat de vorm van de signalen behouden blijft en dat er minder signaalafzwakking plaatsvindt, in vergelijking met andere, vaak toegepaste filtermethodes zoals die van Swenson and Wahr (2006).

Met deze verbeterde data werden vervolgens veranderingen in de massa-inhoud van de oceaan bestudeerd. De GRACE satellieten zijn in staat om de seizoensgebonden cyclus in de massa-inhoud waar te nemen op een globale schaal. In combinatie met radarhoogtemetingen van de zeespiegel kan ook de sterische component (gerelateerd aan de warmte-inhoud en het zoutheidsgehalte van de oceaan) worden gescheiden. Vergelijking met referentiedata toont aan dat lokaal een coherent signaal gemeten wordt met een (Gaussische) resolutie van ongeveer 500 kilometer. De sterische cyclus domineert de zeespiegelvariatie in de meeste delen van de oceaan, maar sterke massafluctuaties worden waargenomen in verschillende regio's, zoals de Golf van Carpentaria en de Golf van Thailand. Langetermijnsveranderingen in de massa- en warmte-inhoud van de oceaan vormen nog een uitdaging, en kunnen enkel nauwkeurig geschat worden met behulp van langere observaties én een betere modellering van processen in de vaste aarde en een betere kennis van de positie van het middelpunt van de aarde, twee factoren waaraan de GRACE metingen erg gevoelig zijn.

Verder is aangetoond dat de sferische harmonische coëfficiënten meer informatie bevatten dan tot nu toe werd aangenomen. Dit werd gedemonstreerd door de GRACE data te gebruiken om de massabalans van de Groenlandse ijskap op een regionale schaal in kaart te brengen. Uit het onderzoek in dit proefschrift blijkt dat Groenland gemiddeld genomen 179 Gigaton per jaar verloor tussen 2003 en 2008, wat een stijging van 0.5 mm/jaar van de gemiddelde zeespiegel veroorzaakt. Een vergelijking van de data in het eerste paar jaren van de observaties met dat in het laatste paar, toont een versnelling van het ijsverlies, wat past in het plaatje van een steeds negatievere massabalans van de ijskap sinds het midden van de jaren '90, aangegeven door bijvoorbeeld regionale klimaatmodellen en radarhoogtemetingen. Het merendeel van de verliezen treedt op in het zuidoostelijke kustgebied. De noordwestelijke kustgebieden waren tot mid-

den 2005 in evenwicht, maar vertonen sindsdien ook een sterke afname. Grote jaar-tot-jaar verschillen worden waargenomen in de massabalans, met een record-verlies in de warme zomer van 2007. Een hoge correlatie wordt gevonden tussen de GRACE waarnemingen tijdens de zomermaanden en de totale oppervlakte met smelt in de toplaag van de ijskap uit satellietwaarnemingen. Ook wordt een goede overeenkomst gevonden met regionale klimaatmodellen, hetgeen het potentieel van de GRACE observaties voor validatie en verbetering van deze numerieke modellen aangeeft.

Een verandering in de massadistributie op de continenten brengt een verandering in de geoïde teweeg. De zeespiegel zal zich, indien er verder geen andere krachten op werken, vormen naar dit equipotentiaalvlak. Daardoor zal bij een uitwisseling van water tussen de continenten en de oceaan (en indien veranderingen ten gevolge van oceaan dynamica buiten beschouwing worden gelaten) de zeespiegel geen uniforme stijging of daling vertonen, wat bekend staat als het 'zelfgravitatie-effect'. Dankzij hun wereldwijde dekking, vormen de GRACE waarnemingen van de continentale massaherverdeling een uitstekend middel om dit effect te modelleren. Op seizoengebonden schaal worden de sterkste afwijkingen van een uniforme oceaanverdeling waargenomen in de Golf van Bengalen en in de kuststreek van Alaska, waar de verschillen kunnen oplopen tot meer dan 100%. Indien het zelfgravitatie-effect wordt meegenomen in numerieke oceaanmodellen, verbetert de overeenkomst tussen modeldata en observatie in deze gebieden.

Zoals blijkt uit het werk dat in dit proefschrift gepresenteerd wordt, zijn de GRACE satellieten een uiterst belangrijk instrument voor het observeren van ons klimaatsysteem. Met behulp van statistische filters kan een schat aan informatie verkregen worden. In combinatie met radarhoogtemetingen kunnen de massa en sterische component van de zeespiegel gescheiden worden op seizoensschaal. Mits langere observaties en verbeterd inzicht in de processen in de vaste aarde – die verwacht worden uit ESA's GOCE missie – kunnen ook langetermijnsveranderingen in deze componenten gescheiden worden. Verder laat de GRACE missie toe om de bijdrage van de Groenlandse ijskap aan zeespiegelveranderingen nauwkeurig vast te leggen. De techniek die hiervoor gebruikt werd kan op eenvoudige wijze toegepast worden in andere gebieden, zoals Antarctica of de gletsjergebieden van Alaska. De synergie tussen de GRACE waarnemingen, toekomstige missies zoals Cryosat-2, die de hoogteveranderingen van de ijskappen nauwkeurig in kaart zal brengen, en regionale klimaatmodellen, die inzicht geven in de fysische processen achter de waargenomen veranderingen, belooft een sprong voorwaarts te leveren in onze kennis van de massabalans van de ijskappen. Tenslotte kan het vergelijken van de gemodelleerde afwijkingen van een uniforme zeespiegelverandering met in-situ data, bijvoorbeeld van getijdestations, leiden tot de directe validatie van de zelfgravitatietheorie met hedendaagse data.

Chapter 1

Introduction

1.1 Background

In the recent report of the Intergovernmental Panel on Climate Change (IPCC) (Solomon et al., 2007), sea level rise is explicitly named as one of the major challenges for human society in the 21st century. A rise of just 20 centimeters, could result in the displacement of more than 300 million people, primarily in low lying countries such as the Netherlands (Parry et al., 2007). Whereas the financial aids to counteract the effect of a rising sea level may be present in well-developed countries, this is by no means true for other locations such as the densely-populated delta regions of the Ganges and Mekong river systems in Asia, where the societal impact of a changing sea level will potentially be dramatic.

Covering approximately 70% of its surface, the World Ocean is an important actor in the Earth's climate system. Due to the large heat capacity of water, the ocean will absorb the majority of the excess energy in the Earth's radiation budget; the total net amount of heat stored by the oceans since the 1960's is roughly 20 times greater than that of the atmosphere (Levitus et al., 2005). Furthermore, changes in the total mass of the ocean are directly linked to changes in the amount of water stored on the continents, reflecting the state of the ice sheets, glaciers and ice caps. This makes a close monitoring and profound understanding of sea level changes, and its dynamics, crucial in the study of a changing climate.

Based on tide gauge observations, the average trend in relative sea level over the 20th century is estimated to be approximately 1.7±0.3 mm/yr (Douglas et al., 2001; Church and White, 2006). This is considerably larger than pre-industrial values, which are estimated to be in the range of 0.0 to 1 mm/yr (see Lam-

beck et al. (2004b) and Donnelly et al. (2004), resp.), and analysis of the tide
gauge indicates an acceleration of sea level rise starting approximately 200 years
ago. It is worth mentioning that sea level changes are associated with large in-
terdecadal variability, due to coupling to internal climate modes such as the El
Niño/Southern Oscillation (ENSO) or the North Atlantic Oscillation (NAO), and
average trends in the order of 3 mm/yr have been observed in 10 years intervals
(e.g., Jevrejeva et al., 2008).

 Since the early 1990's, sea level is monitored on a routine basis by satellite
altimetry missions. Whereas tide gauge studies are typically based on a small
number of observation locations situated along the coast line, satellite altimetry
provides a near-global coverage of the oceans. For the period 1993–2008, global
average sea level rise is estimated to be in the order of 3.2 mm/yr (update of
Leuliette et al. (2004)). The discrepancy with the average 1.7 mm/yr for the 20th
from tide gauge data can be partly explained by the different coverage, i.e. largest
trends in the altimetry data are found in the Southern Hemisphere, where very few
tide gauge stations are available (Cabanes et al., 2001; Wouters, 2004). However,
a comparison of tide gauge and altimetry in the period 1993–2007 results in trend
values that are consistent within the range of error (Jevrejeva et al., 2008; Prandi
et al., 2009), indicating an sea level rise above the 20th average during the last 15
years.

 Changes in sea level can be attributed to two components; i.e. an eustatic and
a steric component. The eustatic component is caused by addition or removal
of mass to the oceans, the steric by changes in density of the ocean water due
to variations in temperature and salinity. A third component, related to solid
Earth processes, plays a role when one considers relative sea level changes, i.e.
changes in the position of the sea level surface with respect to a point fixed on
land. This component can locally be significant and even dominant, e.g., in coastal
regions undergoing subsidence, with strong tectonic activity, or where post-glacial
rebound is present. Furthermore, changes in the shape of the ocean bottom may
result in a change of the total volume of the ocean basin.

 The disadvantage of satellite altimeter data is that they provide only the total
sum of mass and density variations in the water column. Additional information is
therefore required to distinguish between the two components. Since mass redis-
tribution in the oceans will alter the Earth's gravity field, gravity measurements
could potentially be used to recover this component. In combination with the
altimetry observations of total sea level, this will then yield the steric component.
Furthermore, adequately detailed and accurate gravity observations may be used
to identify the contributors to the mass related component. For example, nu-
merous studies have shown that the ice sheets of Greenland and Antarctica have
been losing mass since the mid 1990's (Zwally et al., 2005; Rignot et al., 2008b,a;
Hanna et al., 2008; van den Broeke et al., 2009). Such a mass imbalance of the
ice sheet will present itself as a local negative anomaly in the Earth's gravity field
and should be detectable by dedicated satellite observations from space.

 Since 2002, such observations of the Earth's gravity field are being made by the

Gravity Recovery and Climate Experience (GRACE). The main goal of this dissertation is to explore to which extent these observations can be used to improve our understanding of sea level changes, either as a stand-alone tool or in combination with other observational data such as from altimetry. Since this requires data of a high quality, the dissertation will first concentrate on the post-processing and filtering of the GRACE observations, after which three applications of the data to climate variability will be demonstrated. First of all, the basic principle of the GRACE mission and essential background information will be discussed in this introductory chapter.

1.2 The GRACE Mission

The *Gravity Recovery and Climate Experience* (GRACE) is a joint project of the *National Aeronautics and Space Administration* (NASA) and *Deutsches Zentrum für Luft- und Raumfahrt* (DLR) and was launched on March, 17th 2002 (Tapley et al., 2004a). It consists of two satellites in an identical low, near-circular, near-polar orbit, at an altitude of about 500 kilometers, separated from each other by a distance of a few hundred kilometers along-track. The main objective of the mission is the mapping of the global gravity field at (sub-)monthly intervals. Initially, the mission was targeted to cover a 5-year period, which has long been exceed. Depending on the performance of the individual satellite components, the mission may be extended to 2012 or later. Motivated by the success of the GRACE missions, development studies are currently being carried out for a follow-up mission (Bettadpur, personal communication, 2009).

The GRACE mission is based on the satellite-to-satellite tracking concept (fig. 1.1), which uses variations in the inter-satellite range (and its derivatives) to recover gravitational information (see, e.g., Seeber (1993)). Since the two GRACE satellites are separated by a certain distance, the orbit of each of the satellites will be perturbed differently, i.e. out of phase, by the Earth's gravity field. This will cause the intersatellite distance to vary, with relative changes in the order of a few micrometers, which is measured by means of a dual-one way ranging system, the K/Ka band ranging system (KBR). Non-gravitational forces, such as atmospheric drag, which will also alter the relative distance, are accounted for using onboard accelerometer measurements. The orientation in space of the satellites are mapped by two star-cameras. Since the KBR measurements provide no information on the position in the orbit, the satellites are equipped with GPS receivers.

Generally, the variations in the Earth's gravity field are recovered through an iterative procedure. In a first step, an a-priori model of the Earth's mean gravity field in combination with other force models (e.g., representing luni-solar and third body tides, ocean tides, etc.) is used to determine the orbit of both satellites. Next, the numeric orbit is compared to the GPS and KBR observations and residuals are computed. Also, linearized regression equations are constructed,
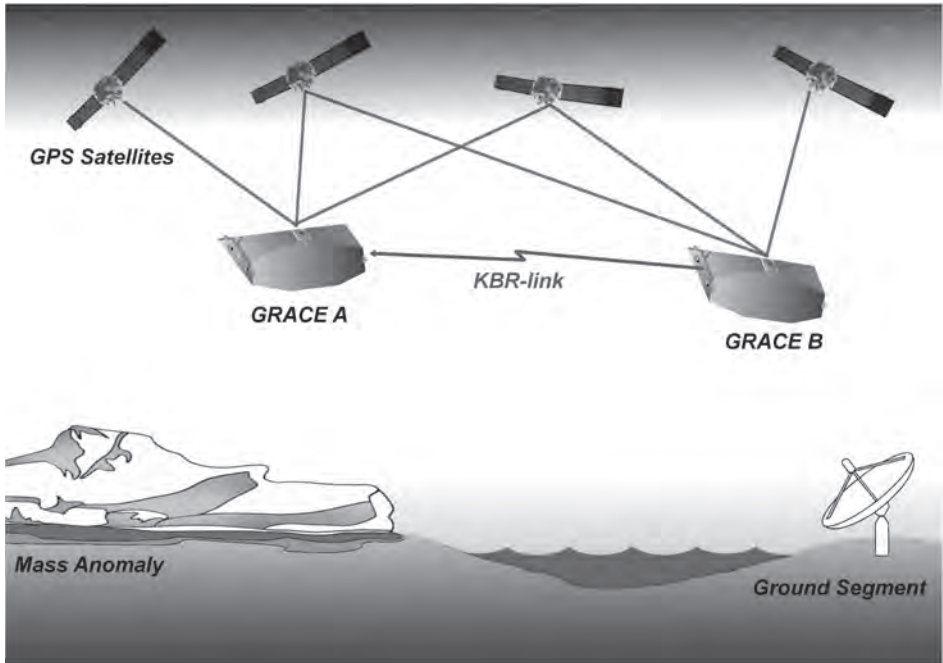
Figure 1.1: *Illustration of the GRACE mission.*

which relate the gravity field (more specifically, the spherical harmonic coefficients as will be explained in section 1.3) and other parameters to the residuals. By combining data of a sufficiently long period, these equations may be used to relate the observations to variations of the gravity field in a least square sense (see Reigber et al. (2005); Tapley et al. (2005)).

The GRACE data are processed at three main science data centers, i.e. the *Center for Space Research* (CSR), *Jet Propulsion Laboratory* (JPL), both located in the U.S.A., and the *GeoForschungsZentrum Potsdam* (GFZ) in Germany, although other institutes are also providing independent gravity solutions nowadays. Differences in the approaches of the processing centers lie in the background force models used, the period over which the orbit is integrated, weighting of the data, the maximum degree of the estimated gravity harmonics, the regional vs. global character of the solutions, etc. (see, e.g., Rowlands et al. (2005); Bettadpur (2007); Flechtner (2007); Watkins and Yuan (2007); Lemoine et al. (2007); Liu (2008)).

1.3   From geopotential to mass

The gravity field of the Earth is described by the geopotential, the sum of the potential of the gravitational field induced by the Earth's mass and the centrifugal potential caused by rotation of the sphere. At a point outside the Earth's figure, the gravitational potential can be expressed as:

$$V(r, \theta, \lambda) = \frac{GM}{a_e} \left\{ \sum_{l=0}^{\infty} \sum_{m=0}^{l} \left(\frac{a_e}{r} \right)^{l+1} P_{lm}(\cos \theta)(C_{lm} \cos m\lambda + S_{lm} \sin m\lambda) \right\} \quad (1.1)$$

where the position in the geocentric frame is defined by the radius r, the co-latitude θ and the longitude λ. On the right hand side, GM is the geocentric gravitational constant of the Earth, a_e denotes its mean equatorial radius, P_{lm} are the fully normalized Legendre polynomials of degree l and order m and C_{lm} and S_{lm} are the spherical harmonic coefficients, which are also fully normalized. Equation 1.1 may be used to define equipotential surfaces, i.e. surfaces of constant potential V. The equipotential surface that would best fit the global mean sea level at rest is referred to as the geoid. Since the shape of the geoid resembles that of an ellipsoid, the gravitational potential is commonly referenced to an ellipsoid which closest approximates the geoid and has a total mass equal to that of the Earth. The height difference between the reference ellipsoid and the geoid is referred to as the geoid height and is approximated by:

$$N \approx \frac{V - U}{\gamma} \quad (1.2)$$

where U is the gravitational potential of the reference ellipsoid and γ the normal gravity on the ellipsoid's surface. The latter can be further approximated by GM/a_e^2, so that the geoid height can be approximated by:

$$N(\theta, \lambda) \approx a_e \sum_{l=0}^{\infty} \sum_{m=0}^{l} P_{lm}(\cos \theta)(\Delta C_{lm} \cos m\lambda + \Delta S_{lm} \sin m\lambda) \quad (1.3)$$

where the Δ's indicate a difference from a reference value.

The main objective of the GRACE mission is to map variations in the gravitational field at (sub-)monthly intervals. Assuming that on short time-scales these changes are caused by redistribution of water in a thin layer of a few tens of kilometers thickness on the Earth's surface, variations in the spherical harmonic coefficients C_{lm} and S_{lm} can expressed as (see Wahr et al. (1998) and also Ch. 6 for a more elaborate discussion):

$$\left\{ \begin{array}{c} \Delta C_{lm} \\ \Delta S_{lm} \end{array} \right\} = \frac{3(1 + k_l')}{4\pi a_e \rho_e (2l+1)} \iint \Delta\sigma(\theta, \lambda) P_{lm}(\cos \theta) \left\{ \begin{array}{c} \cos m\lambda \\ \sin m\lambda \end{array} \right\} \sin \theta \, d\theta \, d\lambda$$

$$(1.4)$$

where $\Delta\sigma(\theta,\lambda)$ is a function describing the surface density redistribution on the Earth's surface and the Δ denotes a deviation from a long term mean. The k'_l coefficients are the elastic load Love numbers describing the additional change in geoid height due to elastic loading and deformation of the solid earth by the surface mass changes, ρ_e is the average density of the Earth. The double integral on the right hand side decomposes the mass redistribution function $\Delta\sigma(\theta,\lambda)$ in spherical harmonics $\Delta\tilde{C}_{lm}$ and $\Delta\tilde{S}_{lm}$, leading to the identity:

$$\left\{ \begin{array}{c} \Delta\tilde{C}_{lm} \\ \Delta\tilde{S}_{lm} \end{array} \right\} = \frac{a_e\rho_e}{3}\frac{2l+1}{1+k'_l}\left\{ \begin{array}{c} \Delta C_{lm} \\ \Delta S_{lm} \end{array} \right\} \tag{1.5}$$

Hence, the surface mass density anomaly can be expressed as:

$$\begin{aligned} \Delta\sigma(\theta,\lambda) &= \sum_{l=0}^{\infty}\sum_{m=0}^{l}P_{lm}(\cos\theta)(\Delta\tilde{C}_{lm}\cos m\lambda + \Delta\tilde{S}_{lm}\sin m\lambda) \\ &= \frac{a_e\rho_e}{3}\sum_{l=0}^{\infty}\sum_{m=0}^{l}P_{lm}(\cos\theta)\frac{2l+1}{1+k'_l} \\ &\quad \times(\Delta C_{lm}\cos(m\lambda) + \Delta S_{lm}\sin(m\lambda)) \end{aligned} \tag{1.6}$$

All computations of surface mass redistribution were performed following the two-step synthesis approach, described in, e.g., Sneeuw (1994).

In its present form, the surface mass density variations $\Delta\sigma(\theta,\lambda)$ are expressed in units of mass per unit of area. A more intuitive unit can be obtained by dividing eq. 1.6 by the density of water, ρ_w, which yields changes expressed in units of equivalent water height (EWH).

1.4 Geocenter motion

The summation in eq. 1.6 starts at degree $l=0$ and theoretically runs to infinity, although in reality the monthly GRACE solutions are typically cut-off at a degree $l = 60$ to 120. Assuming that the total mass of the Earth's system does not change, the degree $l = 0$ coefficient can be ignored. The degree $l = 1$ coefficients are related to the movement of the center of mass of the Earth with respect to the center of figure of the Earth. This is also the center of the orbits of the two satellites, hence changes in the position of this point will have an identical effect and will not result in a change in intersatellite distance. Consequently, the degree $l = 1$ coefficients are not recoverable from the KBR data and need to be provided by external sources.

On seasonal timescales, the geocenter variations are caused mainly by redistribution of mass on the Earth's surface (Dong et al., 1997). A first method to retrieve the seasonal geocenter variations is by combining observations independent of GRACE, or alternatively, the output of numerical climate models of the

	Amplitude (mm)			Phase (doy)		
	x	y	z	x	y	z
Atmosphere	0.4	1.3	0.9	345	357	334
Continental Hydrology	0.8	0.8	2.3	56	274	76
Ocean	0.6	0.7	1.1	340	20	54
Total	1.4	2.1	3.3	11	344	53
Total incl. Mass conservation	1.6	2.2	3.8	12	349	55

Table 1.1: *Estimated contribution of the three surface loading components to the annual geocenter motion, defined as the movement of the center of mass with respect to center of figure. The annual cycle is defined by $A\cos(\omega(t - \varphi))$, with amplitude A, t time in days with respect to January 1st, φ day of maximum and ω equal to $2\pi/365.25$.*

components of the Earth's water cycle (i.e., atmosphere, ocean and continental hydrology). These mass redistributions are related to degree $l = 1$ coefficients by eq. 1.4, which can be converted to geometrical translations (X_g, Y_g, Z_g) of the Earth's center of mass in the terrestrial reference frame (Heiskanen and Moritz, 1967):

$$
\begin{aligned}
\Delta X_g &= \sqrt{3} a_e \Delta C_{11} \\
\Delta Y_g &= \sqrt{3} a_e \Delta S_{11} \\
\Delta Z_g &= \sqrt{3} a_e \Delta C_{10}
\end{aligned}
\tag{1.7}
$$

Table 1.1 gives an overview of the contribution of the individual components of the Earth system to the seasonal displacement of the geocenter. As input for the atmospheric loading, global gridded surface pressure data were used from the National Center for Environmental Prediction (NCEP). Only data over the continents are retained, since the ocean is assumed to respond following the inverted barometer principle at seasonal timescales (Gill, 1982). The contribution of the oceans is represented by TOPEX/Poseidon radar altimetry measurements of the sea level, available between 65°N and 65°S. These sea level variations are dominated by height variations due to density changes, which will not affect the loading of the ocean bottom. A correction for this contribution is applied using monthly climatological values of temperature and salinity anomalies, taken from the World Ocean Atlas 2005 (WOA05) (see Locarnini et al. (2006) and Ch. 4). Variations in continental hydrology are based on the Land Dynamics model (LaDWORLD, version Euphrates Milly and Shmakin, 2002), which provides soil moisture, groundwater and snow pack variations. Glaciated areas, such as Greenland and Antarctica were masked, since the LaDWORLD model does not include ice dynamics, resulting in unlimited accumulation of mass in these areas (Milly, personal communication, 2006). All data sets have been resampled to monthly intervals and only data in the common period of 1993–2002 were used.

source	data	Amplitude (mm)			Phase (doy)		
		x	y	z	x	y	z
Bouillé et al. (2000)	SLR[1]	2.10	2.00	3.50	48	327	43
Crétaux et al. (2002)	SLR[1]	2.60	2.50	3.30	32	309	36
Moore and Wang (2003)	SLR[1]	3.50	4.30	4.60	26	303	33
Dong et al. (2003)	GPS[1]	4.80	3.60	9.40	50	310	165
Lavallée et al. (2006)	GPS[1]	3.93	6.98	7.80	26	336	107
Blewitt et al. (2001)	GPS[2]	3.40	4.93	11.22	86	345	56
Kusche and Schrama (2005)	GPS[2]	9.18	1.87	10.03	25	323	52
Lavallée et al. (2006)	GPS[2]	3.57	2.44	9.93	51	341	30
Wu et al. (2006)	GPS/GRACE[3]	1.80	2.50	3.90	46	329	28
Swenson et al. (2008)	GRACE/ECCO[4]	1.13	2.67	1.23	52	325	55
Swenson et al. (2008)	GRACE/OMCT[4]	1.88	2.59	1.78	46	326	60

[1] Network shift; [2] deformation inversion; [3] deformation & GRACE; [4] GRACE & ocean model

Table 1.2: *Overview of different estimates of the annual variation in geocenter position, defined as the movement of the center of mass with respect to center of figure. The same conventions as in table 1.1 are used.*

Finally, the total system is forced to be mass-conserving by adding a layer of water to the oceans which adjusts passively to the shape of the geoid (see Clarke et al. (2005) and Ch. 6).

Geocenter motion can also be estimated by means of geodetic data and networks. A first method uses the site displacements of the Global Positioning System (GPS), satellite laser ranging (SLR) and/or Doppler Orbit determination and Radiopositioning Integrated on Satellite (DORIS) stations to determine the average shift of the total network, which approximately coincides with the shift of the center of figure with respect to the center of mass (see, e.g., Eanes et al. (1997); Bouillé et al. (2000); Crétaux et al. (2002); Dong et al. (2003); Moore and Wang (2003); Lavallée et al. (2006)). A second method recovers the geocenter motion by inversion of the solid earth deformation caused by mass deformation (e.g., Blewitt et al., 2001). Since this approach requires a dense global network, it is limited to GPS (e.g., Blewitt et al., 2001; Kusche and Schrama, 2005; Lavallée et al., 2006; Wu et al., 2006; Lavallée et al., 2008). Recently, a third method has been developed, which uses GRACE coefficients of degree two and higher in combination with the degree one components of an ocean model, to constrain the global degree one coefficients (Swenson et al., 2008).

Table 1.2 gives an overview of selected geocenter variations based on different observation techniques (kindly provided by D. Lavallée). Agreement between the different estimates is in the order of 20 days in phase and about 2–3 mm for amplitude, which is roughly the same size as the predicted signal (Lavallée et al., 2008). Generally speaking, the SLR and GRACE based estimates fit best to the geocenter variations predicted by the model of table 1.1. As will be discussed in Ch. 4, the geocenter model can significantly influence the GRACE observations,

e.g. seasonal ocean mass estimates may vary by a factor two between the two extreme most models and by about 30% if the group of more consistent models is considered. Also, no accurate estimates of trends in the position of the geocenter are available at present. Reducing the uncertainties in the geocenter variations is therefore one of the key issues to come to more accurate GRACE observations of mass redistributions in the Earth's system.

1.5 Outline of the dissertation

The main goal of this dissertation is to discuss how the GRACE satellite observations can contribute to and improve our understanding of climate variability, with a focus on the processes related to sea level variations, and how the GRACE data should be processed to extract a maximum amount of information from the observations.

A prerequisite for a useful interpretation of the observations is the availability of high-quality data. The GRACE observations as provided by the science processing centers are known to be contaminated by noise, showing up as striping patterns with a distinct north-south pattern in the GRACE maps of equivalent water height. The first part of this dissertation will therefore focus on how to post-process the GRACE data efficiently, in order to increase the quality and spatial resolution of the observations. Chapter 2 discusses Empirical Orthogonal (EOF) analysis and demonstrates how this statistical method can reduce the striping in the GRACE maps. This can be done by either applying the EOF analysis to the equivalent water height maps, or by applying the method directly to the spherical harmonic coefficients, before converting them to spatial maps.

Chapter 3 contains a series of tests that assess the improvement in quality and spatial resolution obtained by EOF post-processing and other commonly used filters. Also, the impact of filtering is discussed by applying the EOF analysis to synthetic data based on numerical hydrology and ocean models.

In the second part of the dissertation, three applications of the GRACE data to observing climate variability are presented. In chapter 4, GRACE is used to obtain fluctuations of ocean bottom pressure (i.e., related to the mass distribution in the ocean). By combining these observations to altimetry measurements of sea level height, the steric component (i.e., related to temperature and salinity variations) can also be retrieved. The maximum resolution of the GRACE data over the oceans and the annual cycle of the two components are discussed.

Next, in chapter 5, the GRACE observations are used to monitor the mass balance of the Greenland ice sheet, one of the most important contributors to present-day sea level rise. A regional analysis of mass changes is presented and differences with earlier GRACE-based studies are discussed. The regional results are compared with independent data sets, such as surface mass balance provided by regional climate models and melt observations acquired by passive microwave satellite instruments.

A third application of the GRACE data is presented in chapter 6, dealing with changes in relative sea level induced by variations in mass distribution on land. Such changes will alter the geoid, to which sea level will adapt. As a secondary effect, the ocean bottom will be displaced. It is shown how the GRACE data can be used to model these variations and how including this forcing into ocean models may improve agreement between model output and observations.

The major findings of this dissertation are summarized in chapter 7, where recommendations for further research are also made.

Chapter 2

Filtering the GRACE data using EOF Analysis

2.1 Introduction

One of the major problems one faces when working with GRACE data, is the increasing error spectrum at higher degrees in the provided Stokes coefficients C_{lm} and S_{lm}. When no a posteriori filtering is applied, these errors show up as unphysical longitudinal striping patterns in the maps of equivalent water height (EWH). This is illustrated in fig. 2.1a, showing a map of EWH anomaly for September 2005. At the full resolution of the GRACE data, the map is dominated by noise and little useful information can be derived.

A clear spatial correlation can be observed in the noise, with alternating bands of positive and negative stripes stretching in the north-south direction. Although the exact cause has not been pinpointed yet, the origin of the striping pattern most likely lies in the orbit geometry of the GRACE satellites (e.g., Ray and Luthcke, 2006; Schrama and Visser, 2007). The intersatellite distance is measured in the along-track direction of the orbital plane, which has a near-polar orientation, therefore the observations bear a high sensitivity in the north-south direction. Errors in the instrument data and shortcomings in the background models used to remove high-frequency atmosphere and ocean signals during the inversion process will consequently result in the meridional striping patterns.

In the spectral domain, this correlation is equivalent to an intercoefficient correlation, as first pointed out by Swenson and Wahr (2006). A possible solution to reduce the striping pattern would therefore be to cut off the spherical harmonics

at a certain degree when converting to EWH maps and continue working only with the coefficients which are not, or only slightly, affected by noise. Given that the errors in the coefficient increase at a degree of approximately $l = 10$, this would seriously limit the resolution of the GRACE solutions and therefore is an unfavorable option. The use of more advanced filtering techniques is preferred, which will be discussed in this chapter.

2.2   Gaussian smoothing

One of the most commonly used techniques to reduce the noise in the EWH maps, is by means of spatial averaging, as proposed by Wahr et al. (1998). In most GRACE studies, the smoothing kernel used is Gaussian bell shaped, with the weighting factor $W(\alpha)$ depending on the distance to the point of interest, but not on the orientation (i.e. the filter is isotropic):

$$W(\alpha) \;\; = \;\; \frac{b}{2\pi}\frac{e^{-b(1-\cos\alpha)}}{1-e^{-2b}} \tag{2.1}$$

$$b \;\; = \;\; \frac{\ln 2}{(1-\cos(r_{1/2}/a_{\mathrm e}))} \tag{2.2}$$

In these equations $a_{\mathrm e}$ denotes mean equatorial radius, α is the angular distance between the center of the kernel at (θ,λ) and a nearby point (θ',λ') and $r_{1/2}$, the smoothing radius of the kernel, is the distance on the Earth's surface at which W has decreased to half its value at the center of the kernel, $\alpha = 0$ (Jekeli, 1981; Wahr et al., 1998). The smoothed maps of equivalent water height anomalies are then given by:

$$\Delta\bar{\sigma}(\theta,\lambda) = \iint \sigma(\theta',\lambda')W(\alpha)\sin\theta'd\,\theta'd\,\lambda' \tag{2.3}$$

where $\bar{\sigma}(\theta,\lambda)$ indicates that the surface mass anomalies are now smoothed.

In the spectral domain, convolving the spatial maps with the above smoothing kernel corresponds to assigning the coefficients a weight depending on the degree l, with a decreasing value as the l increases. The values of the weighting function can be computed using a recursive relation (Wahr et al., 1998), or can be approximated numerically (Chambers, 2006a):

$$W_l = \exp(l^2(\frac{r_{1/2}}{2a_{\mathrm e}})^2/\ln 2) \tag{2.4}$$

Plugging W_l into eq. 1.6, the smoothed maps of EWH can be obtained from the spherical harmonics by:

$$\Delta\bar{\sigma}(\theta,\lambda) = \frac{a_{\mathrm e}\rho_{\mathrm{ave}}}{3}\sum_{l=0}^{l_{\max}}\sum_{m=0}^{l} W_l\tilde{P}_{lm}(\cos\theta)\frac{2l+1}{1+k'_l}[\Delta\tilde{C}_{lm}\cos(m\lambda)+\Delta\tilde{S}_{lm}\sin(m\lambda)]$$

$$\tag{2.5}$$

Figure 2.2 shows the value of W as a function of the distance from the center point as well as of the degree l, for $r_{1/2} = 500$ km. This illustrates how the ill-determined higher degree coefficients are downweighted when using the Gaussian smoother.

However, as pointed out in the introduction, the error has a non-isotropic character and consequently a large smoothing radius is required to remove all stripes in the GRACE maps, which implies a non-negligible loss of the information contained in the GRACE solutions (e.g., Chen et al., 2007a). This is especially the case when considering maps of equivalent water height, since the errors in the higher degree coefficients will be amplified by the $(2l + 1)$ multiplication in eq. 2.5. Moreover, with an increasing smoothing radius leakage between basins (e.g., land/ocean) will increase, making the separation of signals more cumbersome (e.g., Winsemius et al., 2006b). For example, Klees et al. (2007) have shown that signal attenuation and interbasin leakage may cause a bias of 50–70% of the total signal, depending on the smoothing radius $r_{1/2}$ of the Gaussian kernel.

This is illustrated in fig. 2.1, showing EWH for September 2005 for several Gaussian smoothing radii. Without any smoothing (fig. 2.1a), the map is dominated by the meridional stripes and little geophysical signal can be discerned. At a smoothing radius of 350 km (fig. 2.1b), the larger hydrological basins (e.g., Amazon and Zambezi) start to stand out, but are still corrupted by the stripes. Increasing the smoothing radius to 500 km removes most of the striping over land, an only at smoothing radii of 750 km and larger the oceans appear mostly stripe free. Note how the peak values in the maps decrease as the smoothing is applied over a wider area.

2.3   Intercoefficient correlation

A correlation between the spectral coefficients was first noted by Swenson and Wahr (2006), who reported a correspondence in the behavior of the coefficients of even and odd degrees respectively, starting at an order of approximately ~ 10 for the most recent GRACE data releases (RL04). Neither a correlation as a function of order, nor between the mutual C_{lm} and S_{lm} coefficients, appears to exist.

The origins of the correlation between coefficients of even and odd degrees and identical order may be found in the lumped coefficient theory. Assuming an orbit with very small eccentricity and fixed inclination I_0, it can be shown (e.g., Kaula, 1966) that the disturbing potential T° on the nominal orbit of a satellite at a given epoch t can be expressed as:

$$
\begin{aligned}
T^\circ(t) &= \frac{GM}{R} \sum_{n=0}^{\infty} \sum_{m=0}^{n} \sum_{\alpha=0}^{1} (\frac{R}{a_{\mathrm{e}}})^{n+1} \begin{pmatrix} \Delta C_{nm} \\ \Delta S_{nm} \end{pmatrix} \begin{pmatrix} \delta_{\alpha,0} \\ 1-\delta_{\alpha,0} \end{pmatrix} \\
&\quad \times \sum_{p=0}^{n} F_{nmp}(I_0) \cos(f_{nmp}(t) + \lambda_{nmpq\alpha})
\end{aligned}
\tag{2.6}
$$
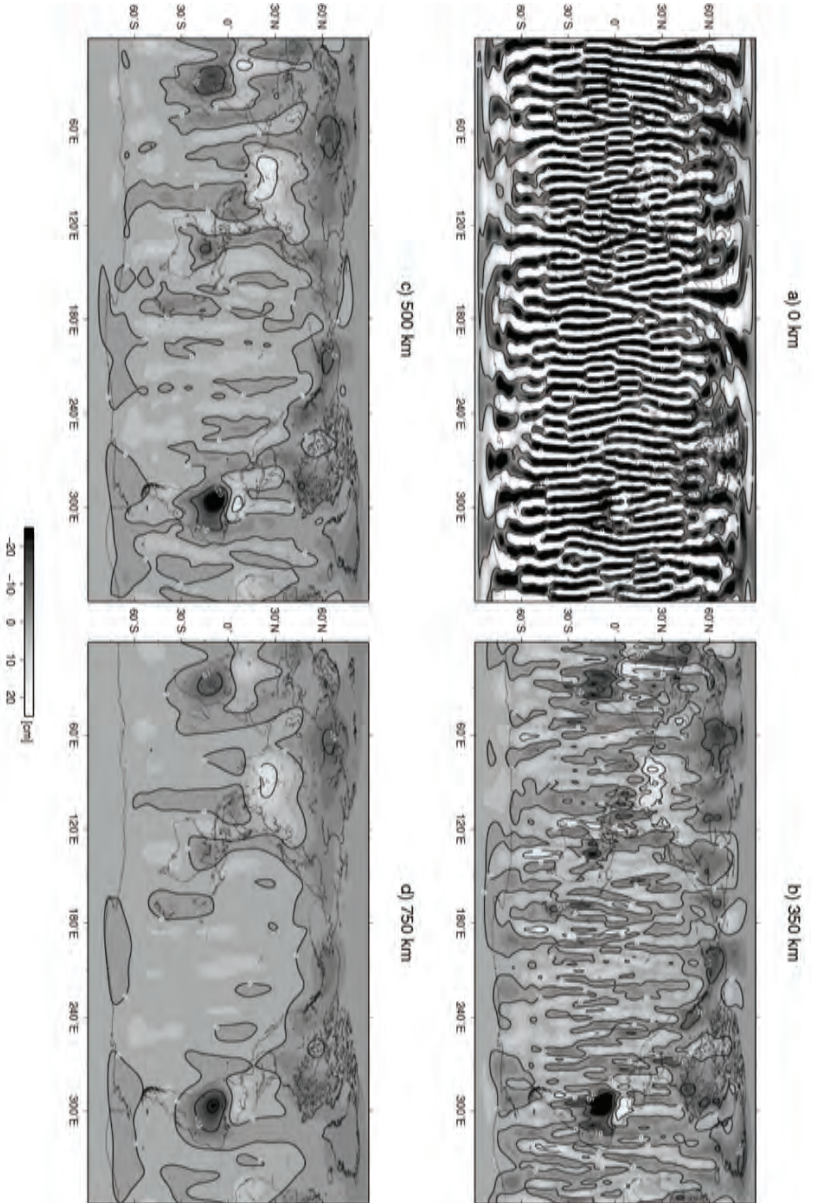
Figure 2.1: *GRACE based maps of EWH anomaly for September 2005, based on CSR RL04 data, smoothed with various radii (a) 0 km; b) 350 km; c) 500 km; d) 750 km). Units are in cm.*
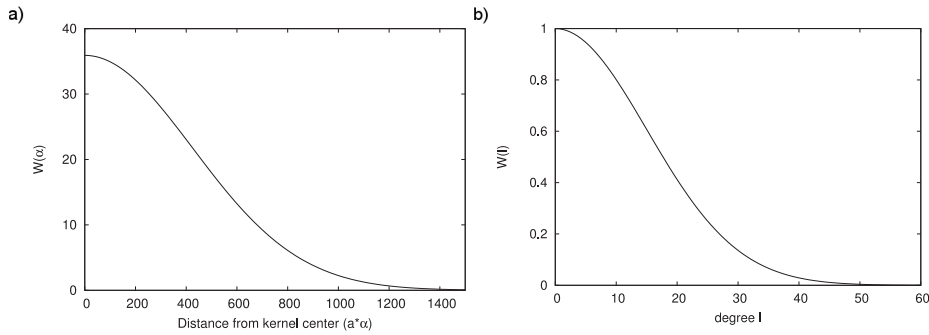
Figure 2.2: *Value of the weighting function W for a smoothing radius $r_{1/2}$ of 500 km, as a function of a) the distance from the center point, and, b) of the spherical harmonic degree l.*

where the frequency term f_{nmp} is equal to:

$$f_{nmp} = (n - 2p)(\dot{\omega} + \dot{M}) + m(\dot{\Omega} - \dot{\theta}) \qquad (2.7)$$

with $\dot{\omega}$ and $\dot{\Omega}$ the precession of the perigee and the right ascension of the ascending node of the orbit under the influence of the equatorial bulge, respectively, $\dot{M}$ the mean motion of the satellite (2π/orbital period $\approx 11 \times 10^{-4} s^{-1}$ for the GRACE satellites) and $\dot{\theta}$ the mean angular velocity of the Earth. $F_{nmp}(I_0)$ is a function depending on the inclination I_0 of the nominal orbit, and $\lambda_{nmpq\alpha}$ is the phase of the potential function, defined by the orbital elements and orientation of the Earth at the time origin t_0. The deviations from the known potential fields are given by ΔC_{nm} and ΔS_{nm}.

Using linearized first-order perturbation theory, Colombo (1986) showed that for a near-repeat orbit with very low eccentricity and near constant inclination, perturbations in a satellite's position and acceleration will become Fourier series with fundamental frequency f_{nmp} and amplitudes which are linear combinations of the associated ΔC_{nm} and ΔS_{nm}. As can be derived from eq. 2.7, combinations for which the order m is fixed and n is either even or odd, depending on the parity of p, will result in a constant frequency. Thus, errors in the coefficients of the potential field fulfilling these conditions will create perturbations at the same frequency, hence the name *lumped coefficients*. Likewise, unmodeled accelerations in the satellite's orbit will result in erroneous values of the Stokes coefficients in the inverse process, which will have the same lumped characteristics.

The orbit of the GRACE satellites almost fulfills the above conditions, so correlations between even and odd degree coefficients may be expected. Figure 2.3 gives an illustration of the correlations. Following Horwath and Dietrich (2006), a constant, trend and an annual and semi-annual cosine function were fitted to all available GFZ RL04 Stokes coefficients for the period 2003–2006 and subse-
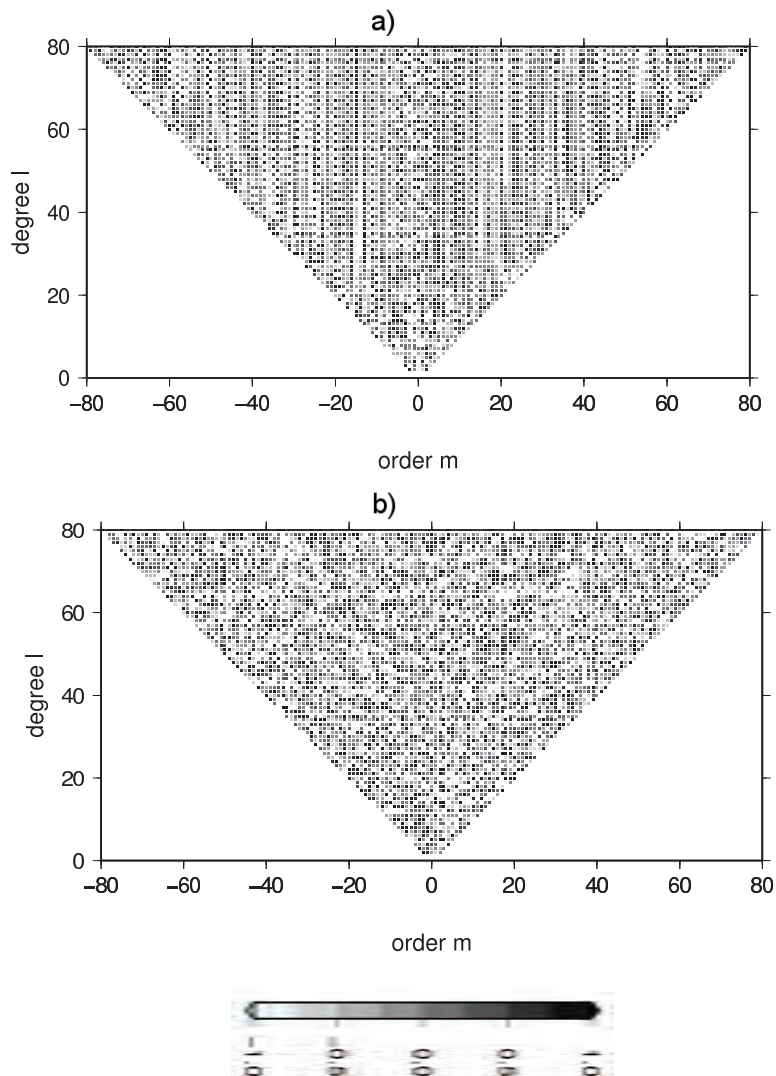
Figure 2.3: *a) Empirical errors normalized by standard deviation for the GFZ RL04 solution of September 2005; b) as a), but based on modeled data for February 2005.*

quently removed from the data. Assuming that the remnant signals is purely non-physical, this gives an upper-bound for the errors in the data. Figure 2.3a shows these *empirical errors* in the solution of February 2005, after normalizing with the standard deviation of the individual coefficients. As a reference, the same procedure has been applied to a simulated data set consisting of modeled land water hydrology (GLDAS, Rodell et al. (2004)) and ocean bottom pressure (ECCO, Fukumori et al. (1999)), see fig. 2.3b. Five years worth of monthly mass anomalies were converted to geopotential coefficients, and again a constant, trend and an annual and semi-annual cosine function were removed. Comparing the variance of the remnant signal to that in the GRACE data, the correlation in the GRACE coefficients clearly stands out, dominating the signal from order 10–12 onward.

2.3.1 Destriping the GRACE solutions

In order to reduce the intercoefficient correlation, Swenson and Wahr (2006) propose to fit a quadratic polynomial in a moving window to the Stokes coefficients of even and odd degrees separately and remove this function from the original Stokes coefficients, for all orders m starting at a certain order m_{min}. Using a slightly modified version, i.e. leaving the lower portion of the coefficients unchanged and fitting a higher order polynomial as a function of degree to the remaining even and odd coefficients up to a maximum degree l_{max}, Chambers (2006b) showed that this reduces the residuals of the GRACE solutions with sterically corrected altimetry data by more than 51% over the oceans.

Figure 2.4 compares the original and destriped map of equivalent water height for September 2005. The method of Chambers (2006b), updated for the CSR RL04 solutions, has been used. The lower 11×11 set of coefficients remains unaltered, a 5th order polynomial is fitted to the other coefficients. Destriping algorithms based on the polynomial fit perform well in removing the coefficient correlations, but have many degrees of freedom. A too high order of the polynomial to be fitted, a too small window width, or a too low starting order m from which of signal is being removed, may result in unwanted removal of real geophysical signals with a near north-south orientation. Moreover, the error characteristics may vary slightly from month to month, whereas the filter setting remain unchanged.

Since possibilities of validating the GRACE data with in-situ data are limited, setting the parameters remains somewhat arbitrary, depending on the user's experience and intuition. A possible alternative is to base the filter on the statistical properties of the signal in the GRACE observations. Empirical orthogonal function (EOF) offer a prime tool for such an analysis, and filtering of the data based on this approach will be discussed in the remainder of the chapter.

a)

b)
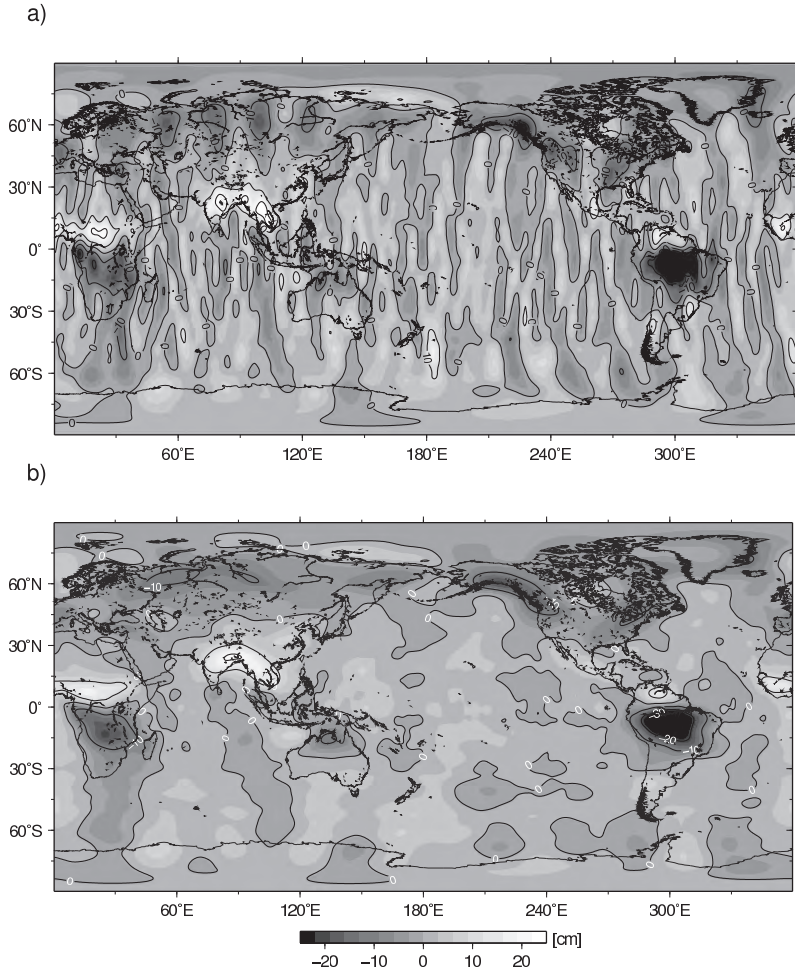
Figure 2.4: *Map of equivalent water height anomaly for September 2005 (CSR RL04), a) smoothed with a 350 km Gaussian, and b) after applying the destriping algorithm of Chambers (2006b) and smoothed with a 350 km Gaussian. Units are cm of EWH.*

2.4   Basic EOF theory

Principal component analysis (PCA) – or alternatively empirical orthogonal function analysis, as it is more commonly referred to in geophysics – is a technique frequently used to study the spatial and temporal variability of a dataset, by separating the directions of the largest variance from each other. Using these principal directions, the multidirectional dataset can be transformed to a reduced subspace

with a lower number of dimensions, but with a minimal loss of information. Its fundamentals were first described in Sylvester (1889), whereas Pearson (1901) appears to be the first to apply the theory in a physical context and visualize the concept of the principal components in an Euclidean space (Preisendorfer, 1988). The PCA technique soon became a popular tool among oceanographers and meteorologist to study patterns in, among others, sea surface temperature and atmospheric pressure (e.g., Lorenz, 1956). More recently, PCA were applied to GRACE data by Chambers (2006a) in order to study the seasonal patterns in steric sea level height and ocean bottom pressure. Rangelova et al. (2007) found a generally good agreement between the leading EOF modes of the GRACE data and those of hydrological models in North-America.

EOF analysis is based on the fact that a general real-valued, scalar, homogeneously dimensioned data set Z with elements $\{z(t,x): x = 1,\ldots,p; t = 1,\ldots,n\}$ consisting of n observations of p variables, has a set of dominant directions of variance in the Euclidean space E_p, see Preisendorfer (1988). These directions may be obtained by finding the eigenvectors e_j of the covariance matrix of the data set $\bar{Z}^T\bar{Z}$ and form an orthogonal basis for the data space, such that:

$$
\begin{aligned}
\bar{z}(t,x) &= \sum_{j=1}^{\rho} a_j(t)e_j(x) \\
\bar{Z} &= AE^T
\end{aligned}
\tag{2.8}
$$

where $a_j(t)$ is a temporal weight to the contribution of the eigenvector e_j, and the overbar indicates that a mean field has been removed. These weights are uncorrelated and their variance is equal to the variance of the data along the direction of the associated eigenvector e_j. The variables a_j and e_j are commonly referred to as the jth principal component and EOF mode, respectively. The number of modes is at most $\min[n-1, p]$, denoted as ρ in eq. 2.8.

A convenient procedure to perform the obtain the EOFs and PCs of a data matrix $\bar{Z}$ is by means of a singular value decomposition (SVD), see, e.g., Golub and Kahan (1965). This will break down the original data matrix into:

$$
\bar{Z} = UDV^T
\tag{2.9}
$$

Comparing this to eq. 2.8, it becomes clear that V contains the EOF modes, whereas UD corresponds to the PCs. The diagonal matrix D elements equal the square root of the eigenvalues λ_i of the covariance matrix $\bar{Z}^T\bar{Z}$, representing the scatter of the data set $\bar{Z}$ along the associated eigenvector e_i. Hence, each EOF mode represents a certain percentage of the total variance in the data set, with the modes with the largest associated eigenvalues corresponding to the directions of largest variance in the data set:

$$
\frac{\text{Variance in Mode } i}{\text{Total Variance}} = \frac{\lambda_i}{\sum_{i=1}^{\rho} \lambda_i} = \frac{D_{ii}^2}{\sum_{i=1}^{\rho} D_{ii}^2}
\tag{2.10}
$$
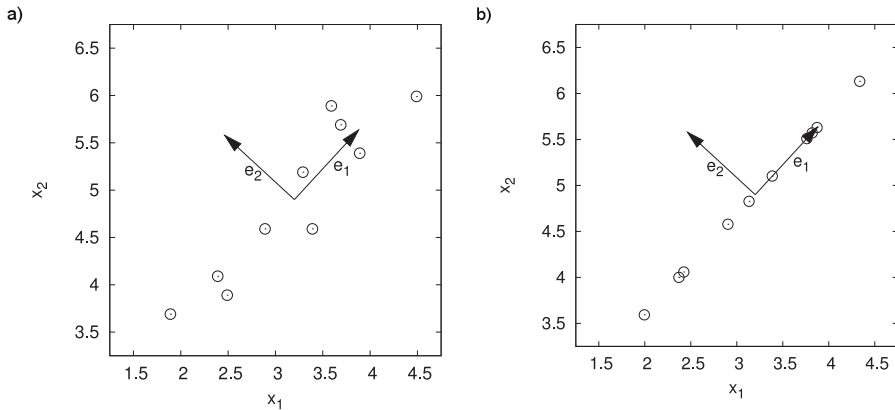
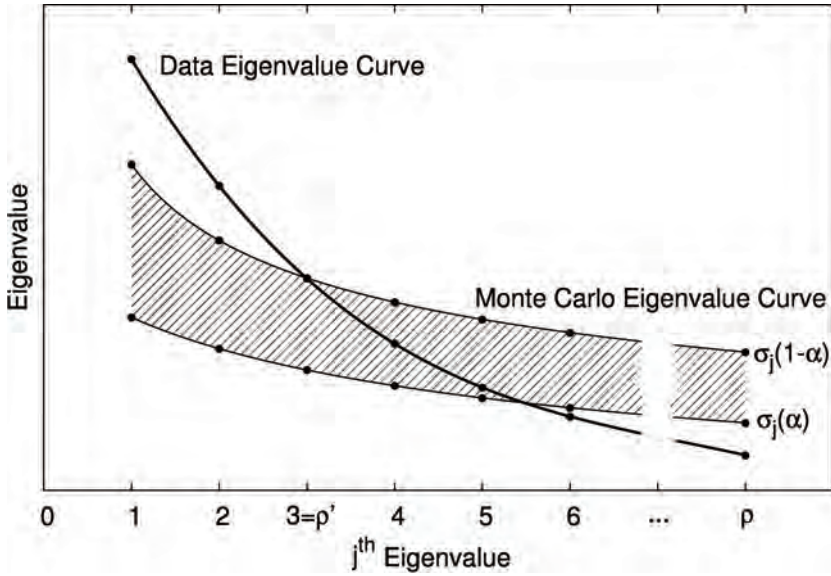**Figure 2.5:** *Basic illustration of the EOF principle: a) The original dataset and the two EOF modes, which are the eigenvectors e_1 and e_2 of the data covariance matrix, and b) the compressed dataset, reconstructed using the first EOF mode and PC only.*

Generally speaking, the first few modes with most power represent significant signal, whereas other modes correspond to superfluous noise in the original data set. Thus, by summing over only a selected set of eigenvectors in eq. 2.8, noise can be greatly reduced and only the signals of interest should remain in the compressed data set.

A basic illustration of principal component analysis is given in fig. 2.5 for a set of 10 observations of two variables x_1 and x_2. After removing the temporal mean, each of the ten pairs (x_1, x_2) are stored as a row in the data matrix $\bar{Z}$ and the eigenvectors $(\bar{e_1}, \bar{e_2})$, or EOF modes, are obtained by performing the singular value decomposition to the covariance matrix. In this case, the first mode is responsible for the majority of the variance in the dataset, with about 96% of it occurring along the direction of the $\bar{e_1}$ vector. Then, the dataset is reconstructed along this direction using only the first EOF mode and the associated principal component, which results in the compressed dataset shown in fig. 2.5b.

2.5 Selection rules

The question that arises from the discussion above is how to chose the modes to use in the reconstruction of the data. In the following, two methods to select these modes in an objective manner will be discussed. The first method, *Rule N*, selects the dominant leading modes by preserving the modes which have an associated variance larger than a certain threshold value, while the second method, *Rule KS2*, looks at the temporal evolution of the principal components.

Figure 2.6: *Illustration of the Rule N principle: A band within which the eigenvalues are expected to fall is constructed using a Monte Carlo procedure. Eigenvalues of the data covariance matrix are considered significant and accepted if they lie above the $\sigma(1-\alpha)$ curve, which is the case for the first two eigenvalues in this illustration (adapted from Preisendorfer (1988)).*

2.5.1 Rule N

The *Rule N* procedure selects the modes to be retained by comparing the amount of variance contained in the leading EOF modes to the variance distribution from a random process, obtained through a Monte Carlo procedure. In order to do so, an $n^1 \times p$ random data matrix R is constructed from a normally distributed population $N(0, \sigma^2)$, where σ^2 is the total variance in the data set $\bar{Z}$ studied (i.e. the sum of the squared diagonal elements from the D matrix obtained in the SVD procedure). For large n, the following will hold:

$$\lim_{n \to \infty} \frac{R^T R}{(n-1)} = \sigma^2 I_p \qquad (2.11)$$

---

[1]In the *Rule N* procedure, the number of time samples n should be corrected for serial correlation first, to assure that the eigenvalues from the Monte Carlo procedure are correctly distributed. Correcting for serial correlation will decrease the effective sample size, so that the sorted eigenvalues are more widely spread and the $(\alpha, 1-\alpha)$ band becomes larger. Generally, this will results in more modes being rejected, see (Preisendorfer, 1988)

, which implies that for large n, the eigenvalues of the covariance matrix $R^T R$ will be centered around a central value. For smaller n a larger spread will be found. Next, the ρ number of eigenvalues of the simulated covariance matrix are computed, sorted according to magnitude and normalized by their mean value (Preisendorfer, 1988). These sorted eigenvalues then form one realization of the Monte Carlo procedure, which is repeated a number of times, say 1000. Given a certain assumed confidence level α, this will define a range $(\alpha, 1-\alpha)$ for each sorted eigenvalue within which the sorted eigenvalues of a covariance matrix of a normal distributed process with properties $N_p(0, \sigma^2 I_p)$ matrix will be contained. The eigenvalues from the covariance matrix $\bar{Z}^T \bar{Z}$ under consideration are then treated similarly, i.e. sorted and normalized by their mean value, and compared to the eigenvalue band from the Monte Carlo simulation, see fig. 2.6. Eigenvalues which lie above the $1-\alpha$ line are considered to be originating from processes significantly different from a random process, whereas the lower values are discerned.

2.5.2   Rule KS2

The dominant variance based *rule N* discussed above retains the first few modes which have a variance larger than that of a random process. However, higher modes associated with a weaker signal may still be associated to a physical process. A one by one inspection of the EOF modes or principal components may therefore reveal information that otherwise would have been lost when selecting only the first few mode.

   To determine which EOF modes should be retained or rejected in the summation, the principal components $a_j(t)$ can be tested for temporal noisy behavior using the Kolmogorov-Smirnov (KS2) test (e.g., Preisendorfer, 1988). Through a Fourier transform the power spectral density (PSD) of each principal component $a_j(t)$ is obtained, which is then tested for spectral whiteness. This is done by comparing the cumulative distribution function (CDF) of the PSD of the principal components a_j with the CDF of the spectrum of a random white noise process. Since the power in the spectrum of such a process is evenly spread out over the frequency band, such a CDF will be a monotonically increasing function between 0 and 1, see fig. 2.7. If the maximum value $D_{\max}$ of the absolute difference between the two CDFs is below a critical value D_{KS2}, the test hypothesis that a_j is a random sample from a white noise process is accepted. The value of D_{KS2} depends on the significance level α and the number of samples, with a larger number of samples or a lower level of significance yielding a smaller critical value D_{KS2} (e.g., Press et al. (1992)).

2.5.3   Sampling errors in the EOF modes

The principal component analysis is based on a data set consisting of a finite number of observations. Changing this number of observations, or shifting the observation period, may therefore result in different patterns in the EOF modes
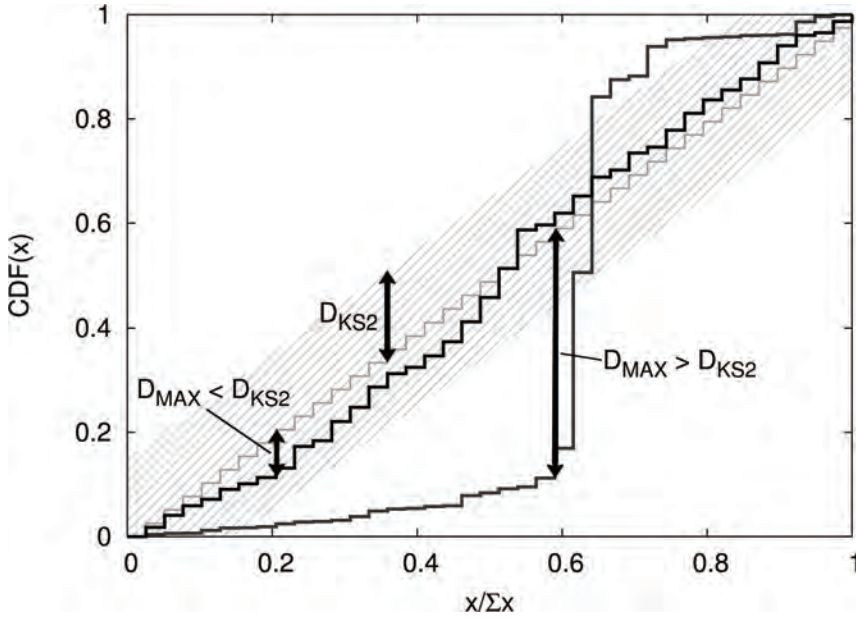
Figure 2.7: *Illustration of the Rule K2 principle: The cumulative distribution function (CDF) of the power spectrum of the principle component (black and dark grey) is compared to the CDF of a white noise process (light grey). If the maximum difference $D_{\max}$ between the two curves is larger than a critical value D_{KS2}, the hypothesis that the principle component stems from a random process is rejected.*

and associated principal components. The first few EOF modes are generally well defined, but the higher modes, in particular pair of modes with closely spaced eigenvalues, may be subject to significant sampling errors. This is due to the fact that any linear combination of the two modes of the pair will also be an EOF of the data set. Such *degenerate multiplets* should therefore be interpreted with caution.

Using a first-order approach, North et al. (1982) showed that for a pair of modes with closely spaced eigenvalues λ_i and λ_j, the change in the eigenvalue λ_i from one set of samples to another is of the order

$$\delta\lambda_i = \mathrm{O}(\lambda_i \sqrt{\frac{2}{N}}) \tag{2.12}$$

where N is the effective sample size, i.e., the number of observations corrected for serial correlation. The change in the EOF mode e_i from one set of samples to another is approximated by the product of $\delta\lambda_i$ and the neighboring mode e_j, times the inverse of the difference $\delta\lambda_{ij} = \lambda_i - \lambda_j$. Consequently, if the distance

between two eigenvalues, $\delta\lambda_{ij}$, is comparable to the sampling error of the eigen-value, $\delta\lambda_i$, then the sampling error in the EOF mode, δe_i, will be comparable to the neighboring EOF (North et al., 1982). As a rule of thumb, for two EOF modes and their PCs to be interpretable unambiguously, the eigenvalues of the two should differ by at least an amount $\delta\lambda_i$.

2.6   Analysis of the GRACE EWH maps

When applying the principal component analysis to maps of equivalent water height anomalies based on the GRACE data, the input data will consist of a number of grids, e.g., fields with a $1° \times 1°$ spacing, stored in the matrix $\bar{Z}$. The output of the analysis will consist of a set of maps, revealing the spatial pattern of the variability contained in each EOF mode, whereas the associated principal components will contain the evolution in time of these patterns.

Some preparatory steps need to be taken before submitting the GRACE maps of EWH anomalies to the principal component analysis. First of all, the variations in the C_{20} coefficients as provided by the GRACE satellites are much larger than those observed by independent techniques, such as satellite laser ranging (Chen and Wilson, 2008). If not corrected for, this will result in a dominant ellipsoidal pattern with limited physical meaning. In this chapter, and the remainder of this dissertation, the original GRACE C_{20} coefficients have therefore been replaced by values derived from satellite laser ranging (Eanes, personal communication, 2008). Furthermore, the solutions for the months July–October 2004 have been excluded. The GRACE satellites were in a near-repeat orbit during this period, which resulted in a less dense coverage and consequently a degraded quality of the gravity solutions. At low smoothing radii, the noise pattern generated during these months would become the main source of variance, accounting for up to 40% of the total variance in the JPL and GFZ solutions, at a 300 km smoothing radius. Finally, an estimate of the seasonal geocenter motion has been included by adopting the degree 1 variations from a combination of the OMCT (Ocean Model for Circulation and Tides) ocean model and GRACE data over land, see Swenson et al. (2008).

The GRACE fields used are composed of a number of $1° \times 1°$ grid cells, which will result in a higher data density at higher latitudes. If not corrected for, these points will dominate the covariance matrix and bias the outcome of the outcome of the principal component analysis. The grid cells of the input fields have therefore been scaled by the square root of the cosine of their latitude, i.e. an equal-area weighting was applied to the covariance matrix. After applying the principal component decomposition, the obtained EOF modes are then deweighted using the inverse of the weights.

The cumulative percentage of total variance contained in the leading modes, for the three main GRACE processing centres and varying Gaussian smoothing radius are shown in table 2.1. The statistics are based on the 52 months that the

three centres have in common between March 2003 and March 2008, excluding the near-repeat event in 2004 and the pre-2003 months, which are more affected by noise (Tapley et al., 2004a). In all three cases, GRACE coefficients up to degree 60 were used.

The larger the smoothing radius, the more the first EOF mode will be representative for the total signal. With a large smoothing radius, the signal contained in the maps of surface water height anomaly will be mainly limited to large (continental) scale phenomena, which are highly correlated in time, such as the seasonal north-south cycle related to continental hydrology. A smaller smoothing radius will reveal more details in the GRACE maps, with signals less correlated both in space and time. Consequently, more modes will be required to describe the total signal. Also, at very low smoothing radii, in the order of 300 km, noise will become the dominant feature in the maps of equivalent water height. Since these signals are less correlated in space and time as well, the power will be distributed over larger number of leading modes.

At all radii, the variance explained by the first mode in the JPL solutions is about 5% greater than those in the CSR and GFZ solutions. This systematic bias indicates that large scale, seasonal signals are dominant in the JPL maps. The difference between the variance of the first few modes in the GFZ and CSR solutions increases as the smoothing radius decreases, which hints at an increasing contribution from noise at higher degrees in the former.

2.6.1   Leading EOF modes

At a 500 km smoothing radius, about 60 to 70 % of the variance is explained by modes 1–3, whereas the higher modes account individually for approximately 3% or less of the total variance. An overview of these first three EOF modes and principal components, which all pass the *Rule N* and *KS2* tests, is given in fig. 2.8 and 2.9, based on the CSR RL04 solutions. The EOFs and PCs are normalized so that the latter reach an absolute maximum of one. To reconstruct the original signal, the EOF maps should be multiplied with the time series of the corresponding principal component. Hence, regions with positive values in the EOF maps are in-phase with the principal component, regions with negative values are out-of-phase.

The first mode, accounting for about 45% of the variance, represents the strong spring-autumn cycle, with largest signal around the major hydrological basins such as the catchments of the Ganges-Brahmaputra and the Amazon-Orinoco systems, which are out-of-phase with each other. Its weaker winter-summer counterpart (11%) is associated with the second EOF mode, and has maximum amplitude in the northern part of the Amazon basin. The out-of-phase nature of the regions of the Amazon basin north and south of the equator can be explained by the seasonal north-south oscillation of the Intertropical Convergence Zone and the associated variations in rainfall (Schmidt et al., 2008). Mode number three (9%) is coupled to the secular trends in the GRACE maps, with a negative signal in, e.g.,

CSR RL04

mode	radius
	300	400	500	600	800	1000
1	19.4	36.5	45.5	50.5	55.9	58.5
2	25.9	46.2	56.2	61.4	66.8	69.1
3	31.1	54.0	65.2	70.8	76.6	79.2
4	34.1	57.1	68.5	74.1	79.9	82.6
5	36.8	59.6	71.0	76.8	82.6	85.3
6	39.4	61.8	73.0	78.7	84.5	87.2
7	41.8	63.8	74.7	80.3	85.9	88.5
8	44.2	65.7	76.4	81.7	87.1	89.6

GFZ RL04

mode	radius					
	300	400	500	600	800	1000
1	11.3	29.9	42.0	48.3	54.7	57.9
2	15.6	37.6	51.2	57.9	64.9	68.7
3	19.7	44.6	60.0	67.2	73.7	76.6
4	23.3	47.8	63.4	70.7	77.3	80.1
5	26.6	50.2	65.7	73.1	79.7	82.4
6	29.7	52.5	67.9	75.2	81.8	84.6
7	32.8	54.6	70.0	77.2	83.6	86.3
8	35.6	56.7	71.6	78.7	84.9	87.5

JPL RL04.1

mode	radius					
	300	400	500	600	800	1000
1	17.8	42.8	54.7	59.8	64.4	66.5
2	23.2	52.1	65.5	71.1	76.0	78.5
3	28.4	60.6	74.7	80.0	84.2	85.9
4	31.9	63.5	77.6	82.9	86.9	88.6
5	35.2	65.7	79.9	85.1	89.2	90.9
6	38.0	67.4	81.5	86.7	90.7	92.4
7	40.8	69.0	82.8	87.9	91.8	93.4
8	43.3	70.5	83.9	88.8	92.6	94.2

Table 2.1: *Cumulative variance percentage explained by EOF modes 1–8 as a function of smoothing radius, for the three main GRACE processing centres.*

Greenland, Antarctica and the Patagonian glacier fields, and post-glacial rebound components around, e.g., Fenno-Scandia, the Hudson Bay and West-Antarctica. The fingerprint of the 2004 Sumatra-Andaman earthquake also clearly shows up in the South-East Asia region.

As mentioned earlier in this chapter, one of the major advantages of the principal component analysis is that it offers a tool to transform a multidirectional dataset to a reduced subspace with a lower number of dimensions, with a minimal loss of information. This can be done by limiting the number of modes retained in eq. 2.8 to a number ρ' smaller than the total number of modes ρ. In the case of $\rho' = 3$ the reconstructed maps would be representative for the annual and secular signals, as discussed above. Since these first three modes show little signs of the north-south striping and most of the noise is absorbed by the higher EOF modes, the reconstructed maps will be relatively stripe-free as well (fig. 2.10a).

As is evident from fig. 2.10b, signal with a systematic character is still contained in the EOFS modes four and upward. In Schrama et al. (2007) it was shown that part of this can be linked to the semi-annual hydrological cycle and to the aliasing of the S_2 tide. With the extended time-series available at present, a better decoupling of these signals is attainable and they can be traced down to specific EOF modes (Schrama and Wouters, 2008). Although modes five and up do not pass the r*ule N* test, as they represent an insufficient amount of variance and are generally not well separated from their neighboring modes, some of them show distinctive temporal patterns and do pass the *KS2* test, and are worth discussing in more detail.

2.6.2 Short-periodic signals

Mode 5 shows a pronounced semi-annual behavior, with about 45 % of the total variance in the principal component explained by a semi-annual harmonic (fig. 2.11). Large amplitudes are observed in the Indian subcontinent, in South-America southeast of the Amazon and around the Rio Negro, North-Australia, the Congo and Zambezi basins in Africa and the main flows in Siberia. These patterns match well with predictions of the twice-yearly continental hydrology signals from numerical models, such as GLDAS (Rodell et al., 2004), as illustrated in Schrama et al. (2007).

Evidence of the S_2 tide are found in a number of higher modes. Errors in the FES2004 tidal model used in the background processing of the GRACE data will alias into spurious signals in the GRACE monthly observations, which can have a period a multiple of the original tidal constituent's period. One of the tidal constituent that raises most concern is the semi-diurnal S_2 tide, which consists of two components, i.e. the gravitational tide and the atmospheric tide. Since the latter is due to thermal excitations by the solar radiation in the upper atmosphere, it can not be modeled by the (numerically) solving of the Laplace tidal equation (LTE) using the gravitational potential forcing only and has to be estimated through assimilation of tide gauge and altimetry data (for more details, see Lyard et al.

a)

b)

c)
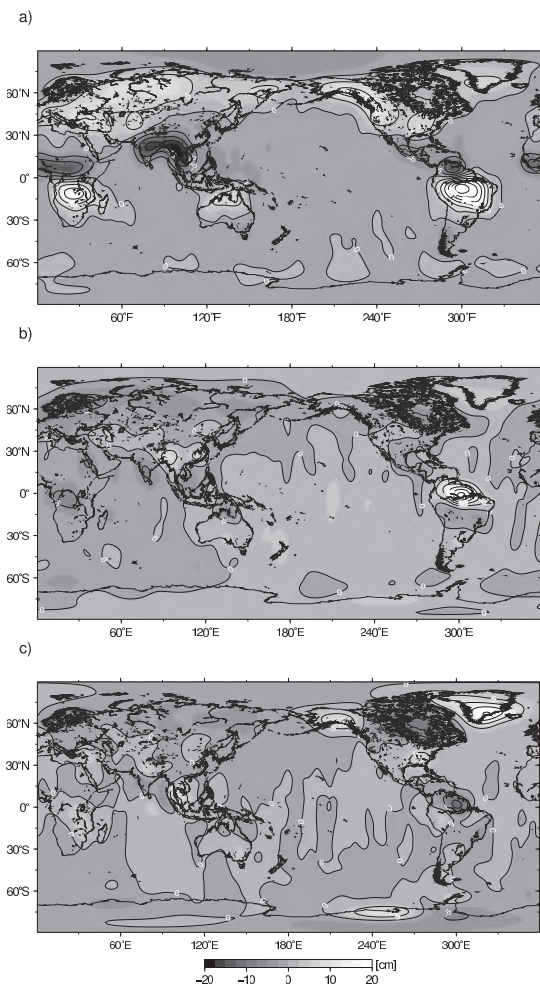
Figure 2.8: *a) First EOF mode associated with the spring-autumn cycle, accounting for 45.5 % of the total variance in the data set, b) second EOF mode representing the winter-summer cycle (10.7 %), and c) third EOF mode, associated with secular trends in the data (9 %) . In order to reconstruct the signal, the above grids need to be multiplied with the time series of the associated PCs in fig. 2.9. A Gaussian smoothing with a 500 km radius was applied. Maps are based on the CSR RL04 data between 2003 and 2008.*

(2006)). This inherently means that the modeling of the S_2 will be degraded in regions of poor observation quality, such as over the continental shelf where observations are obscured by non-tidal dynamics, and in regions with few observations available, e.g., in high-latitude areas covered with a (semi-)permanent ice-shelf.
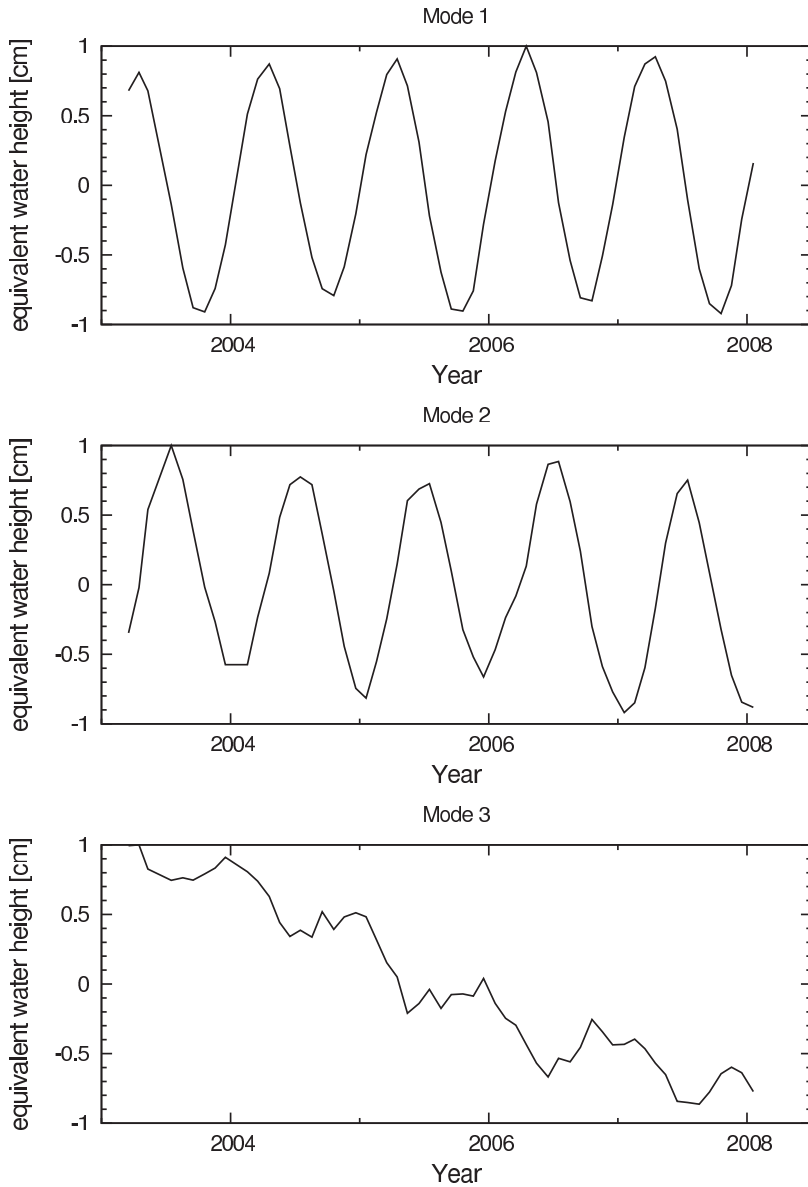
Figure 2.9: *Principal components associated with the first three EOF modes in fig. 2.8. Units are cm equivalent water height.*

The S_2 tide will alias into a signal with a period of approximately 161 days in the GRACE solutions (e.g., Ray and Luthcke, 2006). Such a harmonic is ob-
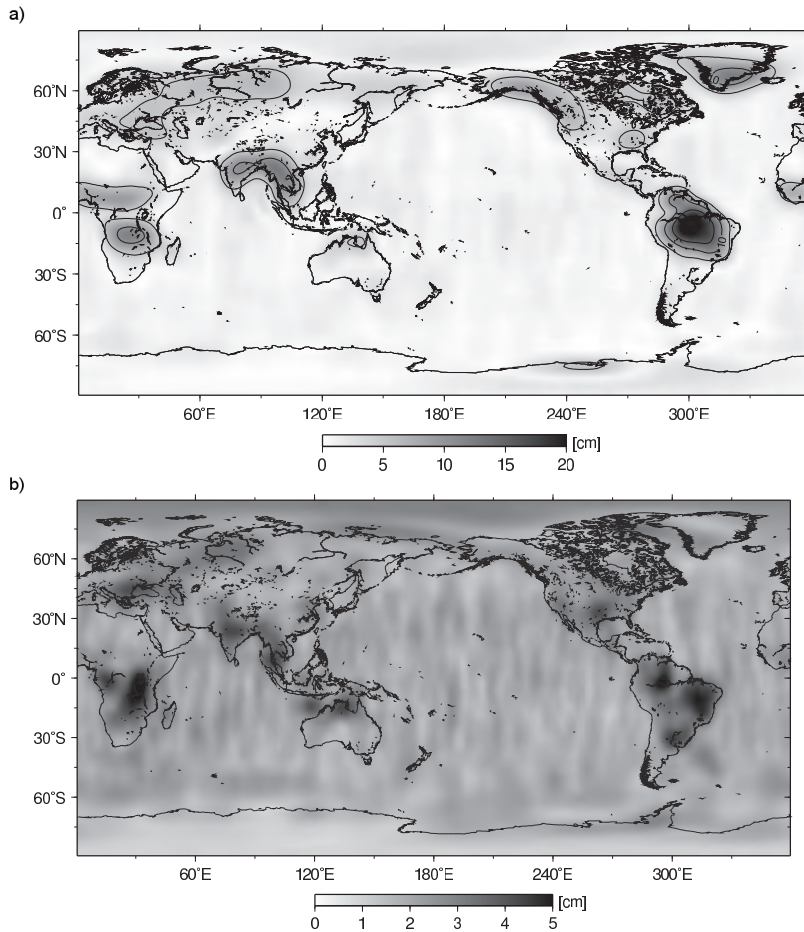
Figure 2.10: *Variance contained in a) the first three EOF modes, and b) modes four and upward. Units are cm equivalent water height. A Gaussian smoothing with a 500 km radius was applied. Note the difference in scale. Maps are based on the CSR RL04 data between 2003 and 2008.*

served in modes 11–15, most prominently in mode 11, where approximately 20% of the variance is explained by a cosine with a 161 days period. For the following modes, the explained variance is in the order of 5% at this period. In the spatial domain, strong amplitudes are found in shallow coastal regions with complicated tidal dynamics (e.g., Australian North West Shelf, Yellow Sea, Gulf of Thailand/Andaman Sea), regions with high meso-scale variability (e.g., Agulhas region) and regions covered with a (semi-)permanent ice-shelf (e.g., Weddell
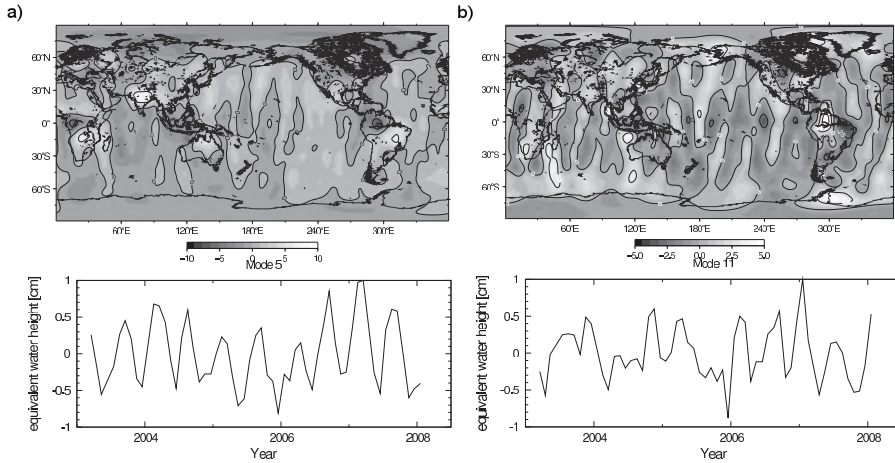
Figure 2.11: *EOF modes 5 and 11 and their respective principal components. Mode 5 is related to the semi-annual hydrological cycle, mode 11 to the aliasing of the S_2 tidal constituent. Maps are based on the CSR RL04 data between 2003 and 2008.*

Sea). A prominent continental signal is observed in the northern part of South America, which is most likely of hydrological origin. It should be remembered that the eigenvalues of the higher modes are closely spaced and therefore do not necessarily represent unique modes. With differences between the eigenvalues in the order of 0.5 %, modes 11–15 do not pass the rule-of-thumb of eq. 2.12 and a mixing of neighboring modes is likely to occur. Further tests show that the strong continental pattern in the Amazon basin vanishes – or rather, is displaced to another mode – when different observation periods and lengths are used in the principal component analysis. The major oceanographic patterns, however, remain grouped within one mode, which indicates that they have a common origin.

2.6.3 Long-periodic signals

A peculiar signal is observed in the principal component of mode number four, which shows variations at the semi-annual period, but in particular, at longer time-scales. The weak semi-annual period can be understood as a result of the fact that the fourth and fifth mode, which contains most of the power at the twice per year frequency, are poorly separated (following the rule of thumb given by eq. 2.12). To obtain a clearer picture of the long period signal, the EOF analysis was repeated after removing the annual and semi-annual signal in the GRACE solutions. The former fourth mode now explains about 10% of the total variance, second after the secular signal discussed in the preceding paragraph.

A possible explanation for this long-term feature could again be the alias-

ing of tidal residuals. For example, the K_2 and K_1 constituents both have an aliasing period of several years, i.e. approximately 3.7 and 7.5 years (Ray and Luthcke, 2006), and could therefore be causing the observed behavior. However, the majority of the signal in the EOF map occurs over land and could therefore be of hydrological origin. To test this hypothesis, the PC procedure was applied to modeled soil moisture and snow pack variations of the GLDAS hydrological model (Rodell et al., 2004), using identical months and following the same approach as used for the GRACE solutions. A similar signal is identified in the second mode, with a correlation between the GRACE and GLDAS principal components of 91% (fig. 2.12). This indicates that the fourth mode represents a true geophysical process and is not a result of tidal aliasing.

Comparing the EOF maps of the two data sets, several similar patterns are apparent. Negative amplitudes are observed in north-eastern South America, the southern regions of Africa, south-central Europe and along the east and west coast of North America. In the GRACE based EOF map, the south of Greenland also shows a positive anomaly (GLDAS does not include ice physics and glaciated areas have therefore been masked before applying the PC analysis). Positive, out-of-phase, patterns are found in eastern-central Africa, southern South America around the Parana river basin, the Ob river basin in Siberia, in North America in the Mississippi region and British Columbia, and to a lesser extent, around the Indus river. The relative amplitude differs between the two EOF maps, but it should be kept in mind that GLDAS does not model open water changes, which may explain the amplitude differences around Lake Victoria and the Black Sea. Moreover, ground water variations are not reproduced by the model (Rodell et al., 2004), which may cause underestimation of the variability of the total terrestrial water storage. In the Zambezi region, for example, groundwater variations contribute a non-negligible 10–20% of the total signal (Winsemius et al., 2006a).

Many of the regions described above are frequently mentioned in studies concerning the impact of the El Niño/Southern Oscillation (ENSO) on land hydrology. ENSO events are characterized by an above-average sea level pressure over the western Pacific, and a below-average pressure in the eastern Pacific. This causes the easterly equatorial trade winds to weaken in strength, resulting in a disturbance of the thermocline and ocean currents. Through atmospheric and oceanographic teleconnections, this will impact global weather, with precipitation anomalies occurring over 20–30% of the land area (Mason and Goddard, 2001). Precipitation increases in the southwestern and southeastern United States, the south of South America, southeastern Africa and in central Russia. Below-normal precipitation is prevalent over northern South America, southern Africa and parts of Australia. During La Niña events, when the aforementioned sea level pressure anomalies are reversed, opposite patterns are observed, although asymmetries exist (Mason and Goddard, 2001; Ropelewski and Halpert, 1996).

A commonly used indicator for ENSO events is the departure in sea surface temperature from the long-term mean averaged over a rectangle stretching from 5 N–5 S and 120–170 W in the Pacific. Periods in which the 5-month running mean
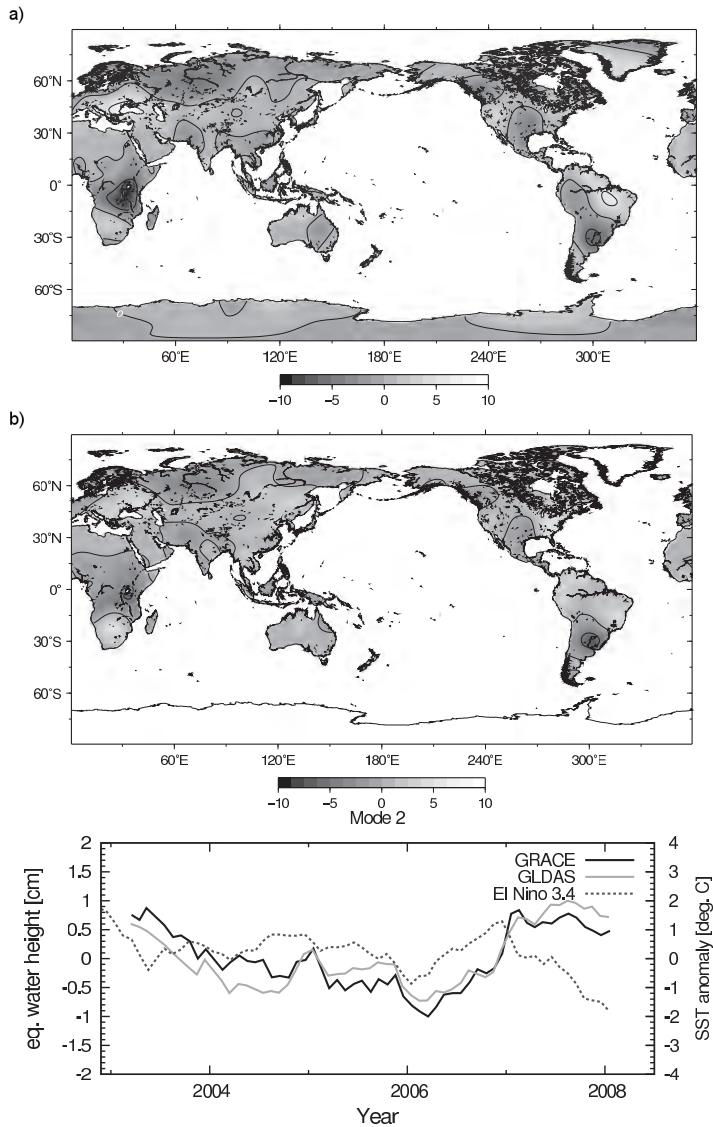
Figure 2.12: *Second EOF mode of a) the GRACE CSR RL04 data and b) the GLDAS model, after removing the annual and semi-annual components. The bottom figure shows the associated principal components and the El Niño 3.4 index.*

of this El Niño 3.4 index exceeds 0.4°C for at least 6 months in a row, are defined as El Niño events (Trenberth, 1997). Most recent El Niño events took place in

2002–2003 and 2006–2007, whereas a La Niña event occurred in 2007–2008. Late 2005-early 2006 the La Niña condition was almost met as well.

The temporal evolution of both the GRACE and GLDAS principal component corresponds relatively well with the El Niño 3.4 index, with a correlation in the order of 0.6, after smoothing both time series using a 5-month boxcar window. The principal components of the GRACE and GLDAS maps show a maximum around the aforementioned El Niño periods and a minimum during the La Niña episode. Maximum correlation is obtained at a lag of 3 to 4 months, i.e. surface water anomalies in GLDAS/GRACE lags relative to the El Niño 3.4 index. A divergence between the GLDAS/GRACE PC and El Niño 3.4 index seems to take place after 2007.

Given the fact that only relatively weak ENSO events occurred during the period under consideration, the GLDAS time-series was extended back to 1985 in order to test the significance of the correlation. A correlation of 0.62 is found between the El Niño 3.4 index and the second GLDAS mode, however, correlation between the latter and the second GRACE PC is marginal ($r \approx 0.35$) for the period 2003–2008. In contrast, the fourth 1985–2008 GLDAS PC is highly correlated (r=0.87) with the 2003–2008 GRACE PC, but the former correlates only weakly with the El Niño 3.4 index ($r \approx 0.3$). Whether this is a result of intercycle variability in the impact of the ENSO phenomenon on continental hydrology, or is due to another cause, remains to be studied. A longer observation period, covering more and, preferably, intenser ENSO events would be required to answer this question.

2.7 Filtering of the GRACE coefficients using EOF analysis

As shown in the previous sections, the striping patterns in the GRACE maps of EWH anomalies, can be significantly reduced by means of principal component analysis. However, more information might be revealed if a variation on this approach is used and the analysis is applied to groups of spherical harmonics directly, rather than to the maps based on the coefficients (Wouters and Schrama, 2007). Hence, instead of decomposing one time series of n maps into $n-1$ modes, a number of l_{max} groups of coefficient time-series will each be decomposed into $\max(n-1, q)$ modes, where q is the group size and l_{max} the maximal degree of the GRACE coefficients. This has the advantage that noise and signal can be separated in the individual time series of the coefficients, rather than in the smoothed sum of the whole (eq. 2.5). As a consequent, short-wavelength signals, which are suppressed in the smoothed maps of surface water height anomalies, may be retained more efficiently. If necessary, the filtered coefficients can still be combined with other filtering methods, e.g., a simple Gaussian smoother, to suppress any remaining noise.

2.7.1 Method

Given the correlation between the GRACE coefficients of even and odd degree l for a constant order m, as discussed in section 2.3 and Swenson and Wahr (2006), the spherical harmonics are grouped by keeping the order m fixed. Next, the EOF decomposition is applied to each of these series $\{C_m(t,l): l = m,\ldots,l_{\max}\,;\, t = 1,\ldots,n\}$ for $m = 0,\ldots,l_{\max}$ (and equivalent for the S_{lm} coefficients). For example, the data matrix Z for the C_{l0} coefficients will be:

$$
Z_{C_{m=0}} = \begin{pmatrix} C_{00}(t=1) & \cdots & C_{00}(t=54) \\ \vdots & \ddots & \vdots \\ C_{l_{\max}0}(t=1) & \cdots & C_{l_{\max}0}(t=54) \end{pmatrix} \tag{2.13}
$$

After obtaining the EOF modes e_j and associated PCs a_j, $j = 1,\ldots,\rho$, the selection rules – in this dissertation either the *Rule N* or *KS2* test – can be performed on each mode. If an EOF mode and/or principal component is identified by the test procedure as not being of random nature, the mode is retained and used to rebuild the series $C_m(t,l)$ and $S_m(t,l)$ using eq. 2.8. For m=$l_{\max}$, there is only one variable and the *KS2 test* is applied directly to the coefficients series, whereas in case of the *Rule N* it is simply omitted.

This procedure is illustrated in fig. 2.13 for $C_{l,m=0}$. The jth EOF modes $e_j(l)$ are plotted, for $j = 1 - 3$ in fig. 2.13a, and three higher modes, $j = 16 - 18$, in fig. 2.13b, together with the associated PCs $a_j(t)$. The results are based on 57 monthly CSR RL04 solutions, spanning March 2003 to January 2008. Because the construction of the PSD requires continuous data sets, two missing months in the time series (June 2003 and January 2004), were interpolated, yielding a set of 59 solutions. Since the GRACE project does not supply degree 1 coefficients, the model of Swenson et al. (2008) is used for seasonal variations of the geocenter.

The PCs of the first three modes exhibit a clear annual, semiannual, interannual and intra-annual signal and pass the *KS2 test*. Most power is contained in the Stokes coefficients of lower degrees up to degree $\sim$20. In contrast, the power in the EOF modes for j=13–15 is spread out over the entire range of coefficients with a bias towards the higher degrees. The temporal evolution of the PCs a much more random pattern and does not pass the *KS2 test*. Also, they represent an insufficient amount of variance to pass the *Rule N*. Consequently, these modes are not used to rebuild the filtered Stokes coefficients for order $m = 0$.

The number of accepted EOF modes depends on the order m and the kind of test used to select the EOF modes. Figure 2.14 shows the amount of original variance of the GRACE spherical harmonics retained after applying the *Rule N* and *KS2* test, respectively, i.e. the sum of the variances of the PCs a_j passing the tests normalized by the sum of variances of all PCs a_j. In case of the KS2-test, up to an order of ~ 10, almost all variance is retained, which agrees with the finding of Swenson and Wahr (2006) that the correlation between the even and odd coefficients starts at approximately this order. The *Rule N* is less selective
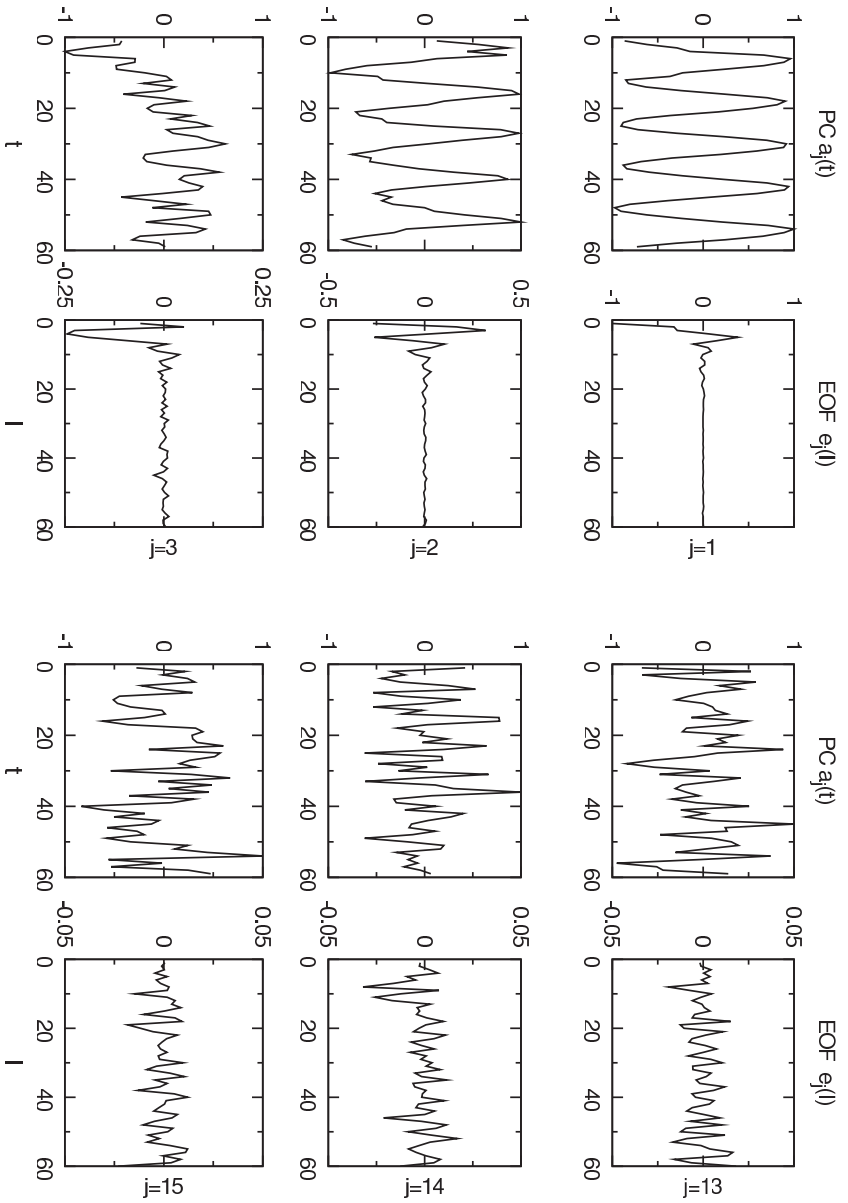
Figure 2.13: *Principal components and EOF modes of the $C_{m=0}$ Stokes coefficients: a) for EOF mode 1–3, passing the Rule KS2; b) for EOF mode 13–15, failing the KS2 test. The PC's have been scaled by 3.9e+09 to enhance presentation. Results are based on the CSR RL04 data between 2003 and 2008.*
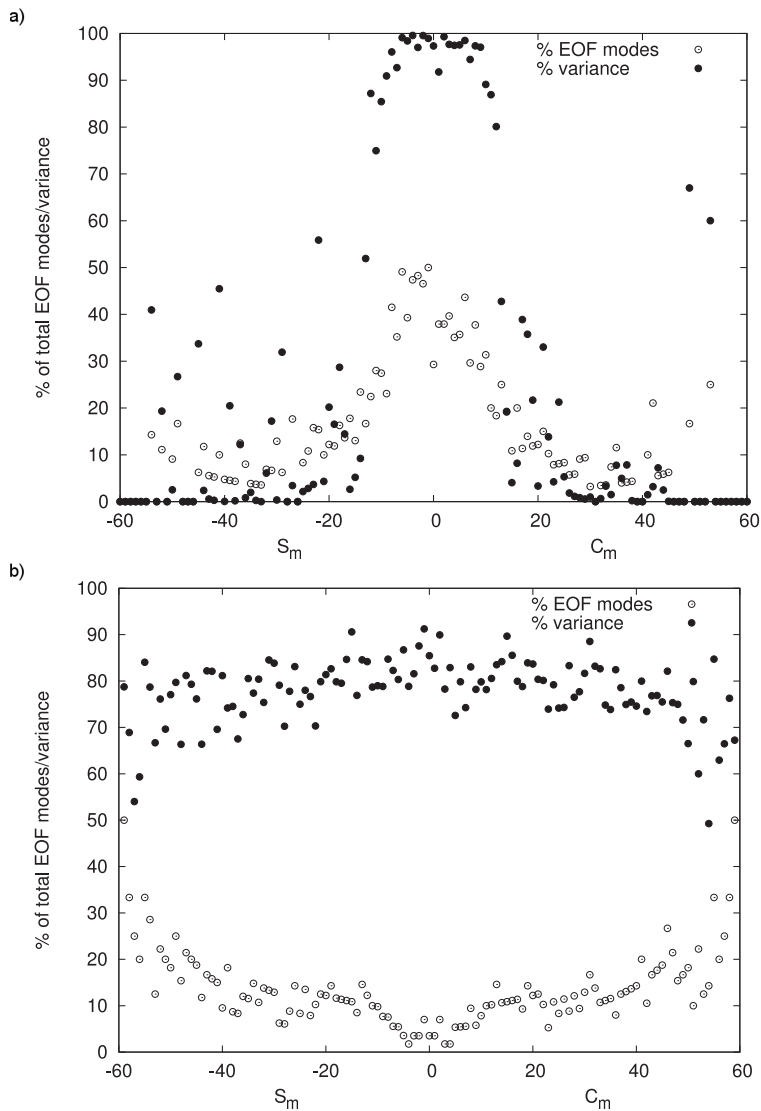
Figure 2.14: *a) Percentage of total EOF modes accepted by the Rule KS2 test (open circles) and percentage of the original variance contained in these accepted modes (black circles) for each order m series of Stokes coefficients; b) as a), but for the Rule N test. Data are based on the CSR RL04 data between 2003 and 2008.*

and retains all leading modes with a variance above the theoretical noise level, regardless of the order m.

2.7.2   Results

Figure 2.15 shows the variance in the maps of EWH anomalies before and after applying the EOF analysis to the spherical harmonics. Additionally, the maps have been smoothed with a 350 km Gaussian to suppress remaining noise. Although both selection rules reduce the variance significantly, the *Rule KS2* test clearly outperforms the *Rule N*, especially over the oceans. Furthermore, the latter results in a reduction of the signal present in the unfiltered GRACE maps, especially at higher latitudes (e.g., in the coastal zones of Greenland and East-Antarctica). The apparent reduction in noise level may therefore be a side effect of an overall reduction in the power of the signal. This is inherent to the nature of the *Rule N*, which lets pass the first few EOF mode without any further restrictions. However, there is no guarantee that these accepted modes represent true signal, or vice versa, that the rejected modes are related to noise. Given these limitation and limited quality improvement obtained by the Rule N in fig. 2.15, the focus of the remainder of this chapter will be on the KS2-test.

Figure 2.16 illustrates the effect of the *KS2* filtering method on the GRACE monthly EWH anomaly maps, when combined with Gaussian smoothing with various radii. The figures in the top row display the original fields, the middle row figures the fields after applying the EOF filtering to the spherical harmonics, the bottom row the difference between the filtered and unfiltered fields. Since almost all original variance is retained in the lower order spherical harmonics, the effect of the filter increases with decreasing smoothing radius.

At 350 km smoothing, little to none residual stripes are apparent in the filtered fields. Reducing the smoothing radius to 250 km results in some striping over the oceans and a of a horizontal pattern of alternating low and high variance along the Equator. As in the case of the 350 km smoothed fields, only a small amount of the original signal is removed in the polar regions, where the orbital groundtracks of the GRACE satellites converge, resulting in a better spatial and temporal coverage. Toward the equator, more signal is removed, with maxima along three bands approximately 30°N and 30°S and along the Equator. No coherent geophysical patterns are discernible, except for the traces of the 2004 Sumatra-Andaman Earthquake in South-East Asia. A plausible explanation is that episodic events are not well represented in the covariance matrix used in the PCA procedure, and are therefore not recognized as real signal (Klees et al., 2008).

Without any Gaussian smoothing (fig. 2.16a), the striping is still significantly reduced and the major hydrological signals are still easily discerned, although noise dominates the regions along the Equator. Additional analysis shows that this is caused by the near-sectorial ($l \approx m$) Stokes coefficients for $m > 45$, where the EOF decomposition is based on fewer data points and thus will be less effective. This phenomenon will be discussed in more detail in section 2.7.4.

a)

b)

c)
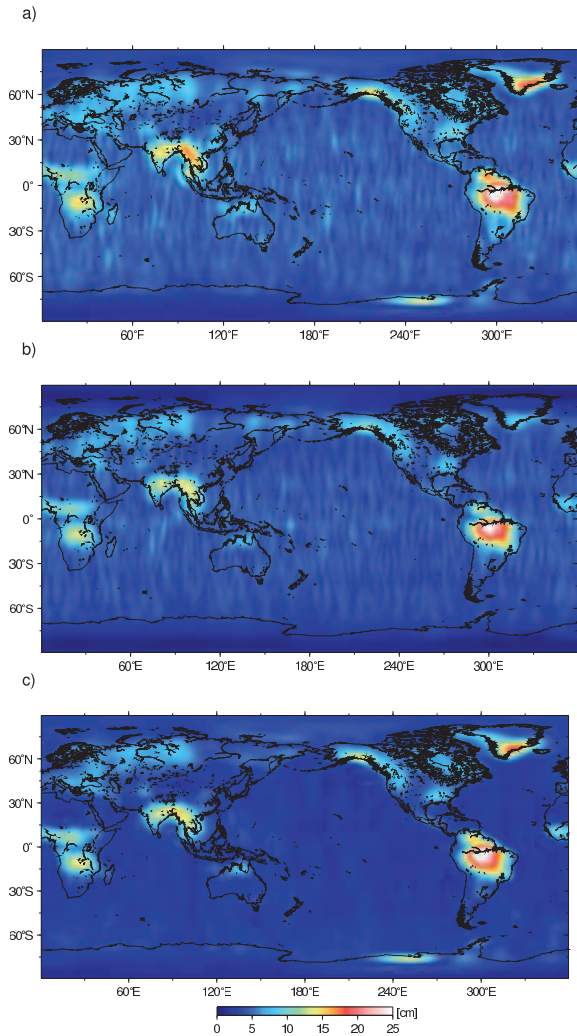
Figure 2.15: *Variance in the GRACE maps of EWH with a) no EOF filtering applied, b) selecting the EOF modes using the rule N test, and c) the Rule KS2 test on the principal components. Additionally, the results have been smoothed with a 350 km Gaussian to suppress remaining noise. Units are cm equivalent water height. Maps are based on the CSR RL04 data between 2003 and 2008.*

2.7.3 Spectral characteristics of the filtered coefficients

The degree amplitude of both the filtered and unfiltered GRACE coefficients, expressed in terms of geoid height, is depicted in fig. 2.17. Up to degree 12,
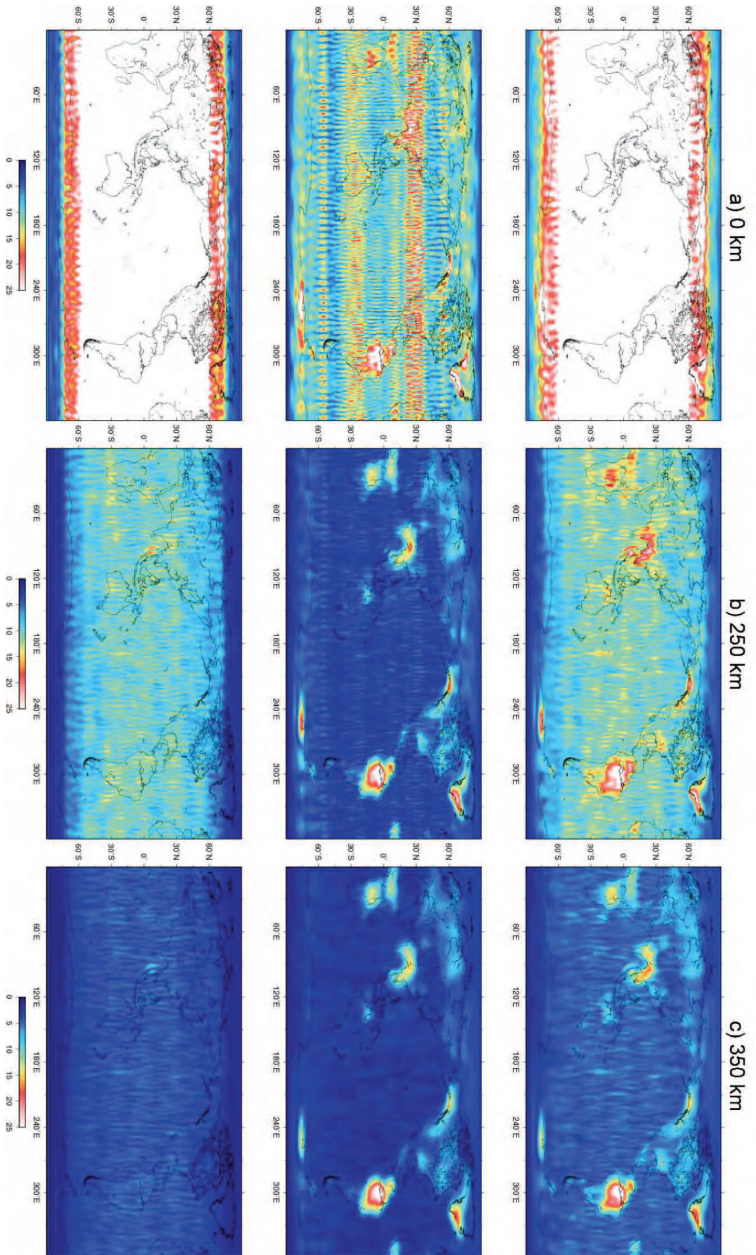
Figure 2.16: *Variance in the GRACE maps (2003–2008) of EWH smoothed with various radii (a) 0 km ; b) 250 km ; c) 350 km). The upper figures show the unfiltered fields, the middle figures are filtered with the EOF method. The lower figures represent the difference between the figures in the upper and middle row. Units are in cm. Maps are based on the CSR RL04 data between 2003 and 2008.*

the filtered and unfiltered curve follow each other closely. At higher degrees the degree amplitude of the unfiltered coefficients gradually increases as a result of an increasing contribution of measurement and other errors, whereas the degree amplitude of the filtered coefficients continues to decrease up to degree $l \approx 30$. A significant amount of the signal is removed for degree 15 and onward, with a degree amplitude reduction of up to 80% for the intermediate and higher degrees. Peaks in the filtered degree amplitude curve are found at degrees 50, 54 and 60, due to a contribution of the near-sectorial coefficients.
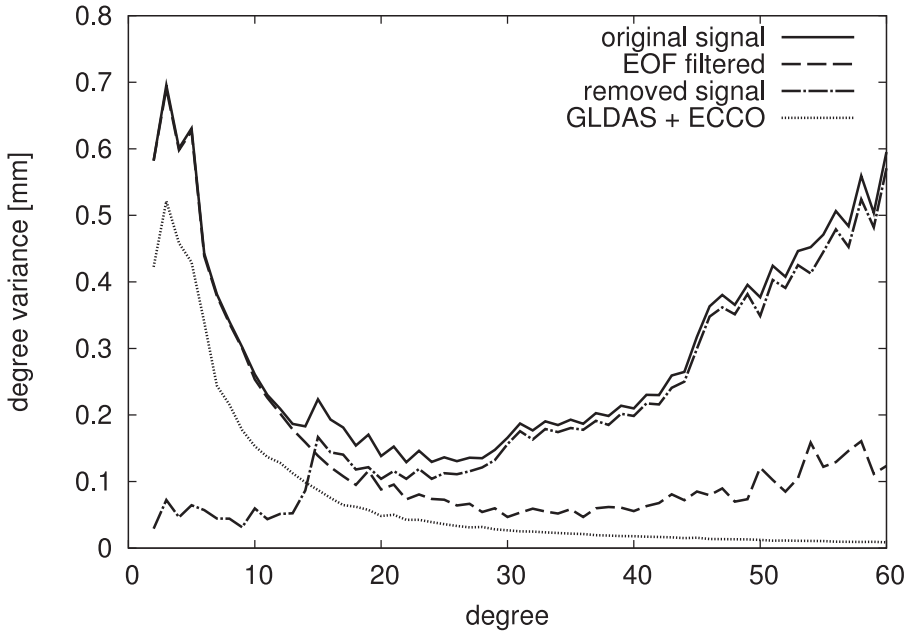
Figure 2.17: *Degree amplitudes of the geoid height anomalies before and after applying the EOF filter to the GRACE CSR RL04 coefficients, and of the difference between the two. As a comparison, the degree amplitude of geoid height anomalies based on a combination of the GLDAS and ECCO models is included.*

Figures 2.18a shows the variance in the individual spherical harmonics for the period 2003–2008. Most power is found in the coefficients of low degree and order, with a pattern comparable to what is obtained when using spherical harmonics based on a GLDAS and ECCO model combination for an identical period (fig. 2.18c). Notable differences arise at higher order, with three distinctive bands of high variance are visible at the orders $m \approx 15, 30$ and 45 and the zonal coefficients ($m = 0$). These are the order at which eq. 2.7 equals nearly zero, resulting in amplification of errors due to resonance (Kaula, 1966; Colombo, 1986). Furthermore, at higher degree and order the power of the coefficients becomes unrealistically high.
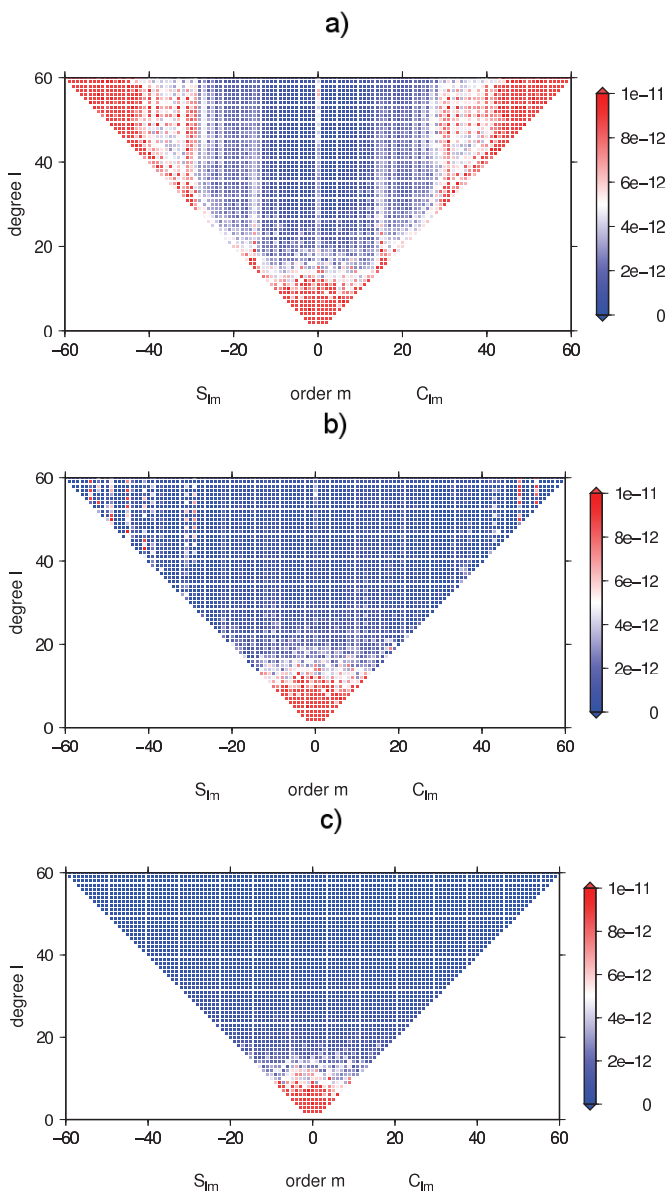
Figure 2.18: *a) Variance in the GRACE spherical harmonics for the period 2003–2008, b) as a), but after applying the EOF filtering to the coefficients, c) variance in the coefficients constructed using the GLDAS and ECCO model combination.*
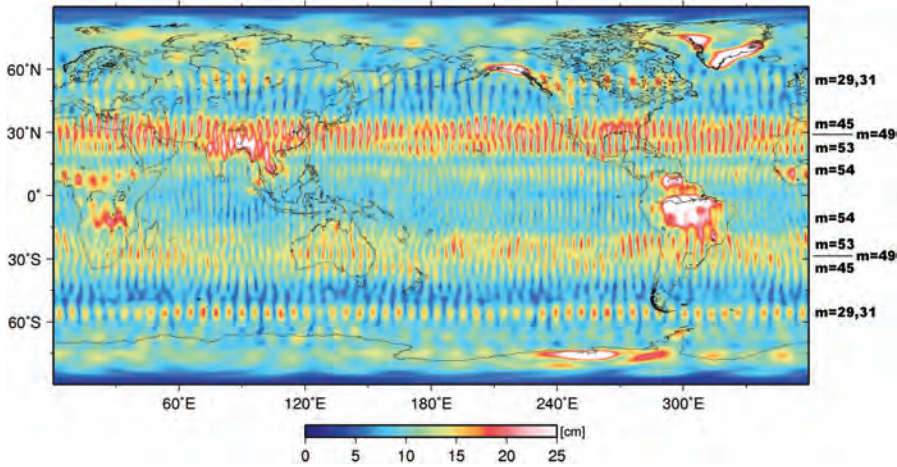
Figure 2.19: *Variance in the monthly CSR RL04 GRACE maps (2003–2008) after applying the EOF filter to the spherical harmonics. No additional Gaussian smoothing is applied. The orders m of the coefficients assumed to be responsible for the horizontal striping patterns are indicated in the right margin.*

Applying the EOF filter to the GRACE coefficients removes most of the power at the higher order and degree coefficients (fig. 2.18b) and brings the pattern of variance in close agreement with the GLDAS plus ECCO based predicted values. The variance in the GRACE coefficients remains higher at the lower orders and degrees, but it should be taken into account that the models lack several components of the water cycle, such as groundwater storage, glacier dynamics, etc.

2.7.4   Residual noise

As is evident from fig. 2.18b, some residual noise remains present at coefficients of specific order m, most prominent for $m = 29, 45, 49$ and $53 - 54$. This will result in the horizontal, latitudinal bands seen in fig. 2.19. By setting specific coefficients to zero, one may deduce the order of the coefficients responsible for the signal contamination at a certain band. This way, it is found that the bands at $\sim 60°$N and $60°$S are caused by the order $m = 29$ coefficients, and to a lesser extent also by those of order $m = 31$. Coefficients of order $m = 49$ and $m = 45$ are responsible for the contamination at $\sim 30°$N, whereas order $m = 53$ and $m = 54$ contribute to the noise further equatorward.

A closer inspection of the results of the principal component analysis learns that these signals are generally caused by the first or second EOF mode. The associated principal components show a non-random behavior, and pass the *Rule KS2* test. The majority of the PC time series show a peak during the sec-

ond half of 2004, when the GRACE satellites were in a near repeat orbit, re-
sulting in degraded quality of the recovered spherical harmonics, especially at
the small wavelengths. Besides the 2004 peak, some of the PCs show a peri-
odical variation. A spectral analysis indicates that most of the power is con-
tained at the annual ($C_{m=49}$; $S_{m=45}$, $S_{m=49}$ and $S_{m=54}$) and semi-annual fre-
quency ($C_{m=49}$, $C_{m=53}$; $S_{m=49}$).

Similar horizontal stripping patterns are found in the filtered JPL and GFZ
maps, indicating that the cause of the problem may lie in the GRACE groundtrack
characteristics, the satellite's instruments or one of the common correction models
used in the processing of the data, rather than in the procedures followed by the
different science centers.

2.7.5   Scaled errors of the filtered coefficients

The monthly releases of the GRACE spherical harmonic coefficients are accompa-
nied by calibrated error standard deviations for each coefficient, based on sub-set
and inter-month comparisons. Only the diagonal elements of the covariance ma-
trices are provided. These errors are calibrated for the unfiltered coefficients and
therefore are not representative for the errors in the filtered coefficients. To ob-
tain an estimate for the error standard deviations after filtering, the approach of
Liu (2008) is followed, and the provided standard deviation for each coefficient,
$\sigma_{lm,\text{C/S}}$, is rescaled using a factor $k_{lm,\text{C/S}}$ computed as the ratio of the temporal
variance of the filtered and unfiltered coefficient:

$$\sigma_{lm,\text{C}}^{\text{filtered}} \quad = \quad k_{lm,\text{C}}.\sigma_{lm,\text{C}} \qquad\qquad (2.14)$$

$$k_{lm,\text{C}} \quad = \quad \sqrt{\dfrac{\displaystyle\sum_{t=1}^{n}\{C_{lm}(t) - \overline{C}_{lm}\}^2_{filtered}}{\displaystyle\sum_{t=1}^{n}\{C_{lm}(t) - \overline{C}_{lm}\}^2_{\text{unfiltered}}}} \qquad\qquad (2.15)$$

, where the bar denotes the temporal average of the coefficient and $\sigma_{lm,\text{C}}^{\text{filtered}}$ the
estimated standard deviation after applying the EOF filter. A similar method is
used for the S_{lm} coefficients. Figure 2.21a shows the geographical distribution
of the calibrated error standard deviations for the CSR RL04 solutions, averaged
over the period 2003–2008, in terms of equivalent water height. No further Gaus-
sian smoothing is applied. The errors are mainly latitudinal dependent, with a
minimum in the polar regions where the satellites' groundtracks converge, and a
maximum near the equator.

A second method to estimate the errors in the GRACE EWH maps, is by
assuming that signals deviating from the secular trend and annual and semi-
annual harmonic are purely due to errors in the GRACE solutions (Wahr et al.,
2006). On one hand this approach may be overly pessimistic, since part of the
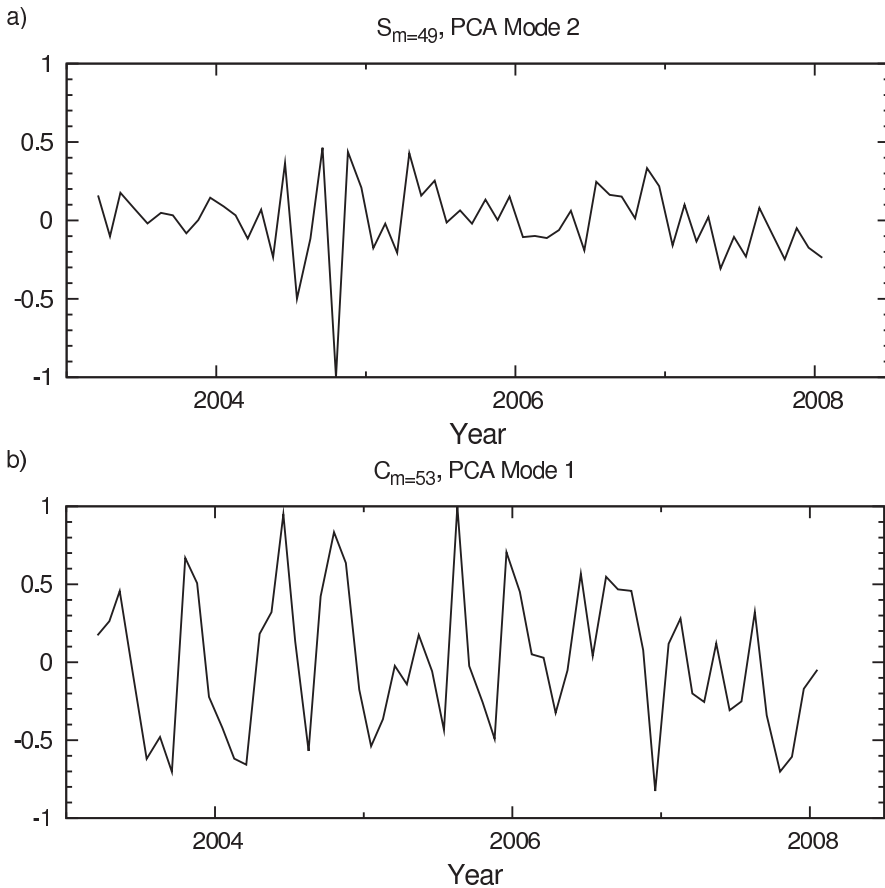
Figure 2.20: *Principal component of a) the second mode of the $S_{m=49}$ series and b) the first mode of the $C_{m=53}$ series. The former is related to the 2004 near-repeat orbit event, the latter shows a strong signal at the semi-annual frequency. Data are based on the CSR RL04 data between 2003 and 2008.*

residuals will represent geophysical signal. On the other hand, errors with (semi-)annual characteristics – which appear to be present the GRACE coefficients, as shown earlier – will be removed and not accounted for. Nevertheless, the error estimates obtained using this method, shown in fig. 2.21b, show good agreement with the calibrated errors. The errors are still mainly dependent on latitude, but longitudinal variations exist. The estimated errors are slightly lower at the poles and higher at the equator and display the horizontal striping patterns at 60°N and 60°S, discussed earlier.
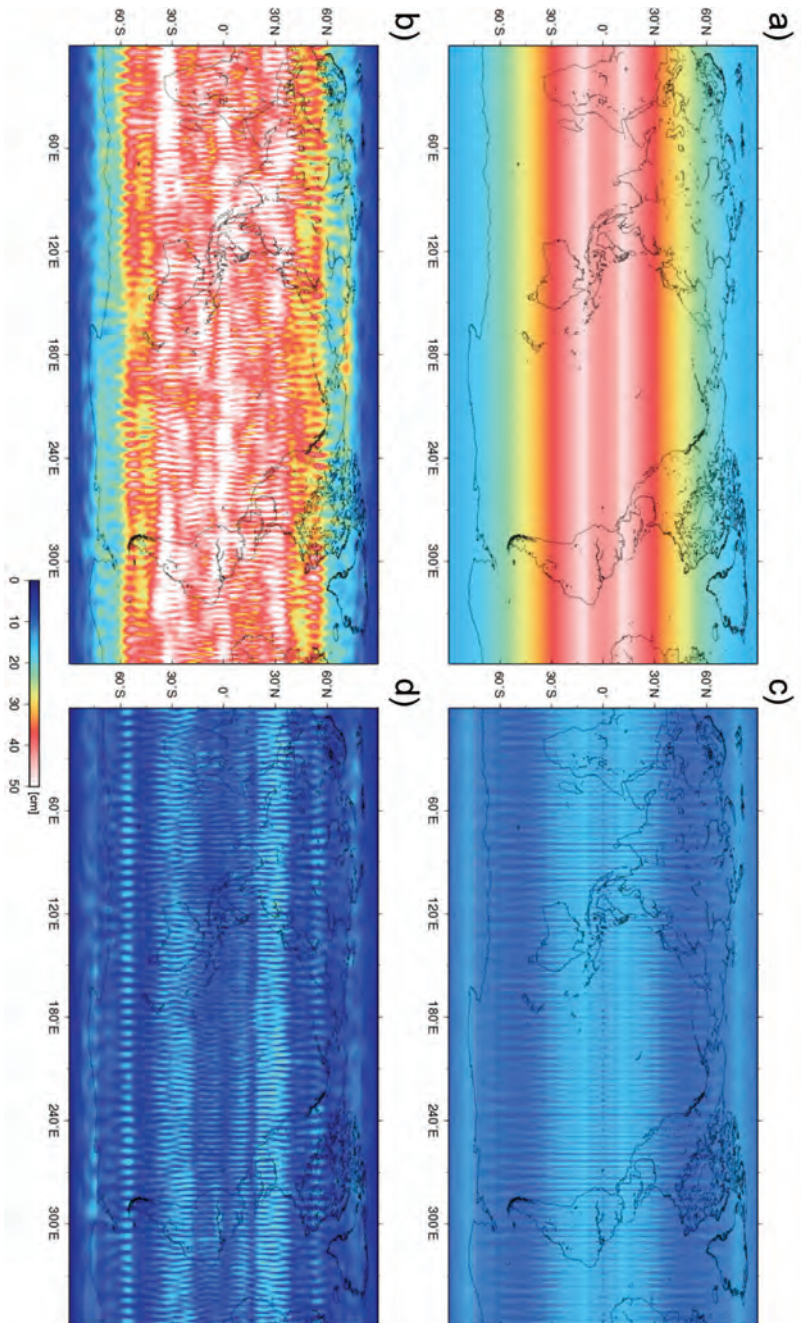
Figure 2.21: a) Geographical distribution of the calibrated error standard deviations for the CSR RL04 solutions, averaged over the period 2003–2008, in terms of equivalent water height. No further Gaussian smoothing is applied; b) RMS of the residual signal in the monthly GRACE maps, after removing a trend, annual and semi-annual signal; c) + d): as in a) and b), but after applying the EOF filter to the coefficients.

2.8   Conclusions

In this chapter, it has been shown how principal component analysis can be used to analyze and improve the GRACE data. By decomposing the GRACE maps of EWH to the orthogonal EOF maps and their associated principal components, the dominant signals can be separated from signals which are less coherent in space and time. This way, the typical north-south striping in the GRACE solutions is reduced in the leading modes and an improved spatial resolution is obtained. The first three modes are related to the annual, secular and semi-annual components. A long-period signal is observed in the fourth mode, with most of its signal in the regions typically affected by the ENSO cycle, however, a longer period of observations is required to confirm the relation between the two.

The noise in the GRACE solutions can be even further reduced by applying the principal component analysis directly to the spherical harmonics. This way, a maximum amount of information contained in the original spherical harmonics solutions can be retained. After decomposition, the principal components modes are tested for temporal noisiness and rejected if their power density spectrum resembles that of a white noise process. In contrast to most other filtering methods (e.g Chen et al., 2006a; Swenson and Wahr, 2006; Kusche, 2007), the EOF filter is based on the entire temporal history of the monthly GRACE solutions. This means that solutions with a lower quality will have an influence on the other solutions in the data sets. In some of the higher near-sectorial coefficients, remnant noise is observed after applying the EOF filter. This results in a distinct horizontal striping patterns at certain latitudes. The signal is non-random and appears to be partly related to the 2004 near-repeat orbit event.

It should be stressed that the two EOF methods presented in this chapter are complementary. Applying the analysis to the spherical harmonics directly is a tool to reduce the striping patterns, whereas applying the analysis to the (then filtered) maps of EWH serves as a tool to interpret the observed signals. By combining the two, a higher spatial resolution in the latter step can be obtained. For example, whereas in the original, unfiltered maps the fifth (semiannual) EOF mode starts to shows signs of stripes at a Gaussian resolution of 500 km, an analysis at a resolution of ∼350 km is possible when the spherical harmonics are filtered with the EOF technique first, as illustrated in fig. 2.22.

a)

b)
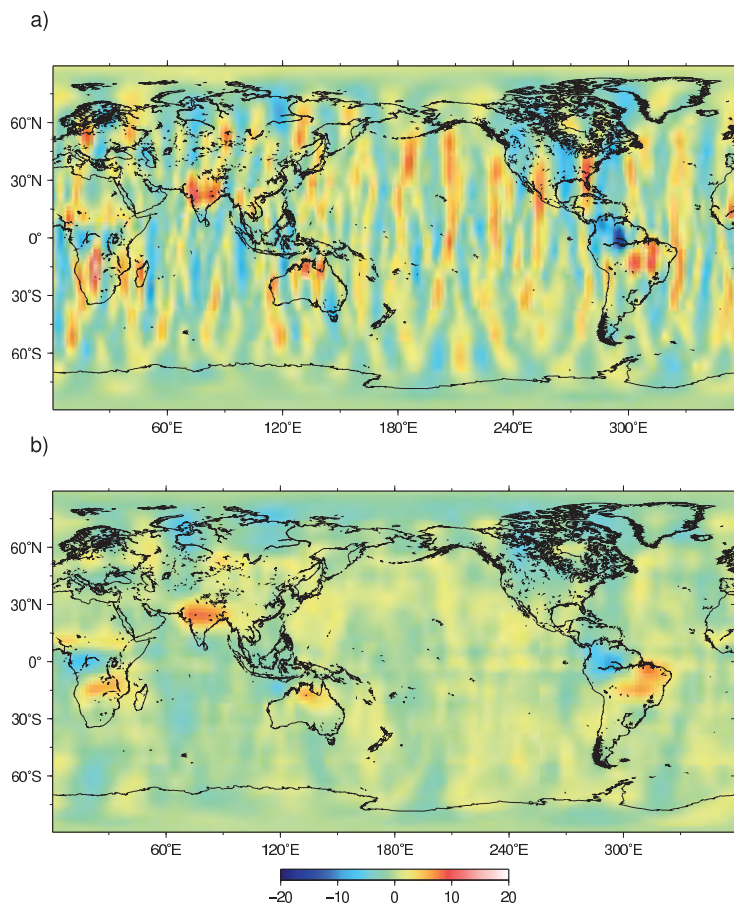
Figure 2.22: *Fifth EOF mod EOF the GRACE EWH maps, associated with the semi-annual cycle as discussed earlier; a) Gaussian smoothing with 350 km radius applied, b) idem, but with the EOF filter applied to the spherical harmonics first. Maps are based on the CSR RL04 data between 2003 and 2008, units are cm.*

Chapter 3

Assessing the Performance of the EOF Filter

3.1 Introduction

In the preceding chapter, it was shown how the north-south striping in the GRACE solutions can be reduced by applying EOF decomposition to the GRACE spherical harmonics (see also, Wouters and Schrama (2007)). In this chapter, the improvement in quality and resolution realized by this filtering technique will be quantified. The effect of applying the EOF filtering to the GRACE spherical harmonics will be discussed for three different levels of α in the Kolmogorov-Smirnov (KS2) test ($\alpha = 0.01, 0.025$ and 0.05), and will be compared to one of the presently most commonly used post-processing filter, i.e. the destriping filter of Swenson and Wahr (2006) as adapted by Chambers (2006b). This type of filter removes an nth order polynomial from even and odd coefficient series starting at an order m_{start}, leaving the lower degree/order coefficients unchanged. Of the latter, two different versions will be studied, i.e. one filter based on a 5th order polynomial starting at order 12 (updated version of Chambers (2006b), tailored for the CSR RL04 data (Chambers, personal communication, 2008)) and one filter based on a 4th order polynomial starting at order 6 (as in Chen et al. (2007b,c)). In the plots following, these two filters will be referred to as the 'O5M12' and 'O4M06' destriping filters respectively, according to the order of the fitted polynomial (O) and the order (M) of the coefficient at which the fit is started.

Since no in-situ data set directly comparable to the GRACE data is available at present, no straightforward method exists that give a conclusive answer about

the obtained improvement by filtering. However, several tests can give an impression of the decrease in contamination by noise of the GRACE maps, or likewise, the possible increase in resolution, after filtering. In a first test, the residual signal after removing seasonal and secular variations will be discussed. Secondly, GRACE observations in a region where little hydrological activity is expected is studied. Thirdly, vertical deformation of the solid Earth based on the GRACE data is compared to vertical deformation observations from GPS stations.

Filtering the GRACE fields will inevitably remove some of the real signal in the GRACE solutions (e.g., Swenson and Wahr, 2006). In a second part of this chapter, this problem is addressed by applying the filters to synthetic maps of surface water height anomalies based on numerical models. Special attention is paid to trends in the data. In the last section, the influence of the filtering on secular trends is studied through a case-study of the Greenland ice sheet.

3.2 Non-seasonal signals

As discussed in Ch. 2, the errors in the GRACE EWH maps can be estimated using the empirical approach of Wahr et al. (2006), by assuming that signals deviating from the secular trend and annual and semi-annual harmonic are purely due to errors in the GRACE solutions. On one hand this approach will be overly pessimistic, since part of the residuals will be real geophysical signal. On the other hand, errors with (semi-)annual characteristics – which are present in the GRACE coefficients, as shown in Ch. 2 – will be removed and not accounted for. Nevertheless, this method can give a rough impression of the impact of filtering on the overall quality of the GRACE solutions.

The method used is fairly straightforward: by means of least squares linear regression, the annual and semi-annual harmonic, together with a mean value and a secular trend, are estimated at every grid point in the EWH maps, using data of the period 2003–2008. These signals are then removed from the grids and the mean root mean square (RMS) is calculated. This procedure is then repeated for the different filters and a range of Gaussian smoothing radii between 750 and 0 kilometers.

At the larger smoothing radii, the signal in the GRACE maps is governed by the lower degree spherical harmonics, which are largely unaltered by both types of post-processing filters (fig. 3.1). The effect of filtering is noticeable at a (Gaussian) resolution of ∼600 km and higher. Divergence between the different techniques occurs at approximately 300 km, when the higher order coefficients become relevant. Due to its higher polynomial order, the destriping algorithm of Chambers (2006b) will remove more signal than the 4th order polynomial used by Chen et al. (2007b,c). Likewise, lowering the α-level of the KS2 test results in a stricter selection of the EOF modes to be retained, thus lowering the residual signal RMS. When no Gaussian smoothing is applied, the RMS is reduced by 60 to 80%, depending on the filter type. Results for the destriping filter of Chambers
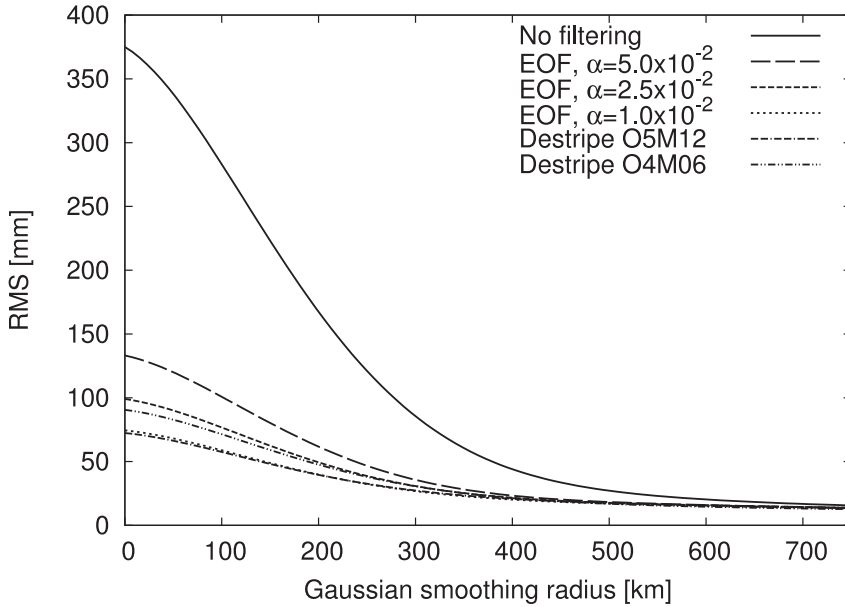
Figure 3.1: *RMS of the signal in the unfiltered and filtered GRACE CSR RL04 EWH fields, after removing the secular trend and annual and semi-annual harmonic, for varying smoothing radius. Filters used are the EOF filter applied to the spherical harmonics, with varying α-level of the KS2-test, and two destriping algorithms with different polynomial order (O) and starting order (M). Units of RMS are millimeters.*

(2006b) are about equal to those obtained by the EOF filter with α_{KS2} set sto 0.01.

3.3 Arid region test

A second empirical method to asses the obtained improvement, is by comparing the signal in regions where little to no signal is expected to occur (e.g., Klees et al., 2008). Assuming that all observed variability is due to erroneous signal in the GRACE data, this gives an indication of the residual noise in the observations. A prime candidate for such an *arid region test* is the Sahara desert, which is known to exhibit only marginal variations in groundwater and surface water storage.

For this test, a region in northern Africa was selected where the GLDAS hydrological model (Rodell et al., 2004) shows an RMS of 2.5 cm EWH or lower between 2003 and 2008. Locations within 500 kilometers of the coast were omitted to reduce leakage from signal in the neighboring oceans and seas, see inset of fig. 3.2.

The root mean square of the signal in the Sahara region was computed for the period 2003–2008, for varying Gaussian smoothing radii and the filters under

Figure 3.2: *RMS of unfiltered and filtered GRACE CSR RL04 fields in the indicated region, for various Gaussian smoothing radii. Filters used are the EOF filter applied to the spherical harmonics, with varying α-level of the KS2-test, and two destriping algorithms with different polynomial ord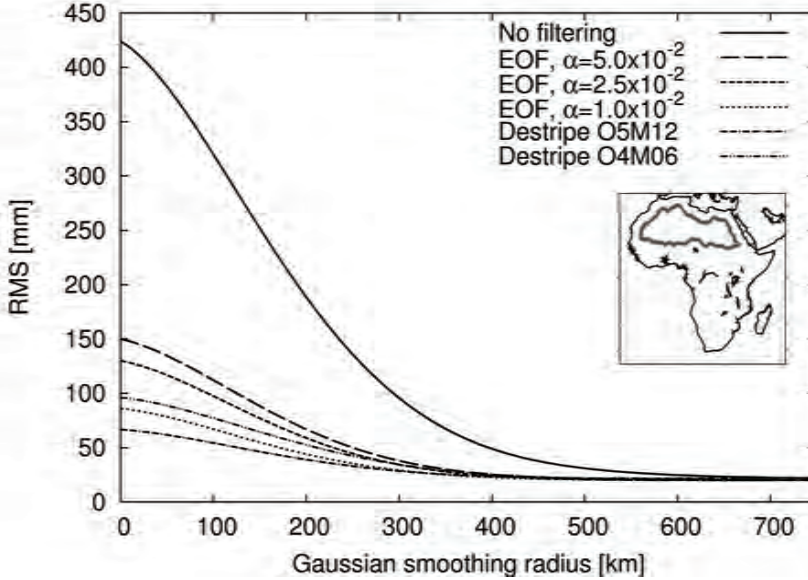er (O) and starting order (M). Units of RMS are millimeters. Inset: Area used in the arid region test, roughly corresponding to the Sahara–Sahel.*

consideration. When no additional filtering is applied to the spherical harmonics, the RMS increases rapidly from ∼20 mm at 750 km Gaussian smoothing, to approximately 110 mm and 425 mm, at 250 km and 0 km respectively. Applying filtering results in an nearly constant RMS up to a smoothing radius of ∼350 km, regardless of the filter type. At higher resolutions, the RMS in the maps based on the EOF filtered spherical harmonics increase most rapidly for $\alpha = 0.05$ and $\alpha = 0.025$. Reducing the α-level of the KS2-test to 0.01 results in RMS values comparable to those obtained by the polynomial destriping procedure. The destriping filter based on Chambers (2006a) yields the lowest overall RMS, due to the fact that nearly all signal in the higher order coefficients is removed by the 6th order polynomial fit.

The different results between the different filtering techniques can partly be explained by the nature of the remnant noise. For the destriping algorithms, traces of residual noise are most eminent in a band around the equator (Swenson and Wahr, 2006). In Ch. 2 it was shown that when applying the EOF filtering to the spherical harmonics, these noise artifacts are most dominant at ∼ 30°N (and S), i.e. the latitude where the Sahara is approximately situated.

3.4   GPS test

Variations in loading of the Earth's surface by changing water mass loads will cause an elastic deformation of the solid Earth. Measurements of these vertical displacements, such as made by GPS stations, offer a possibility to validate the GRACE measurements, as demonstrated in, e.g., van Dam et al. (2007) and Schrama et al. (2007). In contrast to the previous to tests, this approach does not solely depend on the GRACE observations and makes use of independent data.

Variations of the GRACE geopotential coefficients are directly related to radial displacements of the Earth's surface, $\Delta \bar{r}(\theta, \phi)$, through the vertical load Love numbers h_l':

$$\Delta \bar{r}(\theta, \phi) = a_e \sum_{l=0}^{l_{\max}} \sum_{m=0}^{l} W_l \tilde{P}_{lm}(\cos \theta) \frac{h_l'}{1 + k_l'} [\Delta \tilde{C}_{lm} \cos(m\phi) + \Delta \tilde{S}_{lm} \sin(m\phi)] \quad (3.1)$$

where the symbols are conform to those used in eq. 1.6, (e.g., Kusche and Schrama, 2005).

In this section, measurements at 206 GPS sites are compared to filtered and unfiltered GRACE data. The data represent weekly GPS height residuals with respect to the International Terrestrial Reference Frame and were processed by R. Ferland by combining solutions from several International GNSS Service (IGS) processing centers (Ferland et al., 2000). Only data between 2003 and 2008, corresponding the GRACE observation period, were used.

A fundamental difference between the GRACE and GPS data is the type of reference frames they are provided in. Due to the mission's structure (see Ch. 1), the GRACE satellites cannot observe changes in the Earth's center of mass and degree 1 coefficients are missing in the monthly solutions. On the other hand, the GPS stations are fixed to the Earth's surface and are relative to the center of figure (CF) of the Earth. Therefore, the geocenter motion model of Swenson et al. (2008) was added to the GRACE solutions. When translating these degree 1 coefficients to radial deformation, use was made of the CF load Love coefficients h_1' and k_1' (Blewitt, 2003).

The weekly GPS observations contain a significant amount of noise at periods of less than a month. Both data sets are therefore pre-processed by fitting an annual, semi-annual and tri-annual harmonic to the observations and removing the residuals. A linear trend is fitted as well, but is not used in the comparison (Schrama et al., 2007).

During the processing of the GRACE data, high-frequency ocean and atmosphere mass variations are removed to prevent aliasing. To obtain a representative loading signal, the ocean component is added back to the GRACE observations. Atmospheric variations are not considered, but are removed from the GPS data by means of the National Center for Environmental Prediction (NCEP) reanalysis surface level pressure data (Schrama et al., 2007).
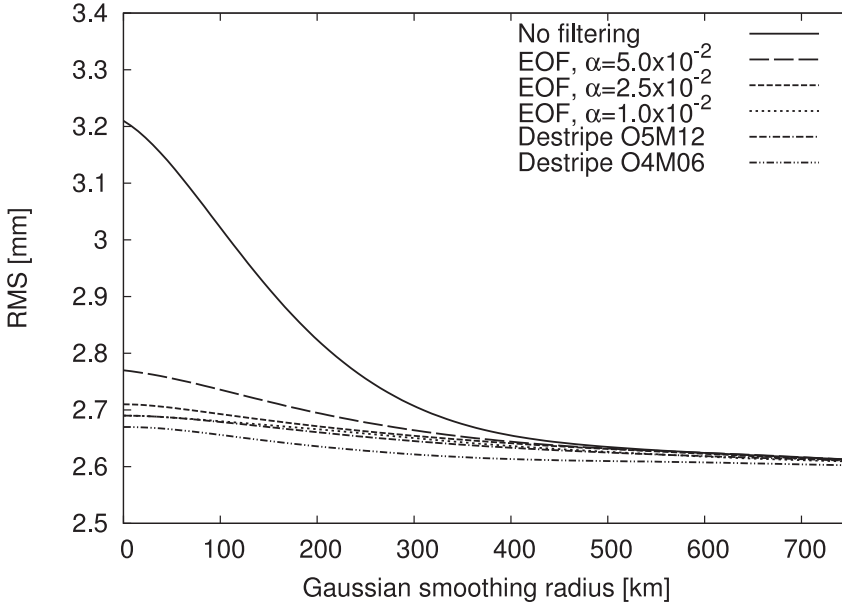
Figure 3.3: *Global mean RMS of the difference between vertical deformations as measured by GPS and derived from the unfiltered and filtered GRACE CSR RL04 fields, for various Gaussian smoothing radii. Filters used are the EOF filter applied to the spherical harmonics, with varying α-level of the KS2-test, and two destriping algorithms with different polynomial order (O) and starting order (M). Units of RMS are millimeters.*

After pre-processing, the vertical deformations from the GRACE and GPS data are differenced, and the mean weighted RMS is computed. Depending on the smoothing radius of the GRACE solutions, the RMS varies between 2.6 and 3.2 millimeters, see fig. 3.3. Differences between the two data sets can be attributed to errors in the GRACE data, increasing when decreasing the smoothing radius, and errors in the GPS data due to various sources, such as mismodeling of tidal loading, orbital errors, multipath scatter, etc. Many of these errors are known to have an annual or semi-annual dependence (see, e.g., Dong et al., 2002; van Dam et al., 2007, for an overview). A further discussion of these differences is out of the scope of this dissertation, the focus of the remainder of this section is on the reduction of the difference obtained through filtering of the GRACE data.

Compared to maps of equivalent water height, the radial deformation maps are less sensitive to higher degree coefficients. The lower degree coefficients are largely unaffected by the applied filtering and the effect of filtering is less pronounced than in the previous two sections. Nevertheless, a reduction of the RMS between 14 and 17% is obtained after filtering at the full resolution of the GRACE data, depending on the filter type (fig. 3.3). The reduction Γ for a station is computed as:

$$\Gamma = \frac{\mathrm{RMS}(\mathrm{GRACE}_{\mathrm{nofilter}} - \mathrm{GPS}) - \mathrm{RMS}(\mathrm{GRACE}_{\mathrm{filter}} - \mathrm{GPS})}{\mathrm{RMS}(\mathrm{GRACE}_{\mathrm{nofilter}} - \mathrm{GPS})} \qquad (3.2)$$

The destriping filter of Chambers (2006b) and the EOF filter with $\alpha_{\mathrm{KS2}} = 0.01$, perform about equally well. Slightly lower RMS values are found when using the filter of Chen et al. (2007b,c). The fact that the RMS is systematically lower at all smoothing radii, indicates that part of the difference between the GPS and GRACE data is caused by a signal in the lower spherical harmonics of orders $6 < \mathrm{m} < 11$.

Figure 3.4 illustrates the reduction in RMS of the GRACE-GPS differences at the individual GPS stations, obtained after filtering the GRACE spherical harmonics with the EOF filter ($\alpha_{\mathrm{KS2}} = 0.025$). No further Gaussian smoothing is applied to the GRACE solutions. At the individual stations sites, the median reduction is 16%. A maximum reduction of 80% is found at the San Fernando (SFER) station, located at ($353.8°$ E; $36.3°$ N), a minimum (i.e. increased RMS) of -64% at Guatemala (GUAT) at ($269.5°$ E; $14.5°$ N). Of the 206 GPS sites, the majority (80%) shows a reduction, although in some cases (20%) the RMS increases slightly. The effect of applying the EOF filter to the spherical harmonics is illustrated in fig. 3.5, for the BRAZ station located at ($312.12213°$ E; $15.84°$ S).

3.5 Effect on modeled signals

3.5.1 Method

In the previous three sections, in was shown that post-processing of the GRACE data, either through the destriping algorithm or by applying EOF decomposition to the spherical harmonics, significantly reduces the variance of the signal in the GRACE solutions. Based on the spatial characteristics of the removed signal, it can be assumed that the majority consists of noise. However, any kind of filtering will inevitably affect the real geophysical signals present in the observational data.

In the following, it will be discussed to which extent the EOF filtering of the spherical harmonics influences the behavior of geophysical signals, and the results will be compared to those of the destriping algorithms of Chambers (2006b) and Chen et al. (2007b,c).

For this purpose, a set of 100 monthly synthetic geopotential solutions was created, using surface mass anomalies obtained by combining output from the hydrological GLDAS model with the ocean bottom pressure estimates from the OMCT baroclinic model (Dobslaw and Thomas, 2007). At each time-step, a uniform layer of water was added to the oceans to ensure mass conservation in the system. These monthly fields were first converted to spherical harmonics of the geopotential field (up to degree $l_{\mathrm{max}} = 60$), to which then the different filter
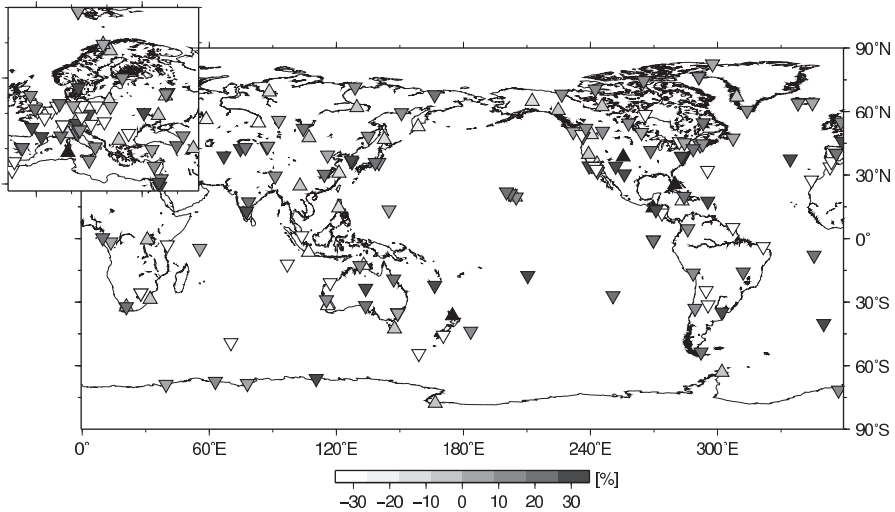
Figure 3.4: *Reduction in RMS of the difference between vertical deformation observed by GPS and GRACE, at the 206 individual GPS stations, obtained after filtering the GRACE spherical harmonics with the EOF filter ($\alpha_{\mathrm{KS2}} = 0.025$). No Gaussian smoothing is applied to the GRACE maps. Downwards pointed triangles symbolize a reduction of the variance, i.e., a better agreement between GPS and GRACE observations. Units are percents.*

methods were applied. After converting back to EWH anomalies, the filtered and unfiltered fields are compared and the variance of the individual monthly differences is computed. The variance of the difference is preferred above the mean difference, since the latter may be influenced by artificial signals introduced by the filter, as will be demonstrated later.

3.5.2   Results

Figure 3.6 shows the variance in 60 monthly fields of simulated equivalent water level anomalies, a) for the unfiltered maps, b) after filtering with the destriping algorithm of (Chambers, 2006b) and c) EOF filtering applied to the spherical harmonics. Major geophysical signals are largely unaffected by the two filtering methods, but nevertheless there are significant differences at some locations. Most striking is the fact that the destriping algorithm (only the version of Chambers (2006b) is shown, results for Chen et al. (2007b,c) are similar) appears to introduce artificial signals to the variance map, e.g., of the coast of Alaska and north of the Amazon estuary. This is even more evident in fig. 3.7, where the variance of the differences of the filtered and unfiltered maps are shown.

Most of the variance patterns introduced by the destriping filter are orientated diagonally and along the north-south direction. A possible explanation could be
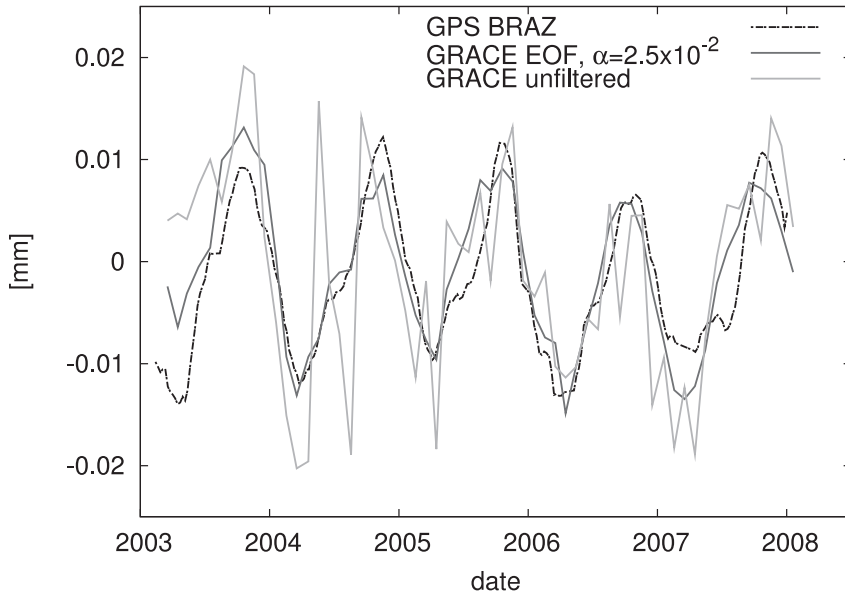
Figure 3.5: *Comparison of vertical deformation measured by GPS at the BRAZ station (312.12213° E; 15.84° S), and by GRACE at the same location, with and without EOF filtering of the spherical harmonics applied. The weekly GPS data is smoothed using a 2-month moving boxcar filter.*

that the filter amplifies the Gibbs phenomenon, occurring through the limited spatial resolution of the models and the discontinuities along the coasts. However, applying the same procedure to fields smoothed at 500 km radius before decomposition to spherical harmonics (which should eliminate the Gibbs phenomenon to a large extent), shows the same features. Therefore it may be concluded that the introduced signals are a result from the filter itself, which removes preferably signals orientated in a quasi north-south direction by "reducing the contribution of a central stripe (via negative lobes) while increasing the contribution of neighboring stripes which are out of phase with the central stripe" (citing Swenson and Wahr (2006), see also fig. 4 herein). Besides introducing artificial signals, this also results in the removal of real signal with a quasi north-south orientation, e.g., along the westcoast of North America and the tip of South America. Furthermore, the destriping filter tends to stretch the signal in the east-west direction, e.g., in Central Europe.

In contrast with the destriping algorithm filter, the EOF filter is shape preserving, i.e. the spatial characteristics of the variance maps are retained. No artificial signals are introduced and no stretching of the variance patterns is observed. This can be explained by the fact that the EOF filtering is based on the temporal behavior of the data, rather than on the spatial orientation of the signal. Hence, the

a)

b)

c)
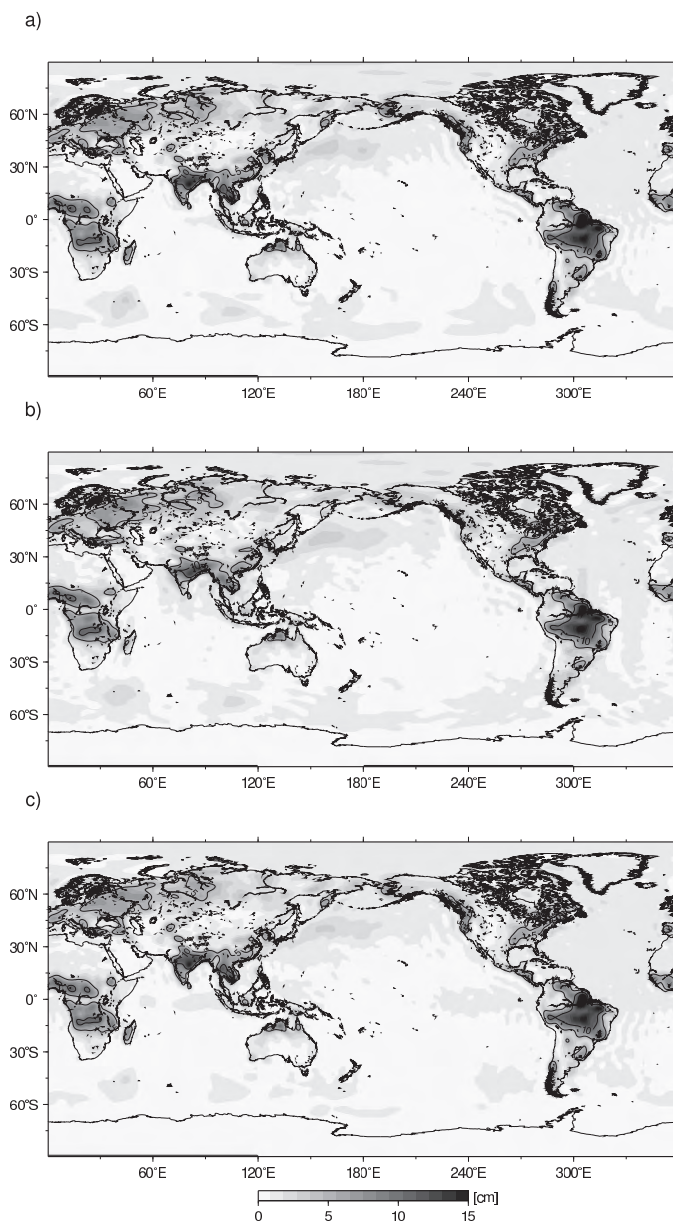
Figure 3.6: *Maps of the variance in 60 monthly maps of simulated surface water loading, unsmoothed and truncated at degree $l = 60$. a) Unfiltered field, b) destriping algorithm of Chambers (2006b) filter applied, and c) EOF filter applied to spherical harmonics ($\alpha_{KS2} = 0.025$). Units are millimeters.*
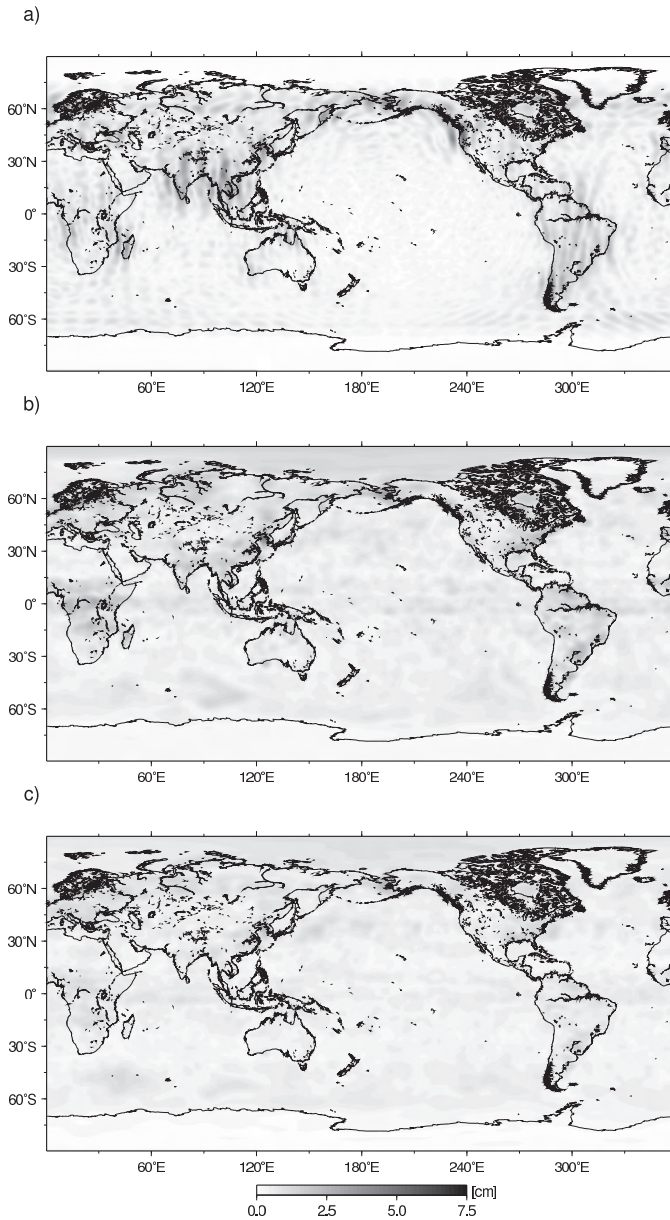
Figure 3.7: *Variance of the monthly differences between the unfiltered and filtered solutions of simulated surface water loading, unsmoothed and truncated at degree $l = 60$. a) Destriping algorithm of Chambers (2006b) filter applied, based on 60 monthly solutions, b) EOF filter applied to spherical harmonics ($\alpha_{\mathrm{KS2}} = 0.025$), based on 30 monthly solutions, and c), as b) but based on 60 monthly solutions. Units are millimeters.*
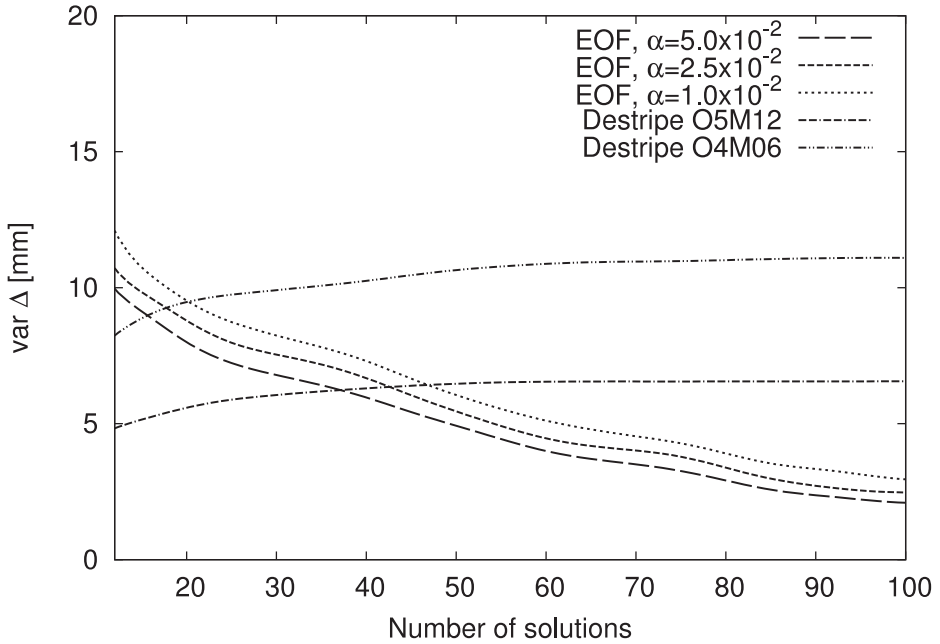
Figure 3.8: *Variance of the difference between the filtered and unfiltered fields for a simulation period ranging from 12 to 100 months. Filters used are the EOF filter applied to the spherical harmonics, with varying α-level of the KS2-test, and two destriping algorithms with different polynomial order (O) and starting order (M).*

EOF filter has no preference for signals along a specific direction, as is the case for the destriping algorithms. The main effect of the filter will therefore be limited to an attenuation of the signal, which can be observed in some regions, especially in the ocean at higher latitudes. For an observation period of 60 months, maximum differences are about 20% of the original variance, similar to the attenuation observed in the maps filtered with the destriping method. Increasing the observation period increases the amount of retained signal, as the EOF decomposition will become more effective and signal will be better separated from noise. This is illustrated in fig. 3.7, showing the variance of the difference for 30 and 60 months.

Figure 3.8 shows the global mean variance of the difference between the individual unfiltered and filtered fields, as a function of the (simulated) observation period. Again, this illustrates that the EOF filter is dependent on the number of solutions available. In contrast, the results of the polynomial filters are relatively time-independent and the variance of the difference is proportional to the total variance of the unfiltered fields. For observation lengths longer than 40–50 months, the variance of the difference is lower for the EOF filtered fields. Increasing the α-level of the KS2 test reduces the amount of retained signal slightly.

3.6 Effect on modeled trends

3.6.1 Method

GRACE data have been used extensively to study secular changes in the Earth's water mass distribution. The effect of filtering on trends therefore deserve some special attention. As a test domain, the ice sheet of Greenland is selected and a mass loss signal equivalent to a total effect of 1 mm globally averaged sea level rise, i.e. a loss approximately 360 Gt yr^{-1} of ice mass, is modeled. In accordance with recent observations and model predictions (independent of GRACE data), e.g., Thomas et al. (2006), the mass loss is uniformly distributed over the regions below 2000 m, while the mass in higher regions remains constant. The mass lost by the ice sheet is uniformly distributed over the ocean and hydrological mass variations outside the Greenland region are modeled using monthly mass anomaly fields from the GLDAS model. A uniform layer of water was added to the ocean at every time step to conserve the total mass of the system. In terms of equivalent water height, the mass anomalies in the coastal areas have an average value of ~ 0.47 m yr^{-1}.

As in the previous section, the obtained grids are converted to spherical harmonics of the geopotential. In a next step, the filters are applied to the sets of spherical harmonics and the result is converted back to equivalent water height anomalies. Finally, the secular signal is recovered from the filtered grids through a least-square fit and compared to the trend in the unfiltered grids. To study the influence of the observation period, this procedure is repeated for a set of solutions spanning 12 to 100 months.

The trend recovered from the unfiltered fields will be used a reference. Due to the limited spectral resolution of the GRACE data ($l_{\max} = 60$), the modeled trend reduces by $\sim 41\%$ and the mean trend in the coastal regions of Greenland then becomes 0.278 m yr^{-1}. As test statistics the mean trend over the Greenland region below 2000 m will be used, as well as the spatial rms of the difference between filtered and unfiltered trends, which can be seen as measure of how well the spatial pattern is preserved by the filtering methods.

3.6.2 Results

In contrast to other filters, the EOF based filtering method depends explicitly on the temporal characteristics of the GRACE solutions. As more solutions become available, both the EOF decomposition and the KS2 test allow a more accurate separation of signal and noise. This is evident in fig. 3.9, where the mean trend (fig. 3.9a) and the spatial rms of the difference between filtered and unfiltered trend maps (fig. 3.9b) are plotted as a function of the observation interval. Note that all statistics are expressed in equivalent water height (not equivalent sea level rise), and are averaged over the Greenland region below 2000 m.
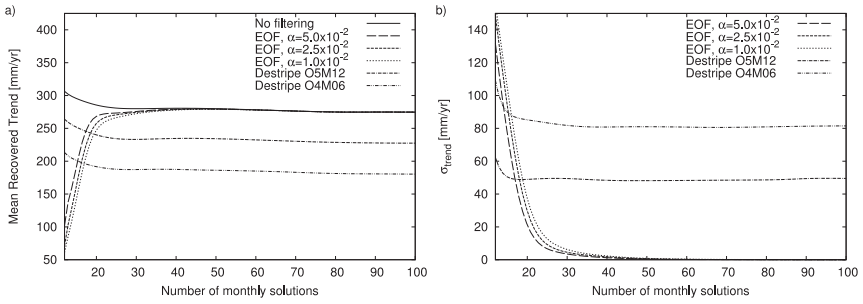
Figure 3.9: *a) Mean trend in the coastal zone of Greenland, based on simulated maps, truncated at degree $l = 60$. Results are shown for the unfiltered and filtered fields. Filters used are the EOF filter applied to the spherical harmonics, with varying α-level of the KS2-test, and two destriping algorithms with different polynomial order (O) and starting order (M); b) spatial RMS (σ_{trend}) of difference between the trends recovered from the filtered and unfiltered synthetic fields. Units are mm/yr.*

When applying the EOF filter to the spherical harmonics of a short data set, a relatively large part of the trend is removed. For observation lengths longer than 15–20 months, the EOF filter recovers more of the original mass loss signal than the destriping algorithms. This point of crossing of the curves depends slightly on the α-level of the KS2-test, decreasing α_{KS2} requires a slightly longer observation period to obtain similar results. In all cases, the difference between the simulated and retrieved trend is negligible for records lengths exceeding 35–40 months. The spatial RMS of the difference between filtered and unfiltered trend maps is nearly zero for such observation lengths, as is illustrated in fig. 3.9b and 3.10b.

Figure 3.10 illustrates the effect of filtering on the spatial pattern of the modeled mass loss signal. The destriping algorithm will affect signals with a meridional orientation and removes part of the trend along the east- and westcoast of Greenland, but simultaneously introduces a signal in the adjacent regions (fig. 3.10c–d). As explained in the previous section, this is due to the spatial characteristics of the filter, which is most sensitive to signals with a north-south orientation and reduces these patterns while amplifying the neighboring signals by means of side-lobes (Swenson and Wahr, 2006). As a consequence, the trend over the interior region becomes slightly more negative, which might be misinterpreted as a mass deficit of the high elevation inland regions. Areas with an east-west orientation, such as the northern part of the ice sheet, are hardly affected by the destriping filter of Chambers (2006b) filter. In contrast, the Chen et al. (2007b,c) destriping filter, which starts removing signal at a lower order, appears to cause an increase of trends with a east-west orientation in the northernmost part of Greenland. These alterations of the spatial trend patterns are also reflected in the spatial rms of the difference between filtered and unfiltered fields (fig. 3.9b), which is about 50 and 85 mm yr^{-1} for the Chambers (2006b) and Chen et al. (2007b,c)-like de-
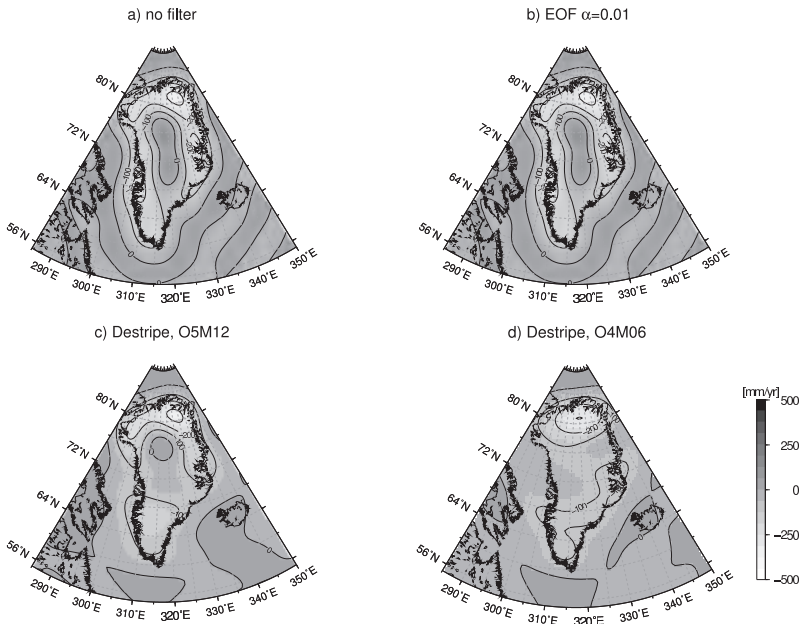
Figure 3.10: *Maps of simulated trends over Greenland, based on 60 simulated monthly fields, truncated at degree l = 60. a) Unfiltered field, b) EOF filtering applied to spherical harmonics (α_{KS2} = .01); c) destriping algorithm of Chambers (2006b) and d) of Chen et al. (2007b,c) applied. Units are mm/yr.*

striping filters, respectively. Apart from slight fluctuations due to signals outside the region of interest, the difference between the simulated and retrieved trend remains constant (fig. 3.9a). Depending on the filter settings, some 20% to 35% of the signal is removed, averaged over the entire region. Locally, the filter may cause differences as large as $\sim 65\%$ and $\sim 85\%$ of the original signal for Chambers (2006b)'s and Chen et al. (2007b,c)'s filter, respectively.

3.7   Conclusions

In this chapter, the performance of the EOF filter, applied to the spherical harmonics, has been assessed. Although no direct measure exist for the improvement obtained by filtering, the tests in the first three sections of this chapter show that noise is significantly reduced after filtering. The RMS of residual signal after removing the (semi-)annual harmonic and secular trend is reduced by 60%–80%. A similar reduction in variance is observed in the approximate Sahara region in North-Africa, where little to no signal is observed. Comparing GRACE derived vertical deformation variations with observations by GPS stations, shows that

filtering of the GRACE data results in a better agreement between the two data sets.

Applying a filter to observational data will inevitably remove part of the signal. By testing the EOF filter on synthetic maps of EWH, based on numerical models, it is demonstrated how the amount of removed signal depends on the length of the observation set. This is a fundamental difference between the EOF filter and the destriping filters of Chambers (2006b) and Chen et al. (2007b,c). These types of filters are based on the spatial orientation of the signal and do not have a temporal dependence. Given a sufficiently long observation period, the EOF based filter will remove less geophysical signal than the destriping filters. The latter remove signal with a predominant north-south orientation, and may also introduce artificial signals due to the filter's sidelobes.

From the tests performed in this chapter, and the results in Ch. 2, it emerges that the effect of filtering depends strongly on the geographical location under consideration. Testing of the filter on simulated data to obtain an impression of the filter's effect is therefore recommended. A case-study of trends on the Greenland ice sheet shows that the spatial pattern and magnitude of the signal are very well preserved by the EOF filter, whereas he destriping algorithms cause a significant reduction of the signal and alteration of the spatial patterns.

Chapter 4

Monitoring Ocean Mass and Steric Variations

4.1 Introduction

For more than six years now, the Gravity Recovery and Climate Experiment (GRACE) twin satellites have been orbiting the Earth (Tapley et al., 2004a). Since its launch, GRACE has become an invaluable tool for monitoring changes in mass distribution on the Earth's surface. Several studies have shown good agreement between modeled water store changes and those observed by GRACE. In Tapley et al. (2004b) it is demonstrated that GRACE is able to observe large-scale hydrological changes over the continents, such as the annual cycle over the Amazon basin. Owning to the increased quality of the newest GRACE products – either due to improved de-aliasing products, software and processing changes or to post-processing of the provided GRACE solutions, see, e.g., Swenson and Wahr (2006); Kusche (2007); Wouters and Schrama (2007); Klees et al. (2008) – studies at the scale of a few hundred kilometers have now become within reach.

Most of the GRACE studies analyze phenomena occurring over land, where strong hydrological signals are expected, such as fluctuations in the mass balance of the ice sheets (e.g., Luthcke et al., 2006; Velicogna and Wahr, 2006a; Wouters et al., 2008), changes in terrestrial water storage (e.g., Ramillien et al., 2007) or internal processes such as post-glacial rebound (e.g., Tamisiea et al., 2007). In contrast, fewer studies have been devoted to mass changes over the oceans, as mass variations over the oceans are generally about an order smaller than those in the major river basins, turning the retrieval of ocean mass distribution

from GRACE into a challenging task. On a global scale, Chambers et al. (2004) found a good agreement between GRACE observations of the total ocean mass and those obtained from altimetry data corrected for steric variations, which was later validated in studies such as Chen et al. (2005) and Lombard et al. (2007). Comparison of modeled ocean bottom pressure variations with GRACE data averaged over large regions has been proven successful in some areas such as the North Pacific (Bingham and Hughes, 2006; Chambers and Willis, 2008) and parts of the Antarctic Circumpolar Current (Zlotnicki et al., 2007). Locally, GRACE measurements have been validated successfully against ocean bottom pressure recorders (BPR) in the Crozet-Kerguelen region (Rietbroek et al., 2006), but showed only marginal agreement with BPR data in the tropical northwest Atlantic Ocean (Kanzow et al., 2005).

Despite the small magnitude of the signal, comparing GRACE data with independent data over the oceans does have several advantages. First of all, the oceans are almost globally mapped by altimeter satellites, providing a nearly complete reference set, in contrast with the pointwise character of, e.g., GPS observations. Moreover, except for a number of assumptions made during the processing of the altimeter data, the observations directly represent a true geophysical signal, whereas most studies of GRACE over land need to revert to simulated data, e.g., coming from numerical hydrology models. Secondly, the fact that the signal is small makes it sensitive to the way the GRACE data is processed. Hence, comparison of GRACE data and altimetry observations acts as a beneficial tool to study improvements made in new GRACE releases or post-processing filtering techniques.

Variations in sea level consist of two components, i.e. a steric component, related to density changes, and an eustatic component, related to the exchange of water masses between land, atmosphere and ocean. Ignoring contributions of ocean tides and atmospheric pressure, which both can be removed relatively well by means of ocean tide models (e.g., Schrama and Ray, 1994) and the inverse barometer (IB) approach (Gill, 1982), respectively, total sea level ξ can be expressed as the sum of the steric ξ_ρ and eustatic ξ_{mass} components:

$$\xi(\theta, \lambda, t) = \xi_\rho(\theta, \lambda, t) + \xi_{\mathrm{mass}}(\theta, \lambda, t) \qquad (4.1)$$

By combining mass changes ξ_{mass} over the ocean, as measured by GRACE, with observations of the total sea level ξ (i.e. the sum of steric and eustatic signal) made by altimetry, one can obtain the remaining steric component ξ_ρ.

The goal of this chapter is threefold. First of all, the work of Chambers (2006a) will be revisited by comparing the GRACE data with altimetry observations to validate the newest available GRACE releases. Secondly, a lower bound for smoothing radii for GRACE applications over the ocean will be defined. As discussed in Ch. 1, noise in the GRACE data, either in the original solutions or after applying some form of post-processing filtering, is commonly suppressed by applying a Gaussian smoothing filter (see Ch. 1) with a specific bandwidth re-

ferred to as the smoothing radius. Until now, most studies have used a somewhat arbitrary smoothing radii, ranging from 2000 km down to 300 km. King et al. (2006) compared the first GRACE releases with GPS data of island sites and found optimum correlation for smoothing radii of at least 2000 km. However, this analysis was based on a limited number of points only and the GPS observation themselves are prone to site or network specific technique errors. For example, a strong disagreement between GPS and GRACE observations in European coastal zones was found in van Dam et al. (2007), which was mainly attributed to mismodeling of the semidiurnal ocean tidal loading effects in the GPS processing. Consequently, a 2000 km smoothing radius might be an overly pessimistic estimate, especially since new GRACE releases and post-processing filters have become available. Indeed, the good results obtained in the aforementioned studies indicate that use of GRACE data at a higher resolution is possible. In this study, an estimate of the error in the GRACE observations over the oceans for a range of smoothing radii will be provided, which allows the determination of a maximum spatial resolution at which the error is still acceptable. In the third part of this chapter, the seasonal cycle in the observations will be discussed.

4.2 Description of data sets

In the following, the three data sets used in this chapter will be discussed; altimetry data from JASON-1, representing total sea level, gravity data from GRACE converted to equivalent water height (EWH) and steric sea level from the World Ocean Atlas 2005 (WOA05) (Locarnini et al. (2006)). Note that all trends were removed from the data sets and that they are referenced to their mean value over the observation period.

4.2.1 GRACE Release 04 data

In this chapter, GRACE data from the three principal data processing centers, i.e. *Center for Space Research* (CSR), *Jet Propulsion Laboratory* (JPL) and *GeoForschungsZentrum Potsdam* (GFZ), are used, available online at the PODAAC (`ftp://podaac.jpl.nasa.gov`) and the GFZ ISDC (`http://isdc.gfz-potsdam.de/grace/`) archive centers. All major GRACE processing centers periodically revise their processing standards and release a new set of gravity solutions. Here, the latest available releases (RL), RL04 for CSR and GFZ and RL04.1 for JPL, are used. Most significant changes in the new release 04 with respect to the older releases are the updated static background gravity model, inclusion of an ocean pole tide model cf. Desai (2002) in all solutions, changes in the ocean tide model and an update of the de-aliasing ocean model. Since this paper concerns ocean mass variations, the latter two will be discussed briefly, for further information on the other changes the reader is referred to the documentation of the respective centers (Bettadpur (2007) for CSR, Watkins and Yuan

(2007) for JPL and Flechtner (2007) for GFZ).

All processing centers currently use the FES2004 tidal model (Lyard et al., 2006) for the diurnal and semi-diurnal harmonics, though there are small differences in the degree of expansion (ranging from 80 to 100). The model removes the majority of the tidal signal, but it will as well introduce erroneous signals, especially in regions where the assimilated observations are sparse or of low quality. Using simulated GRACE gravity solutions, Knudsen (2003) and Ray and Luthcke (2006) have shown that imperfections in the tidal model will result in errors in the final gravity solutions. Most notably, the S_2 and K_2 tides might result in large errors primarily in polar regions, with an aliasing period of 162 days and $\sim$3.7 years respectively. As will be shown later on in this chapter, aliasing of the S_2 tide is clearly distinguishable in the current GRACE solutions. No definite conclusion can be drawn about the K_2 tide, as not enough data is currently available to separate the aliasing error from other long-term variations.

Non-tidal ocean mass effects are de-aliased by means of numerical ocean models. For the release 04, CSR, GFZ and JPL have selected the updated version of the baroclinic *Ocean Model for Circulation and Tides* (OMCT; Thomas (2002)). The major change in the updated OMCT consists of a switch to a mass-conserving parameterization, since an earlier non-mass conserving version introduced artificial geoid heights slopes over land. Besides this, homogenization of the land/ocean mask and bathymetry with the ECMWF forcing model, a new data set for surface salinity relaxation and an improved sea ice model were implemented in the model (Thomas, personal communication, 2007). The OMCT model has a fixed spatial mesh of $1.875° \times 1.875°$.

The GRACE solutions are provided as sets of fully normalized Stokes coefficients of the gravity field relative to a static field, ΔC_{lm} and ΔS_{lm}. As shown in the introduction of this dissertation, these coefficients can be related to changes in surface mass loading and converted into smoothed maps of EWH $\Delta\xi_{\mathrm{mass}}(\theta, \lambda, t)$ using eq. 1.6. Missing in this equation are the degree 1 components, related to the center of mass of the Earth, which cannot be observed by the GRACE satellites and therefore have to be modeled using independent sources (Chambers et al. (2004)). In this study, the annual displacement of the geocenter is modeled using the parameters of Swenson et al. (2008), based on a combination of the OMCT ocean model and GRACE data over land. Also, the original C_{20} coefficients, corrupted by aliased ocean tide model errors (Chen and Wilson, 2008), were replaced by values derived from satellite laser ranging (Eanes, personal communication, 2008). Finally, in order to obtain a complete picture of the mass variations in the ocean, the monthly averages of the atmospheric and oceanic mass anomalies removed during the background processing need to be added back. These fields are provided by the respective GRACE teams and are set to zero over land to avoid leakage of the atmospheric signal over land into the ocean domain (the so-called GAD-fields, see Flechtner (2007)).

Hydrological signals on the continents are generally an order of magnitude larger than the variations in the ocean. Due to the smoothing of the GRACE
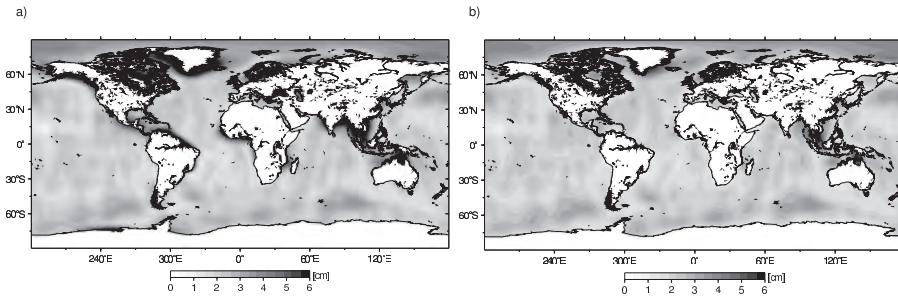
Figure 4.1: *Variance in the GRACE maps of equivalent water height, before and after correcting for leakage of continental signals following the procedure of Wahr et al. (1998). The GRACE solutions are smoothed with a Gaussian radius of 500 km. Units are cm.*

observations, which is still required after post-processing filtering, these continental signals will be spread out and corrupt the much weaker oceanic signals in the coastal areas. This phenomenon can be significantly reduced by the procedure proposed in Wahr et al. (1998). In a first step, the GRACE coefficients are converted into a map of EWH with no additional smoothing applied. The ocean area in this map is then masked and the result is converted back to geopotential coefficients, representing the signal over land. These coefficients are subtracted from the original GRACE solutions, which now have most of the continental signal removed and show a significant leakage reduction when converted back into smoothed maps of EWH. Figure 4.1 illustrates the reduction in signal variance in the coastal zones after applying this procedure.

Based on the standard errors provided by the GRACE processing centers, the error bounds on the estimates of global ocean mass variations are in the order of 2 millimeters. Reducing the correlated errors by means of EOF filtering of the spherical harmonics reduces this to approximately 1 millimeter, using the scaled standard errors described in Ch. 2.

4.2.2 Altimetry data

In this study, observations of total sea level ξ obtained by the NASA/French Space Agency JASON-1 altimetry satellite are used, processed with the DEOS Radar Altimeter Database System (RADS) software (Naeije et al., 2002). The data, Version C of the Geophysical Data Records (GDR), contains satellite orbits based on EIGEN-GL04C gravity field and recalibrated JASON-1 Microwave Radiometer (JMR) data. The tropospheric correction in the original Version A GDR data displays a linear trend as well as several jumps in the three channels of the retrieved brightness temperatures, resulting in an instantaneous artificial increase in global mean sea level of approximately 1 cm in total (e.g., Scharroo et al. (2004)). The new processing algorithm results in a stable wet tropospheric

correction, so that this problem is no longer an issue at the moment (R. Scharroo, personal communication).

Besides the wet tropospheric correction, all the standard corrections have been applied to the altimetry data, including a correction for ionospheric refraction, sea state bias, ocean tides (based on the FES2004 model), solid earth tide, pole tide, ocean load tide and the local IB correction. Based on comparison with tide gauge data, the accuracy of global mean sea level is estimated to be at the 5 millimeter level for the 10-day repeat cycle of JASON-1 (Leuliette et al., 2004).

In addition to the static IB correction, valid at periods longer than a few days, the altimetry data is also corrected for high-frequency oceanic signals due to wind and pressure forcing. Since every point is sampled only once every ∼10 days (in case of JASON-1), any unresolved signal with a period less than the Nyquist period of 20 days will be undersampled by the altimeter and hence will alias into spurious signals with a longer period. This might become especially troublesome at higher latitudes, where the oceanic response is dominated by barotropic motion at periods of less than 20 days (e.g., Fukumori et al. (1998)). One way to prevent, or at least minimize, this, is to correct the altimeter data samples using the output of available ocean models. For this study, 6-hourly output from two ocean models used in the GRACE processing, i.e., the OMCT model (Thomas et al. (2001); kindly provided by Maik Thomas and Henryk Dobslaw) and the finite element model *Modèle 2D d'Ondes de Gravité* (MOG2D, Carrère and Lyard (2003); processed by Remko Scharroo), used in the GRACE solution of the French CNES/GRGS center, were compared. The 6-hourly sea surface height output of the model are interpolated, both in space and time, to the location and epoch of the altimeter observation, and are then subtracted from the 1 Hz altimeter samples. In order to retain as much of the long-periodic signals contained in the altimeter measurements, the model output is high-pass filtered using a Butterworth filter with a cut-off period of 20 days.

The performance of the ocean models is tested by means of satellite crossover

Region	MOG2d	OMCT	Region	MOG2d	OMCT
Global	7.7	5.4	low latitude[a]	2.9	1.4
Pacific Ocean	8.0	6.2	high latitude[a]	9.4	6.7
Indian Ocean	8.5	5.1	shallow water[b]	17.3	6.7
Atlantic Ocean	5.9	4.5	deep water[b]	8.0	5.5

Table 4.1: *Mean variance reduction at JASON-1 crossover points in 2006. The reduction is defined as [var(IB)−var(model)]/var(IB), in which var(IB) stands for the variance at the crossover points, with the altimetry data corrected with the static IB correction, and, var(model) for data corrected using the model for atmospheric wind and pressure forcing.*

[a]low latitude: $< 30°$; high latitude: $> 30°$
[b]shallow water: d < 1000 m; deep water: d > 1000 m

a)

b)
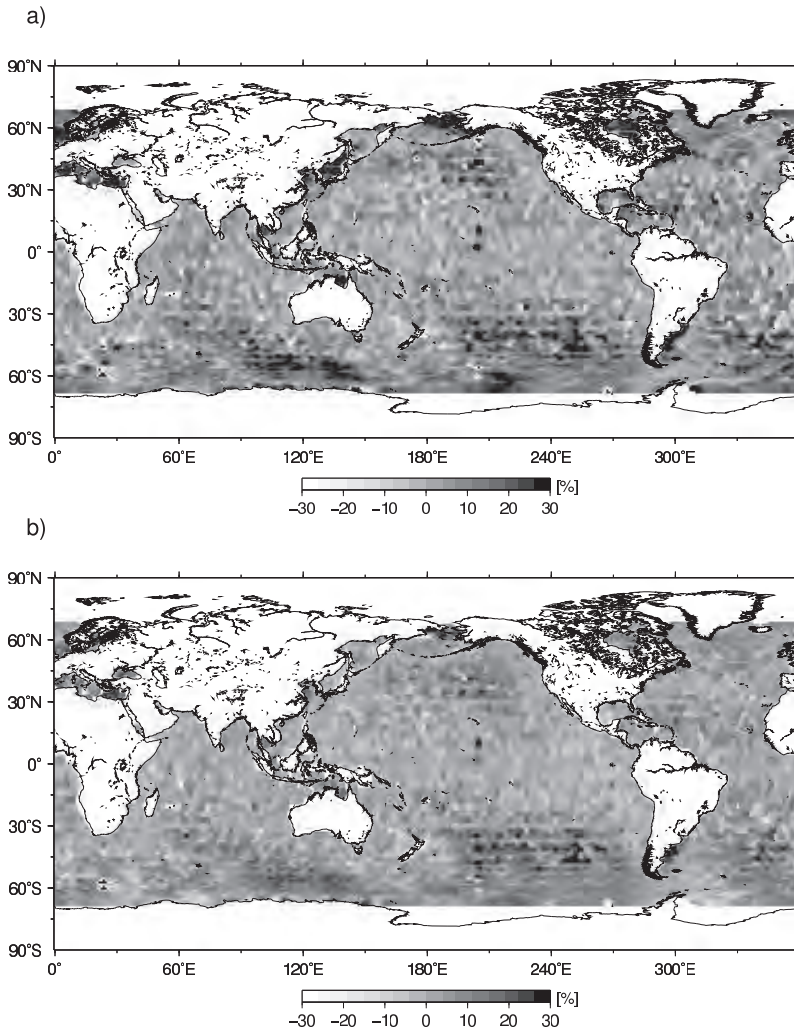
Figure 4.2: *Variance reduction at altimeter crossover points for a) the MOG2D and b) OMCT ocean model in 2006. Units are %.*

analyses. Crossover points are points are where ascending and descending satellite tracks cross, hence by taking the difference of two passes at such a point any error constant in time will be eliminated and only time dependent signals remain. By comparing the variance of the sea level height at the crossover points before and after correcting with the model, the improvement introduced by adding the model data can be assessed (a reduced variance indicates that the correction improves

the measurement quality et vice versa). Table 4.1 gives an overview of the results of the two models, while fig. 4.2 illustrates the geographical distribution. As expected, the reduction in variance is largest in regions with high barotropic variability, i.e. at latitudes greater than 30° and shallow waters (e.g., Fukumori et al., 1998). Overall, the MOG2d model performs best, with a global mean reduction of the variance of approximately 8%. The finite element MOG2d model particularly stands out in the shallow water regions, where grid sizes are as low as 20 km, whereas the OMCT model has a fixed resolution of 1.875°.

After correcting the raw data, the altimetry measurements are binned into 1° by 1° grids, averaged over the same time span as the GRACE gravity solutions and smoothed with a Gaussian filter identical to the one used in the GRACE data processing. The smoothed mean monthly fields from the removed ocean model data are added back, comparable to what is done in the GRACE data processing described earlier.

For comparison and combination with the GRACE observations, the metric of interest is the height of the water column between the sea surface and the ocean floor. As discussed in section 3.4, redistribution of mass on the Earth will cause a radial displacement of the solid Earth. Although this effect is generally an order of magnitude smaller than the changes in EWH as described by eq. 1.6, one should correct for this phenomena in either the GRACE or altimetry observations in order to combine the two in a consistent manner. Using the horizontal load love numbers $h_l^{'}$ in eq. 3.1, the radial displacement can be obtained from the GRACE gravity coefficients and removed from the altimetry observations. The magnitude of this correction is in the order of a few millimeters at most, in the vicinity of the larger continental hydrology basins. Averaged over the global ocean, the amplitude of this correction is in the order of $\sim 0.5 \pm 0.1$ millimeter, peaking on day of year 90 ± 5.

4.2.3 Temperature and salinity data

To validate the results from space-born observations with in-situ data, the World Ocean Atlas 2005 (Locarnini et al. (2006), Antonov et al. (2006)), hereafter referred to as WOA05, is selected as a reference. The WOA05 consists of a set of objectively analyzed temperature and salinity measurements binned in 1° by 1° grid cells at a number of depth levels and contains the long-term mean salinity and temperature for each month of the year, based on more than 50 years of observations. Using the equation of state defined by the UNESCO Joint Panel on Oceanographic Tables and Standards (UNESCO, 1981), pressure, temperature and salinity anomalies can be related to density anomalies $\Delta\rho$, which can be integrated to obtain steric sea level height variations ζ_ρ, see, e.g., Gill (1982):

$$\zeta_\rho = \int_{-H}^{0} \frac{\Delta\rho}{\rho_0} dz \tag{4.2}$$

where ρ_0 is a reference density and H the maximum depth level of integration.

For the WOA05 monthly ocean climatology sets, the measurements are grouped in 24 layers to a depth level of -1500 m. Each monthly grid is based on approximately 4–5.5 million individual temperature measurements and 1–2 million salinity measurements respectively. Due to the scarcity of measurement campaigns in southern regions, there exists a strong geographical bias in the distribution of the observations, with only 10–30% of the data located in the Southern Hemisphere, depending on the season (maximum in austral summer). Moreover, most of the data, approximately 90%, is located in the upper 700 m of the ocean.

Arguably, the largest difference compared to the other two data sets is that WOA05 represents the monthly climatological mean and does not contain interannual variations. In contrast, the GRACE and JASON-1 satellites both will observe year-to-year differences. The Argo project, a pilot program of the Global Ocean Observing System (`http://www.argo.ucsd.edu`, `http://argo.jcommops.org`), consisting of approximately 3000 floating devices measuring temperature and salinity in the upper 2000 meters every 10 days (e.g., Gould et al., 2004), has already resulted in an exponential increase of available data and now make monthly maps of steric height anomalies a feasible option. However, since the ARGO array has been fully deployed since November 2007 only and biases between different types of ARGO floats may affect the results (Willis et al., 2007), these data have not yet been used in this study, although preliminary studies show a good agreement between the different data sets (e.g., Willis et al., 2008; Leuliette and Miller, 2009) on seasonal and interannual timescale. To assess the impact of interannual variations the monthly objectively analyzed subsurface temperature and salinity grids of Ishii et al. (2006), available in the upper 700 m for the period 1945–2005, are used. For all 12 months, a mean climatological value of the steric height anomaly is computed in a 5-year sliding window and the variations between all climatologies were used to obtain an error estimate for each month. Typical RMS values are in the order of 0.8 mm for the globally averaged steric height anomalies.

4.3 Methodology

4.3.1 Combining the data sets

The observations made by the GRACE satellites can improve our understanding of sea level variations ξ variability in two ways. First of all, the Stokes coefficients ΔC_{lm} and ΔS_{lm} can be directly converted to variations of ocean mass ξ_{mass} by applying eq. 1.6 over the ocean domain. Secondly, the ocean mass variations from GRACE can be subtracted from the total sea level ξ as observed by altimetry to obtain the steric sea level ξ_ρ (after correcting for displacement in the ocean floor in the altimetry observations as discussed earlier).

As mentioned in section 4.2, steric sea level ξ_ρ can also be retrieved from insitu measurements of salinity and temperature, such as those in the WOA05 atlas. In this study, the WOA05 climatological steric variations are used as a reference

for those obtained from the combination JASON-GRACE (hereafter referred to as ξ_{WOA05} and $\xi_{\text{J-G}}$, respectively). As a measure of quality for the latter, the following three criteria are applied:

- First of all, the variance of the residuals of the two data sets at a point $p(\theta, \lambda)$, i.e.:

$$\sigma(\theta, \lambda) = \sqrt{\frac{1}{N-1} \sum_{i=1}^{N} [\xi_{\text{J-G},i}(\theta, \lambda) - \xi_{\text{WOA05},i}(\theta, \lambda)]^2} \qquad (4.3)$$

  where N represents the total number of monthly GRACE solutions used. A global latitude-weighted average of the variance is also computed, which will be indicated by σ. Neglecting errors in the WOA05, the variance of residuals $\sigma(\theta, \lambda)$ can be seen as a measure of the error in the $\xi_{\text{J-G}}$ maps and, by extension, as the error in the GRACE solutions over the oceans. In reality, the latter is likely to be an overestimation, since this assumes the altimetry data to be error-free as well and neglects the impact of interannual variations not represented in the WOA05 atlas..

- Secondly, a signal-to-noise (SNR) function defined as the ratio of the variance in the reference WOA05 steric anomalies to the variance in the residuals:

$$SNR(\theta, \lambda) = \frac{\sqrt{\sum_{i=1}^{N} [\xi_{\text{WOA},i}(\theta, \lambda)]^2}}{\sqrt{\sum_{i=1}^{N} [\xi_{\text{J-G},i}(\theta, \lambda) - \xi_{\text{WOA},i}(\theta, \lambda)]^2}} \qquad (4.4)$$

  which indicates where the expected signal is greater than the estimated errors in the data.

- When taking the global average of above two quantities, regions with poor performance of the altimetry-GRACE combination (high residual variance/low SNR) might be masked by areas with above average performance. Therefore a third variable is introduced, which helps to interpret the results. The SNR area ratio Φ is defined as the ratio of the area where the expected signal is greater than the residual variance and the total observational area, i.e. the percentage of the total ocean where $SNR(\theta, \lambda)$ greater than unity:

$$\text{SNR area ratio } \Phi = \frac{\text{Area with SNR} > 1}{\text{Total ocean area}} \qquad (4.5)$$

All statistics are computed for the period February 2003 to January 2008. The global statistics are computed using equal-area weighting.

4.4 Discussion of results

4.4.1 Global statistics

Figure 4.3 shows the global test statistics (variance of residuals and SNR area ratio) for the CSR RL04 monthly GRACE maps (data from other processing centers shows comparable behavior), for a set of radii ranging from 2000 km to 0 km. Results are shown for unfiltered GRACE solutions and after applying the EOF filtering technique to the spherical harmonics (see Ch. 2 and Wouters and Schrama (2007)), for three different α-levels of the KS2-test (0.05, 0.025 and 0.01). At larger smoothing radii, between 2000 and 1000 km, all data sets perform equally well and the application of the EOF filters do not cause a significant improvement. At these smoothing radii the majority of the signal in the GRACE fields is obtained from the spherical harmonic coefficients up to a degree of approximately 10, where only minor correlation exists between the odd and even coefficients. At lower smoothing radii, the correlated coefficients become increasingly important and the filter becomes more efficient. At 500 km smoothing, applying EOF filtering to the spherical harmonics result in a decrease of the residual variance of $\sim$ 15%, whereas the SNR area ratio increases by as much as 50%, indicating that the GRACE data must be filtered to obtain useful results over the ocean.

When applying Gaussian smoothing only, the residual variance shows a slight linear increase for radii between 2000 and $\sim$800 km, while the SNR area ratio decreases monotonically from 70% to 55 %. At about 700 km, a transition takes place and the variance increases rapidly and the SNR area ratio decays to zero. Visual inspection learns that at this point the north-south stripes become the dominant features over the oceans in the maps of surface mass anomalies. Similar behavior is observed after destriping the GRACE data with the EOF method, but the transition point is shifted 150 km to the lower end of the spectrum. This clearly demonstrates the power of the EOF filtering method: at a smoothing radius of 300 km the variance of the residuals is at the 7.0 cm level without any form of filtering, which reduces to approximately 3 cm after filtering by the EOF method. The SNR area ratio increases from 1% to 40%.

For all data sets, best results are obtained with the maximum smoothing radius of 2000 km. However, after filtering the GRACE solutions, acceptable results are obtained for radii down to 500km. After this point, the performance decreases rapidly and thus 500 km is chosen as a lower bound for the smoothing radius for applications of GRACE data over the oceans. With no filtering applied the minimum smoothing radius increases to 700 km. This is considered to be a rather conservative estimate, since this approach neglects the effect of interannual variability unrepresented in the WOA05 data and mapping errors in both the altimetry and WOA05 observations.

Considering only the annual cycle in the three datasets results in similar results. The variance of the residuals is significantly reduced and is at the 5 millimeter level for smoothing radii in the range of 1000–2000 kilometers. This can
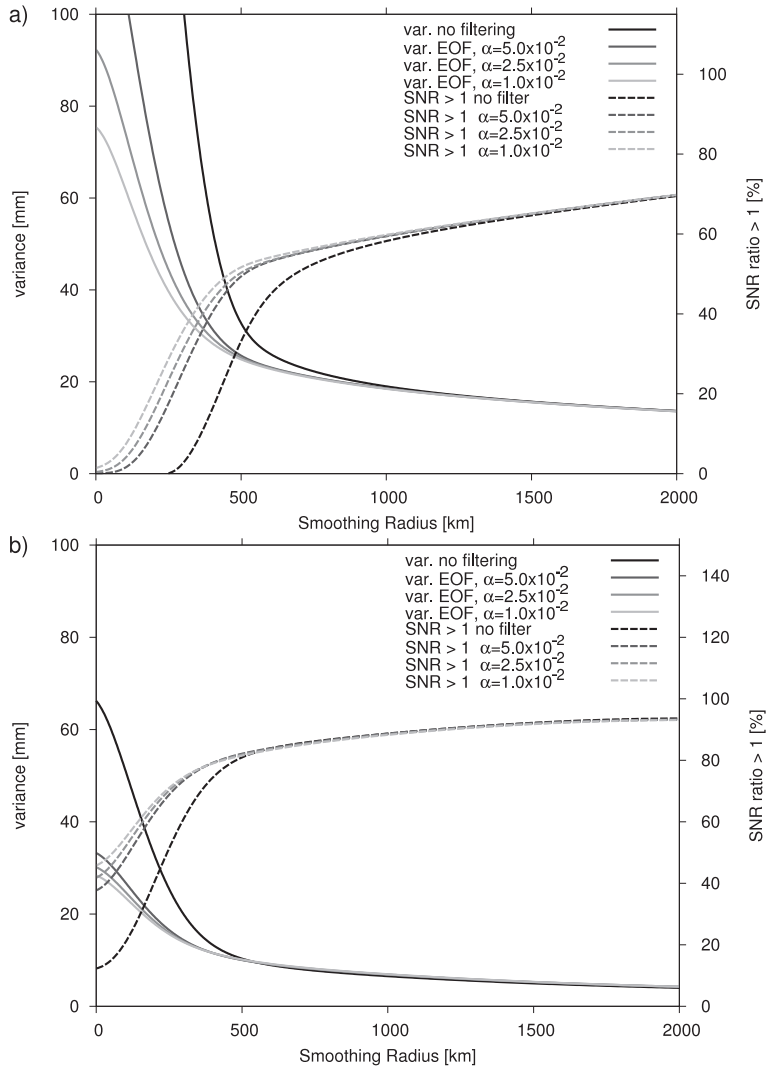
Figure 4.3: *a) Variance of residuals σ and SNR area ratio Φ as a function of Gaussian smoothing radius. Results are shown for the CSR RL04 GRACE solutions. All data used are detrended; b) as a), but for the annual cycle.*

partly be attributed to the lower amount of signal in the individual datasets, but also to an improved agreement between $\Delta\xi_{\mathrm{WOA05}}$ and the $\Delta\xi_{\mathrm{J-G}}$ combination, since extracting the annual cycle from the data sets acts as an additional filter process. This results in an increased SNR area ratio, with a signal-to-noise factor greater than 1 in more than 90% of the observation domain for the larger smoothing radii. The transition point moves further downward to approximately 400 kilometers for the filtered solutions.

4.4.2 Local statistics

Figure 4.4 illustrates the geographical distribution of the residual variance and estimated SNR in the $\Delta\xi_{\mathrm{J-G}}$ maps, using $\Delta\xi_{\mathrm{WOA05}}$ as a reference. Following the results of the previous section, a Gaussian smoothing radius of 500 km was selected and the GRACE spherical harmonics were filtered be means of the EOF filter, using $\alpha = 0.05$ in the KS2 test. A good performance, i.e., low residual variance and high SNR, is observed in several regions, of which the western boundary current regions in the Northern Hemisphere are the most distinct (SNR≈2.5). Relatively poor performance is found in the tropical band between 15°N and 15°S in the Pacific and Indian Oceans. Strong intraseasonal and interannual variability is present in these regions, e.g., due to internal modes of variability such as ENSO and the Indian Ocean Dipole (IOD) events (e.g., Saji et al., 1999; Trenberth, 1997; Chambers, 2006b; Vinogradov et al., 2008). Also, the mainly wind-driven circulation is predominantly zonally-orientated at these low latitudes (Fukumori et al., 1998; Vinogradov et al., 2008), i.e., almost orthogonal to the groundtracks of the GRACE and JASON-1 satellites. Moreover, this is the region where sea level is most poorly sampled by the satellites, since the JASON-1 groundtrack spacing is maximal in this area. The GRACE groundtracks in the region are less dense here than near the poles, causing a higher expected error in the GRACE observations (see Ch. 2 and Schrama et al. (2007) for a plot of the expected error based upon a GRACE covariance matrix).

A region of particularly poor SNR ratio is the Antarctic circumpolar current (ACC) region, where the residuals are relatively small, but where fig. 4.4 shows a poor SNR. Zlotnicki et al. (2007) found a high correlation between ocean bottom pressure in the ACC region estimated from GRACE and with the *Estimating the Circulation and Climate of the Ocean* model (ECCO, e.g., Fukumori et al. (1999)), but with the GRACE signal twice as strong as that in ECCO. Since the expected signal in the WOA05 the expected signal is small, such an overestimation will result in a marginal SNR. Furthermore, it should be remarked that few in-situ temperature and salinity observations are available in these regions.

The findings in fig. 4.4 corroborate the results of earlier studies using ocean bottom pressure recordings; Kanzow et al. (2005) found no significant correlation with the BPRs located at ∼(15°N, 300°E), Rietbroek et al. (2006) found good agreement between the GRGS GRACE data and BPRs at he Kerguelen Island (47°S, 60°E). Here, we find a SNR of 0.75 and 1.3 respectively at these locations.

a)

b)
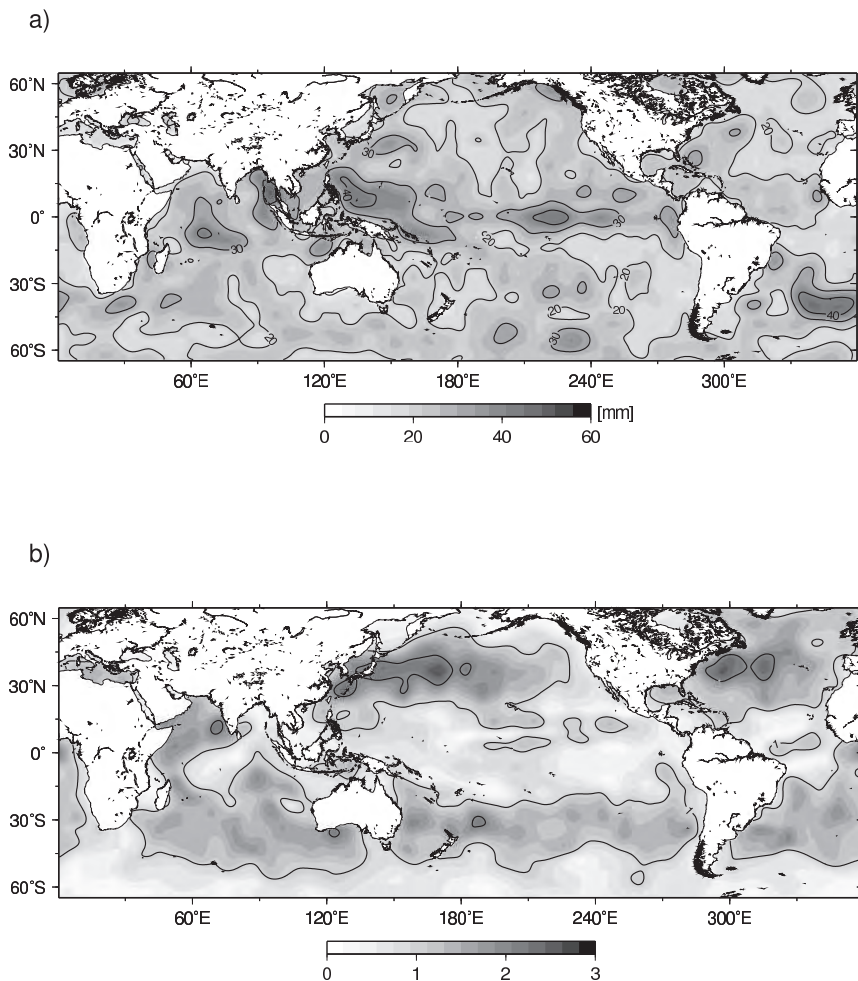
Figure 4.4: *a) Variance of the residuals in the JASON-GRACE based steric anomaly maps, referenced to the WOA05 climatology. Units are mm, contours every 10 mm; b) Estimated SNR of the JASON-GRACE based steric anomaly maps. Units are dimensionless, contours every unit. The GRACE data in both maps are filtered by applying the EOF filter to the spherical harmonics and smoothed with a 500 km Gaussian radius kernel.*

Beside the ACC and the tropical band, there are various other regions with significant residuals. A distinct feature is the in the South Atlantic Ocean, where the residuals show a variance of more than 40 millimeters. Despite the large residuals, the signal-to-noise ratio is greater than one, indicating that the JASON-GRACE combination retrieves at least part of the signal. Further analysis shows that a strong seasonal cycle exists in both the WOA05 data and the JASON-GRACE combination, with the amplitude in the former being about the double of that in the latter. Again, it should be noted that the WOA05 climatology is based on a very limited number of samples in these areas, which could cause biased results.

Tidal aliasing

Low SNR to noise ratios are found in most of the coastal zones, which can be at least partly explained by leakage of residual hydrological signal. However, there are several regions in which one would not expect any significant hydrological signal, but where variance of the residuals are large. Part of these discrepancies can be attributed to tidal aliasing, which will be discussed in the following.

All three processing centers use the FES2004 model (Lyard et al., 2006) to remove short-term tidal mass variations in the background processing. The FES2004 tidal atlas is based on the numerical solution of the Laplace tidal equation (LTE), combined with assimilation of tide gauge and altimetry data to improve the level of accuracy. Although the FES2004 is generally accepted as being one of the most reliable global tidal atlases, some specific aspects with regard to the GRACE processing deserve special attention.

Various studies examined the impact of errors in tidal modeling on the GRACE gravity fields (e.g., Knudsen (2003), Ray and Luthcke (2006)) and found that several residual tidal components will alias into the solutions as signals with a period longer than 30 days. The diurnal tide errors are expected to be partly reduced in the monthly GRACE solutions due to averaging over the ascending and descending passes because of the nearly 180 degrees phase difference in sampling (Ray and Luthcke, 2006), although this is not necessarily true in polar regions (Moore and King, 2008). The aliasing of the K_1 constituent, with an aliasing period of about 7.5 years, may put a constraint on the interpretation of long-periodic signals in certain regions (Ray and Luthcke, 2006). Semi-diurnal tides tend to show a phase offset different from 180 degrees and consequently will not average out (Ray and Luthcke, 2006; Moore and King, 2008). Particularly the S_2 and K_2 constituents raise concern, since they alias with a period longer than one month, i.e. approximately 162 days and 3.7 years, respectively. As not enough data is currently available to separate the aliasing error from other long-term variations, no definite conclusion can be drawn about the K_1 and K_2 tides. However, the S_2 tide should be clearly distinguishable and can be separated from other signals in many regions, such as the semi-annual hydrological cycle (Han et al., 2005; Schrama et al., 2007).
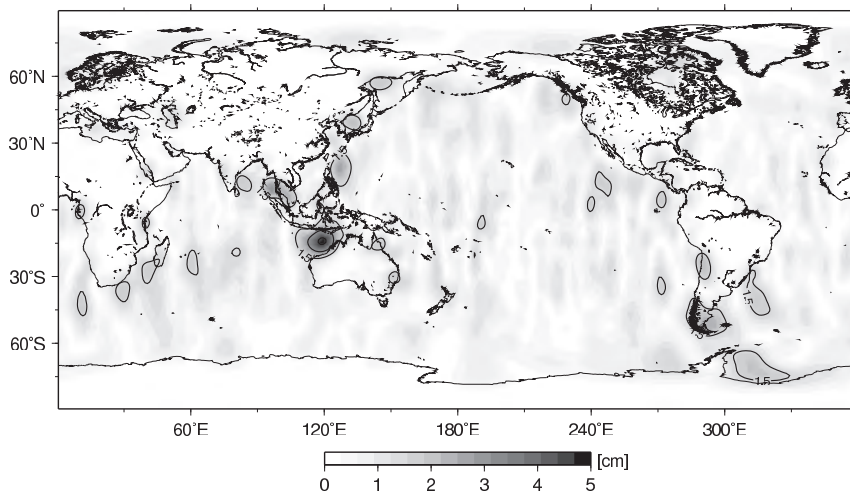
Figure 4.5: *Amplitude of the S_2 signal estimated from the CSR RL04 GRACE data, smoothed at 500km (no filtering applied). Units are cm.*

The semi-diurnal S_2 tide consists of two components, i.e., the gravitational tide and the atmospheric tide. Since the latter is due to thermal excitations by the solar radiation in the upper atmosphere, it can not be modeled by the (numerically) solving of the LTE using the gravitational potential forcing only and has to be estimated through assimilation of tide gauge and altimetry data (for more details, see Lyard et al. (2006)). This inherently means that the modeling of the S_2 tide will be degraded in regions of poor observation quality, such as over the continental shelf where observations are obscured by non-tidal dynamics, and in regions with few observations available, such as in high-latitude areas covered with a (semi-)permanent ice-shelf.

To asses the impact of mismodeling of the S_2 tide in the FES2004 atlas on the GRACE solutions, the amplitude of the S_2 signal is estimated by fitting a cosine function with a 162 day period to the available GRACE data. Several areas show significant amplitudes in the GRACE solutions of all three processing centers (see fig. 4.5 for the CSR RL04 solutions), mainly over shallow regions (Australian North West Shelf, Andaman Sea, Patagonian Shelf) and at high-latitudes such as under the Antarctic Larsen and Filchner-Ronne Ice Shelves, see also Han et al. (2005). This corroborates the findings of Ch. 2. Removing the signal associated with the S_2 aliasing from the GRACE solutions further lowers the variance of the ξ_{J-G}-ξ_{WOA05} residuals, most notably in the regions showing up in fig. 4.5, where the residuals variance σ decreases by up to 35% (Australian North West Shelf).

4.5   Annual cycle

The total mass of the world ocean is known to vary throughout the year due to exchange of water between atmosphere, land and ocean (e.g., Cazenave et al., 2000). In opposition, global mean steric height changes predominantly due to variations in heat input during the seasonal cycle. The two processes are about 6 months out of phase; Global ocean mass is at a minimum in late boreal winter/early spring, when a maximum amount of water is stored on the continents and to a lesser extent in the atmosphere, whereas global steric sea level peaks in austral summer, when expansion of the water mass on the Southern Hemisphere is at a maximum, attributable to a peak in solar heat input. In this section, it will discussed how well GRACE is able to detect these changes, both on global and local scale.

4.5.1   Global results

Global latitude-weighted mean steric height variations from the JASON-GRACE combination and ocean mass from GRACE alone are shown in fig. 4.6. As a reference, the steric height variations from WOA05 and mass variations from altimetry corrected for steric effects (JASON-WOA05) are also computed. Yearly amplitude and phase of the signals are given in table 4.2, along with correlations of the GRACE based estimates with the respective reference sets. Only data between 65°N and 65°S, the observation domain of the JASON-1 satellite, are used. No Gaussian smoothing has been applied since tests indicate that this has a negligible effect on the global results, indicating that the noise averages out over the ocean domain.

A periodogram of the altimetry data shows significant variability at the ~60-day period, due to aliasing of the S_2 and M_2 tides. This is attributable to the orbit geometry of the JASON-1 satellite and inaccuracies in the FES2004 model used to remove tidal fluctuations in the altimetry. To reduce this effect, a moving window with a 3 month width is applied to the altimetry data, comparable to the approach in Willis et al. (2008) and Leuliette and Miller (2009). For consistency, the GRACE and WOA05 data have been treated likewise.

The GRACE data based on the CSR and GFZ solutions show a comparable phase and amplitude for the ocean mass time series, with an amplitude of ±7.8 mm and a maximum in early October. This is in agreement with the estimates from sterically corrected altimetry, which shows an amplitude of 7.2 mm and a maximum on day of year 280 (early October), as well as estimates from previous studies based on earlier GRACE releases (e.g., Chambers et al. (2004), Chen et al. (2005), Lombard et al. (2007)). The amplitude of the JPL based estimate is slightly lower. Correlations between the GRACE based estimates and the sterically corrected altimetry data are high at the 95% level for all three centers. As noted in Willis et al. (2008), the effect of excluding regions outside 65°N and 65°S from the GRACE data is small but non-negligible. The difference
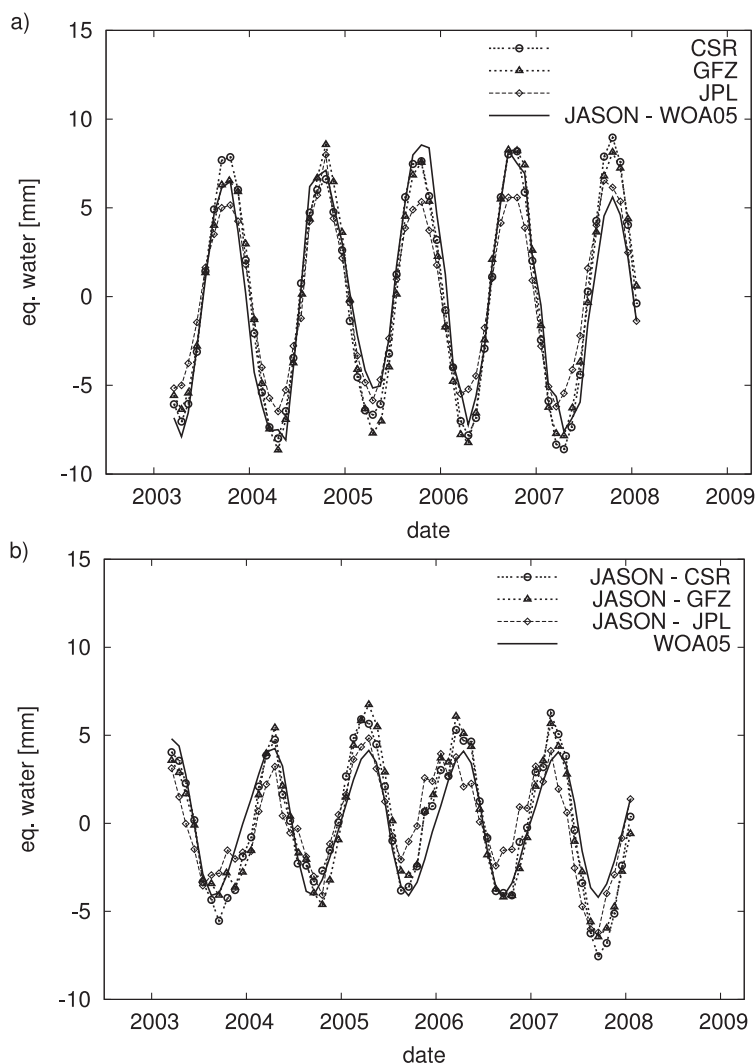
Figure 4.6: *a) Global ocean mass and steric height b) variations for the three main GRACE processing centers. Also shown are the reference data sets, JASON-WOA05 and WOA05 respectively. Only observations between $\pm 65°$ latitude are used.*

between GRACE-derived global mass estimates obtained with and without these regions shows a standard deviations of 0.8 mm.

Steric height variations derived from combining JASON altimetry and GRACE show an amplitude which is somewhat higher than what can be expected from the

non-steric GMSL	amplitude (mm)	phase (day)	correlation
JASON–WOA05	7.2 ± 0.6	280 ± 6	1
CSR	7.9 ± 0.4	277 ± 3	0.97
GFZ	7.8 ± 0.4	281 ± 3	0.96
JPL	5.9 ± 0.4	275 ± 4	0.95

steric GMSL	amplitude (mm)	phase (day)	correlation
WOA05	4.1 ± 0.2	85 ± 3	1
CSR	4.8 ± 0.6	84 ± 6	0.92
GFZ	4.6 ± 0.6	89 ± 7	0.91
JPL	3.1 ± 0.6	68 ± 13	0.77

Table 4.2: *Amplitude and phase of variations of global mean non-steric and steric sea level and correlations of the GRACE based estimates with their reference data sets. The amplitude and phase were computed using a $\cos(\omega t - \lambda)$ definition, with phase in days relative to January 1. Reference data sets are JASON-WOA05 data for non-steric variations and WOA05 for steric variations. Only data between $65°N$ and $65°S$ are used. Error bars are based on the 95% confidence interval of the least-square analysis.*

WOA05 for two of the GRACE data sets (CSR, GFZ), but consistent within the range of error. A maximum of ~ 4.7mm is reached on day of year 85 (late March), corresponding to austral summer. Again, only data within the $\pm 65°$ latitude band were used. Estimates based on the full WOA05 observation domain show comparable behavior, with a standard deviation of the differences of 0.4 mm. Again, the estimate obtained with the JPL data set show an amplitude lower ($\sim$3 mm) than the other estimates and a slightly lower correlation with the reference set (note however that due to the small sample size (57 monthly solutions), this difference is not significant at the 5 % level). It is unclear what causes the lower amplitude in the JPL RL04.1 solutions. Most likely, this is due to the parameterization used for the JPL harmonic solutions, which differs mostly at the lower degrees from the other processing centers. This reduces the north-south striping pattern but may also attenuate part of the signal (M. Watkins, personal communication, 2007). A full investigation of this is beyond the scope of this dissertation.

In both the global mass and steric height time series, most pronounced differences between the GRACE based observations and the reference sets are observed in the second part of 2007. The global mean steric height is at an anomalously low level, which is most likely attributable to the onsetting La Nina event in this period and the associated cool ocean conditions. In-situ temperature profiles, mainly obtained from the ARGO array (kindly provided by Josh Willis), show a similar negative anomaly during this period (J. Willis, personal communication, 2009).

geocenter model	data source	Amplitude (mm)	phase
No Geocenter correction	-	7.0 ± 0.4	286 ± 3
Model based (table 1.1)	model	8.6 ± 0.41	271 ± 3
(Bouillé et al., 2000)	SLR[1]	8.7 ± 0.4	268 ± 2
(Eanes et al., 1997)	SLR[1]	8.1 ± 0.4	274 ± 2
(Crétaux et al., 2002)	SLR[1]	8.2 ± 0.4	265 ± 2
(Moore and Wang, 2003)	SLR[1]	8.5 ± 0.4	256 ± 2
(Dong et al., 2003)	GPS[1]	10.4 ± 0.4	305 ± 2
(Lavallée et al., 2006)	GPS[1]	11.1 ± 0.4	276 ± 2
(Blewitt et al., 2001)	GPS[2]	13.8 ± 0.5	261 ± 2
(Kusche and Schrama, 2005)	GPS[2]	14.4 ± 0.5	249 ± 2
(Lavallée et al., 2006)	GPS[2]	11.9 ± 0.5	250 ± 2
(Wu et al., 2006)	GPS & GRACE[3]	8.3 ± 0.4	264 ± 2
(Swenson et al., 2008)	GRACE & ECCO[4]	7.4 ± 0.4	280 ± 3
(Swenson et al., 2008)	GRACE & OMCT	7.9 ± 0.4	277 ± 3

[1] Network shift; [2] deformation inversion; [3] deformation & GRACE; [4] GRACE & ocean model

Table 4.3: *Overview of estimates of the annual variation in ocean mass content based on CSR RL04 GRACE solutions, for different estimates of the annual variation of the geocenter. For details on the different models, see table 1.2.*

4.5.2   Uncertainties related to geocenter variations

In Ch. 1 the importance of the degree 1 coefficients, related to the position of the Earth's center of mask, was discussed. Since these variables cannot be observed by the GRACE satellites directly, external estimates are required. Several different methods exist to recover the geocenter position (e.g., based on displacements of geodetic networks, numerical climate models or the GRACE data itself), yielding annual variations with differences exceeding the margin of error significantly (see table 1.2). Given the global scale of the degree 1 coefficients, these uncertainties will also affect the GRACE based estimates of ocean mass (and consequently, also the estimation of steric variations through the JASON-GRACE combination). Table 4.3 gives an overview of estimates of the annual variation in ocean mass content using the different estimates of the annual variation of the geocenter presented in table 1.2. Not adding a geocenter correction yields an amplitude which is about 1 mm lower than the estimates including geocenter variations, and a slightly lagging phase maximum. Depending on the geocenter model, amplitude and phase may vary by almost 100 % and one month, respectively, although estimates based on either climate models, SLR observations or GRACE data show good agreement.
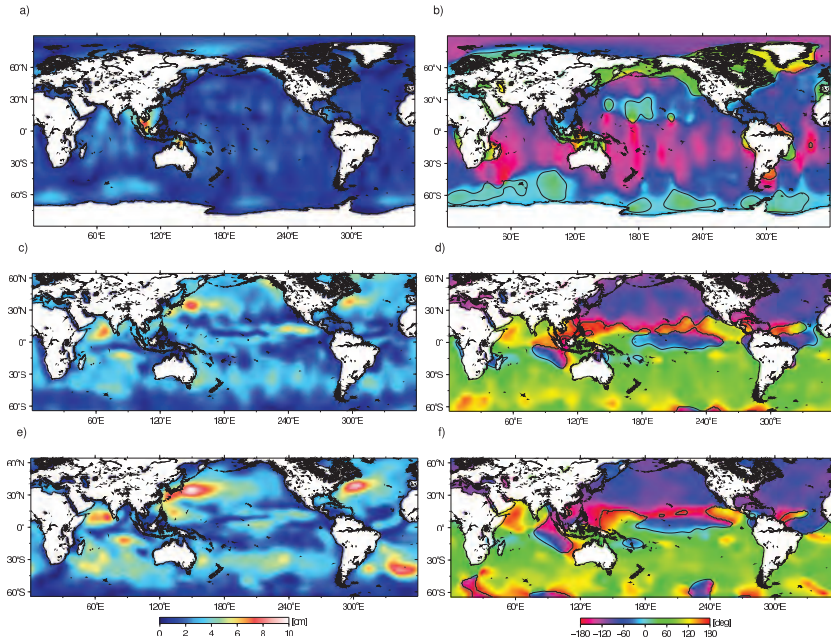
Figure 4.7: *a) Amplitude and b) phase of the annual cycle in ocean bottom pressure based on the GRACE RL04 solutions; c+d) for steric height from the JASON-GRACE combination; e+f) for steric height from the WOA05 climatology.*

4.6   Local results

Strong regional variations exist in the amplitude of the annual signal. In most regions, the annual amplitude is at most 2–3 centimeters, when smoothing the maps with a 500 km Gaussian kernel. Two prominent features are observed in the Gulf of Carpentaria and in the Gulf of Thailand, respectively. In both regions, the annual amplitude reaches values of $\sim$ 8 cm. Given the vicinity of these areas to land, the question arises whether these signals are due to non-tidal mass movements in these coastal zones, or are caused by leakage of neighboring continental sources.

Therefore, the GRACE observations were compared to data from nearby tide gauge stations. For the Gulf of Thailand, the station at Geting, Malaysia $(6°14'N, 102°15' E)$ was selected, for the Gulf of Carpentaria, the tide gauge at Milner Bay, Australia $(13°50' S, 136°30' E)$ is used. Figure 4.8 compares the tide gauge observations to the GRACE derived EWH variations at the nearest grid points. At both locations, excellent agreement is found between the data sets, with correlations of 0.92. Amplitudes and phase are comparable, although the tide gauge at Milner Bay, Australia shows a slightly larger amplitude than the
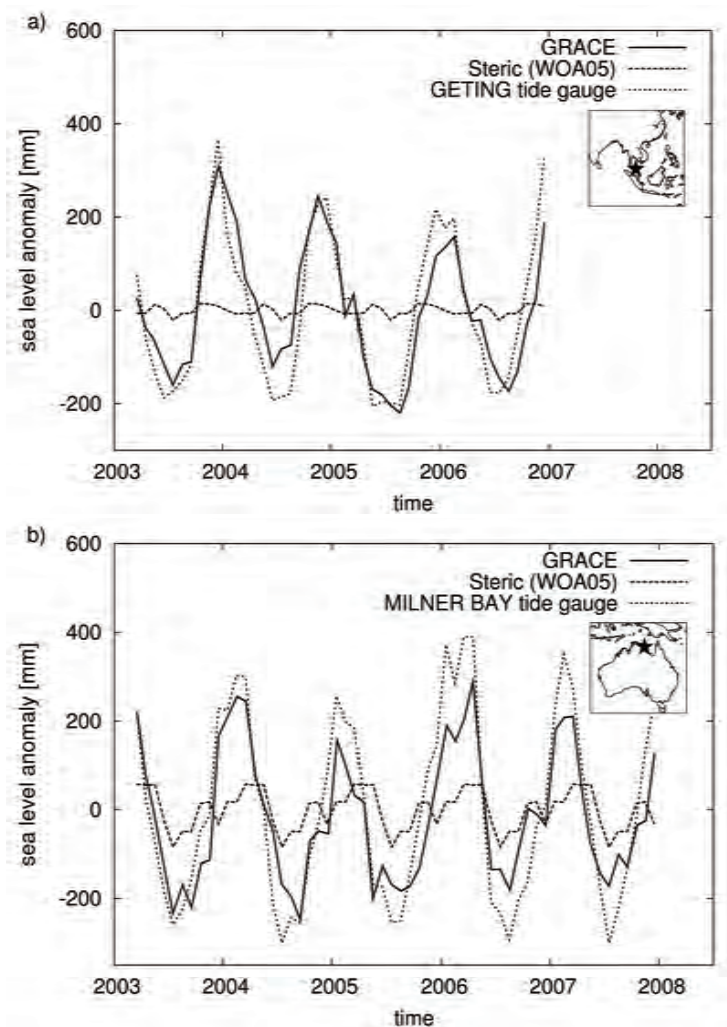
Figure 4.8: *a) Variations in sea level anomaly at Geting, Malaysia (6° 14′ N 102° 15′ E) based on tide gauge data, steric height anomalies from WOA05 and GRACE observations; b) as a), but for Milner Bay, Australia (13° 50′ S 136° 30′ E). Units are mm of water. The CSR RL04 GRACE data are filtered applying EOF analysis to the spherical harmonics, no additional smoothing is performed. Insets show the locations of the tide gauge stations.*

GRACE data (28±3 mm versus 19±3 mm), in line with the findings of Tregoning et al. (2008). This can be attributed to residual thermohaline variability, with an annual cycle of approximately 4.4 cm and a maximum in mid-March (based

on the WOA05 climatology). The sea level variations at Geting, Malaysia are nearly completely explained by the eustatic fluctuations as observed by GRACE (21±2 mm versus 17±3 mm), both on annual and interannual timescales. Differences may arise due local environmental influences at the tide gauge locations, residual interannual steric variations, and because of signal attenuation due to the limited spatial resolution of the GRACE data, compared to the point-like character of the tide gauge measurements. A possible driving mechanism behind the observed ocean bottom pressure fluctuations could be related to the piling up of water in these shallow regions (not exceeding ∼80 m) driven by seasonal wind forcing, e.g., due to the northeastern winter monsoon in South Asia (Morimoto et al., 2000).

Part of the signals in the GRACE data can be attributed to the baroclinic OMCT model, that is used in the background processing of the satellite data to remove the effects of short term non-tidal ocean mass variations, but is added back later. In the Gulf of Thailand, the OMCT model explains about 75% of the total signal, compared to 35% in the Gulf of Carpentaria. This implies that a significant part of the ocean bottom pressure fluctuations in these shallow regions are not well represented in the numerical ocean model, but are captured by the GRACE satellite observations.

Returning to fig. 4.7, other regions with a prominent annual variation in ocean bottom pressure are the Indian Ocean and the western South Pacific. In the Southern Ocean, the region situated southwest of Australian clearly stands out. In this region, bottom pressure variability induced by wind-stress will be enhanced by bathymetric effects, because of closed contours of potential vorticity, f/H, with f being the Coriolis parameter and H the ocean depth, see, e.g., Fukumori et al. (1998). The above-average annual amplitude in the western sector of the North Pacific is also attributed to this mechanism (Bingham and Hughes, 2006).

An inspection of the phase of the annual ocean bottom pressure cycle reveals a coherent pattern in the major oceans. Ocean bottom pressure in the Southern Ocean reaches its maximum in boreal winter, whereas the Pacific and Indian Ocean peak in boreal summer. An exception to this is the region at $\sim 30°$N in the North Pacific, which shows a phase difference of approximately 120 degrees compared to the surrounding regions. This node has also been observed in numerical ocean models (Ponte, 1999; Bingham and Hughes, 2006; Vinogradov et al., 2008) and indicates a seasonal amplification of the North Pacific gyre in boreal winter (Ponte, 1999). The (North) Atlantic is nearly 90 degrees out of phase with the Pacific and Atlantic, indicating a seasonal exchange between the major ocean basins, although the phase differences appear to be smaller than those suggested by numerical ocean models (Ponte, 1999; Vinogradov et al., 2008).

Stronger annual variations are observed in steric sea level from the JASON-GRACE combination. Notable areas of above-average amplitudes are the western boundary currents, the Arabian Sea and the tropical Indian ocean and the zonal band in the eastern tropical Pacific. Low amplitudes are observed in the Southern

Ocean. These features compare well with the patterns found in the WOA05 climatology, although amplitudes are slightly higher in the latter.

The annual steric cycle in the Northern and Southern Hemisphere show a pronounced phase opposition, with peak values in their respective summer months. Within each hemisphere, annual phase shows a coherent large-scale pattern, except for the tropics regions. In the tropical Indian and Pacific Ocean westward propagating phase patterns are observed, indicative of annual Rossby waves traveling along the equator (e.g., Masumoto and Meyers, 1998; Kessler, 1990). Again, the JASON-GRACE phase patterns compare well with those of the WOA05 climatology.

Assuming momentarily that both the GRACE and JASON data are error-free, the amount of annual variance in the JASON-1 observations of total sea level (ξ) explained by the steric (ξ_ρ) and mass (ξ_{mass}) variations may be assessed. The variance explained by a component ξ_i, or skill, is computed as:

$$1 - \frac{\sigma^2_{\xi - \xi_i}}{\sigma^2_\xi} \tag{4.6}$$

where $\sigma^2_{\xi - \xi_i}$ is the residual variance after removing component ξ_i from the total sea level ξ, the variance of which is indicated by σ^2_ξ. As is evident from fig. 4.9, steric variability is responsible for the majority of the signal in the oceans. In the Atlantic and North Pacific, typically 60% to 80% of the variance is due to steric effects, which qualitatively agrees with the results of Vinogradov et al. (2008) based on a numerical ocean model. Mass variations are the dominant mechanism in the Southern Ocean and in shallow waters such as the Gulf of Carpentaria as discussed before. Note that negative variance explained may occur when the individual variance components and/or total variance are out of phase.

4.7   Conclusions

In this chapter, it was shown that the newest GRACE releases observe changes in ocean mass and steric sea level accurately on a global scale. GRACE gravimetry was used to estimate ocean mass variations and, in combination with JASON-1 altimetry, to obtain changes in steric sea level. A good agreement is found for both amplitude and phase between the estimates based on GRACE data observations and independent reference sets (sterically corrected JASON-1 altimetry and WOA05 respectively), although the final result depends strongly on the choice of the model of seasonal geocenter motion.

As demonstrated in Ch. 2 and 3, the north-south stripes in the GRACE maps can be efficiently suppressed by applying EOF filtering to the spherical harmonics. By comparing local estimates of steric sea level anomalies from the combination JASON-1 altimetry and GRACE gravimetry with in-situ observations from WOA05, it is found that applying this filtering technique reduces the variance of

a)

b)
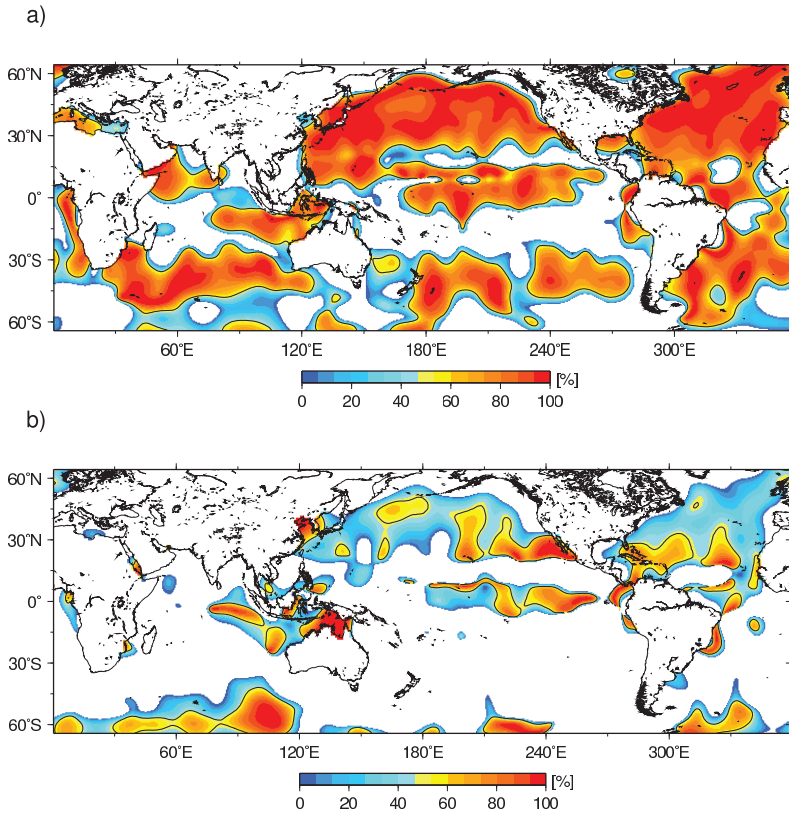
Figure 4.9: *Variance explained in the annual cycle of total sea level as observed by JASON-1, by a) steric height from the JASON-GRACE combination, and b) mass variations based on the GRACE RL04 solutions. Negative values are colored white.*

the residuals by ∼15% to 2.5 cm at 500 km smoothing. The variances of residuals increases rapidly for Gaussian smoothing radii lower than 500 km. The ocean area where the expected signal from WOA is greater than the estimated error in the steric maps is about 50% at this point, but decreases rapidly at higher resolution. Therefore, a 500 km smoothing radius is taken as a (conservative) lower bound for applications of GRACE data over the oceans. When no post-processing filtering is applied, this increases to approximately 700 km.

One shortcoming of this study is the fact that the WOA05 reference set cannot account for interannual variability, whereas this effect is observed by both altimetry and GRACE. Therefore the variances of residuals given in this study, which can be taken as a measure for the error in the GRACE observations over the oceans, should be seen as an upper bound for the accuracy of GRACE over the

oceans. With the recent completion of the ARGO array, real-time salinity and temperature observations have become available which may improve the error estimates in the future, when sufficiently long time series are available.

Strong evidence for aliasing of the S_2 tide is found in several regions, most prominently in the Australian North West Shelf region (Schrama et al., 2007). Removing this signal results in a significantly better agreement of the GRACE data with the reference data in these regions. Clearly, improved tidal models are a requirement to come to more accurate GRACE solutions in the future. However, the tidal aliasing footprints in the GRACE observations also offer an opportunity to improve such models in poorly constrained areas, such as underneath the Antarctic ice shelves as was shown in the study of Han et al. (2005).

In the majority of the ocean, the annual variability in total sea level as observed by the JASON-1 altimeter is governed by changes in steric sea level. Locally, the steric sea level derived from the altimetry and gravimetry data shows good agreement with the reference WOA05 data. Mass variations are dominant in a limited number of regions, mostly in the Southern Ocean. Strong annual variations are observed in the Gulf of Carpentaria and Thailand, respectively. The GRACE observations in these areas correlate well with local tide gauge data, indicating that these ocean bottom pressure variations are not an artifact of deficiencies in the GRACE solutions. The barotropic OMCT model used in the GRACE background processing underestimate the signal in these areas, highlighting the potential of the GRACE mission to provide new insights in ocean dynamics and improve the performance of numerical ocean models.

The good agreement between the GRACE observations and independent reference data at the annual timescale, gives confidence in the possible retrieval of interannual and secular variations of the ocean's mass content and steric sea level. Over the oceans, trends in the GRACE data are small, i.e. in the order of a few tens of millimeters per year globally. The key uncertainty in estimating ocean mass changes is therefore the correction for glacial isostatic adjustment (GIA), the viscoelastic response of the solid Earth to changes in surface loading since the last glacial maximum. Depending on the chosen viscosity profile and deglaciation history, this correction may alter the global trend by 1 to 2 millimeter per year (Willis et al., 2008; Leuliette and Miller, 2009; Cazenave et al., 2009). Furthermore, trends in the position of the geocenter are currently not accounted for. A trend of 1 mm/year in the X, Y or Z direction will result in a trend in global ocean mass content of 0.4, 0.3 and 0.5 mm/yr respectively. Narrowing the uncertainties in the GIA models and geocenter position is therefore of paramount importance to improve our understanding of changes in the ocean's heat and mass content and of the climate as a whole.

Chapter 5

Weighing the Greenland Ice Sheet

5.1 Introduction

Despite its relatively small volume, the Greenland ice sheet is an important actor in the field of study of global climate change. Its proximity to other land masses, and in particular the Gulf Stream, makes it vulnerable to even small changes in the Earth's climate, much more than its counterpart in the Southern Hemisphere, the Antarctic ice sheet, which is governed by its own climate (Rignot and Thomas, 2002).

Several studies have addressed changes in the behavior of the Greenland ice sheet over the last few years. Many of the outlet glaciers have increased in speed, with most pronounced changes in the southeast and west; three of the largest glaciers (Helheim Glacier, Kangerdlugssuaq Glacier and the Jakobshavn Isbræ glacier) have almost doubled their outlet velocities, accompanied by a large retreat of their terminus positions (e.g., Stearns and Hamilton, 2007; Rignot and Kanagaratnam, 2006; Joughin et al., 2004; Howat et al., 2008b; Luckman et al., 2006). Along the coast, strong negative trends in the elevation of the ice sheet have been observed by altimetry, while regions in the interior are showing slightly positive rates (e.g., Thomas et al., 2006; Zwally et al., 2005; Johannessen et al., 2005). Summer temperature increased by 1.7°C between 1991 and 2006, with 2003, 2005 and 2007 having the highest summer temperature in 61 years (Mote, 2007; Hanna et al., 2008).

Concurrent with the increase in near surface summer temperature, passive microwave satellite observations have shown record melt extents during the last years, reaching an absolute maximum in 2007 in the regions situated above 2000 m

(Tedesco, 2007; Mote, 2007). Numerical ice sheet models, driven by atmospheric data, confirm the change in the ice sheets behavior, with increasingly positive runoff rates and negative trends in the surface mass balance (Hanna et al., 2008; Fettweis, 2007; van den Broeke et al., 2009). It should be kept in mind that the Greenland ice sheet is not only affected by changes in the atmosphere, since its many marine terminating glaciers bear a strong sensitivity to changes in ocean temperature. For example, the dramatic 1997 speed-up of the Jakobshavn Isbræ and the associated retreat of the glacier tongue has been linked to intrusion of warm subsurface waters from the Irminger Sea, driven by changes in the atmospheric circulation (Holland et al., 2008).

Unfortunately, much of the behavior of the Greenland ice sheet and its (future) contribution to sea level change remains unclear. Due to the vast size of Greenland and its hostile environment, most of the (in-situ) observation based studies rely on extrapolation of a sparse set of samples. The physics of glacier dynamics are also far from understood and are lacking in the current generation of ice sheet models (Bamber et al., 2007). In the following chapter, it will be shown how GRACE can contribute to obtain a better understanding of the present-day changes in the mass balance of Greenland. The results presented are based on 58 monthly observations (CSR RL04) between, and including, February 2003 to January 2008. A forward modeling technique is used which allows the recovery of the mass variations at a regional scale.

5.1.1   Observation methods

The mass balance of an ice sheet is defined as the difference between mass accumulation and mass outflux. Accumulation mainly occurs through precipitation, i.e. snow deposition and rainfall, the mass outflux is governed by ice discharge by glaciers and by sublimation or melting of the snow or ice, mainly at the top or bottom of the snow/ice column, and subsequent water runoff:

$$\dot{M} = M_{\mathrm{a}} - M_{\mathrm{r}} - M_{\mathrm{s}} + M_{\mathrm{b}} - M_{\mathrm{i}} \tag{5.1}$$

where $\dot{M}$ is the change in total ice mass, M_{a} the surface accumulation, $-M_{\mathrm{r}}$ the loss by surface runoff, $-M_{\mathrm{s}}$ the loss through sublimation, M_{b} the balance at the bottom and $-M_{\mathrm{i}}$ represents the loss through ice discharge at the boundaries (e.g., van den Broeke et al. (2009)). Neglecting basal melting and grouping the processes occurring in the top layer of the ice sheets into the surface mass balance (SMB), eq. 5.1 may be rewritten as

$$\dot{M} = SMB - M_{\mathrm{i}} \tag{5.2}$$

Due to the vast size of the Greenland ice sheet, an accurate assessment of the change in total mass based on in-situ data only would be a costly and labor intensive matter. Space based observations, often providing a near-global coverage, offer an excellent tool to obtain a picture of the state of the ice sheet. Generally,

the approaches used to monitor the changes in the ice sheet mass can be divided into three categories: (1) comparing the mass input to the mass output (the budget method); (2) using changes in surface elevation (e.g., from ICESat), and (3) gravity (e.g., from GRACE). These three approaches will be briefly discussed in the following sections.

Budget method

The budget (or flux) method combines estimates of surface mass balance (accumulation minus ablation) with ice flow over the grounding line of the ice sheet's outlet glaciers, the so-called flux method. The surface mass balance is either obtained from stratigraphic analyses of the ice cores at selected locations, or from snowfall and melt output from regional climates models, as in, e.g., Rignot and Kanagaratnam (2006). To calculate the mass output, two quantities have to be known: the ice thickness and the mean horizontal velocity of the vertical ice column at, or close to, the grounding line. Most of the ice thickness data are obtained by airborne or groundbased radio echo sounding and have an accuracy in the order of 10 meters. Ice flow velocities are generally obtained by means of interferometric synthetic aperture radar (InSAR) measurements, in which two different radar images made at a different location and/or time are combined. Comparing the phase of the two images for one point yields the displacement (after correction for topography) during the two passages of the satellite and therefore can be used to deduce the flow velocity. The main limitations of the InSAR observations are that the flow velocity can only be measured in the look direction of the radar aperture and that the radar path length is sensitive to variations in atmospheric water vapor content (Bamber et al., 2000). Velocities are measured with an accuracy of approximately 10–30 m/yr (Rignot and Kanagaratnam, 2006). The result of the budget method strongly relies on the surface mass balance estimates provided by the regional climate models, which vary depending on the model used. Rapid changes in the flow velocity of outlet glaciers, such as observed at Jakobshavn Isbræ (Joughin et al., 2004), may also corrupt the results.

Altimetry measurements

Altimeter measurements allow the detection of changes in the ice surface height through repeat measurements of surface elevation (e.g., Zwally et al., 2005). These height changes can, after correction for bedrock movement, be related to changes in mass by multiplication with the appropriate density, which is unfortunately less trivial than one would assume. The density at the surface varies roughly between 350 kg/m^3 and 920 kg/m^3, depending on the relative amount of snow and ice at the surface layer. Moreover, variations in snow accumulation and temperature result in a non-uniform densification of the snow pack, which will be misinterpreted as mass changes if not accounted for (e.g., Helsen et al., 2008).

Furthermore, the radar altimeter missions used in most studies so far were

designed to sample height variations over the ocean surface, which is relatively flat compared to the strong undulating topography of the outlet glaciers at the ice sheet's edges. Over flat surfaces the first returned radar pulse will be associated with the point beneath the satellite, but along-track variations in the ice surface will move this point away from nadir, causing an ambiguity in the determination of the echo position. This becomes especially problematic in the coastal regions, where outlet glaciers are located in narrow fjords with a cross section smaller than the radar footprint (Thomas et al., 2008). The observations may therefore be biased toward the less temporarily variable inland regions and most studies relying on data obtained from ocean altimeter instruments do indeed produce trends that are less negative than estimates based on other observations techniques.

ICESat, launched in 2003, is using a laser altimeter with a footprint of about 60 meter, spaced at about 172 meter. Unfortunately, the lasers aboard ICESat deteriorated much faster than anticipated and measurements are now being taken three times a year at 33-day measurements campaigns (Schutz et al., 2005). Due to the small footprint, the measurements are much less affected by topography errors, although correction for surface slope is still required (e.g., Slobbe et al., 2009). Also, the laser signal is only marginally affected by changes in the di-electric properties of the snow layer, which is another major problem of radar altimetry (e.g., Zwally et al., 2005). Nevertheless, glaciers located in between the ground tracks of the satellite will remain unsampled, which may cause underestimation of the mass changes. This can be partially overcome by combining the ICESat observation with regional observations to fill in the gaps, e.g., using differenced digital elevation models such as from the Advanced Spaceborne Thermal Emission and Reflection radiometer (ASTER; Howat et al., 2008b).

Gravimetric measurements

The Gravity Recovery and Climate Experiment (GRACE) satellites have been providing the scientific community with a quasi-continuous record of the Earth's gravity field over the last 6 years. Due to their global coverage, they offer an excellent opportunity to study mass changes over large areas. Assuming the majority of the change is related to water mass transport (Wahr et al., 1998), several authors have used GRACE data to estimate the rate of mass loss over Greenland. Due to the limited spatial resolution and the presence of non-random noise, obtaining mass estimates from GRACE data is not straightforward and results vary widely between 101 Gt/yr and 227 Gt/yr (Luthcke et al., 2006; Ramillien et al., 2006; Velicogna and Wahr, 2006b; Chen et al., 2006b; Wouters et al., 2008).

The large differences in the estimates can be partly attributed to the different observation periods used in these studies combined with the large variability in Greenland's mass balance, but also to the different methods and GRACE data used. Besides differences introduced by the different groups processing the raw satellite data, differences can be caused by truncating coefficients differently, using area smoothing functions or averaging gridded and smoothed data, different ap-

proaches to correct for leakage from neighboring signals and from failing to restore power lost by smoothing. Also, GRACE measurements are especially sensitive to mass redistribution within the Earth, since the average density of the Earth is about five times as large as that of water. The majority of this signal comes from the glacial-isostatic adjustment (GIA) due to the melting of the major ice domes of the last Ice Age.

5.2 Method

The first GRACE data was released in April/May 2002 and a quasi-continuous series of gravity solutions are made available at monthly intervals since August 2002, but there were fundamental changes in on-board software in January 2003. Following these changes, the raw data became significantly less noisy, which leads to cleaner solutions after January 2003 (Chambers, personal communication, 2008). Therefore, observations prior to February 2003 have been excluded from this study.

The GRACE solutions are provided in terms of Stokes coefficients and are known to be contaminated by noise at the shorter wavelengths. A post-processing step is therefore applied to the monthly solutions, using a filtering technique based on empirical orthogonal function (EOF) decomposition of the spherical harmonics grouped by order, as discussed in Ch. 2. The obtained principal components (PC) are tested for temporal random behavior and the series of coefficients are then rebuilt using the non-random PCs and associated EOFs. Since the GRACE satellites are insensitive to changes in the Earth's center of mass, seasonal geocenter variations were implemented using a combination of the OMCT ocean model (Thomas, 2002) and GRACE data over land (see Swenson et al., 2008). Also, the C_{20} terms were replaced by values derived from satellite laser ranging data (Cheng and Tapley, 2004). After filtering, the coefficients are converted to maps of equivalent water height. To suppress any remaining noise in the maps of monthly mass anomalies, the solutions are convolved with a Gaussian smoothing kernel with a 250 km halfwidth radius. A trend as well as an annual and semi-annual varying signal is estimated through a least squares fit to the monthly observations.

The GRACE data has a limited spatial resolution, which will, in combination with the smoothing required to suppress noise in the data, inevitably lead to attenuation of the original signal. Furthermore, it will cause the signal to spread over a larger area, which can be clearly seen in fig. 5.1, where strong negative trends are observed beyond Greenland's coastal line. An additional complicating factor is that contamination from external signals, such as changes in the continental hydrology or ocean bottom pressure in the regions surrounding Greenland, will occur. Simply considering the trend values within the Greenland area does therefore not suffice and will lead to biased results. Velicogna and Wahr (2006b)
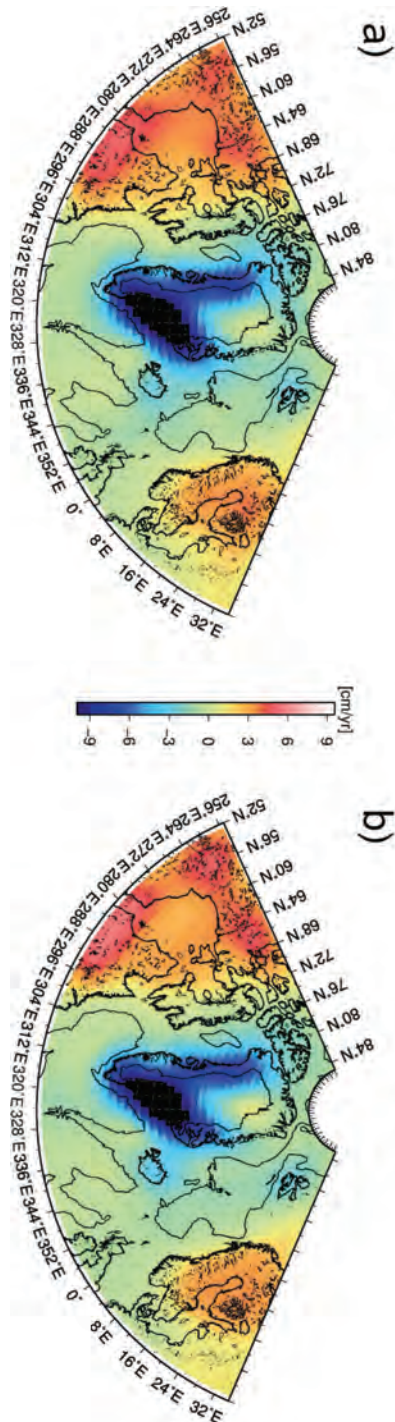
Figure 5.1: a) Trend in equivalent water height over Greenland between February 2003 and January 2008 as observed by GRACE and b) simulated with the forward model, both smoothed with a 250 km Gaussian filter. A maximum negative value of 12.5 cm/yr is found at (39.5° W, 66.5° N), close to the Helheim glacier. Elevation contours are plotted at 2000 m intervals. Black color is off-scale.

estimated a scaling factor to compensate for signal attenuation caused by smoothing and truncation of the spherical harmonics and removed the effect of external mass changes by means of geophysical models. However, this method was used to obtain temporal mass variations over the whole ice sheet or large portions, i.e., the northern and southern part, only.

In this study, a different approach is taken based on forward modeling of higher resolution mass variations that agree with the GRACE observations once smoothed. Similar methods have been used before, based on either the global spherical harmonics provided by the GRACE science teams (Chen et al., 2006b), or using direct ranging measurements between the GRACE satellites (Luthcke et al., 2006). However, in contrast to Chen et al. (2006b), this study is not limited to the regions of largest losses, but estimates mass changes over the entire ice sheet. To do so, the ice covered area is divided into 8 different zones corresponding to the major glacier drainage systems, based on climatology and satellite radar and airborne laser altimetry observations (Zwally et al., 2005). Furthermore, each of the basins is partitioned into two zones, located above and below the 2000 m elevation contour respectively (see fig. 5.2). This – relatively arbitrary – altitude was chosen in order to allow comparison to earlier results of Luthcke et al. (2006); Zwally et al. (2005); Thomas et al. (2006) and other studies.

Each of the 16 basins is then assigned a preliminary estimated mass change rate, based on Rignot and Kanagaratnam (2006). Note that the final result does not depend on the starting values. This has been verified by initializing the procedure with random values in the basins (within a reasonable range, i.e. $[-1000 \text{ Gt}; 1000 \text{ Gt}]$) and indicates that the results are not 'local minima/maxima' in the solution space. However, initiating the procedure with values close to the expected values does reduce the computing time significantly. The same procedure is repeated for the regions surrounding Greenland, where relatively large basins over the oceans are used, since the expected signals are small here.

An iterative procedure is then started, which uses a variation on the bisection algorithm (e.g., Wood, 1992) to reach an optimized agreement between the simulated mass distribution in the basins and the GRACE observations. In a first step, the value in the first basin is adapted so that it takes a number of possible values within a specified search domain, e.g., $[-1000; 1000 \text{ Gt/yr}]$. Initially, this is done with relatively large steps of, e.g., 100 Gt/yr, so that a set of possible solutions exist. For example, in case of the aforementioned search domain and step size, the number of possible solution, n_s, equals 20.

Next, these solutions, which are maps of surface mass trend, are converted to Stokes coefficients up to degree 60 and the Gaussian smoothing kernel is applied, so that they resemble the GRACE data. The coefficients are then converted back to maps of surface mass and compared with the GRACE trend map. As a measure of quality, the spatial root-mean-square (RMS) of the difference between GRACE and model trend map is computed. The triplet of models (i−1; i; i+1) for which $\text{RMS}_i < \text{RMS}_{i-1}$ and $\text{RMS}_i < \text{RMS}_{i+1}$ then defines the next search domain for the first basin. If no such *RMS minimum* is found, the search domain is extended.

The procedure is then applied to the other basins as well and is repeated until no changes occur in the basins between two successive iterations. After this, the step size reduced by a factor of 10 and the root finding algorithm is re-initiated for all basins. When the step size reaches a value smaller than 0.1 Gt/yr, the procedure is stopped. The mass variations in each of the 58 monthly solutions are estimated using a similar methodology. The performance of the forward model is discussed in Appendix A.

5.3   Results

After convolving with the 250 km Gaussian smoothing kernel, excellent agreement is obtained between the forward model and GRACE observations (fig. 5.1). Integrated over the entire ice sheet, the mean difference between the (smoothed) observations and model is in the order of 1–2 Gt/yr, whereas the absolute differences sum up to 8 Gt/yr, with values for the individual basins in the order of 0.5 Gt/yr. The unsmoothed forward model provides an average water height change for each basin (fig. 5.2), which can be multiplied by the its area and the density of water to obtain an estimate of the total mass change in the basin (table 5.1). By summing the results for all basins, a total mass loss over Greenland (continental ice only, 1.768×10^6 km^2 in total) of 171±13 Gt/yr for the period of February 2003 to January 2008 is found through linear regression, see fig. 5.3. Error bars are discussed in section 5.3.2.

Trends based on previous releases of different GRACE processing centers have been known to show little agreement (e.g., Slobbe et al. (2009)). To test the robustness of the obtained estimates, a trend based on the GFZ RL04 solutions was also estimated, using the same processing steps applied to the CSR solutions. Over a similar period, excluding the period of June–September 2004 when the GRACE satellites were in a near-repeat orbit resulting and the GFZ solutions are of degraded quality, a trend of −165±18 Gt/yr is found, which is well within the error bounds of the trend based on the CSR data.

5.3.1   Glacial isostatic adjustment correction

Part of the signal observed by the GRACE satellites is due to redistribution of mass in the solid earth, in response to past changes in the geometry of the cryosphere. Mantle material in the Earth's interior will flow toward the unloaded area, causing a disturbance in the geoid. Since the average density of the Earth's interior is about five times as large as that of ice, the GRACE observations are particularly sensitive to this phenomenon, known as glacial isostatic adjustment (GIA). In order to obtain an estimate of the present-day mass changes of the Greenland ice sheet, the GIA signal needs to be removed from the GRACE observations, which is usually done by means of a GIA model. Errors in the correction are mainly caused by mismodeling in the evolution of the ice load through time
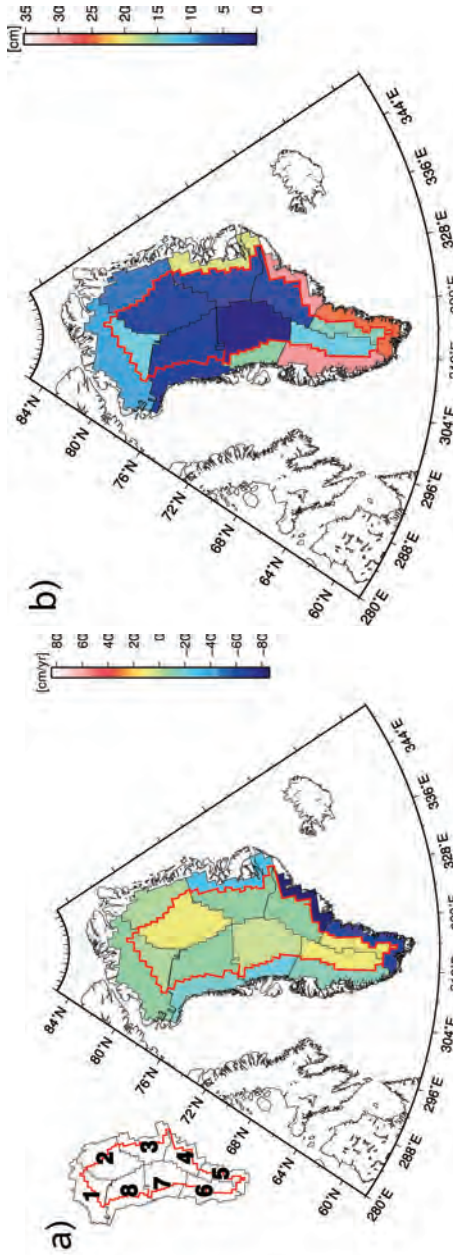
**Figure 5.2:** *a) Trends for 2003–2007, and, b) amplitude of annual signal estimated from the forward model. The inlay in the upper left corner shows the basin numbers used throughout the text. The bold red line delimitates the approximate 2000 m elevation contour. Trends have been corrected for post glacial rebound effects.*

Basin number		Basin area (10^3 km^2)	trend (Gt/yr)	avg. trend (cm/yr)	amplitude (Gt)	phase (day)
Greenland						
1:	< 2000 m	177	−12 ± 4	−6.8 ± 2	19 ± 3	71 ± 24
	> 2000 m	81	−1 ± 4	−1.2 ± 5	9 ± 4	222 ± 88
	total	258	−13 ± 4	−5.0 ± 2	9 ± 5	99 ± 26
2:	< 2000 m	112	−6 ± 4	−5.4 ± 4	11 ± 3	119 ± 38
	> 2000 m	197	19 ± 6	9.6 ± 3	9 ± 5	329 ± 181
	total	309	13 ± 6	4.3 ± 2	3 ± 8	41 ± 85
3:	< 2000 m	84	−25 ± 5	−30 ± 6	17 ± 5	128 ± 37
	> 2000 m	136	−10 ± 5	−7.3 ± 3	10 ± 4	53 ± 50
	total	220	−35 ± 5	−16 ± 3	20 ± 8	102 ± 21
4:	< 2000 m	58	−49 ± 4	−85 ± 7	17 ± 4	102 ± 21
	> 2000 m	111	−7 ± 3	−6.3 ± 3	7 ± 3	113 ± 41
	total	169	−56 ± 4	−33 ± 3	24 ± 5	108 ± 15
5:	< 2000 m	80	−51 ± 5	−64 ± 7	21 ± 5	135 ± 36
	> 2000 m	55	6 ± 6	11 ± 11	8 ± 6	35 ± 79
	total	135	−45 ± 4	−33 ± 3	20 ± 6	116 ± 20
6:	< 2000 m	104	−13 ± 5	−13 ± 5	31 ± 4	122 ± 20
	> 2000 m	94	11 ± 5	12 ± 5	11 ± 4	277 ± 66
	total	198	−2 ± 5	−1 ± 3	21 ± 8	140 ± 32
7:	< 2000 m	55	−14 ± 3	−25 ± 6	10 ± 3	115 ± 37
	> 2000 m	179	2 ± 5	1.1 ± 3	2 ± 4	258 ± 258
	total	234	−12 ± 5	−5 ± 2	7 ± 6	138 ± 58
8:	< 2000 m	93	−16 ± 4	−17 ± 5	3 ± 2	242 ± 259
	> 2000 m	152	−13 ± 5	−8.6 ± 3	8 ± 5	108 ± 48
	total	245	29 ± 6	−12 ± 2	6 ± 9	135 ± 70
Total:	< 2000 m	763	−186 ± 19	−24 ± 2	106 ± 15	112 ± 12
	> 2000 m	1005	7 ± 18	0.7 ± 2	24 ± 11	354 ± 176
	total	1768	−179 ± 23	−10 ± 2	95 ± 9	101 ± 13
Non-Greenland						
Svalbard		179	−8.8 ± 3	−4.9 ± 1	10. ± 3	160 ± 50
Iceland		181	−11.4 ± 3	−6.3 ± 1	11 ± 3	98 ± 28
Ellesmere Isl.		428	−15.8 ± 9	−4 ± 2	7.2 ± 6	153 ± 50

Table 5.1: *Overview of the trends and annual amplitudes observed in the individual basins between February 2003 and January 2008. Statistics are given for regions below and above 2000 m in Greenland as well as some selected neighboring regions. The average trend is obtained by dividing the basin trend by its area and density of water.*
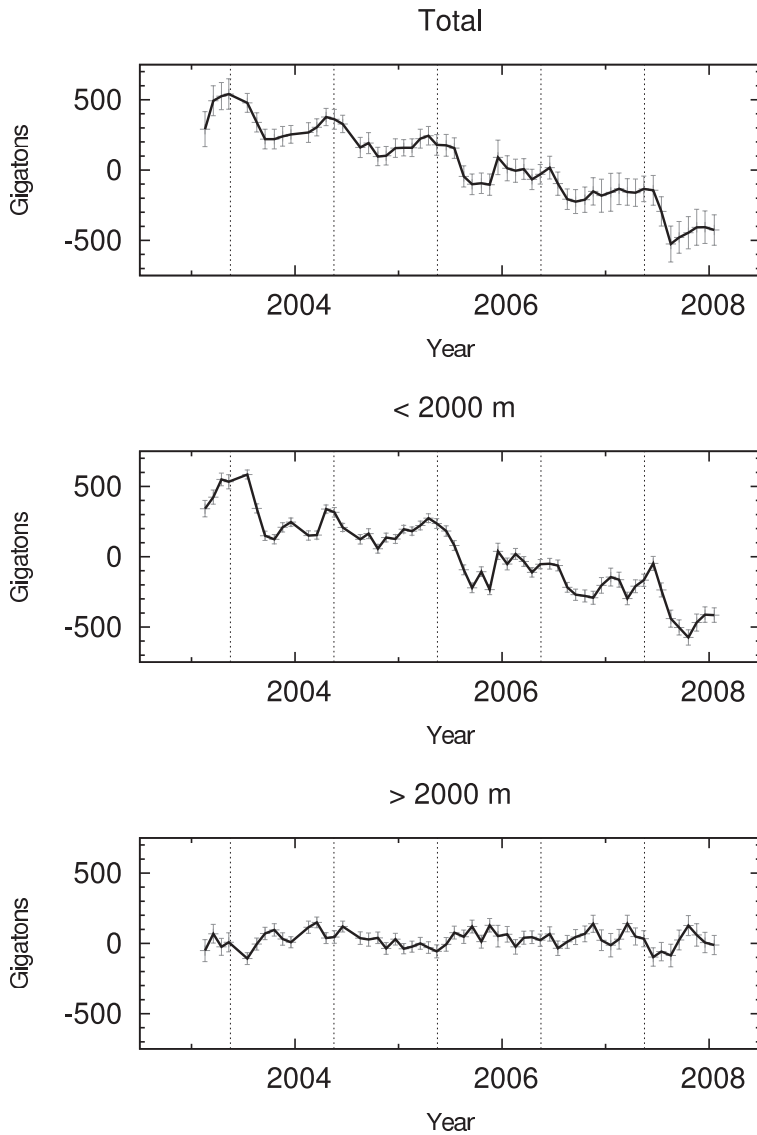
Figure 5.3: *Time series of the monthly GRACE solutions between February 2003 and January 2008, for the entire Greenland ice sheet (top), the regions below 2000 m (middle) and the regions above 2000 m (bottom). The vertical dashes indicate the middle of month May for each year, roughly coinciding with the start of the summer season.*
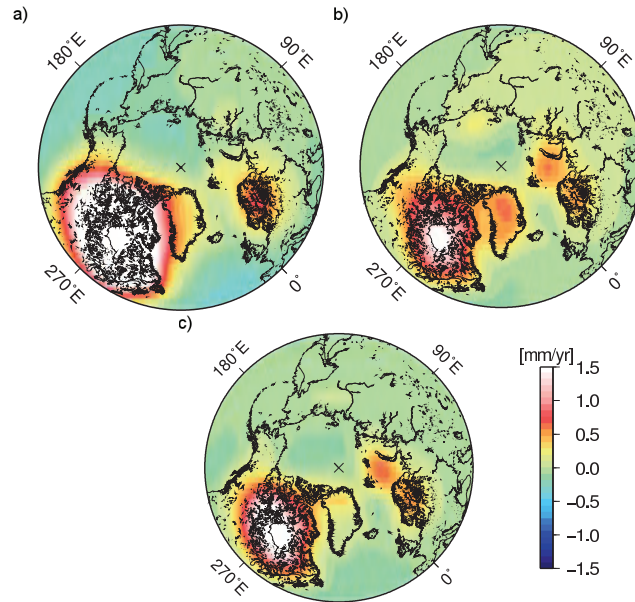
Figure 5.4: *Present-day GIA rates in geoid height, based on a) the ANU deglaciation and viscosity profile, b) ICE-3G, combined with the VM2 viscosity profile, and c) ICE-5G, combined with the viscosity profile of Paulson et al. (2007).*

and by uncertainties in the viscosity of the Earth's mantle. In Greenland, the GIA signal is the combined effect of the partial deglaciation of Greenland and disintegration of the Laurentide ice sheet situated in the west and the associated collapse of its forebulge. Additionally, a readvance of the Greenland ice sheet took place during the last 4000 years, mainly in west Greenland. Since the readvancing ice covered most geomorphological evidence used to constrain the ice model history and mantle viscosity, uncertainties in the predicted GIA signal are relatively large in Greenland, although the total expected signal is small (Dietrich et al., 2005). This is illustrated in fig. 5.4, which shows the present-day rate in geoid height from three different GIA models (kindly provided by Paolo Stocchi).

In this study, the GRACE derived maps of mass changes are corrected using the GIA model of Paulson et al. (2007), based on the ICE-5G ice load history of Peltier (2004) and a solid Earth model adjusted to match GRACE observations over Hudson Bay. To estimate the GIA correction error, the signal is recomputed using various deglaciation history models (ICE-3G of Tushingham and Peltier (1991), ICE-5G of Peltier (2004) and the ANU model of Lambeck et al. (2004a)) and earth models (Lambeck et al. (2004a), Paulson et al. (2007); VM-1 and VM-2 of Peltier (2004)) and the variance over Greenland (18 Gt/yr) is computed. Correcting for the effects of GIA adds an additional −8 Gt/yr to the estimated

trend, resulting in a mean trend of -179 ± 23 Gt/yr between February 2003 to January 2008. Note that recent results (e.g, Ivins and Wolf, 2008, and references therein) suggest that the GIA error might be underestimated, particularly due to ambiguities in the Laurentide ice model and the reconstruction of Greenland's ice history. Also, the three ice models used are not completely independent, since they depend partly on identical data. Further investigation of this issue is crucial to come to smaller and more reliable error bars on the GRACE based mass change estimates over Greenland.

5.3.2 Error sources

The error bars in the estimated trends above (± 23 Gt/yr) are obtained by quadratically summing (1) the absolute difference between the forward model and the GRACE observations, integrated over the basin, (2) the 95% confidence bounds of the regression analysis and propagation of the calibrated errors in the GRACE Stokes coefficients (10 Gt/yr), (3) the uncertainty in the GIA correction as discussed above, (4) a correction for the influence of the EOF filter (2 Gt/yr), and (5), an estimate of tidal errors (2 Gt/yr), which will be discussed below.

Filter induced errors

The GRACE observations have been filtered in order to remove the north-south striping patterns, using a filter method based on the temporal behavior of the spherical harmonics. Since a trend has a non-random nature, it is expected to pass the *Rule KS2* test used in the EOF filtering (See Ch. 2). Thus, it may be expected that the estimated trend is only marginally changed by the filtering. Moreover, filters based on the temporal behavior of the signal do not have a preference toward the spatial orientation of the signal. This is in contrast with other types of filters, e.g., the destriping filter of Swenson and Wahr [2006], which considers the spatial patterns of the signal and removes signals with a strong north-south orientation. As a result, meridional signals, such as mass changes along the east and west coast of Greenland, may be removed by such filters depending on the shape of the signal. The (simplified) simulation tests of Ch. 3 did indeed show that the estimated trend is only slightly affected by the EOF filter, provided that sufficient observations are available.

As a second test, EOF filtering is applied to the modeled monthly grids, after which a trend is fitted to the filtered grids. The difference in trend obtained from the unfiltered and filtered data is found to be 1.7 Gt/yr, with a root sum square sum of 2.1 Gt/yr. A maximum value of 1 Gt/yr is found in basin 5, for the region above 2000 m. This confirms the results from the earlier test on the simplified model.
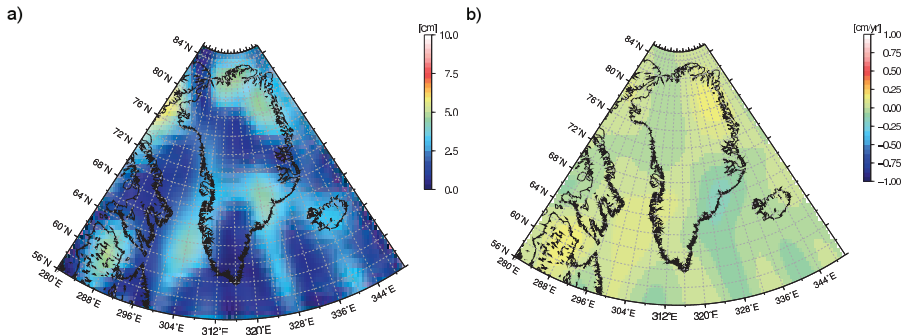
Figure 5.5: *a) Amplitude of the 3.8 yr harmonic in the CSR RL04 GRACE observations, and, b) difference in trend estimated with and without removing the K_2 signal.*

Tidal errors

Errors in the tidal model used in the background processing of the GRACE data will alias into spurious signals in the GRACE monthly observations, which can have a period a multiple of the original tidal constituent's period. The three most critical constituents are assumed to be the K_1, K_2 and S_1 tide, (e.g., Ray and Luthcke, 2006). The K_2 tide will alias into a signal with a period of approximately 1400 days, which is close to the total observation period of 5 years used in this study.

In the GRACE background processing, the FES2004 model is used to remove the tidal high-frequency signals from the raw range-rate observations. As described in Lyard et al. (2006), the ERS1/2 altimeter observations used in the assimilation of the K_2 tide solution appear to be of limited accuracy and therefore it is recommended to replace this particular constituent by the previous FES2002 K_2 solution, which does not rely on ERS1/2 data for this component. The GFZ processing decided to follow this recommendations, whereas the CSR use the K_2 tide solution as given in FES2004.

To assess to which extent errors in the K_2 constituent propagate into the trend estimates, the difference between trends estimated with and without a 3.8 year sinusoid removed is calculated, as in Willis et al. (2008). For the CSR solutions, the difference is rather moderate, with an overall mean of 0.9 Gt/yr and a root mean squared sum over the ice sheet area of 1.2 Gt/yr (fig. 5.5). The differences in trends for the GFZ solutions almost cancel out over the entire Greenland sheet (0.4 Gt/yr), but show slightly larger spatial variations, with a root mean squared sum equal to 2.5 Gt/yr. Given the fact that the observation period covers only ~1.5 cycles of the K_2 alias and the estimated signal is therefore quite uncertain (Blewitt and Lavallée, 2002), the signal is not actually removed, but included in the error estimate. This procedure is also applied for the S_2 constituent, which has an alias period of about 161 days, but the difference is found to be negligible

(less than 0.1 Gt/yr), which could be expected since the observation period used covers a sufficient amount of full cycles of the S2 alias. Unfortunately, not enough data is yet available to estimate the effect of the K1 constituent (alias period of about 7.5 years).

Atmospheric errors

A correction for atmospheric errors has not been applied, since the effect is expected to be small. Ramillien et al. [2006] found that the trend in the ECMWF surface pressure is typically less than 0.2 mm/year equivalent water level over Greenland. Integrated over the entire ice sheet (1.7×10^6km^2), this amounts up to 0.35 Gt/yr. The associated error in the trend is likely to be smaller or of the same order of magnitude. Velicogna and Wahr [2006] compared the ECMWF surface pressure fields with in-situ observations from Greenland automatic weather stations and state that "The variance of atmospheric errors is less than 3% of the GRACE variance, implying a negligible contribution".

Based on measurements between 1958 and 1999 from 6 weather stations located along the coast in South Greenland (located below 70°N), Hanna and Cappelen (2002) reported no statistical significant trends in mean air pressure, except at station 04360, located in Tasiilaq (65.36° N, 37.38° W).

The trends in air pressure have been reassessed in the framework of this study. Using the slightly extended (7 coastal stations) and updated set of observations of Cappelen et al. (2007), no significant trends in mean sea level pressure were found between 2003 and 2006, roughly matching the observation period of the GRACE observations (no data for 2007 and 2008 were available at time of writing).

5.3.3   Temporal variations in observed trends

The trends mentioned in the preceding section apply to the period of February 2003 to January 2008, but it should be stressed that fitting a linear trend is an oversimplification of reality. Because of the strong temporal variability in the mass balance of the ice sheet, the exact trend value will depend strongly on the length and starting point of the period under consideration. Fig. 5.6 shows the evolution in time of a trend fitted to a moving window of 24 and 36 months respectively. When applying a window width of 24 months, a strong interannual signal is apparent. This may be attributed to the large year-to-year differences between melting events during summer, as will be shown later on. Furthermore, the trend is strongly sensitive to the beginning date of the observation window, shifting the starting point by one month may cause a change of rate of up to 25 Gt/yr in case of a 24 month window (inset of fig. 5.6). Moving the start date by 6 months may case even larger differences of approximately 60 Gt/yr. Extending the window width to approximately 3 years or longer alleviates this problem, with maximum differences in the order of 5 Gt/yr between consecutive window starting dates. Most of the year-to-year variability is suppressed, although it is evident
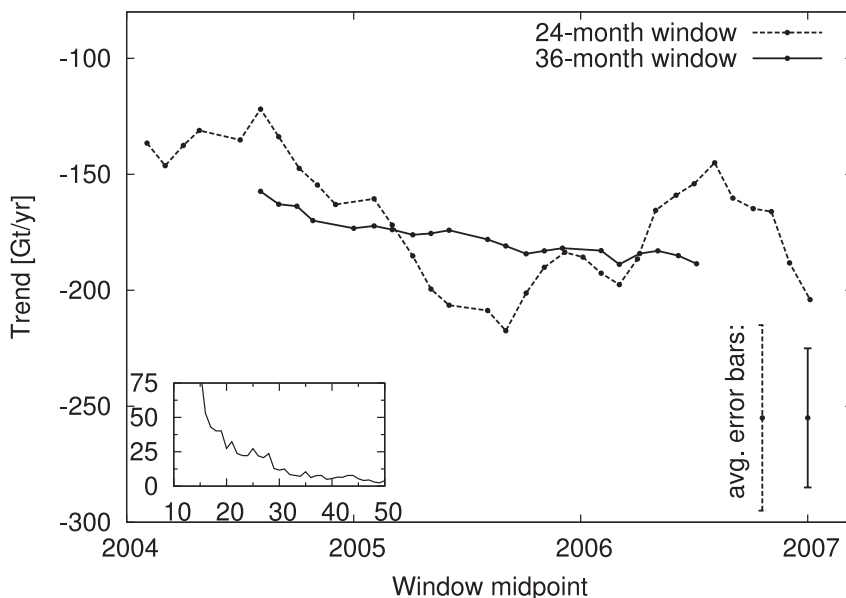
Figure 5.6: *Trends fitted to a 24 month and 36 month sliding window, respectively. The x-axis indicates the midpoint of the sliding window. Inset: Maximum difference in trend obtained after shifting window starting date by one month, as a function of the window width (x-axis).*

that the trend has become increasingly more negative in recent years, indicating an acceleration of the mass loss in the last few years.

5.4   Discussion

5.4.1   Regional changes

Regional trends

As in previous studies (Ramillien et al., 2006; Velicogna and Wahr, 2006b; Chen et al., 2006b), the approach of this study is based on global Stokes coefficients, but allows one to allocate the changes in mass to specific basins. The spatial distribution of the mass trends and annual amplitude per region is shown in fig. 5.2, numerical values are given in table 5.1. Mass losses are mainly taking place in the regions situated below 2000 m, where a negative trend of 186±19 Gt/yr is observed. Most pronounced negative trends are found in the coastal zones ranging from the east to the southeast (basins 4 and 5), with values up to −51±3 Gt/yr in basin 5. Relative to its size, basin 4 is losing mass most rapidly. This basin

contains two of Greenland's fastest flowing outlet glaciers, i.e. Kangerdlugssuaq Glacier (68.5°N,33°W) and Helheim Glacier (66.5°N, 38°W). Rapid retreat and thinning have been observed for these glaciers between 2001 and 2006 (Stearns and Hamilton, 2007; Luckman et al., 2006). Mass loss in the coastal zones of the two glaciers was estimated to be 47±7 Gt/yr (assuming an ice density of 917 kg/m^3) between 2001 and 2006 by Stearns and Hamilton (2007), which compares well with the trend of −49±2 Gt/yr found in this study. Howat et al. (2008b) combined ICESat altimetry observations with ASTER digital elevation models in the eastern coastal zones between roughly 62°N and 68°N and found a mean trend of approximately −100 Gt/yr between 2002 and 2005, with the regions below 2000 m accounting for 74% of the losses. This region covers about two-third of the combined basins 4 and 5, where a total mass loss of 111±6 Gt/yr is observed by the GRACE satellites.

Significant flow accelerations were observed by Rignot and Kanagaratnam (2006) for the 21 largest glaciers located in basin 5 (southeast), which doubled their speed between 1996 and 2005. Furthermore, flow accelerations were also observed in the northwest, corresponding to basins 7 and 8. Of these two areas, the former shows the largest losses in the GRACE observations, at a rate of −14 Gt/yr in the coastal zone. Basin 7 roughly coincides with Greenland's largest outlet glacier, Jakobshaevn Isbræ glacier, which almost doubled its speed between 1996 and 2003 after rapid thinning (and ultimately disintegration) of its floating ice tongue (Joughin et al., 2004). Based on laser-altimeter surveys, net ice loss in the 2002–2003 period was estimated at 18.3 Gt/yr by Krabill et al. (2004). The two northernmost coastal basins, 1 and 2, are close to being in balance, with trends in the order of −10 Gt/yr. Slightly higher values are found along the southwestern coast (basin 6).

The mass losses in the coastal areas are in contrast with the small positive trend found in the areas above 2000 m. The interior of Greenland (> 2000 m) shows an insignificant positive trend of 7±18 Gt/yr and appears to be in balance. The growth is most pronounced in the northern basin 2 and the southern basins 5 and 6, gaining mass at a rate of 19±4 Gt/yr, 6±3 Gt/yr and 11±3 Gt/yr, respectively. Positive elevation changes have been observed using satellite radar (Zwally et al., 2005; Johannessen et al., 2005) and laser altimetry (Thomas et al., 2006), particularly in the south of Greenland (basins 5 and 6 in this study), but such altimeter measurement are greatly affected by uncertainties in the density profile of the ice, driven by variability in accumulation and temperature.

Regional annual cycle

The coastal zones south of ∼74° show a pronounced seasonal signal (fig. 5.2), with mass accumulation peaking in late April to early May (day 112). Integrated over the coastal zones, the amplitude totals 106±12 Gt. This behavior is most accentuated along the south coast, with a maximum amplitude in the zone stretching from the southeast to the southwest (basins 4–6), with a maximum in basin 6,

where precipitation and runoff values are among the highest in Greenland (Ettema et al., 2009). The regions at higher elevations show little or no annual signal, with a total mass amplitude of 24 ± 11 Gt. The overall annual amplitude for the Greenland ice sheet is 95 ± 9 Gt, reaching its maximum on day of year 101 ± 13.

Basin characteristics

Figures 5.7 and 5.8 show the temporal evolution of the mass balance in the individual basins. Basin 1 shows a slightly negative trend in the first few years, which has stagnated since the winter of 2005–2006. Little annual variability is observed. Basin 2 is the only region showing a mass gain, at a rate becoming increasingly more positive since mid-2005. No significant changes in ice flow have been reported in these regions by Rignot et al. (2008b), hence the changes in the northern regions most likely originate in changes in surface mass balance. Regional climate models indicate an increase in precipitation in combination with a slight decrease in runoff around this time, although these events appear to be limited to 2006 only (Van den Broeke, personal communication, 2009). Given the relatively large amplitude of the K_2 tide in this region (fig. 5.5), part of the behavior may be explained by aliasing of tidal errors.

Further south, a record mass loss is observed in the summer of 2005 in basin 3, with similar events occurring in the summers of 2003 and 2007. The two regions on the southeastern coast, basins 4 and 5, show similar behavior, with strong losses during summer superimposed on a negative trend. This can be attributed to an increase in glacier flow velocity, e.g., that of the Helheim and Kangerdlugssuaq Glaciers (Stearns and Hamilton, 2007; Rignot and Kanagaratnam, 2006; Joughin et al., 2004; Howat et al., 2008b; Luckman et al., 2006), and a negative trend in surface mass balance caused by an anomalously high runoff and a decrease in precipitation (van den Broeke et al., 2009). An interesting feature in basin 5 is the yearly rapid mass gain occurring in spring, generated by orographic precipitation where the steep regional topography causes the moist ocean air – advected westward by the Icelandic Low – to rise, resulting in adiabatic cooling and eventually causing an increase in rain and snowfall at a certain distance inland (Ettema et al., 2009).

In the south-west, basin 6 is close to being in balance. This is the region where the strongest melt day anomalies were reported in 2007, which is reflected in the large mass losses occurring in the corresponding summer. Continuing north, basin 7 is relatively stable until the summer of 2004, after which a slightly negative trend initiated along the coast. A similar but even more pronounced evolution can be seen in the northwest, basin 8, which appeared to be in a stable regime until the summer of 2005. Since then, a negative trend is observed, comparable in magnitude with the changes observed in the southeast. The shift from near-balance toward the strongly negative trend appears to be caused by changes in runoff as well as an increase in ice flow of the many calving glaciers in this region (Rignot et al., 2008b; van den Broeke et al., 2009).
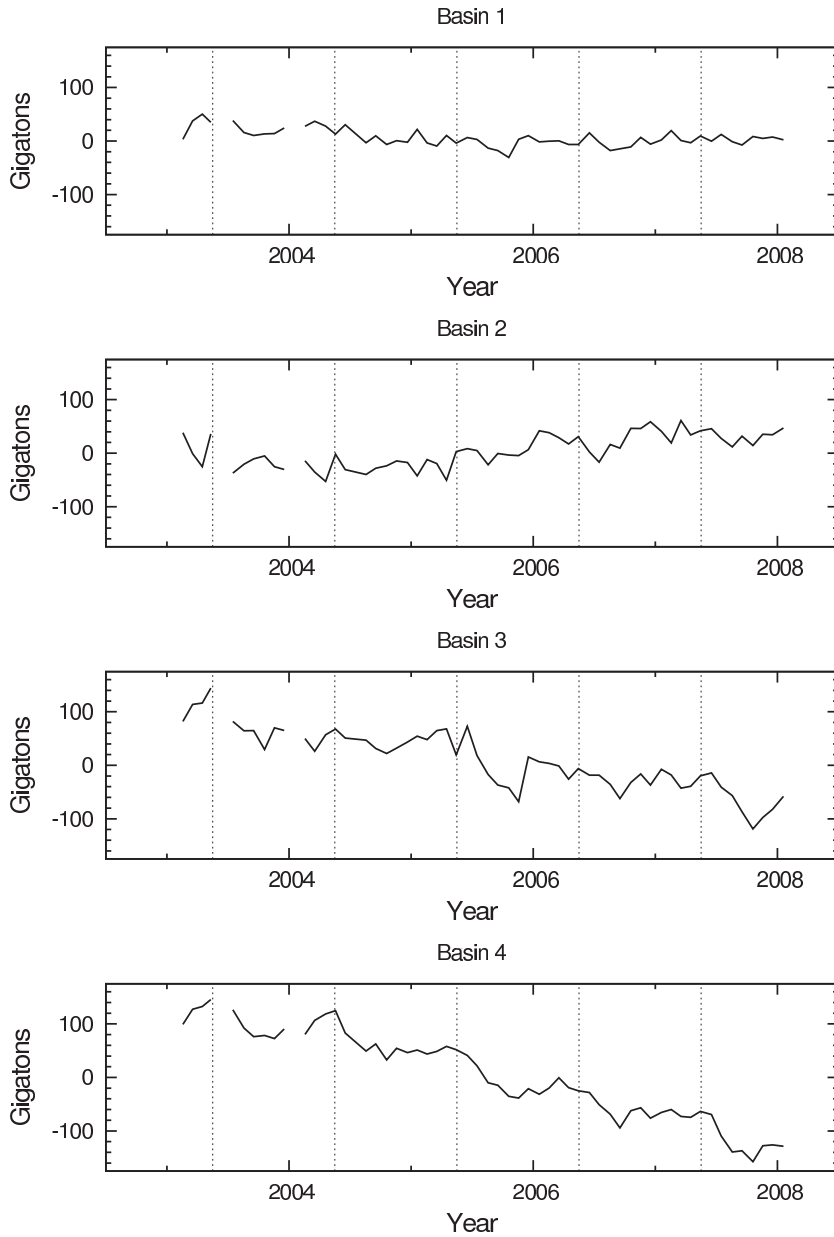
Figure 5.7: *Time series of the monthly mass variations in basins 1–4.*
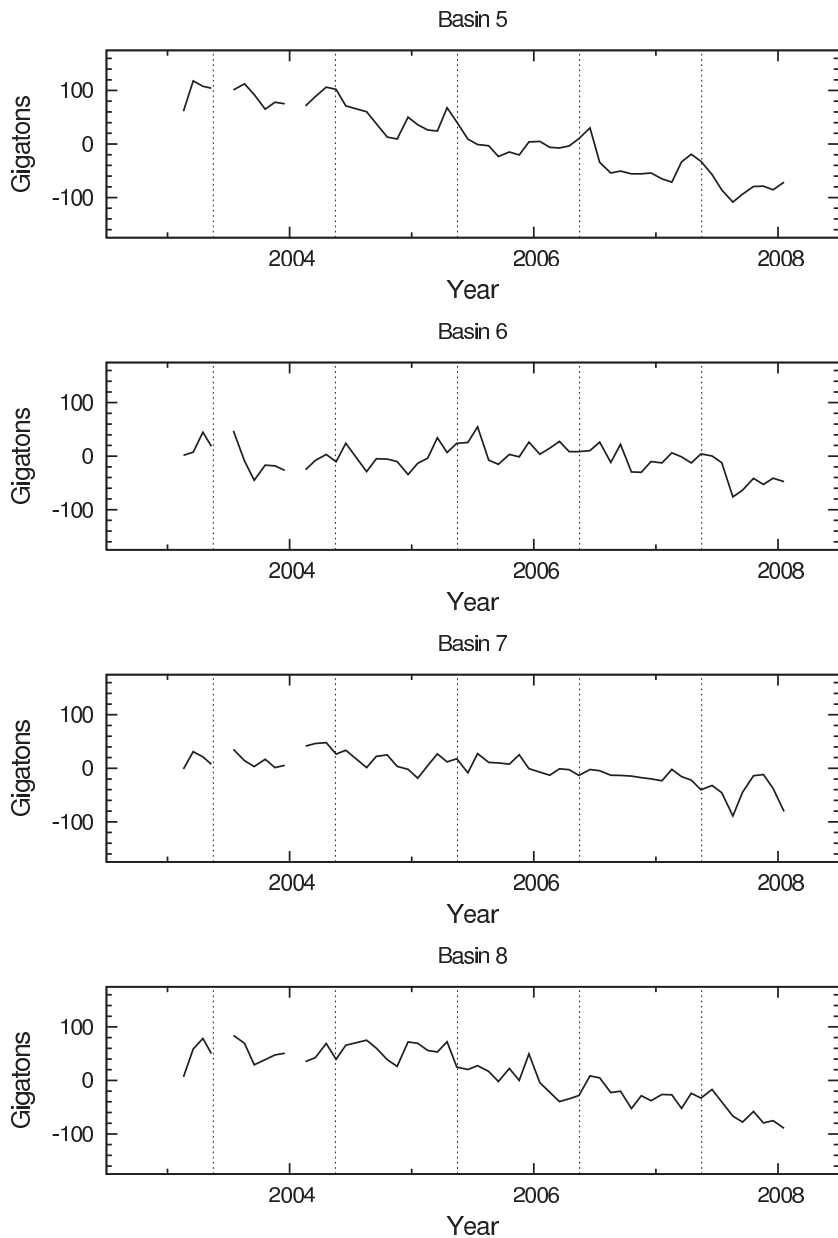
Figure 5.8: *Time series of the monthly mass variations in basins 5–8.*

Year	A-M-J	A-S-O	Winter gain	Summer loss	Net balance
2003	525	260	235[1] (249)	−265 (−324)	−30 (−75)
2004	355	149	95 (153)	−206 (−285)	−111 (−132)
2005	199	−80	50 (144)	−279 (−353)	−229 (−209)
2006	−26	−214	54 (118)	−188 (−232)	−134 (−114)
2007	−146	−484	68 (76)	−338 (−397)	−270 (−304)

Table 5.2: *Overview of the mass changes over the entire Greenland ice sheet. Average values of the total mass with respect to the 2003–2008 mean are given for April-May-June (A-M-J) and August-September-October (A-S-O), together with winter gain, summer loss and net balance. The numbers between brackets denote the peak-to-peak values. Units are Gt.*

5.4.2 Summer mass losses

The mass variations observed over the Greenland ice sheet in fig. 5.3 are the combined effect of a linear trend, due to the quasi-constant mass output through ice discharge by outlet glaciers, superimposed on a yearly repeating pattern of mass accumulation and ablation. Mass builds up slowly between October and April, followed by rapid loss of mass between May and September. The amplitude of the summer ice loss varies between the years, with a maximum in 2007, in which 338 Gt was lost in summer (table 5.2, calculated as the difference between the April-May-June and August-September-October mean mass over Greenland, to account for different timing of the onset and end of the melt season, and random errors in the GRACE observations). Similar values are found for 2003 and 2005, in which 265 Gt and 279 Gt were shed respectively.

The losses occurring during summer are only partially compensated by mass accumulation in the preceding winter seasons. A large mass gain is observed in early 2003, almost completely offsetting the succeeding mass loss. During the 2006–2007 winter season, the Greenland ice sheet gained only 68 Gt, resulting in a net loss of 270 Gt for the entire 2006–2007 balance year. Mass accumulation was comparable in the 2004–2005 winter season, totaling 50 Gt, which gives a net ablation of 229 Gt for the 2004–2005 year.

A strong correlation exists between summer temperature and the amount of summer mass loss. Hanna et al. (2008) observed a significant warning of 1.7°C in summer temperature for 1991–2006. The summers of 2003, 2005 and 2007 were the warmest three since 1961 (Hanna et al., 2008; Mote, 2007). Two independent numerical models of the Greenland ice sheet (Hanna et al., 2009), suggest a record surface melt of the Greenland ice sheet during the summer of 2007, preceded by very low snow accumulation in the winter months (Hanna et al., 2009). The driving mechanism behind the record mass loss may be found in this low accumulation of fresh snow during winter and consequent exposure of (darker)

old snow or ice during the following melt season, which both have a low surface albedo and thus reflect less of the incoming radiation (Tedesco et al., 2008). The GRACE observations do indeed indicate a large mass loss in 2007 and a low mass growth in 2006–2007, although not lower than the 2005 minimum. However, when comparing the two data sets, it should be kept in mind that such numerical models represent surface mass balance only and do not include ice dynamics (M in eq. 5.1).

The summer mass loss is dominated by ablation occurring along the coast (fig. 5.3). Most of the melt takes place in the regions situated below $\sim$70°N, although the exact location varies strongly throughout the years (fig. 5.9). A yearly repeating pattern is the mass loss occurring along the southeastern coast between $\sim$60°N to 70°N, and, in the warmer years of 2003, 2005 and 2007, in the northeast. In the higher elevation zones no clear repeating pattern of summer mass loss is discernable (fig. 5.3c), however, rapid ice loss appears to have occurred between April and August 2007 in the southern regions, with a peak to peak difference of 238 Gt (summed over all regions situated above 2000 m), followed by a period of mass accumulation. A possible mechanism for the mass loss could be a temporary decrease in snowfall at higher regions, with ice streams continuing to transport ice to lower elevations (Helsen, personal communication, 2008).

Although periods of small negative trends have occurred above 2000 m before, the duration and magnitude of the summer 2007 anomaly is unprecedented during the observation period. This validates surface melt studies based on satellite microwave data (Tedesco, 2007), reporting a 2007 surface melt index (the melting area multiplied by the number of melting days) of 153% greater than the average over the last 18 years for regions above 2000 m. Based on a longer data set, Mote (2007) reported melt frequency anomalies of up to 50 days for the regions above 2000 m in 2007, with a melt onset occurring up to 30 days earlier than the 1973–2007 average. Both studies report the most pronounced anomalies in the southern part of Greenland, which coincides with the region where the largest summer mass losses are observed by the GRACE satellites (fig. 5.9).

5.5   Comparison to other studies

As indicated in the introduction of this chapter, several observation techniques exist to observe the mass balance of an ice sheet. Figure 5.10 shows a set of estimates from recent studies of the Greenland ice sheet. Over the past two decades, mass change rates have become increasingly more negative, although differences exist depending on the observation platform used. In the following, the estimates obtained in this chapter will be compared to results from a number of earlier studies. The focus will be on other GRACE based studies, with a discussion of similarities and possible causes for differences, but observations from laser altimetry and InSAR will also be considered. After correcting for ice discharge through outlet glaciers, the GRACE observations may be used to validate the
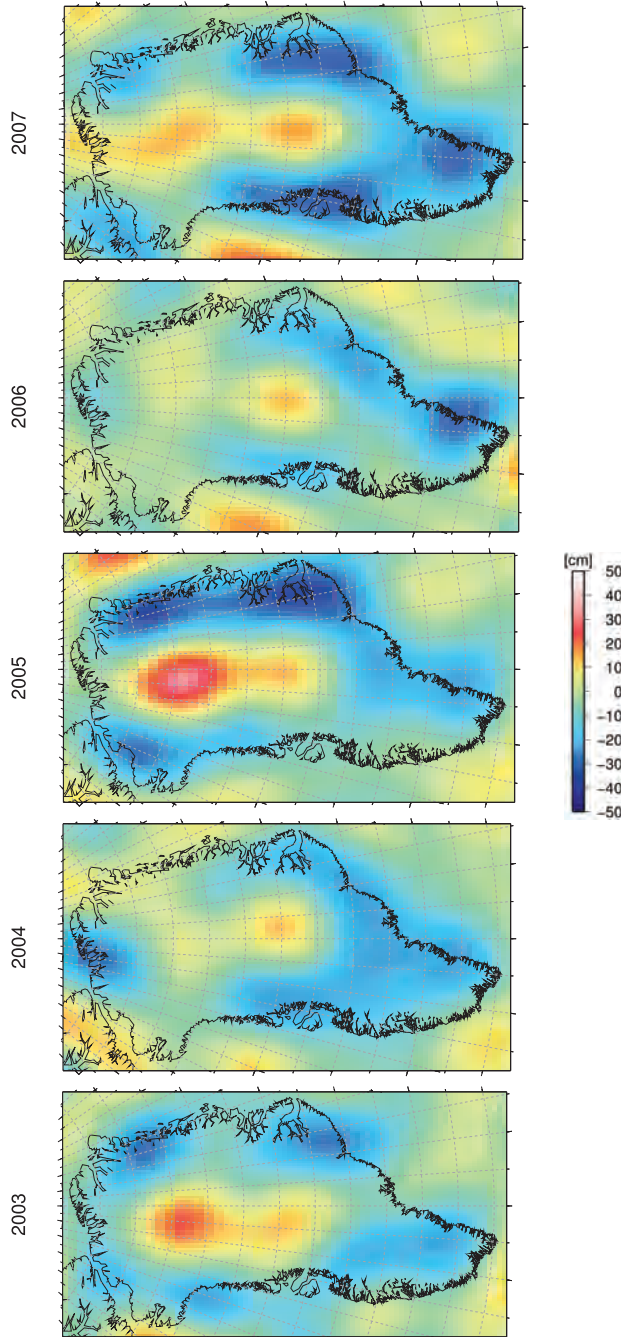
Figure 5.9: *Changes in mass distribution over Greenland during the summer months of 2003–2007, computed as the difference between the April-May-June and August-September-October means.*
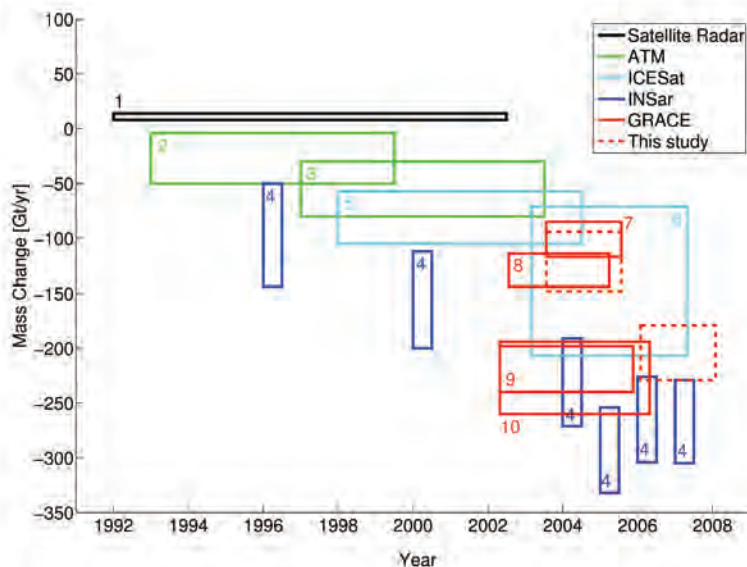
Figure 5.10: *Mass change rates observed by different platforms and in different time periods. The width of a box indicates the period considered, the height the estimated trend and associated error bars, after Thomas et al. (2006). Black: satellite radar altimetry, (1) Zwally et al. (2005); Green: Airborne Topographic Mapper laser altimeter, (2) Krabill et al. (2004), (3) Krabill et al. (2004); Blue: InSAR, (4) Rignot et al. (2008b), Cyan: ICESat, (5) Thomas et al. (2006), (6) Slobbe et al. (2009); red: GRACE, (7) Luthcke et al. (2006), (8) Ramillien et al. (2006), (9) Velicogna and Wahr (2006a), (10) Chen et al. (2006b); Red-dashed: This study.*

output of regional climate models. Furthermore, the relation between the GRACE observations and indirect proxy measures of the mass balance of the Greenland ice sheet, such as surface melt extent will be elaborated on.

5.5.1   Earlier GRACE based studies

The mass change estimates over Greenland obtained in this study are considerably larger than those reported in some earlier GRACE based studies, which reported a trend of −129±15 Gt/yr (July 2002 to March 2005; Ramillien et al., 2006) and −101±16 Gt/yr (July 2003 to July 2005; Luthcke et al., 2006). Over an identical period as the latter, a comparable trend of −121±27 Gt/yr is retrieved, consistent within the range of error. The pattern of mass change matches well, with thinning along the coast and a slight growth in the inland regions observed in both studies. Between January 2006 and January 2008, a trend of −204±25 Gt/yr is found here, which implies that the larger mass loss rate over the entire

period (-179 ± 23 Gt) of this chapter is due to a change in the behavior of the Greenland ice sheet rather than to the different method and data used.

On the other hand, the estimate for 2003–2005 obtained here is notably smaller than the trends obtained in Velicogna and Wahr (2006b) and Chen et al. (2006b), which are in the order of 230 ± 30 Gt/yr between mid-2002 and the end of 2005. Possible causes for these significant differences will be discussed in the following paragraphs.

Velicogna and Wahr (2006b)

The study of Velicogna and Wahr (2006b) differs on three points from the method presented in this chapter. First of all, the trend in Velicogna and Wahr (2006b) is obtained using a smoothed regional averaging kernel over Greenland that minimizes the combined GRACE measurement error and signal leakage, as described in Swenson and Wahr (2002). This averaging kernel is convolved with the maps of equivalent water level, which then yields the trend. Secondly, their estimates were based on earlier data releases (CSR RL01). A third point of difference is the method used to correct for leakage from exterior signals.

a. Regional averaging kernel

The most fundamental difference lies in the method used to extract trends in the mass of the Greenland ice sheet from the GRACE data. Velicogna and Wahr (2006b) make use of a kernel $\vartheta(\theta, \lambda)$, which has – in its exact form – a value of unity over Greenland and zero elsewhere:

$$\vartheta(\theta, \lambda) = \begin{cases} 1 & \text{for Greenland} \\ 0 & \text{elsewhere} \end{cases} \tag{5.3}$$

The change in mass in Greenland $\Delta\bar{\sigma}_{\mathrm{G}}$ can then be obtained by evaluating the integral:

$$\Delta\bar{\sigma}_{\mathrm{G}} = \iint\limits_{\Omega} \Delta\bar{\sigma}(\theta, \lambda)\vartheta(\theta, \lambda)\sin\theta\, d\Omega \tag{5.4}$$

In the spectral domain, this convolution translates to a multiplication of the GRACE coefficients in eq. 1.6 with the spherical harmonics ϑ_{lm}^{C} and ϑ_{lm}^{S} of the kernel:

$$\Delta\bar{\sigma}_{\mathrm{G}} = \frac{a_{\mathrm{e}}\rho_{\mathrm{ave}}}{3} \sum_{l=0}^{l_{\max}} \sum_{m=0}^{l} \frac{2l+1}{1+k'_l} [\Delta\tilde{C}_{lm}\vartheta_{lm}^{C} + \Delta\tilde{S}_{lm}\vartheta_{lm}^{S}] \tag{5.5}$$

Truncating the kernel coefficients at a certain finite degree $l_{\max}$ will distort the shape of the kernel near its boundaries, the so-called Gibbs phenomenon. This can be reduced by using a smoothed kernel, which gradually changes from unity to zero (see Swenson and Wahr, 2002).

Due to the limited resolution of the GRACE observations and the applied smoothing, the kernel will have values smaller than unity over most of Greenland, which would lead to results biased low. To compensate for this, Velicogna and Wahr (2006b) apply an empirical scaling factor, approximately equal to 2. The choice of this scaling factor is based on a (noise-free) synthetic trend map, in which it is assumed that a uniform mass change of 1 cm equivalent water height takes places within a few hundred km of the Greenland coast, with no changes in the interior (i.e., comparable to the map used in Ch. 3). After truncation of the spherical harmonics and convolution with the averaging kernel, about 50% of the original signal, averaged over the ice sheet, remains. As is evident from fig. 5.2, assuming a uniform melt along the coast is an oversimplification, which may result in an incorrect scaling factor and introduce an additional bias.

In order to explain the discrepancy between the results presented here and those of Velicogna and Wahr (2006b), the trend between February 2003 and January 2008 was re-estimated using the averaging kernel of fig. 5.11, comparable to the one used in Velicogna and Wahr (2006b). After correcting for leakage from the surrounding regions, a trend of -87 Gt/yr is obtained. Comparing this with the -171 Gt/yr obtained with the forward modeling technique (excluding the GIA correction), this implies a scaling factor of 1.97, close to the value of ∼2 used in Velicogna and Wahr (2006b).

However, the scaling factor is rather sensitive to the spatial distribution of the mass changes. Concentrating all the mass loss in the coastal basins would result in scaling factor about 2% larger than in the more realistic setting of fig. 5.2. On the other hand, spreading the mass loss uniformly over Greenland decreases the scaling factor by 3%. Although such differences seem minor, it should be kept in mind that the differences are amplified through the multiplication with the relatively large (unscaled) trend. Consequently, a 1% difference in scaling factor will result in increase of total mass loss of 1–2 Gt/yr. Basing the scaling factor on a realistic setting is therefore critical to come to a realistic result. Velicogna and Wahr (2006b) included an scaling factor uncertainty of ± 0.05 in their error bounds, which translates to approximately ± 5 Gt/yr in terms of mass trend.

b. GRACE data

A second major point of difference is the GRACE data Velicogna and Wahr (2006b) based their estimate on. The CSR RL01 solutions used were significantly more contaminated by noise, and consequently displayed stronger north-south striping patterns in the maps of equivalent water height. No attempt was made to remove the correlation between the spherical harmonics of even and odd degree in Velicogna and Wahr (2006b). Based on a comparison of CSR RL01 and RL02 data with sterically corrected altimetry data over the oceans, Chambers (2006a) observed a reduction in the variance of the residuals of 17% at a 500 km Gaussian smoothing, with a further reduction of more than 50% if the destriping filter of Swenson and Wahr (2006) is applied. Hence, it is reasonable to assume that the estimate of Velicogna and Wahr (2006b) is more affected by noise.
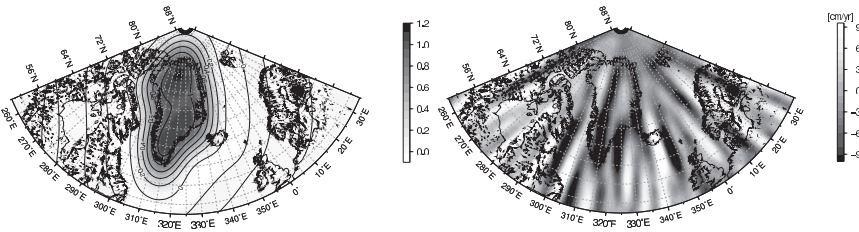
Figure 5.11: *a) The scaled averaging kernel used to estimate mass changes over Green-land following the approach of Velicogna and Wahr (2006b); b) trends in equivalent water level from the CSR RL01 GRACE data between April 2002 and April 2006, illustrating the negative lobe in the center of Greenland. No EOF filtering is applied. The map was smoothed with a Gaussian radius of 250 km to enhance presentation and highlight the mid to long wavelength features.*

Indeed, the trend obtained using unfiltered CSR RL01 data is significantly larger than the trend obtained after applying the EOF filter to the CSR RL01 Stokes coefficients. Following the approach of Velicogna and Wahr (2006b) – i.e. replacing the C_{20} values by SLR estimates, eliminating months of degraded quality, etc. – and using the scaling factor of above, a value of -187 ± 29 Gt/yr is obtained (April 2002–April 2006). After applying the EOF filter to the spherical harmonics, a trend of -143 ± 25 Gt/yr is obtained, a reduction of approximately 45 Gt/yr. The cause of this difference can be identified in fig. 5.11b, which shows the trends in equivalent water height in the period considered, based on the CSR RL01 data. A negative lobe runs from the southern tip of Greenland towards the north, roughly following the 318° meridian. The smoothed averaging kernel (fig. 5.11a) reaches its maximum value in these regions, hence amplifying the effect of the unphysical north-south stripe.

The averaging kernel technique minimizes the combined GRACE measurement error and signal leakage, but assumes that there is no correlation between the errors of the Stokes coefficients of different degree and order, and, that the errors are independent of orientation (Swenson and Wahr, 2002, eq. 9–12). This is clearly not the case for the current GRACE data, and for kernels associated with length scales that are close to the (longitudinal) correlation length of errors in the GRACE data, the random errors will not average out and cause biased mass estimates. Applying the EOF filter largely removes the negative stripe along the central meridian of Greenland, resulting in a less negative trend.

Estimates based on a newer, cleaner data release (RL04) show a better agreement between the regional kernel method (approximately -230 ± 30 Gt/yr for 2003–2008 (Velicogna, personal communication)) and the method of this chapter (-179 ± 25 Gt/yr). This supports the hypothesis that at least part of the difference is caused by the use of the older data.

c. Leakage correction

A third point of difference is the correction for leakage from signals in the regions surrounding Greenland. The regional averaging kernel has a non-zero value outside Greenland. Therefore, the result obtained after convolving the kernel with the GRACE data will partly depend on the mass fluctuations in the surrounding regions and a correction for these signals is required. Using the kernel of fig. 5.11, it is found that a mass change of 1 Gt in Ellesmere Island will alter the result by 0.3–0.5 Gt, depending on the exact location. Given the estimated mass loss of 15.8±9 Gt/yr in this location (table 5.1), leakage may result in a bias of 5 to 8 Gt/yr. Other regions have a smaller effect, with a bias of approximately 0.05 Gt for every 1 Gt of change in Baffin Island, whereas the contribution of Iceland is limited to less than 0.01 Gt.

In this study, these effects are removed by estimating the signals in the neighboring regions from GRACE data directly. If this procedure is omitted, the trend increases by approximately 15 Gt/yr. The majority of this signal is caused by negative mass trends in the Canadian Arctic Archipelago, such as Ellesmere Island and Baffin Island, and in the Artic Ocean. The study of Velicogna and Wahr (2006b) follows a different approach and uses the output of the Global Land Water Storage (GLDAS) model (Rodell et al., 2004), in combination with ocean bottom pressure estimates from the baroclinic OMCT ocean model (Thomas, 2002).

Interannual changes in waters storage are generally not well represented in global hydrology models such as GLDAS, which are forced by highly variable fluxes. Errors in these forcings may result in large biases or random errors in the interannual variation (Shmakin et al., 2003). This is especially true in areas of permanent snow, where the model results are based on a relatively simple snow module that does not take into account snow compaction, heat storage and liquid water storage, et cetera (Rodell and Houser, 2004). Inclusion of satellite based observations (e.g., from MODIS) of snow cover does improve the results slightly, although primarily in areas with ephemeral snow, because no information on the depth of the snow layer is added. Hence the influence on far northern locations that are snow covered for most of the year is limited (Rodell, personal communication, 2008). Moreover, in glaciated areas, mass will accumulate indefinitely due to the lack of ice physics in the GLDAS model. In the Canadian Arctic Archipelago, the GLDAS model and GRACE observations show trends of opposite sign. Overall, the correction for leakage in Velicogna and Wahr (2006b) increases the total trend by ∼15 Gt/yr, about the opposite of the correction suggested by the forward model used in this study.

Chen et al. (2006b)

This study also relied on the CSR RL01 data, hence the result (219±21 Gt/yr) may also have been affected by the aforementioned errors in the GRACE data. Moreover, the estimate may also have been biased by the fact that only regions showing large ice mass losses were modeled, which ignored that some areas are

gaining mass or are in balance. Furthermore, leakage was removed by estimation of exterior signals in a limited number of areas only, which may introduce an additional bias.

5.5.2 Laser altimetry

Changes in surface elevation of the Greenland ice sheet were estimated recently by Slobbe et al. (2009), based on laser altimetry observations made by the ICESat satellite between February 2003 and April 2007. Overlapping laser footprints were combined and a trend estimated, after applying a correction for slope induced errors using a digital elevation model. Elevation variations were monitored on a regional scale in 6 different basins, as well as below and above the 2000 m elevation line, and converted into mass changes assuming a density of 600 ± 300 kg/m^3 above 2000 m and 900 ± 300 kg/m^3 below 2000 m.

Generally, a good agreement exists between the ICESat results and those presented in this chapter, see table 5.5.2. Slobbe et al. (2009) find a total mass change of -139 ± 68 Gt/yr, mainly occurring below 2000 m (-151 ± 52 Gt/yr) with a small mass gain above 2000 m (12 ± 16 Gt/yr). Over a similar period (Feb. 2003–Apr. 2007), GRACE observes a slightly larger mass loss of 169 ± 24 Gt/yr, which agrees within the error bounds. Trends below 2000 m are slightly larger (180 ± 22 Gt/yr), whereas values at higher elevations are comparable (11 ± 19 Gt/yr). Positive trends are observed in both data sets in basin 2.

Differences are largest in the southeast (basins 3/4), where GRACE observes significantly larger losses. This region is drained by a large number of smaller outlet glaciers, which may be missing in the ICESat measurements due to the relatively large groundtrack spacing at this latitude (Howat et al., 2008b). Further differences may be caused by the fact that ICESat performs measurement during three campaigns each year only, an oversimplified snow/ice density distribution and compaction of the firn layer due to variations in accumulation and temperature (Helsen et al., 2008).

5.5.3 InSAR observations

In Rignot et al. (2008b), changes in ice discharge rates were combined with surface mass balance estimates from regional climate models to obtain variations in the total mass bass balance of the Greenland ice sheet. Ice discharge was estimated using ice thickness from airborne radio echo soundings at fluxes gates, combined with ice surface velocity from InSAR and in-situ observations at these locations. Calculations were first made for 1996 (or 2000, when no earlier data is available) and then scaled by the relative velocity increase for following years, assuming a constant ice thickness (except for the rapidly thinning glaciers in east and west Greenland). In total, 38 basins were monitored, representing approximately 92% of the ice sheet area. Surface mass balance deviations from a long-term average (1961–1990) from two regional climate models (Hanna et al., 2008; Box et al.,

Basin	1	2	$3/4^1$	$4/5^1$	$6/7^1$	8	Total
ICESat (Slobbe et al., 2009)							
> 2000 m	3±2	7±3	0± 0	−10± 5	10±5	2±1	12±16
< 2000 m	−3±2	3±1	−30±10	−57±19	−39±13	−25±8	−151±52
Total	0±3	10±4	−30±10	−67±24	−29±18	−23±9	−139±68
GRACE (This study)							
> 2000 m	0±5	19±6	−12±6	2±7	15±6	−13±7	11±19
< 2000 m	−15±5	−6±5	−50±6	−74±5	−21±4	−14±5	−180±23
Total	−15±6	13±7	−62±8	−72±7	−6±6	−27±8	−169±24

Table 5.3: *Mass changes of the Greenland ice sheet from ICESat observations (Slobbe et al., 2009) and GRACE observations (this study), between February 2003 and April 2007*

[1] Some of the basins were combined to match the geometry of Slobbe et al. (2009).

2006) were added to obtain the total mass balance. For the period corresponding to the GRACE observations, a yearly negative mass balance in the order of −250±40 Gt/yr was found, with a maximum of −293±39 Gt/yr in 2005 and a minimum of −231±40 Gt/yr in 2004.

Comparing this to the values of table 5.2, shows a relatively good agreement for 2005 and 2007, but significant differences are found for 2004 and 2006. Overall, the GRACE observations tend to be lower and show more variability than values obtained with the budget method. A possible explanation for the differences could be a misrepresentation and/or underestimation of annual SMB and its variability in the models. Comparing the SMB of the models used in Rignot et al. (2008b) to the high-resolution RACMO2.1/GR model learns that the interannual variability is about 70 Gt higher in the latter for 2004–2007. Differences for individual years range from approximately 60 to 200 Gt for the model of Hanna et al. (2008) in 2006 and 2004 respectively, and 25 to 100 Gt for the model of Box et al. (2006) (Ettema, personal communication, 2009). The outcome of the mass budget method therefore depends strongly on the SMB model used, as is also demonstrated in van den Broeke et al. (2009).

Qualitatively, the pattern of the mass losses matches well, with largest trends observed in the southeast, with both data sets showing an acceleration starting in 2004–2005. Widespread losses are also found in the northwest (basins 7–8), although the GRACE trends become increasingly more negative over time whereas the budget method shows a relatively constant trend (except for the Jakobshavn Isbræ basin). However, it should be noted that no ice flux observations were available in about 45% of this area. The two methods differ most in the northeast (basin 2), where GRACE shows a positive signal, but the budget method shows a small negative trend. Again, large parts of this area remained unsurveyed in Rignot et al. (2008b).

5.5.4   Regional climate models

Climate models provide estimates of variations of the surface mass balance (SMB) and its individual components (eq. 5.1), such as snowfall, melt, melt water retention and refreezing, etc. Because of the complexity of the processes involved and the highly variable topography of Greenland along the coast, high-resolution models are required to come toward realistic patterns of SMB. Due to computational limitations, current global atmospheric climate models have a too coarse spatial resolution to properly simulate the small-scale processes associated with the irregular topography of Greenland, necessitating the use of regional models, forced at the boundaries by a global model or reanalysis/operational analysis data (Ettema et al., 2009). In the following, SMB data of two regional climate models will be compared with the GRACE data and a first step toward validation of the model output using the observations, on an island-wide scale, is made.

MAR model

The MAR model (Modèle Atmospherique Régional; kindly provided by Xavier Fettweis) couples a regional climate model with 25×25 km horizontal resolution to a land surface scheme to compute transfer of energy and water vapor, among others. At the boundaries, the atmosphere module is forced by ECMWF (re-)analysis data. The model is described in detail in Fettweis (2007). The model output consists of the individual components of eq. 5.2, which, when summed, give the evolution in time of the surface mass balance of the Greenland ice sheet. It should be kept in mind that the model, as most present-day numerical models of the Greenland ice sheet, reproduces SMB and does not incorporate any ice dynamics. Consequently, the model represents only part of the total mass balance of the ice sheet, as output through glacier discharge (M_i in eq. 5.1) is not included. To allow a first order comparison with the GRACE data, which observes both changes in the surface mass balance and glacier output, the yearly ice discharge estimates of Rignot et al. (2008b) have been subtracted from the cumulated surface mass balance time series, as shown in fig. 5.12.

The timing of the minima and maxima in the two time series shows excellent agreement, with a correlation coefficient of 0.98 which can be partly explained by large trends in both data sets. The corrected model data shows a trend of approximately −360 Gt/yr, about 100% larger than the trend observed by GRACE. This divergence between the two data sets is mainly caused by the amplitude of the summer melt signal in the MAR model, which is slightly higher than the observed values. The correlation for the detrended series is 0.80, with an RMS of the differences of 79.7 Gt. It should be kept in mind that part of the signal in the GRACE data is caused by intra-annual variations in output through glacier streams. Increases of about 10% in glacier velocity have been observed at certain locations during summer (e.g., Howat et al., 2008a). Since no detailed estimates of seasonal ice discharge variability are available no attempt has been made to
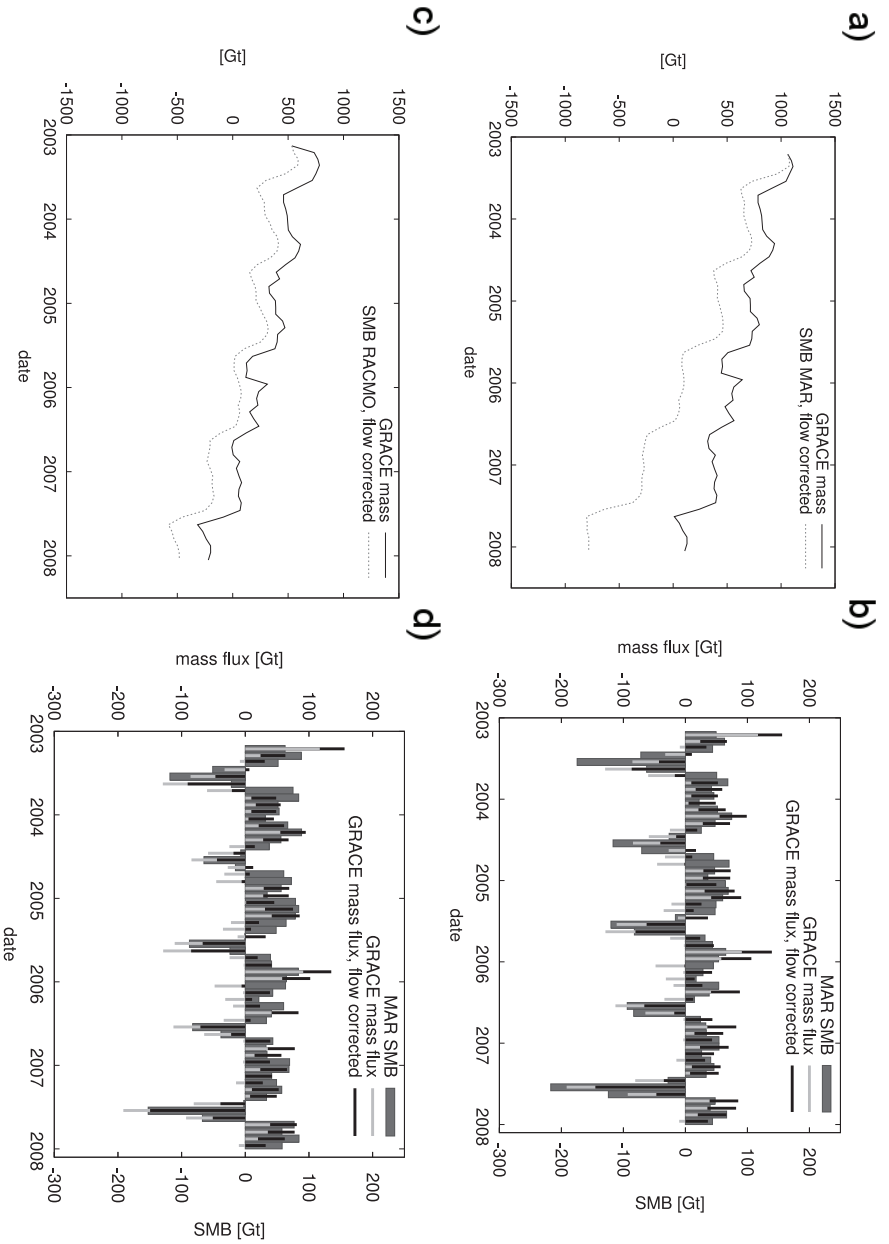
Figure 5.12: *a+c) Time series of cumulated surface mass balance from the MAR and RACMO model respectively, corrected for ice discharge, and detrended GRACE observations. Correlation (inset) between the two time series is 0.98 and 0.97, resp.; b+d) monthly fluxes in the GRACE observations, with (black) and without (gray) correction for ice discharge, and in the MAR and RACMO surface mass balance, respectively.*

.

include a correction for this effect. Furthermore, differences may be caused by hydrological signals in the tundra regions in the coastal zones, which are not included in the MAR output in fig. 5.12.

The regional climate models simulate changes in the input and output fluxes of the ice sheet. Errors in theses variables may therefore accumulate into larger error. Comparing the changes between months might reveal what causes the difference between the MAR results and GRACE observations, see fig. 5.12b. At first sight, the MAR results appear to be biased positive during the winter months, i.e., the amount of snowfall is larger than expected based on the GRACE observations. Again, it should be pointed out that the GRACE changes include output through ice dynamics, which is not included in the MAR model. Correcting the GRACE fluxes using the yearly discharge estimates from InSAR observations of Rignot et al. (2008b), results in a better agreement between model and observations in winter (September–May) months, but simultaneously increases the difference in the summer months (June–August). Correlation between observations and modeled mass changes in summer months is 0.74 with a mean difference of 49 Gt (RMS=43 Gt), i.e. the model produces larger mass losses than observed in these months. During winter, the modeled snowfall is underestimated on average by 5 Gt (RMS=33 Gt), with a weak correlation of 0.23 existing between the two time series. Therefore, the divergence between the GRACE mass estimates and the cumulated surface mass balance in fig. 5.12b can be mainly attributed to a difference in the mass changes occurring during summer.

RACMO2.1/GRN

The Regional Atmospheric Climate Model 2, version Greenland (RACMO2/GR; kindly provided by Janneke Ettema and Michiel van den Broeke) is an adaptation of the regional climate model RACMO2.1, described in Van Meijgaard et al. (2008), tailored for use over Greenland through a coupling to a physical snow model, see Ettema et al. (2009) for a detailed description of the model physics. What distinguishes the RACMO2.1/GRN model from previous models is its high resolution in the horizontal plane, with a spacing of approximately 11 km between gridpoints. This allows for a representation of small-scale atmospheric patterns, such as local snowfall maxima along the northwestern coast. As a result, SMB in the RACMO model is about 60% larger than in the MAR model, mainly due to a larger amount of precipitation deposited on the ice sheet ($\sim$24%) and a lower estimated melt (~ -40%), which is partially offset by lower refreezing and retention of melt water. Averaged over the period 1958–2007, runoff is 60 Gt/yr lower compared to the MAR model (Ettema et al., 2009).

The same procedure as explained above is applied to the RACMO data. A similar correlation of 97% is found after correcting the RACMO SMB values for ice discharge M_i, which lowers to 78% after detrending both data sets. Trends in the two time series agree relatively well, with the corrected RACMO data showing a negative balance of -209 Gt/yr, about 17% larger than the GRACE

based value.

Compared to the MAR model, residuals between the detrended data series are 19% lower, with an RMS of 66 Gt. As is evident from fig. 5.12d, this improvement is mainly due to a better agreement during the summer months. On average, GRACE fluxes and RACMO SMB disagree by 5.2 Gt, with an RMS of 36 Gt. During winter months, precipitation in the model is overestimated with respect to the GRACE observations, with a difference of 5.8 Gt and an RMS of 34 Gt. Correlations are comparable to those obtained with the MAR model, with values of 0.74 and 0.25 for summer and winter respectively.

5.5.5 Surface melt observations

An indirect measure for the changes in the mass balance of an ice sheet is the total area undergoing melt at the surface. Such melt events are directly linked to runoff (after accounting for refreezing and retention of the meltwater), which contributes negatively to the total mass balance of the ice sheet. Hence, a correlation between observations of surface melt and the mass losses in the GRACE data may be expected. Observations of surface melt are based on differences in emissivity between dry and wet snow, which increase as the amount of liquid water increases. This will cause a large change in the brightness temperature (T_B) at certain frequencies, which can be measured from space using passive microwave radiometers. Mote (2007) combined data from three such radiometers over Greenland, to track brightness temperature variations at the 18.0 and 19.35 GHz frequencies at a 25×25 km resolution between 1972 and 2007. These data were compared with the output from a microwave emission model which produces brightness temperatures associated with snowpack melt conditions for each grid cell and for each year. If the observed T_B exceeds the modeled threshold at a certain time and location, the corresponding grid is marked as melting (Mote, 2007).

Figure 5.13a shows yearly values of the mean melt area, computed as the total sum of the daily melt area divided by the number of observation days in a year (kindly provided by Thomas Mote). Since the satellite microwave observations have provided full coverage over the entire ice sheet for most (99.9%) of the GRACE period, the effect of missing observations is negligible. A record melt is observed in 2007, followed by 2005 and 2003 (Mote, 2007). This corresponds to the years of largest summer mass losses observed by GRACE (table 5.2), in a corresponding order. Minimal melt was observed in 2006 and 2004, the summers with the respective lowest and second lowest mass losses. Yearly average melt extent and the summer mass losses of table 5.2 correlate at the 95% level.

The correlation holds when comparing the monthly mean melt area to the mass fluxes from GRACE, as shown in fig. 5.13b. July 2007 stands out as the month with the largest areal melt extent and the largest amount of mass lost. Likewise, months with a large mean melt area generally show large mass losses, although the correspondence is not absolute. Notable exceptions are the mass losses observed

a)

b)
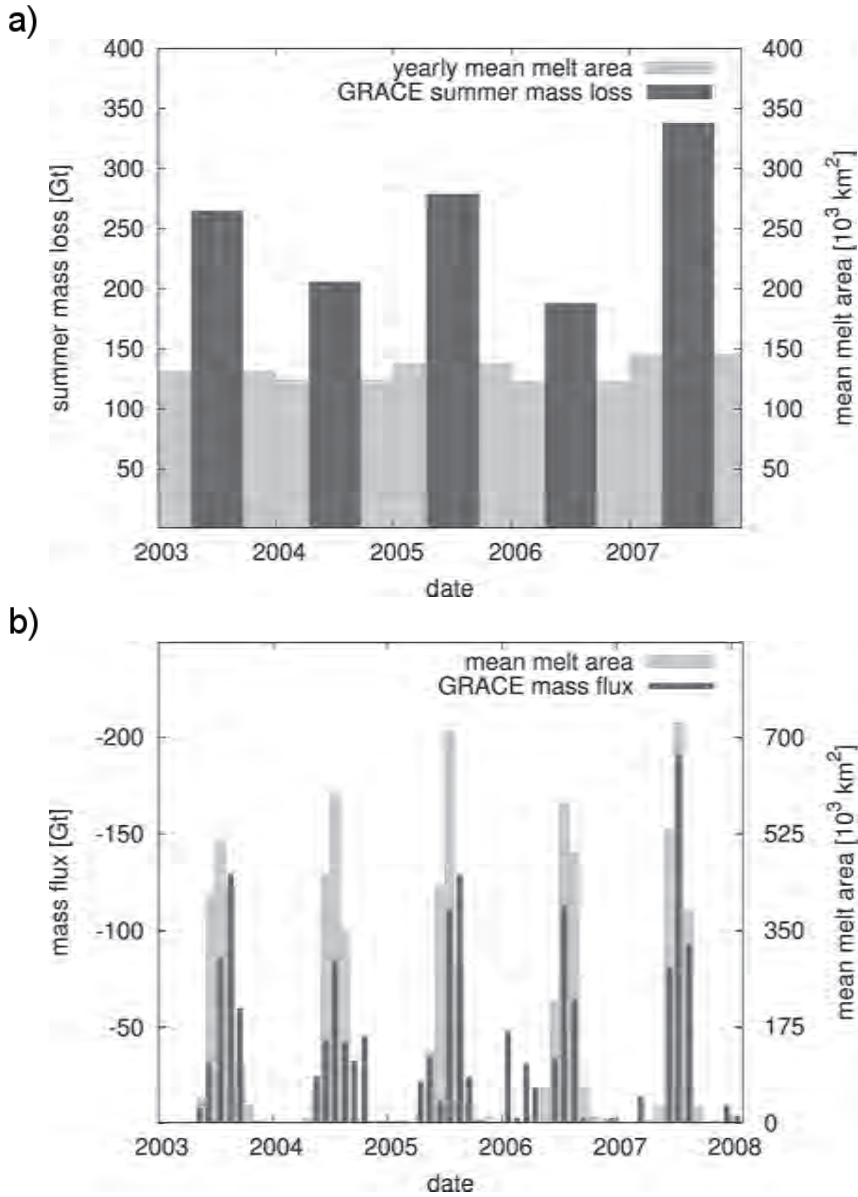
Figure 5.13: *a) Mean yearly melt area from passive microwave observations and summer mass losses as observed by GRACE, b) monthly mean melt area and mass fluxes from GRACE.*

by GRACE in spring 2006, which may be due to temporal accelerations of ice streams or due to a negative precipitation anomaly. Overall, when comparing the monthly amount of mass lost with the areal extent of surface melt, a correlation of 82% is found.

5.5.6   Indirect observations

Other, indirect observations may help to constrain the changes in the behavior of the Greenland ice sheet, either quantitatively or qualitatively. Two of them will be briefly discussed in the following paragraphs.

A change in the mass redistribution on the Greenland ice sheet, will cause a change in the Earth's inertia tensor and hence alter the magnitude and direction of the Earth's rotation vector. Although other processes, such as glacial isostatic adjustment, play an important role, the Greenland mass losses estimated in this chapter could explain about 40% of the observed polar wander signature (3.3 milliarcseconds per year, James and Ivins, 1997), with a good agreement in direction as well (224° vs. 282° observed) (Ivins, personal communication, 2008).

Finally, it is noteworthy that the locations of largest mass decrease, the coastal zones of basins 3–5 and 7, agree with the locations of seismic events associated with sudden discharges of ice by outlet glaciers, which have been reported to be increasing in these areas (e.g., Ekström et al., 2006).

5.6   Conclusions

As in Ramillien et al. (2006), Velicogna and Wahr (2006b) and Chen et al. (2006b), the approach in this chapter is based on the global spherical harmonic Stokes coefficients provided by the GRACE science teams, but allows one to allocate the mass loss signal to specific basins. Moreover, it is straightforward to include other regions of interest or can be applied to other regions, such as Antarctica. As a side result of our study of the Greenland ice sheet, melting signals are also observed over Svalbard, Iceland and the glaciers on Ellesmere Island, corresponding to mass changes of -8.8 ± 2, -11.4 ± 2 and -15.8 ± 9 Gt/yr, respectively.

Between July 2003 and July 2005, Greenland lost mass at a rate of -121 ± 25 Gt/yr, consistent with Ramillien et al. (2006) and Luthcke et al. (2006), who based their study on a different parameterization of the GRACE data, giving confidence in the robustness of the approach presented in this chapter. Over the entire data span between February 2003 and January 2008, a mass loss rate of -179 ± 25 Gt/yr is observed, equivalent to a global sea level rise of 0.5 mm/yr. The difference between the trend observed in the first and last period of observations, indicates a speed up of the mass losses during the last few years.

The trends observed in this study are significantly smaller than those reported in Velicogna and Wahr (2006b) and Chen et al. (2006b). Differences can be ex-

plained by the use of a different GRACE data releases, correction for external signals and the method used to extract mass changes. When using a regional kernel, the use of scaling factor is required. Basing the scaling factor on a realistic setting is therefore critical to come to a realistic result. The outcome of this method is also dependent on the correlated noise in the GRACE solutions. Estimates based on a newer, cleaner data release (RL04) show a better agreement between the regional kernel method (approximately -230 ± 30 Gt/yr for 2003–2008 (Velicogna, personal communication)) and the method of this chapter (-179 ± 25 Gt/yr). Nevertheless, a significant difference remains, which deserves further study.

Large interannual variations in the mass balance of Greenland are observed and an observation period of at least 3 years or longer is desirable to reduce the year-to-year variability. Most of the mass loss is occurring in the southeast and northwest during summer, with maxima in 2003, 2005 and an absolute maximum in 2007, when approximately 338 Gt of ice was lost, enough to rise global mean sea level by 0.9 mm. Part of this 2007 maximum is associated with melt at higher elevations. Given the relatively short observation period, it is too early to conclude whether this is part of a change in the behavior of the Greenland ice sheet or merely due to natural variability, underlining the need for extended time series and continued observations of the Earth's gravity signal as provided by GRACE.

A strong coupling exists between the observed areal extent of surface melt and the amount of mass lost during summer. Also, a relatively good agreement is found between the latter and the surface runoff during summer as predicted by regional climate models. This highlights the potential of the GRACE observations to validate and improve the numerical models. The synergy between GRACE data, the upcoming Cryosat-2 altimeter mission, and regional climate models, uncovering the physical processes behind the observed changes, promises a leap forward in our understanding of the ice sheets. With GRACE observing the total change in mass and surface mass balance provided by climate models, a better understanding of changes in ice dynamics may be obtained as well. The latter are currently poorly understood and undersampled, but are of paramount importance to come to a full understanding of the behavior and evolution of the Greenland ice sheet,

Chapter 6

On Seasonal Variations in Sea Level due to Gravitational Forcing

6.1   Introduction

A popular unit of measure to express changes in the Earth's water cycle, such as the annual ice loss of Greenland's ice sheet described in Ch. 5, is the effect on the global mean sea level, with 360 cubic kilometers of water equaling approximately one millimeter of global sea level rise. Generally, it is assumed that the water added to the ocean is distributed eustatically over the globe, i.e. as a uniform layer over the ocean. This intuitive approach would be correct if the water were to be added from an extra-terrestrial source on a non-rotating, ocean covered, rigid Earth fully covered with water, but fails to predict the resulting mean sea level in a more realistic setting. In the case where water is exchanged between land and ocean, the interaction between changes in the gravity field, deformation of the solid Earth and disturbances in the Earth's rotation vector will yield a distribution that is more complicated than a uniform rise or fall of the ocean's surface.

The theory behind this phenomenon was first described more than 120 years ago, by Woodward (1888). The topic received renewed attention in the mid 1970's, when Farrell and Clark (1976) developed their now classical sea-level equation. Their work still serves as a basis for many studies in the field of postglacial rebound, where the sea-level equation is applied to match observed curves of relative sea level change with models of the viscosity profile of the Earth and deglaciation history of the ice caps during the last few glacial cycles. Other

studies attempted to match the distinct spatial patterns in sea level associated with the mass changes in the major ice sheets or mountain glaciers (the so-called fingerprints) to tide-gauge records to constrain the present-day mass loss rates. Several refinements have been incorporated in the original sea-level equation since the work of Woodward (1888) and Farrell and Clark (1976), such as the effects of perturbations in the rotation vector of the Earth and changes in the ocean-continent geometry (e.g., Milne and Mitrovica, 1998). Furthermore, the sea-level equation was rederived by Fang and Hager (1999) using an independent approach based on the principle of least potential energy, yielding essentially the same results.

Most studies so far have focused on the effects of long term trends in the mass distribution of the Earth's system, with time scales in the order of hundred to thousands of years. However, similar effects can be expected on shorter time scales as well, e.g., due to seasonal snow accumulation in the cryosphere or changes in the water table of the larger river basins. In this chapter, space borne observations of changes in the Earth's gravity field, made by the GRACE satellites, will be used. This allows the retrieval of changes in mass distribution on the continents, which then can be used as an input into the sea level equation to model the variations in relative sea level. The main focus of this chapter will be on the seasonal cycle in relative sea level and the resulting spatial departures from a uniform, eustatic cycle, as described by, e.g., Chambers et al. (2004). Furthermore, present-day trends in relative sea level based on the GRACE observations will also be touched upon.

6.1.1   The sea-level equation

The effect of perturbations in the Earth's surface load on the sea level has been extensively discussed in literature focusing on glacial isostatic adjustment (GIA), (e.g., Milne and Mitrovica, 1998). Timescales involved with GIA are typically of the order of 1–10 kyr, which requires the incorporation of the viscous redistribution of material in the Earth's interior. The associated equations involve convolutions both in space and time, making the computation of the sea level response a numerical challenging task. However, over shorter time spans, in the order of 1–10 years, it suffices to model response of the Earth using elastic properties only, which leads to a great simplification of the sea level equation. In the following, a brief overview of the relevant equations for these shorter timescale will be given, building on the work of Farrell and Clark (1976) and Milne and Mitrovica (1998).

Assume an ice mass (or any other kind of water mass anomaly) located on land disappears, the meltwater flowing to the oceans. Following Farrell and Clark (1976), the gravitational perturbation at a point $p(\theta, \lambda)$ on the Earth's surface due to a redistribution in surface load $M(\theta', \lambda')$ may be expressed as:

$$\phi(\theta,\lambda) = \iint\limits_{\Omega'} \frac{a_e^3 g}{M_E} \frac{M(\theta',\lambda')}{2\sin\phi/2} \ d\Omega' \tag{6.1}$$

, with M_E and a_e the mass and radius of the Earth respectively, g the gravitational acceleration and ϕ the angular distance between (θ,λ) and (θ',λ'). The related change in geoid height is given by:

$$N(\theta,\lambda) = (\phi(\theta,\lambda) + \text{cst})/g \tag{6.2}$$

where the constant is used to ensure conservation of mass, as will be explained further on. For convenience, the constant will be ignored temporarily in the derivation. The sinusoid in eq. 6.1 may be expressed as an infinite series of Legendre polynomials, yielding:

$$N(\theta,\lambda) = \iint\limits_{\Omega'} \frac{a_e^3}{M_E} M(\theta',\lambda') \sum_{l=0}^{\infty} P_l(\cos\alpha) \ d\Omega' \tag{6.3}$$

The surface mass change function $M(\theta',\lambda')$ can be expanded to spherical harmonics, using the addition theorem for surface harmonics:

$$\iint\limits_{\Omega'} M(\theta',\lambda') P_l(\cos\alpha) \ d\Omega' = \frac{4\pi a_e}{2l+1} \sum_{m=0}^{l} (C_{lm}^M \cos m\lambda$$
$$+ S_{lm}^M \sin m\lambda) P_{lm}(\cos\theta) \tag{6.4}$$

leading to:

$$N(\theta,\lambda) = \sum_{l=0}^{\infty} \sum_{m=0}^{l} \frac{3a_e}{\rho_e(2l+1)} (C_{lm}^M \cos m\lambda$$
$$+ S_{lm}^M \sin m\lambda) P_{lm}(\cos\theta)$$
$$= \sum_{l=0}^{\infty} N_l(\theta,\lambda) \tag{6.5}$$

, with ρ_e the average density of the Earth.

An additional disturbance in the geoid will be caused by elastic deformation within the earth, which can be accounted for using the elastic load Love numbers k_l':

$$N'(\theta,\lambda) = \sum_{l=0}^{\infty} (1 + k_l') N_l(\theta,\lambda) \tag{6.6}$$

Likewise, the redistribution of mass will cause a radial displacement $R(\theta, \lambda)$ of the solid Earth surface, which can be found using the elastic load Love number for radial displacement h'_l:

$$R(\theta, \lambda) = \sum_{l=0}^{\infty} h'_l N_l(\theta, \lambda) \tag{6.7}$$

In the remainder of this chapter, the combined effect of the geoid and radial displacements over the ocean will be referred to as *selfgravitational* effects. Defining the relative sea level $S(\theta, \lambda)$ as the vertical distance between the geoid and the solid Earth over the oceans leads to:

$$S(\theta, \lambda) = O(\theta, \lambda) \sum_{l=0}^{\infty} (1 + k'_l - h'_l) N_l(\theta, \lambda) \tag{6.8}$$

with $O(\theta, \lambda)$ the ocean function, having a zero value over land and being unity over the ocean. Likewise, the land function $L(\theta, \lambda)$ is defined, having a zero value over the ocean and being unity over land:

$$O(\theta, \lambda) = \left\{ \begin{array}{ll} 0 & \text{for land} \\ 1 & \text{for ocean} \end{array} \right. , \text{ and, } \quad L(\theta, \lambda) = \left\{ \begin{array}{ll} 1 & \text{for land} \\ 0 & \text{for ocean} \end{array} \right. \tag{6.9}$$

, which is, in the spectral domain, equivalent to:

$$\begin{aligned} O(\theta, \lambda) &= \sum_{l=0}^{\infty} \sum_{m=0}^{l} (C_{lm}^{\mathrm{O}} \cos m\lambda + S_{lm}^{\mathrm{O}} \sin m\lambda) P_{lm}(\cos \theta) \\ &= \sum_{l=0}^{\infty} O_l(\theta, \lambda) \end{aligned} \tag{6.10}$$

$$\begin{aligned} L(\theta, \lambda) &= \sum_{l=0}^{\infty} \sum_{m=0}^{l} (C_{lm}^{\mathrm{L}} \cos m\lambda + S_{lm}^{\mathrm{L}} \sin m\lambda) P_{lm}(\cos \theta) \\ &= \sum_{n=0}^{\infty} L_n(\theta, \lambda) \end{aligned} \tag{6.11}$$

The effect on the geoid will consist of two parts, i.e. one part caused directly by the change in the mass distribution on land, and another caused by the change in the mass distribution in the ocean (which can be found by replacing $M(\theta, \lambda)$ by $\rho_{\mathrm{w}} S(\theta, \lambda)$, i.e. the relative sea level height S times the density of water ρ_{w}, in eq. 6.4):

$$
\begin{aligned}
N'(\theta, \lambda) &= \sum_{l=0}^{\infty} \sum_{m=0}^{l} \frac{3a_{\mathrm{e}}(1+k_l')}{\rho_{\mathrm{e}}(2l+1)} \{(C_{lm}^{\mathrm{M}} + \rho_{\mathrm{w}} C_{lm}^{\mathrm{S}}) \cos m\lambda \\
&\quad + (S_{lm}^{\mathrm{M}} + \rho_w S_{lm}^{\mathrm{S}}) \sin m\lambda\} P_{lm}(\cos \theta) \\
&= \sum_{l=0}^{\infty} N_l'(\theta, \lambda)
\end{aligned}
\tag{6.12}
$$

where $(C_{lm}^{\mathrm{M}}, S_{lm}^{\mathrm{M}})$ and $(C_{lm}^{\mathrm{S}}, S_{lm}^{\mathrm{S}})$ are the spherical harmonics coefficients of $M(\theta, \lambda)$ and $S(\theta, \lambda)$, respectively. The latter is defined by:

$$
\begin{aligned}
S(\theta, \lambda) &= \sum_{l=0}^{\infty} O_l(\theta, \lambda) \sum_{l=0}^{\infty} \sum_{m=0}^{l} \frac{3a_{\mathrm{e}}(1+k_l'-h_l')}{\rho_{\mathrm{e}}(2l+1)} \\
&\quad \times \{(C_{lm}^{\mathrm{M}} + \rho_{\mathrm{w}} C_{lm}^{\mathrm{S}}) \cos m\lambda + (S_{lm}^{\mathrm{M}} + \rho_{\mathrm{w}} S_{lm}^{\mathrm{S}}) \sin m\lambda\} \\
&\quad \times P_{lm}(\cos \theta) \\
&= \sum_{l=0}^{\infty} S_l(\theta, \lambda)
\end{aligned}
\tag{6.13}
$$

Now the constant in eq. 6.2 can be determined by imposing mass conservation:

$$
\begin{aligned}
A_{\mathrm{o}} \frac{\mathrm{Cst}}{g} + \iint_{\Omega} S(\theta, \lambda)\, d\Omega + \frac{1}{\rho_{\mathrm{w}}} \iint_{\Omega} M(\theta, \lambda)\, d\Omega &= 0 \\
\frac{\mathrm{Cst}}{g} &= -\frac{1}{A_{\mathrm{o}}} \left(\iint_{\Omega} S(\theta, \lambda)\, d\Omega + \frac{1}{\rho_{\mathrm{w}}} \iint_{\Omega} M(\theta, \lambda)\, d\Omega \right)
\end{aligned}
\tag{6.14}
$$

and

$$
A_{\mathrm{o}} = \iint_{\Omega} O(\theta, \lambda)\, d\Omega
\tag{6.15}
$$

In the spectral domain, eq. 6.14 equals:

$$
\frac{\mathrm{Cst}}{g} = -\frac{1}{C_{00}^{\mathrm{O}}} \left(C_{00}^{\mathrm{S}} + \frac{1}{\rho_{\mathrm{w}}} C_{00}^{\mathrm{M}} \right)
\tag{6.16}
$$

The relative sea level change $S(\theta, \lambda)$ appears on both sides of eq. 6.13. A computational efficient way to solve such an integral equation is by means of an iterative approach (e.g., Farrell and Clark, 1976). In a first step, it is assumed that all water added to the ocean is distributed as a uniform layer, i.e. an eustatic sea level change. From this load, the geoid and relative sea level change can be
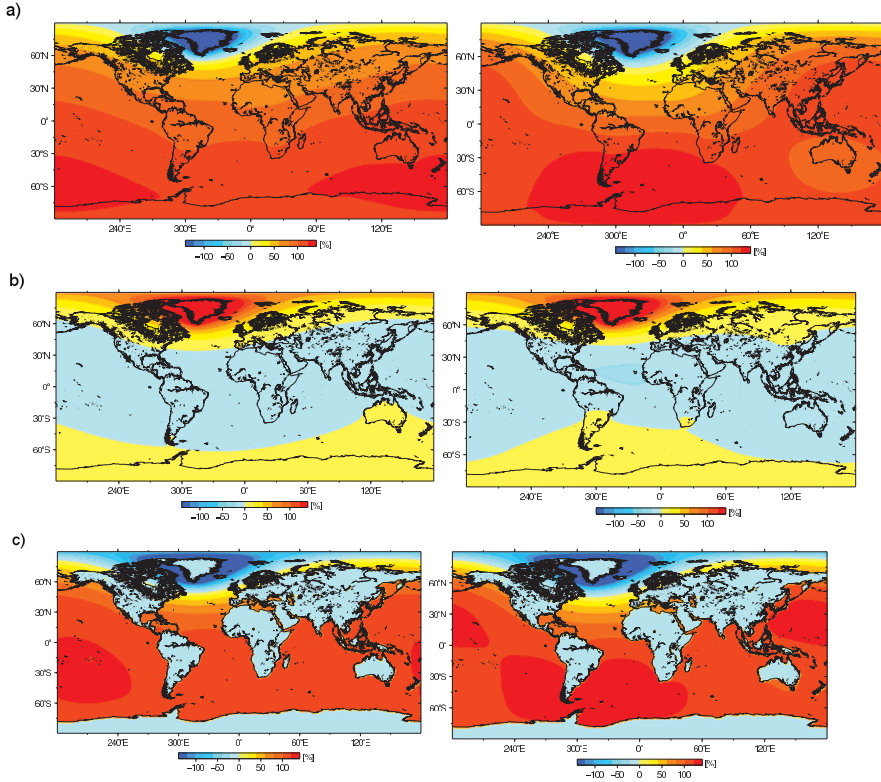
Figure 6.1: *Changes in a) the geoid, b) solid Earth and c) relative sea level, following a uniform mass loss over Greenland. Units are scaled by the eustatic sea level change. In the left column effects of rotational changes are excluded, in the right column these are included.*

computed using eq. 6.13. The resulting $S(\theta, \lambda)$ is used as an input in the next iteration step, and the procedure is repeated until convergence is reached, which usually occurs after 3–4 runs. In this study, the pseudo-spectral approach (Mitrovica and Peltier, 1991) is used, i.e. only the convolution of the relative sea level with the ocean function takes places in the spatial domain, all other computations are performed using spherical harmonics.

Figures 6.1a–c show the effect of a uniform mass loss over Greenland on the geoid, the solid surface of the Earth and the relative sea level, for a non-rotating Earth. All quantities have been normalized by the sea level change that would occur if the mass anomaly from Greenland would be distributed uniformly over

the ocean. Computations in the spectral domain were performed up to a degree and order 512.

In the regions closest to the mass changes, a distinct negative geoid anomaly is observed (fig. 6.1a). The decrease in geoid height is not limited to the immediate surroundings of Greenland, but extends as far as the Svalbard archipelago, which is due to the self-gravitation effect of the negative mass anomaly. At distances further away from Greenland, the geoid becomes increasingly positive, with a positive maximum in the region surrounding Antarctica.

Due to the unloading of mass, either directly due to the mass reduction over Greenland or through a fall in sea level in the surrounding regions, the solid earth will respond elastically and rise in the vicinity of Greenland (fig. 6.1b), whereas over most of the oceans the solid surface is being slightly lowered. The regions in the far field, i.e. Antarctica, rise due to the mass anomaly signal over Greenland.

Subtracting the solid earth deformation from the geoid changes yields the relative sea level change (fig. 6.1c). In the near field, the combination of the reduced gravitational pull and the rebounding ocean bottom results in a relative sea level fall stretching as far as Ireland. Further away, the changes in relative sea level are dominated by the geoid changes, with the area where the relative changes remains below the expected uniform change extending as far as the northern tip of South-America. Due to conservation of mass in the oceans, relative sea level changes further south will be larger than the eustatic change, with a maximum in the South Pacific, where a rise of ~120% of the eustatic value is predicted.

6.1.2 Rotational changes

A secondary effect of the mass redistribution on and within the Earth is the change of the Earth's rotation vector. Both the magnitude of the rotation vector as well as the orientation with respect to a fixed point in space will be altered, which will result in a large-scale geoid change and crustal deformation with a predominantly degree 2, order 1 pattern, as will be demonstrated later on. An extensive discussion of this topic can be found in Milne and Mitrovica (1998), the basic theory is summarized below.

At a point $p(\theta, \lambda)$ located at a distance r from the center of mass of the Earth, the rotational potential can be expressed as:

$$U_c(\theta, \lambda, r) = \frac{1}{3}\omega^2 r^2 + \Delta U_c(\theta, \lambda) \qquad (6.17)$$

where ω^2 is the absolute magnitude of the Earth's rotation vector $(\omega_1, \omega_2, \omega_3)^T$. The first part of the right-hand term describes the rotational potential for a point mass, the second part is the deviation from this homogenous field caused by the equatorial flattening of the Earth. Using Legendre polynomials, the latter can be expressed as:

$$\Delta U_c(\theta, \lambda, r) = \frac{1}{6}r^2(\omega_1^2 + \omega_2^2 - 2\omega_3)P_{20}(\cos\theta)$$

$$-\frac{1}{3}r^2(\omega_1\omega_3\cos\lambda + \omega_2\omega_3\sin\lambda)P_{21}(\cos\theta) \qquad (6.18)$$

$$+\frac{1}{12}r^2((\omega_2^2 - \omega_1^2)\cos 2\lambda - 2\omega_1\omega_2\sin 2\lambda)P_{22}(\cos\theta)$$

If the proportional deviation of the rotation vector from the equilibrium state $(0, 0, \Omega)^T$ is denoted by $(m_1(t), m_2(t), m_3(t))^T\Omega = \vec{m}\Omega$, where Ω is the angular velocity of the Earth, the rotation vector $\vec{\omega}$ can be expressed as:

$$\vec{\omega} = (m_1(t), m_2(t), 1 + m_3(t))^T\Omega \qquad (6.19)$$

Inserting this in eq. 6.19 leads to:

$$\Delta U_c(\theta, \lambda, r, t) = \frac{r^2\Omega^2}{\sqrt{5}}\{\frac{1}{6}(m_1^2(t) + m_2^2(t) - 4m_3(t) - 2m_3^2(t)))P_{20}(\cos\theta) \quad (6.20)$$

$$+ \frac{1}{\sqrt{3}}(m_1(t)(1 + m_3(t))\cos\lambda + m_2(t)(1 + m_3(t))\sin\lambda)P_{21}(\cos\theta)$$

$$+ \frac{1}{\sqrt{12}}((m_1^2(t) - m_2^2(t))\cos 2\lambda - 2m_1(t)m_2(t)\sin 2\lambda)P_{22}(\cos\theta)\}$$

The perturbations from the equilibrium state of the rotation vector, $\vec{m}$, can be related to the surface mass distribution anomalies and the associated change in the potential:

$$m_1 = \frac{\Omega}{A\sigma_0}(1 + k_2')J_{13} \qquad (6.21)$$

$$m_2 = \frac{\Omega}{A\sigma_0}(1 + k_2')J_{23} \qquad (6.22)$$

$$m_3 = -\frac{1}{C}(1 + k_2')J_{33} \qquad (6.23)$$

in which C denotes the Earth's moments of inertia along the polar axis. The moments of inertia along the equatorial axes are assumed to be identical and are denoted by A. Values selected for A and C are 8.0131×10^{37} and 8.0394×10^{37} respectively (Sabadini and Vermeersen, 2004). The Chandler wobble frequency is symbolized by σ_0 and given by:

$$\sigma_0 = (1 - \frac{k_2}{k_f})\frac{(C - A)}{A}\Omega \qquad (6.24)$$

, where k_2 is the tidal degree 2 Love number and k_f is the secular Love number (Sabadini and Vermeersen, 2004).

The J_{i3} ($j = 1 \ldots 3$) terms in equations (6.21)–(6.23) are the changes in the inertia tensor with respect to the polar axis and are related to the spherical harmonical expansion of the surface mass anomalies by, Milne and Mitrovica (1998):

$$J_{13} \quad = \quad \frac{4}{3}\sqrt{\frac{3}{5}}a_{\mathrm{e}}^4\pi(C_{21}^{\mathrm{M}} + \rho_{\mathrm{w}}C_{21}^{\mathrm{S}}) \tag{6.25}$$

$$J_{23} \quad = \quad \frac{4}{3}\sqrt{\frac{3}{5}}a_{\mathrm{e}}^4\pi(S_{21}^{\mathrm{M}} + \rho_{\mathrm{w}}S_{21}^{\mathrm{S}}) \tag{6.26}$$

$$J_{33} \quad = \quad -\frac{8}{3}\sqrt{\frac{1}{5}}a_{\mathrm{e}}^4\pi(C_{20}^{\mathrm{M}} + \rho_{\mathrm{w}}S_{20}^{\mathrm{S}}) \tag{6.27}$$

Now that the perturbations in the rotational potential are expressed in terms of the surface mass anomalies, the effect on the geopotential and radial displacement of the solid Earth can be computed analogous to eq. 6.6 and eq. 6.7:

$$N'_{\mathrm{rot}}(\theta, \lambda) \quad = \quad \sum_{l=0}^{\infty}(1 + k_l^{\mathrm{T}})\Delta U_{\mathrm{c}_l}(\theta, \lambda, a_{\mathrm{e}}) \tag{6.28}$$

$$R_{rot}(\theta, \lambda) \quad = \quad \sum_{l=0}^{\infty}h_l^{\mathrm{T}}\Delta U_{\mathrm{c}_l}(\theta, \lambda, a_{\mathrm{e}}) \tag{6.29}$$

, where k^{T} and h^{T} are the Love numbers for the deformations by a (tidal) potential forcing that does not load the surface. The change in relative sea level due to perturbations in the rotational potential then becomes:

$$S_{\mathrm{rot}}(\theta, \lambda) = \sum_{k=0}^{\infty}O_k(\theta, \lambda)\sum_{l=0}^{\infty}(1 + k_l^{\mathrm{T}} - h_l^{\mathrm{T}})\Delta U_{\mathrm{c}_l}(\theta, \lambda, a_{\mathrm{e}}) \tag{6.30}$$

Adding this result to eq. 6.13 then gives the total change in relative sea level.

From eq. 6.21–6.27 it can easily be seen that in general $m_3 \ll m_1, m_2$. Since the only term in eq. 6.21 involving first order terms in m_1 and m_2 is associated with the P_{21} Legendre polynomial, the sea level response to a change in the Earth's rotation vector will have a distinct degree 2, order 1 pattern, i.e. dividing the Earth's surface into four quadrants of alternating sign. This is illustrated in the right-column of fig. 6.1, where geoid changes, solid Earth deformation and the relative sea level changes following a (uniform) mass loss over Greenland are shown, now including the effects of rotational changes. The most prominent differences between the left and right column are found in the geoid, where the maximum change is now located in the South Atlantic. Also in the North Pacific the geoid changes are amplified, whereas values over Australia are notably smaller than when rotational effects are excluded. Similar conclusions can be made for the

solid Earth deformation, although the differences are smaller. Maximum changes in the relative sea level are now found in the southwest Atlantic, with values up to 135% of the eustatic values.

6.2 The seasonal cycle in relative sea level

6.2.1 The GRACE data

Given their global coverage of mass redistribution on land, the GRACE observations offer a great tool to model self-gravitation and loading signals, using the theory described above. The predicted signal can then be subtracted from the observed mass variations in the oceans, to separate signals due to gravitational effects from signals due to ocean dynamics.

In total, 58 monthly solutions between March 2003 and February 2008, released by the Center for Space (CSR RL04), are used. As discussed in Ch. 1, the GRACE data is distributed in terms of Stokes coefficients, which will be denoted by ($\Delta C_{nm}^{\mathrm{G}}$, $\Delta S_{nm}^{\mathrm{G}}$) in this chapter. Using eq. 1.6, these coefficients can be translated to variations in the surface mass density on land and in the oceans, which is often converted to equivalent water height through division by the density of water.

During the processing of the raw satellite data by the GRACE processing centres, the data is corrected for various short-scale geophysical signals in order to reduce aliasing issues. Among others, high-frequency ocean signals are removed using the output of the barotropic OMCT model (Thomas, 2002). To obtain the full envelope of the ocean variability, the removed signal from the ocean model is added back, with omission of the mean atmospheric pressure over the oceans, so that the signals observed by GRACE over the oceans represents the bottom pressure due to changes in water load only (Chambers, 2006a). The degree 1 coefficients, directly related to the displacement of the earth's center of mass, are not observed by the GRACE satellites. This was corrected for by adopting seasonal geocenter estimates based on a combination of the OMCT ocean model and GRACE data over land (see Swenson et al., 2008). The original C_{20} coefficients, which are strongly affected by aliased ocean tide model errors (Chen and Wilson, 2008), were also replaced by values derived from satellite laser ranging (Eanes, personal communication, 2008).

At the shorter wavelengths, the GRACE data is known to be contaminated by correlated noise. Therefore, the coefficients were filtered using the EOF approach of Ch. 2. After these steps, the Stokes coefficients are converted to maps of equivalent water height, using eq. 1.6. Despite the EOF filtering, some noise-like patterns still show up at the annual frequency: horizontal patterns of alternating positive and negative anomalies become the dominant signals in the regions around the equator and at approximately 30 degree north and south, see fig. 6.2a. Careful inspection of the Stokes coefficients shows that the origin of these horizontal stripes can be traced down to a distinct set of high-order, near sectorial

a)

b)
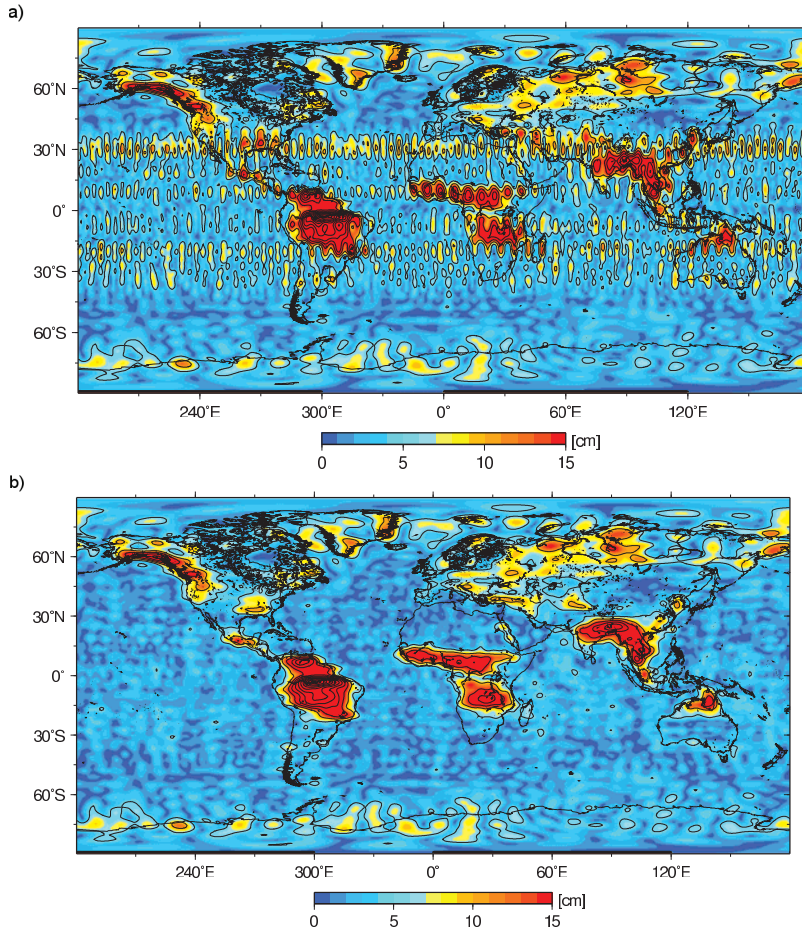
Figure 6.2: *Annual amplitude in equivalent water height from the GRACE observations; a) after EOF filtering, and, b) after setting selected near-sectorial spherical harmonics to zero. Contour intervals are plotted every 5 cm.*

spherical harmonics ($l \approx m$) for the coefficients of order $m = 45$, 49 and 54, see Ch. 2. Setting these coefficients to zero results in maps of equivalent water height that show no prominent unrealistic noise patterns over land at the annual period, see fig. 6.2b.

The filtering and tuning of the Stokes coefficients to suppress noise will inevitably lead to a reduction of some of the real geophysical signal. As will be shown later, the effect on the modeled relative sea level is small, since this mainly depends on the large scale mass redistribution on the continents.

6.2.2   GRACE-derived seasonal variations in relative sea level

On seasonal time scales, the GRACE observations will be dominated by variations in the surface mass load on the continents and fluctuations in the pressure exerted on the ocean floor. The two components are separated by convolving the observed surface mass with the ocean respectively land mask from eq. 6.9:

$$
\begin{aligned}
\Delta\sigma(\theta,\lambda) &= \Delta\sigma_{\text{land}}(\theta,\lambda) + \Delta\sigma_{\text{ocean}}(\theta,\lambda) \\
&= \Delta\sigma(\theta,\lambda) * L(\theta,\lambda) + \Delta\sigma(\theta,\lambda) * O(\theta,\lambda)
\end{aligned}
\tag{6.31}
$$

The land mask function used above changes discontinuously from 0 to 1 at the coastal boundaries. In the spectral domain, due to the limited spectral resolution of the available data ($l_{\max} = 60$), this will lead to a ringing pattern near these discontinuities, known as the Gibbs phenomenon. A possible solution for this problem is the removal of the discontinuous jump at the coasts by smoothing the land mask so that the values changes gradually over a certain distance from one over land to zero over the ocean, see, e.g., Swenson and Wahr (2002). We opt for a land mask smoothed at a Gaussian radius of 300 km, as used in Chambers et al. (2007). The drawback of this method is that it will weaken the hydrological signal over land, which may be relatively large in some coastal areas (e.g., the Ganges-Brahmaputra basin). Also, in coastal regions of large variability in ocean bottom pressure, part of the barotropic signal will be misinterpreted as occurring over land, due to the continuous characteristics of the mask. Both factors will lead to divergence from the 'true' solution during the iterative procedure, since the loading signals over land and oceans are not properly represented. The influence of the landmask will be discussed later using simulated data.

After separating land from ocean signals in the GRACE data, the mass changes in the ocean can be further separated into (1) a component associated with the global bottom pressure averaged over the ocean domain, $\overline{\Delta\sigma}_{\text{eustatic}}$, (2) a component associated with the gravitational and loading effects as discussed above, $\Delta\sigma_{\text{self}}$, i.e. the deviation from the eustatic distribution as a function of the mass distribution on land, (3) and one due to ocean dynamics $\Delta\sigma_{\text{dynamics}}$ (e.g., due to wind forcing or driven by internal density differences):

$$
\Delta\sigma_{\text{ocean}}(\theta,\lambda) = \overline{\Delta\sigma}_{\text{eustatic}} + \Delta\sigma_{\text{self}}(\theta,\lambda) + \Delta\sigma_{\text{dynamics}}(\theta,\lambda)
$$

Note that of these three components, only $\overline{\Delta\sigma}_{\text{eustatic}}$ has a non-zero global mean, which represents the amount of water exchanged between land and ocean, divided by the ocean's area. A seasonal amplitude of 7.9±0.4 mm with a maximum late September (day 273±5) is found, in agreement with earlier studies (e.g., Chambers et al., 2004; Chen et al., 2005; Lombard et al., 2007).

In order to study the effect of selfgravitation due to seasonal changes in mass distribution on the continents on the sea level height ($\Delta\sigma_{\text{self}}$), the GRACE ob-
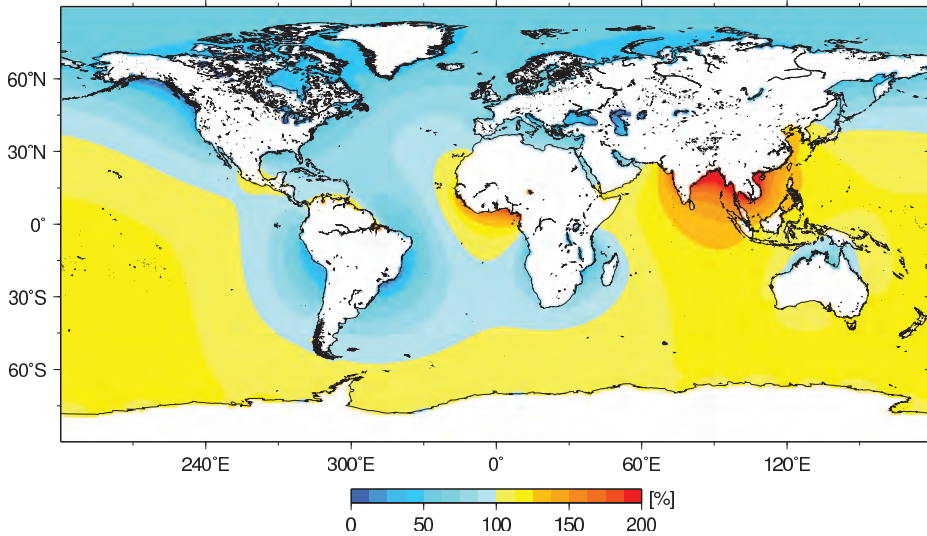
Figure 6.3: *Seasonal amplitude of the relative sea level changes caused by the combined gravitational and radial displacement effects. The values are normalized by the global annual eustatic amplitude.*

served $\Delta\sigma_{\text{land}}(\theta, \lambda)$ are inserted in the sea level equation (eq. 6.13) and the iterative procedure to solve for the relative sea level change is initiated. The effect of perturbations in the Earth's rotation vector has been excluded from the estimates, since the contribution of the pole tide are removed from the gravity solutions during processing of the GRACE data by the distribution centers (Bettadpur, 2007), and are not into account in the ECCO ocean model which will be used later on.

Figure 6.3 shows the annual variations in relative sea level as a result of the changes in the geoid and radial displacement effects. The results have been scaled by $\overline{\Delta\sigma}_{\text{eustatic}}$ (7.9 mm), so that they represent the relative departure from the global mean eustatic annual cycle. Amplitudes smaller than the global mean are colored blue, larger amplitudes are yellow/red. Overall, the relative sea level is characterized by long wavelength patterns. The Northern Hemisphere shows annual amplitudes below the global mean, due to the fact that the gravitational attraction from land reaches a maximum in late winter/early spring, when soil moisture content and snow coverage peak at northern latitudes (see fig. 6.4). This maximum is about 180° out of phase with the eustatic variation, resulting in a reduced amplitude of the sum of the two components. In the Southern Hemisphere, the amplitude is consequently generally larger than the global mean, except for the regions around the major hydrological basins in the Southern Hemisphere, such as the Amazon basin or the Congo/Zambezi basin, where a similar reasoning applies. Maximum amplitudes are found around the major hydrological systems in the northern subtropics, e.g., the Ganges-Brahmaputra or the Volta-Niger basins,

a)

b)
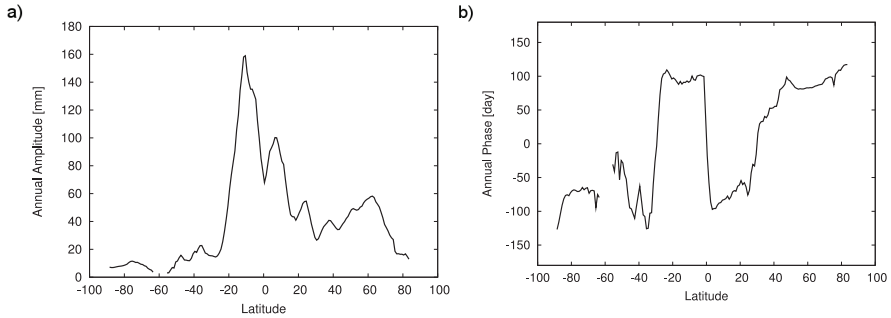
Figure 6.4: *a) Zonally averaged annual amplitude expressed in mm equivalent water level, and, b) day of maximum of the continental water storage from GRACE observations.*

where the peak in gravitational pull of terrestrial water masses coincides with the maximum in eustatic sea level, resulting in an amplified total signal.

On a basin scale, the Pacific Ocean has an amplitude of 105% of the global eustatic mean, with most positive values in the south (108% vs. 101% for the Northern Hemisphere). Slightly higher values are found in the Indian Ocean (111 %). Below-average values are predicted in the Atlantic (88% with 91 % South vs. 85 % North Atlantic) and in the Arctic ocean (53%).

Maximum annual variability is found in the Bay of Bengal, where the annual amplitudes of $\Delta\sigma_{\mathrm{self}}$ and $\overline{\Delta\sigma_{\mathrm{eustatic}}}$ add up to 21 mm, or about 2.7 times the global mean. The smallest signal is found off the coasts of Alaska and British Columbia, where values as small as 0.7 mm, only about 9 % of the eustatic global mean, are obtained. Overall, 55% of the ocean experiences an annual cycle larger than the global average, while amplitudes are smaller in the other 45%.

6.2.3   Validation with the ECCO model

Comparing the GRACE observations over the ocean to bottom pressure estimates from numerical ocean model is frequently applied as a quality check for the GRACE data (e.g., Swenson et al., 2008). However, such numerical models lack the effects of selfgravitation as described above. Including theses effects should therefore result in an improved reconciliation of the two data sets. In the following, this hypothesis is tested by comparing the GRACE data to the output of the ECCO (Estimating the Circulation and Climate of the Ocean) model, with and without the selfgravitation effects included. The ECCO model is a baroclinic model, forced by output from the National Center for Environmental Prediction (NCEP) operational analyses products, for details see, e.g., Fukumori et al. (1999). For consistency, the monthly ECCO grids were first converted to spherical harmonics up to degree 60 and then transformed back to spatial grids.

Since the GRACE data are still relatively contaminated by noise over the ocean, both data sets are smoothed with a Gaussian radius of 350 km, after masking out land.

The ECCO model uses the Boussinesq approach, i.e. it conserves volume rather than mass. The unmodeled volume changes will result in spurious mass variations on global and basin scale (Ponte, 1999). Therefore, before comparing to the GRACE observations, the global mean bottom pressure $\overline{\Delta\sigma}_{\mathrm{eustatic}}$ is subtracted from every grid point in the monthly ECCO grids. Then, the monthly mean ocean mass obtained from the GRACE observations, i.e. $\overline{\Delta\sigma}_{\mathrm{eustatic}}$, is added to the ECCO fields. The differences between the annual cycle in the GRACE observations and ECCO simulations are then computed and the local variance of the seasonal residuals determined (fig. 6.5a). The smallest residuals are found in the southern Indian Ocean and have a variance of ≈ 5 mm, which can be taken as a (rather optimistic) error estimate for the GRACE observations over the oceans at seasonal time-scales.

To test to which extent including the effects of selfgravitation brings the two data sets closer together, the procedure is repeated, but now also $\Delta\sigma_{\mathrm{self}}$ is added to the ECCO fields. The relative change in the variance is depicted in fig. 6.5b. The results of the test appear to be inconclusive for most of the open ocean, where differences are within a few percents of the original variance. Differences between the eustatic mean sea level and the relative sea level are in the order of a 10–20 % in these regions, which translates to 1–2 mm in equivalent sea level height, below the noise level of the GRACE observations mentioned above. In regions where larger differences are expected, compare fig. 6.3, the inclusion of the selfgravitation effects in the ECCO model reduces the variance of the residuals by up to 17 %. Most positive changes are found at regions distant from the major river basins, e.g., the west coast of South America, which indicates that at least part of the signal in the GRACE observations close to the coast, generally attributed to contamination from continental hydrology due to smoothing of the surface water height maps, i.e. the so-called 'leakage' effect, is due to the effect of selfgravitation.

6.2.4 Accuracy assessment using simulated data

The GRACE observations have a limited resolution, with a maximum spherical degree $l = 60$ for the CSR RL04 solutions, corresponding to a spatial half wavelength of approximately 333 kilometers. Hence, small scale signals will not be fully sampled by the GRACE satellites and also the use of a non-exact land function is required. Moreover, a filtering method based on EOF decomposition needs to be applied to yield solutions usable at their optimal resolution. This will result in loss of information on the surface water mass redistribution on land, which in turn will affect the estimates of relative sea level. These issues are addressed here by using a set of synthetic maps of monthly mass anomalies as an input for the sea level equation. To this end, the output of the Global Land Data As-
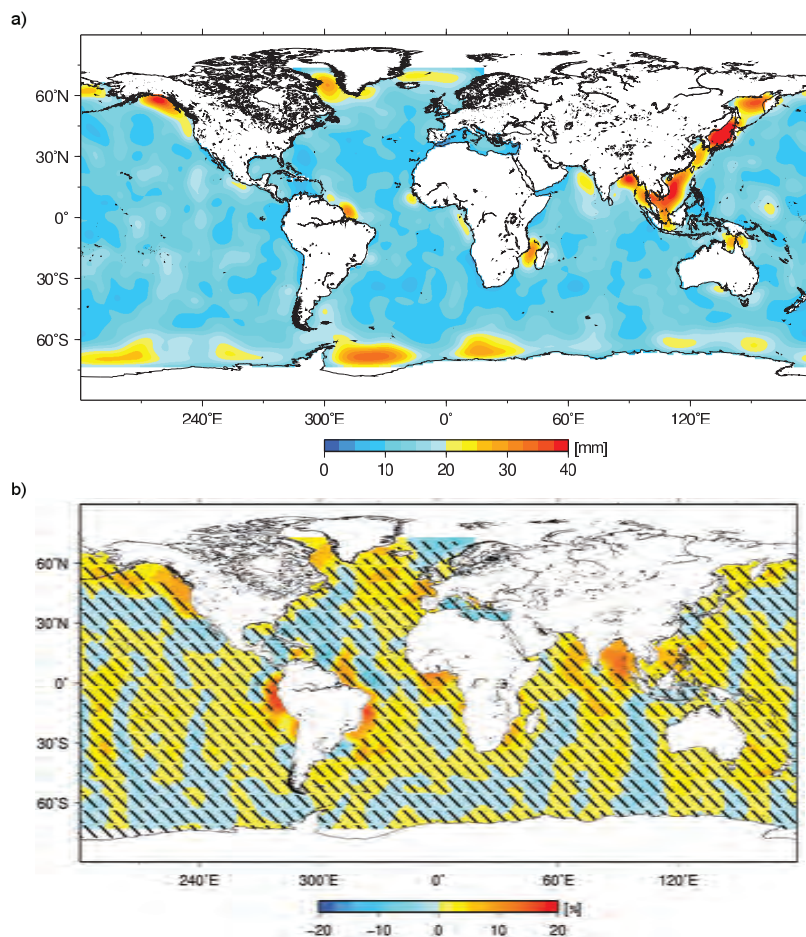
Figure 6.5: *a) Variance of the seasonal residuals of the GRACE observations and bottom pressure from the ECCO model differences, expressed in mm water equivalent, and, b) relative reduction of the variance after including effects of self-gravitation to the ECCO model. Dashed areas are the regions where the annual variance of the expected relative sea level signal (fig. 6.3) is smaller than 5 mm.*

simlation System (GLDAS) (Rodell et al., 2004) is combined with ocean bottom pressure variations from the ECCO model. Glaciated areas, such as Greenland and Antarctica, have been masked since glacier and ice sheet models are lacking in the GLDAS simulations.

The combined fields are converted to spherical harmonics and then used as input in eq. 6.13. In a first run, the spherical harmonic coefficients are truncated

at a degree of $l = 512$. The resulting estimate of relative sea level, which will be used as a reference (RLS_{512}), is given in fig. 6.6a. The effect of the spectral truncation and filtering is estimated by means of a second run (RLS_{60}), in which the smoothed land function is used and the coefficients were limited to degree $l = 60$ and filtered as describe above (fig. 6.6b).

The relative sea level estimated from both runs agrees well in shape and no systematic differences are observed. For the majority of the ocean, the values based on the GRACE-like RLS_{60} data are within 5% of the (normalized) values obtained from the RLS_{512} run. Along some parts of the coastlines, this values increases to ~10%. The limited spatial resolution and the non-exact land mask only become a limiting factor in some regions, such as around the peninsula of Kamchatka (-24%), where the relatively large hydrological signal in the GLDAS model cannot be fully captured, and in some coastal shallow water regions, e.g., the Gulf of Carpentaria (17%), where the large ocean bottom pressure variability is misinterpreted as occurring over land.

Comparing fig. 6.3 and 6.6, an excellent agreement is found between the annual relative sea level predicted from the model data and based on the GRACE observations. Both show matching long-wave length patterns, with a positive dome in the South Pacific and negative values around the continents in the Northern Hemisphere. Differences between the two figures are mainly found around the larger river basins, in particular the Amazon, Ganges-Brahmaputra and Niger basins, where the hydrological model tends to underestimate the annual land water storage variations – presumably due to a lack of groundwater storage modeling – and thus reducing the gravitational forcing and solid earth deformation in these regions. Also in the surroundings of glaciated areas, i.e. the Gulf of Alaska, differences are observed, since the ice physics are not properly modeled in the simulated data.

6.2.5 Present-day trends in relative sea level

Simultaneously with the annual amplitude, the trend in the relative sea level has been estimated. In contrast to the case of seasonal timescales, mass redistribution within the Earth can be expected on secular scales. Effects of global isostatic adjustment (GIA) have been minimized by subtracting the signal of the GIA model described in Paulson et al. (2007) from the GRACE observations. The remaining signal was then used to estimate the changes in relative sea level, analogously to the annual signal as described above. The trends shown in fig. 6.7 therefore are due to present-day mass variations only to the extent that the GIA model is correct. In the far field from the previously glaciated regions, the error in the model are estimated to be at the 20 % level (D. Chambers, personal communication, 2008). Closer to these areas the errors may be larger, hence some of the predicted relative sea level trends may be due to unremoved GIA effects (see Ivins and Wolf, 2008, and references therein for an overview of current state of GIA modeling). Other processes within the solid earth may also play a role
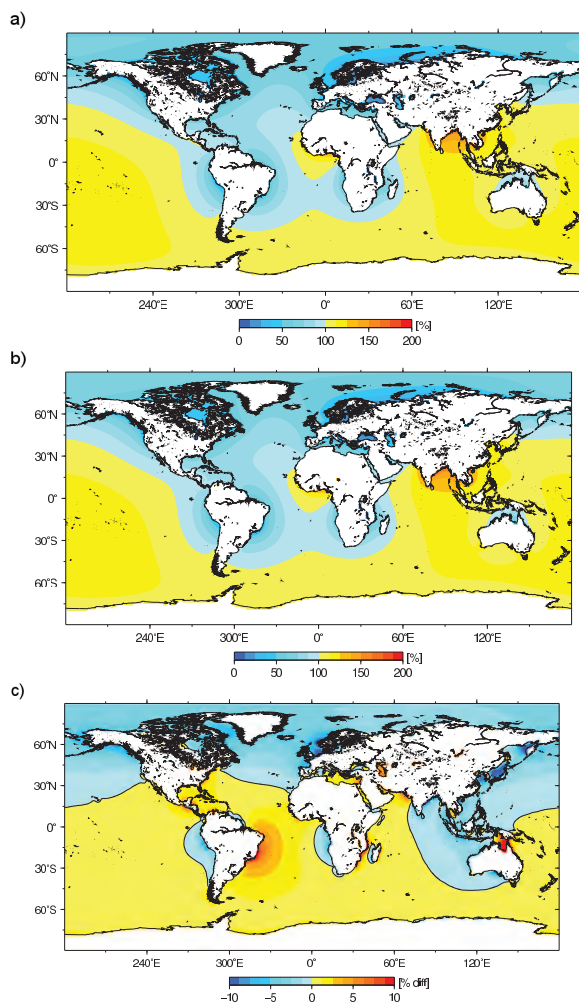
Figure 6.6: *Annual relative sea level amplitude based on modeled data, normalized by the mean global eustatic mass change over the oceans, for, a) the reference run (*RLS_{512}*), and, b) the GRACE-like run (*RLS_{60}*); c) Amplitude of difference between* RLS_{512} *and* RLS_{60}*, with contour lines plotted every 5%. Note the difference in scale.*

of importance, e.g., co-seismic and post-seismic mass redistribution due to the 2004 Sumatra-Andaman, which will be misinterpreted as occurring at the Earth's surface. Since no accurate models exist for such signals, no attempt is made to remove them. The results in the surroundings of such regions should therefore be

interpreted with care.

After removing the GIA contribution, a positive eustatic trend of 0.5±0.4 mm/yr, averaged over the ocean, is obtained. This figure is still open to debate (see, e.g., Chambers et al., 2007; Willis et al., 2008; Cazenave et al., 2009; Leuliette and Miller, 2009) and will not be discussed further. The main interest of this section lies in the spatial pattern of the relative sea level caused by the effects of selfgravitation, which is shown in fig. 6.7 for the period February 2003–January 2008. Comparing this to fig. 6.1c and fig. 1a–c in Mitrovica et al. (2001), it appears that the signal is dominated by the mass loss over Greenland, with negative trends in the North Atlantic, a positive lobe in the South Atlantic/southwest Pacific and slightly less positive values south of Australia. The influence of mass losses of the Alaskan and Patagonian mountain glaciers is also clearly visible on regional scales. A negative trend is visible along the coast of West Antarctica due to thinning of the ice sheet. Apart from cryospheric induced trends, the influence of long-term variations in the continental hydrology is also clearly discernable in fig. 6.7. Positive rates are found in the vicinity of the Amazon basin. In the high Arctic, the expected negative trends induced by the mass losses over Greenland are locally masked by a positive trends due to mass accumulation in the northern regions of the Eurasian continent.

6.3 Conclusions

In absence of any other signals due to ocean dynamics and atmospheric forcing, the annual exchange between land and ocean will result in sea level variations that deviate significantly from a uniform water layer as is assumed in most studies. The differences are most outspoken in the regions close to the main hydrological basins, with basins which are in phase with the annual global land-ocean mass cycle (with a maximum ocean mass late September) causing an amplification effect, and basins out of phase attenuating the amplitude of the relative sea level. Maximum departures are found around the Bay of Bengal, with an annual amplitude of relative sea level of 267±6% of the uniform, eustatic global mean signal. Off the coasts of Alaska and British Columbia, values as small 9±4% of the global mean are found. These amplitudes are comparable to the effect of the long-periodic ocean tides, which generally have a maximum amplitude of less than 1 cm in most of the oceans (Wunsch, 1967).

Generally speaking, the annual amplitudes in the Northern Hemisphere are smaller than the global mean value, whereas the Southern Hemisphere is characterized by larger amplitudes. Exceptions are the regions surrounding the main hydrological basins. Based on simulated data, it is found that the limited spatial resolution and the required filtering of the GRACE data leads to errors smaller than 5% for most parts of the ocean. The small differences between the reference simulation and the 'GRACE-like' simulation runs, and the good agreement between the relative sea level patterns obtained from the simulated data and the

a)

b)
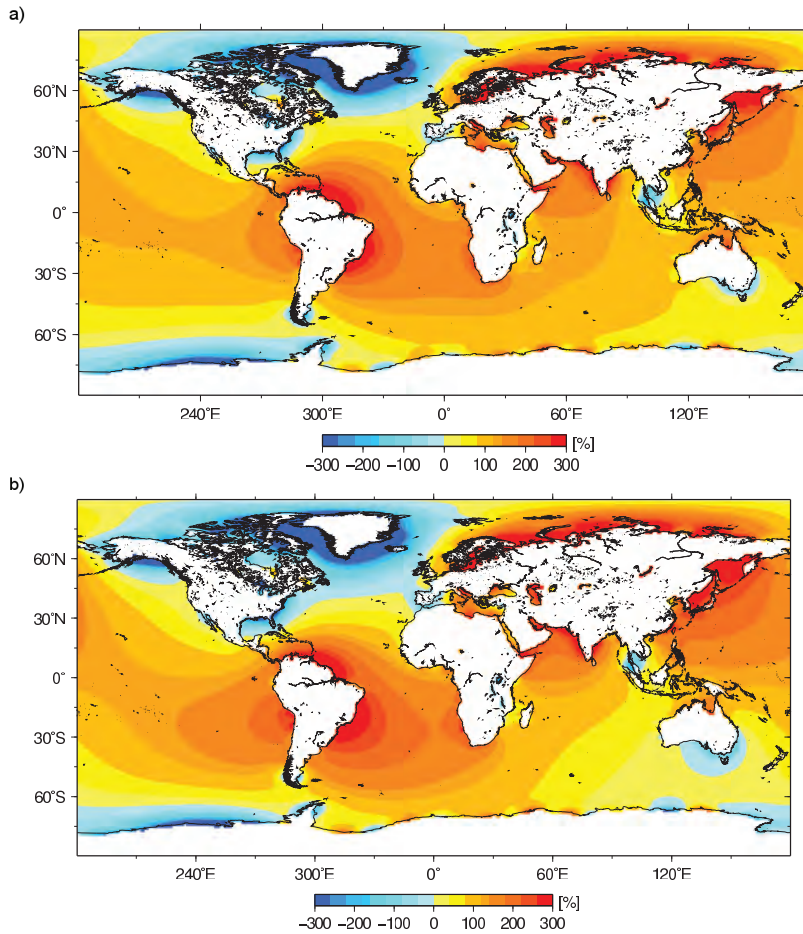
Figure 6.7: *Trends in relative sea level based on GRACE observations between Feb. 2003 and Jan. 2008, a) excluding, and b) including the rotational effects of eq. 6.30. The values are normalized by the mean global eustatic mass change over the oceans.*

actual GRACE data, leads to the conclusion that the spatial resolution of the GRACE observations is sufficient to predict variations in relative sea level.

Trends in the relative sea level signal appear to have been dominated by the mass imbalance of the Greenland ice sheet. Regionally, the trend signal is affected by long term variations in the continental hydrology. This is a topic that deserves further investigation, since such signals may cause a bias in studies that attempt to match tide gauge data to the spatial RSL 'fingerprint' of a specific mass imbalance signal, e.g., that of the Greenland ice sheet (e.g., Wake et al., 2006).

Strong gradients in the annual amplitude of the relative sea level signal are found in, among others, the Gulf of Alaska, the Bay of Bengal and in the vicinity of the Amazon basin. These regions would be the prime candidates for detection of the relative sea level signals by means of ocean bottom pressure (OBP) recorders. Such an effort should focus on annual variations rather than trends, since OBP recorder data have been known to suffer from linear and exponential drifts due to instrumental effects. The noise level in OBP measurements are in the order of 0.5–1 mm (Eble and Gonzalez, 1991), well below the amplitude of the expected signal in the aforementioned regions. Alternatively, tide gauge observations along the coast can be used, assuming that variations due steric variations can be removed with a sufficient accuracy. Detection of the signal in the open ocean by means of satellite altimetry observations is more challenging, since the expected amplitude and their gradients are smaller here, and the sea surface height changes are dominated by steric variations..

Over most of the oceans, changes in relative sea level due to the effects of self-gravitation are found not to be major factor to reconcile ocean bottom pressure from the ECCO model with the GRACE observations, but inclusion of this effect can reduce the variance of residuals between the two by up to 17% in coastal regions. Since large deviations from the global eustatic distribution are observed due to (self)gravitational attraction and solid earth movement in these regions, numerical ocean models attempting to incorporate the global ocean-land water cycle should consider the implementation of this additional forcing mechanism, preferably based on GRACE observations or by making use of hydrological models.

Chapter 7

Conclusions and recommendations

The two main goals of this dissertation were to show how the quality and resolution of satellite gravity measurements can be improved, and, how these improved observations can contribute to a better understanding of variability in our climate system, with a focus on the processes contributing to sea level variations. The first topic was discussed in Ch. 2 and 3, whereas Ch. 4, 5 and 6 discussed three different observational applications of the GRACE data. In the following, the main conclusions of these chapters will be summarized and recommendations are made for further research and improvements.

Chapter 2 and 3: It has been shown that empirical orthogonal function (EOF) analysis is a powerful tool to reduce the noise present in the GRACE solutions. The analysis can be applied to the maps of EWH based on the GRACE spherical harmonic coefficients, in which case the first few EOF modes are related to the annual and secular components. Higher components show traces of semi-annual variations, and aliasing of the S_2 ocean tide. A long-period signal is observed in the fourth mode, which has most of its signal in regions typically affected by the ENSO cycle. A similar EOF mode is found in the GLDAS hydrological model. The associated principal component shows a relatively good correlation with the El Niño 3.4 index, however, a longer period of observations is required to confirm the relation between the two.

Whereas EOF analysis of the GRACE maps delivers insight in the individual modes of variability, the technique can also be used as a tool to remove the inter-degree correlations in the GRACE spherical harmonics. By applying the analysis directly to the coefficients and rejecting certain modes, the north-south striping in the GRACE solutions can be further reduced. The selection of the

modes to be retained is based on a comparison of the cumulative distribution function of the principal component to that of a random process. The variance of signals deviating from the (semi-)annual harmonic and secular trend is reduced by 60%–80%, compared the non-filtered case. A similar reduction in variance is observed in the approximate Sahara region in North-Africa, where little to no signal is to be expected. Comparing GRACE derived vertical deformation rates to observations of IGS GPS stations, shows that filtering of the GRACE data improves the agreement between the two data sets. The results obtained by the EOF filtering of the spherical harmonics are comparable to those obtained by the popular destriping technique of Swenson and Wahr (2006), which fits a polynomial to the even and odd degree coefficients. Tests using synthetic spherical harmonic coefficients based on numerical geophysical models shows that, given a sufficiently long observation period, the EOF filter will remove considerably less signal. This can be explained by the fact that the EOF analysis is based on the temporal behavior of the signal and retains signals that vary coherently in time, whereas the destriping filter of Swenson and Wahr (2006) tends to remove all signals which are predominantly north-south orientated, and may also introduce artificial signals due to the filter's spatial characteristics.

Given that the EOF technique is based on the temporal evolution of the spherical harmonics, monthly GRACE solutions with a lower quality such as those of the 2004 near-repeat event will affect the final result of the analysis. In some of the higher near-sectorial coefficients, remnant noise is observed after applying the EOF filter. This results in distinctive horizontal striping patterns at certain latitudes. These patterns are observed in the data of all three GRACE processing centers, which indicates that the origin lies in the groundtrack characteristics of the satellites, the GRACE instruments or in one or more of the common background correction models.

Applying the EOF procedure to the spherical harmonics is a tool to remove the striping patterns, whereas applying the analysis to the (then filtered) maps of equivalent water height is an aid to interpret the observed signals. The two methods are therefore compatible. Furthermore, they may also be combined with other filtering techniques based on an alternative approach. In the last few years, filters have become available that make use of the full covariance matrix of the GRACE solutions, combined with geophysical model data (e.g., Kusche, 2007; Klees et al., 2008). An in-detail study comparing the different filtering techniques available should be carried out in the future to identify and compare the respective strengths and weaknesses of each of these approaches.

Chapter 4: The GRACE satellites are capable of capturing seasonal changes in the ocean mass content accurately on a global scale. In combination with sea surface height observations made by satellite radar altimeters, the steric sea level component can be recovered as well. Comparisons with in-situ temperature and salinity climatology data show that locally a coherent signal can be obtained at a (Gaussian) resolution of approximately 500 km over the oceans, if the EOF filter

is applied to the monthly GRACE solutions. At this scale, the spatial patterns of the seasonal amplitude and phase of the steric sea variations match well with those in the reference set. The estimated signal-to-noise ratio is greater than one in approximately 50 % of the ocean's area.

Due to the vast size of the ocean, estimates of global ocean mass changes are strongly affected by the choice of the model for the spherical harmonic coefficients of degree 1, which are related to the position of the geocenter of mass and are not observed by the GRACE satellites. Models based on satellite laser ranging observations, combinations of numerical geophysical models and GRACE data itself, yield a good agreement between the GRACE-based estimates of the seasonal cycle in ocean mass content and the reference datasets. However, secular trends in the geocenter's position are less well known, which introduces a larger uncertainty in the estimation of long-term changes in the total ocean mass. Furthermore, the GRACE data need to be corrected for mass distribution within the solid earth due to glacial isostatic adjustment (GIA). Depending on the chosen viscosity profile and deglaciation history in the GIA model, this correction may change the global trend by up to 2 millimeter per year (Willis et al., 2008; Leuliette and Miller, 2009; Cazenave et al., 2009). In order to close the sea-level rise envelope, a better understanding of these phenomena will be required.

In the majority of the ocean, the annual variability in total sea level as observed by the JASON-1 altimeter is governed by steric changes, which typically constitutes 80 % or more of the total signal. Strong ocean bottom pressure fluctuations are observed in the Gulf of Carpentaria and the Gulf of Thailand. These signals are highly correlated with in-situ tide gauge measurements, indicating that these ocean bottom pressure variations are not an artefact of deficiencies in the GRACE solutions or a result of leakage of land hydrology signals. Both of these areas are semi-enclosed seas, of shallow depth. A possible driving mechanism behind the observed ocean bottom pressure fluctuations could therefore be related to the piling up of water driven by wind forcing, e.g., due to the northeastern winter monsoon in South Asia (Morimoto et al., 2000). Future research should be conducted on the link between the amplitude of the observed ocean bottom pressure and the strength of the wind forcing in the adjacent regions.

In several regions of the oceans, evidence of aliasing of the S_2 tide is observed. The S_2 has a relatively short aliasing period of approximately 160 days and can therefore be extracted relatively well from the $\sim$6 years of observations currently available. Other tidal constituents will alias into longer period signals, e.g., approximately 7.4 and 3.7 years for the K_1 and K_2 tides respectively, and therefore less well separable from other low-frequency signals. A longer observation period is required to asses the impact of mismodeling of these constituents on the estimation of long-term and secular variations in the GRACE data.

Chapter 5: The monthly global spherical harmonic coefficients provided by the GRACE science teams contain more information than previously recognized. Using the forward modeling technique described in Ch. 5, changes in surface mass

distribution can be allocated to specific basins, predefined on climatological and topographic grounds. In this dissertation, this technique was applied to the Greenland ice sheet, but it can readily be applied to other regions, e.g., to monitor the mass balance of the Antarctic ice sheet, or to recover fluctuations in the water table of the Amazon-Orinoco river system.

In Greenland, a linear trend of -179 ± 25 Gt/yr is observed in the period between February 2003 and January 2008. In the first half of this period (July 2003 to July 2005), the ice sheet lost mass at a rate of -121 ± 25 Gt/yr. This number is consistent with the findings of Ramillien et al. (2006) and Luthcke et al. (2006), who based their study on a different parameterization of the GRACE data, giving confidence in the robustness of the forward modeling approach. In the last two years of the observations (January 2003 to January 2008), the trend had increased to -204 ± 25 Gt/yr. It should be noted that large part of the estimated uncertainty is due to differences in the models used to correct for glacial istostatic adjustment. Although the overall correction is nearly equal for all models, significant regional differences exist. Improved GIA models are therefore a prerequisite to narrow the error bars of the estimated mass trend.

The mass balance of Greenland shows large interannual fluctuations and an observation period of at least 3 years or longer is desirable to reduce the impact of year-to-year variability in the trend estimation. Doing so, still an acceleration of the mass losses emerges, which fits well in the picture of an increasingly more negative mass balance of the Greenland ice sheet since the mid 1990's (e.g., Rignot et al. (2008b); Ettema et al. (2009)). The current mass loss of 179 Gt/yr of the Greenland ice sheets corresponds to a global mean sea level rise of 0.5 mm/yr, equivalent to approximately 15–20% of the total sea level rise budget for 2003–2008 (e.g., Leuliette and Miller, 2009; Willis et al., 2008).

The majority of the observed mass losses occur in Greenland's coastal regions, predominantly in the southeast and northwest. Whereas the former area shows a persistent negative trend during the entire observation period, the latter was close to be in balance until mid 2005. Mass losses peak during summer months, with maxima in 2003, 2005 and an absolute maximum in 2007, when approximately 340 Gt of ice was removed. During this summer, a persistent negative mass anomaly is also observed in the interior of the ice sheet. The strong coupling with the observed areal extent of surface melt indicates that the majority of the summer mass losses are induced by runoff of meltwater at the surface. This is further supported by the strong correlation between the GRACE observations and surface mass balance estimates from regional climate models.

Whereas the trends presented in Ch. 5 are in close agreement with those obtained using regional GRACE solutions (Luthcke et al., 2006), they are significantly smaller than those reported in studies using the regional averaging kernel approach, such as Velicogna and Wahr (2006b). Although part of the discrepancy may arise due to different GRACE data releases and observation periods, systematic differences remain. Likely candidates to explain these differences are the use of the scaling factor and leakage of unmodeled signals outside of Greenland, in

particular the mass losses in Ellesmere Island. Reconciling the estimates based on these three different approaches should be one of the main focuses for further research.

By combining the GRACE observations with INSar observations of ice discharge rates and surface mass balance estimates of regional climate models, further insight can be obtained in the individual processes contributing to the changes in the mass balance of the Greenland ice sheet. As shown in van den Broeke et al. (2009), who used surface mass balance output of the RACMO2.1/GRN model, the ice flux data of Rignot et al. (2008b) and the GRACE observations presented in Ch. 5, good results are obtained on an island-wide scale by combining the three data sets. Further research should focus on refining this method to a basin-wide scale, which could, for example, identify the underlying causes of the mid-2005 transition from near-balance to persistent mass loss in the northwest of the Greenland ice sheet.

Furthermore, it should be investigated how independent data – such as altimetry measurements of the upcoming Cryosat-2 mission, or the surface mass balance estimates from numerical models combined with glacier discharges from INSar observations – can be used as a constraint in the inverse procedure to improve the spatial resolution of the forward model.

Chapter 6: Changes in the geoid generated by mass redistribution on the continents and deformation of the solid earth create a forcing term that, in absence of ocean dynamics and atmospheric forcing, will cause the sea level to depart from a uniform layer as is assumed in the majority of studies describing water exchange between ocean and land. Although most studies have focused on the long-term effects of this phenomenon, it plays an important role on seasonal time scales as well. Seasonal deviations from a uniform sea level rise and fall are most outspoken in the regions close to the main hydrological basins. Basins which are in phase with the annual land-ocean mass cycle (with ocean mass content peaking late September) cause an amplification effect, e.g., in the Bay of Bengal, where the annual relative sea level cycle measures $267\pm6\%$ of the uniform, eustatic global mean signal. Out-of-phase hydrological forcing attenuates, e.g., off the coasts of Alaska and British Columbia where the annual cycle equals only $9\pm4\%$ of the uniform distribution. In the open ocean, deviations are smaller, but comparable to those of the long-periodic ocean tides, which typically have a maximum amplitude of less than 0.5–1 cm in most of the oceans.

Based on simulated data, it is found that the limited spatial resolution and the required filtering of the GRACE data leads to errors smaller than 5% for most parts of the ocean. The small differences between the reference simulation and the 'GRACE-like' simulation runs, and the good agreement between the simulated data and the actual GRACE data, leads to conclude that the spatial resolution of the GRACE observations is sufficient to predict variations in relative sea level due to gravitational forcing. This error assessment does not include the effect of annual errors remaining in the GRACE coefficients after filtering, which should

be subject of further study.

Trends in the relative sea level signal appear to have been dominated by the mass imbalance of the Greenland ice sheet. Regionally, the trend signal is affected by long term variations in the continental hydrology. This is a topic that deserves further investigation, since such signals may cause a bias in studies that attempt to match tide gauge data to the spatial relative sea level 'fingerprint' of a specific mass imbalance signal, e.g., that of the Greenland ice sheet (e.g., Wake et al., 2006).

The aforementioned regions with strong deviations from the global mean seasonal cycle would be the prime candidates for detection of the relative sea level signals by means of ocean bottom pressure (OBP) recorders, because the signal exceeds the noise level of the instruments here. Such an effort should focus on annual variations rather than trends, since OBP recorder data have been know to suffer from linear and exponential drifts due to instrumental effects. Given the scarceness of OBP recorders and their relatively short life-time, tide gauge observations along the coast can be used as an alternative, assuming that variations due steric expansion and contraction can be removed with a sufficient accuracy. Detection of the signal in the open ocean by means of satellite altimetry observations is more challenging, since the expected amplitude and their gradients are smaller here, and the sea surface height changes are dominated by steric variations in most of the ocean.

Over most of the ocean, changes in relative sea level due to the effects of self-gravitation are found not to be major factor to reconcile ocean bottom pressure from the ECCO numerical ocean model with the GRACE observations, since the strength of the signal is below the noise level in the GRACE data. Nevertheless, inclusion of the selfgravitation effect reduces the variance of residuals between the two by up to 17% in coastal regions. Since large deviations from the a global eustatic distribution are observed due to (self)gravitational attraction and solid earth movement in these regions, numerical ocean models attempting to incorporate the global ocean-land water cycle should consider the implementation of this additional forcing mechanism, preferably based on GRACE observations or by use of hydrological models.

Appendix A

Performance study of the forward model

In order to assess the performance of the forward model used in Ch. 5 to recover the mass balance of the Greenland ice sheet, a synthetic model of surface mass changes is created. The following procedure is followed:

- The secular mass change signal is based on the cumulated surface mass balance (SMB) anomaly of the RACMO model (Ettema et al. (2009)). The linear trend in the model output was added to the glacier discharge trends reported in Rignot et al. (2008b), for the period 2002–2007. The yields a linear trend of −231.6±4.8 Gt/yr for the period April 2002–August 2008.

- Mass fluctuations deviating from the secular signal are modeled using the monthly accumulated SMB RACMO output, after removing a bias and a linear trend estimated in the previous step.

- For regions outside Greenland, the GLDAS model (Rodell et al. (2004)) is used. Glaciated areas such as Antarctica have been masked because of the known problems of the GLDAS model in these areas. In Svalbard, Iceland, Baffin and Ellesmere Island, the GLDAS data is replaced by the RACMO surface mass balance, with a scale factor applied so that the total linear trend is equal to the results found in Ch. 5.

- Mass variations in Antarctica are based on GRACE observations (kindly provided by Isabella Velicogna).

- Mass redistribution due to global isostatic adjustment is implemented using the model of Paulson et al. (2007).

- At every time step, a layer of water is added to the oceans to conserve mass in the system. This water layer follows the gravitational forcing of the geoid, taking into account deformation of the solid Earth, as described in Ch. 6.

- In the final step, the combined grids are converted to spherical harmonics coefficients up degree/order 60. Two data sets are created, one in which the degree 1 coefficients are set to zero, in compliance with the GRACE processing standards, and one in which these coefficients are kept at their original values.

This way, 73 monthly solutions (April 2002–August 2008; May–July 2002 and June 2003 are missing, as in the GRACE time series) are created. The monthly sets of spherical harmonics are converted back to maps of surface mass distribution, and used as an input for the forward model to estimate the mass anomaly of the Greenland ice sheet.

The linear trend over the entire model period in the combined SMB and glacier discharge anomalies, estimated in combination with a bias, annual and semi-annual harmonic, amounts to -231.6 ± 4.8 Gt/yr (error margins indicate the formal error of the fit, at the 95% confidence level), see fig. A.1 and table A.1. If no information on the degree-1 coefficients is used in the forward model, a mass loss signal of 223.7 ± 5.7 Gt/yr is recovered. The standard deviation of the differences between the monthly modeled and recovered mass anomalies of the Greenland ice sheet is approximately 34 Gt, well below the standard error of the GRACE observations (about 80 Gt for a typical month). The modeled and recovered time series correlate at the 99.7% and 94.2% level, before and after detrending the time series, respectively.

Adding the degree-1 the coefficients greatly improves the performance. The linear trend recovered by the forward model increases to -231.8 ± 5.3 Gt/yr. The standard deviation of the residuals reduces to 19 Gt, due to a better representation of the temporal variability of the signal. Correlations increase to 99.9% and 98.3%, before and after detrending, respectively. This, again, highlights the importance of reliable geocenter motion estimates to complement the GRACE observations.

	Trend (Gt/yr)	Correlation w. model	St. dev. residuals (Gt)
Model	-231.6 ± 4.8	1/1	–
Recovered (excl. geocenter)	-223.7 ± 5.7	0.997/0.942	34.6
Recovered (incl. geocenter)	-231.8 ± 5.3	0.999/0.983	18.7

Table A.1: *Statistics of the time series of monthly mass anomaly of the Greenland ice sheet, in the synthetic model and recovered by the forward model. Correlations between modeled and recovered data are given for the original/detrended time series.*
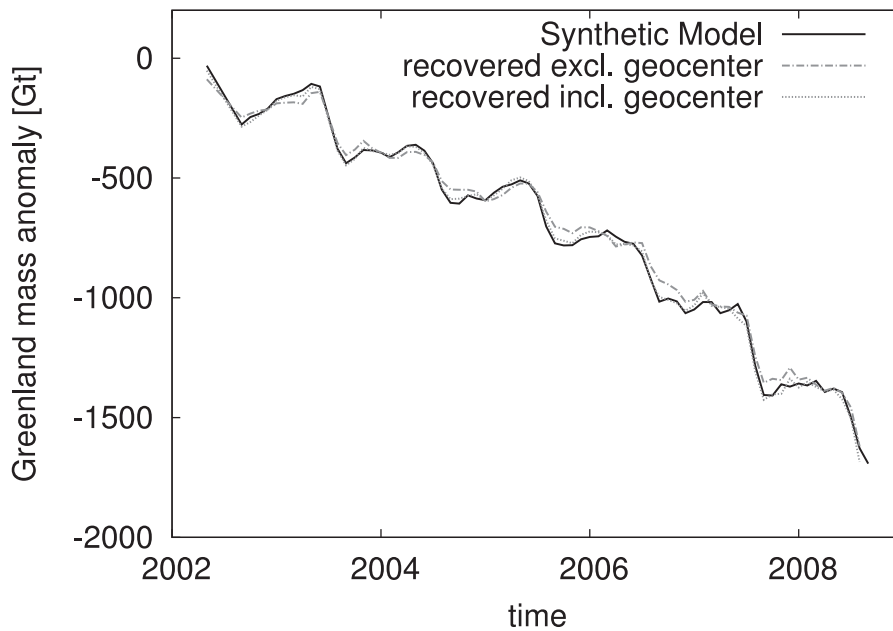
Figure A.1: *Time series of the modeled and recovered mass anomalies of the Greenland ice sheet.*

Bibliography

J. I. Antonov, R. A. Locarnini, T. P. Boyer, A. V. Mishonov, and H. E. Garcia. *World Ocean Atlas 2005, volume 2: Salinity*. U.S. Government Printing Office, Washington, D.C., USA, 2006. 182 pp.

J. L. Bamber, R. J. Hardy, and I. Joughin. An analysis of balance velocities over the Greenland ice sheet and comparison with synthetic aperture radar interferometry. *Journal of Glaciology*, 46:67–74, 2000.

J. L. Bamber, R. B. Alley, and I. Joughin. Rapid response of modern day ice sheets to external forcing. *Earth and Planetary Science Letters*, 257:1–2, May 2007. doi: 10.1016/j.epsl.2007.03.005.

S. V. Bettadpur. UTCSR level-2 processing standards document for level-2 product release 0004. Technical Report GRACE 327-742, CSR, Austin, TX, USA, 2007.

R. J. Bingham and C. W. Hughes. Observing seasonal bottom pressure variability in the North Pacific with GRACE. *Geophys. Res. Lett.*, 33:L8607, April 2006. doi: 10.1029/2005GL025489.

G. Blewitt. Self-consistency in reference frames, geocenter definition, and surface loading of the solid Earth. *J. Geophys. Res. (Solid Earth)*, 108:2103–+, February 2003. doi: 10.1029/2002JB002082.

G. Blewitt and D. Lavallée. Effect of annual signals on geodetic velocity. *J. Geophys. Res. (Solid Earth)*, 107:2145–+, July 2002. doi: 10.1029/2001JB000570.

G. Blewitt, D. Lavallée, P. Clarke, and K. Nurutdinov. A new global mode of earth deformation: seasonal cycle detected. *Science*, 294:2342–2345, December 2001. doi: 10.1126/science.1065328.

F. Bouillé, A. Cazenave, J.M. Lemoine, and J.F. Crétaux. Geocentre motion from the DORIS space system and laser data to the LAGEOS satellites: comparison with surface loading data. *Geophys J. Int.*, 143:71–82, 2000.

J. E. Box, D. H. Bromwich, B. A. Veenhuis, L.-S. Bai, J. C. Stroeve, J. C. Rogers, K. Steffen, T. Haran, and S.-H. Wang. Greenland ice sheet surface mass balance variability (1988 2004) from calibrated polar MM5 output. *Journal of Climate*, 19:2783–+, 2006. doi: 10.1175/JCLI3738.1.

C. Cabanes, A. Cazenave, and C. Le Provost. Sea level change from TOPEX-POSEIDON altimetry for 1993-1999 and possible warming of the southern oceans. *Geophys. Res. Lett.*, 28:9–12, January 2001. doi: 10.1029/2000GL011962.

J. Cappelen, E.J. Laursen, P.V. Jrgensen, and C. Kern-Hansen. DMI monthly climate data collection 1768-2006, Denmark, The Faroe Islands and Greenland, DMI technical report No. 07-06. Technical report, 2007.

L. Carrère and F. Lyard. Modeling the barotropic response of the global ocean to atmospheric wind and pressure forcing - comparisons with observations. *Geophys. Res. Lett.*, 30:8–1, March 2003.

A. Cazenave, F. Remy, K. Dominh, and H. Douville. Global ocean mass variation, continental hydrology and the mass balance of Antarctica ice sheet at seasonal time scale. *Geophys. Res. Lett.*, 27:L3755, 2000.

A. Cazenave, K. Dominh, S. Guinehut, E. Berthier, W. Llovel, G. Ramillien, M. Ablain, and G. Larnicol. Sea level budget over 2003-2008: A reevaluation from GRACE space gravimetry, satellite altimetry and Argo. *Global and Planetary Change*, 65:83–88, January 2009.

D. P. Chambers. Observing seasonal steric sea level variations with GRACE and satellite altimetry. *J. Geophys. Res. (Oceans)*, 111:C3010, March 2006a. doi: 10.1029/2005JC002914.

D. P. Chambers. Evaluation of new GRACE time-variable gravity data over the ocean. *Geophys. Res. Lett.*, 33:L17603, September 2006b. doi: 10.1029/2006GL027296.

D. P. Chambers and J. K. Willis. Analysis of large-scale ocean bottom pressure variability in the North Pacific. *J. Geophys. Res. (Oceans)*, 113:11003–+, November 2008. doi: 10.1029/2008JC004930.

D. P. Chambers, M. E. Tamisiea, R. S. Nerem, and J. C. Ries. Effects of ice melting on GRACE observations of ocean mass trends. *Geophys. Res. Lett.*, 34:5610–+, March 2007. doi: 10.1029/2006GL029171.

D.P. Chambers, J. Wahr, and R.S. Nerem. Preliminary observations of global ocean mass variations with GRACE. *Geophys. Res. Lett.*, 31:L13310, 2004. doi: 10.1029/2004GL020461.

J. L. Chen and C. R. Wilson. Low degree gravity changes from GRACE, Earth rotation, geophysical models, and satellite laser ranging. *J. Geophys. Res.*, 113: 6402–+, June 2008. doi: 10.1029/2007JB005397.

J. L. Chen, C. R. Wilson, B. D. Tapley, J. S. Famiglietti, and M. Rodell. Seasonal global mean sea level change from satellite altimeter, GRACE, and geophysical models. *Journal of Geodesy*, 79:532–539, December 2005. doi: 10.1007/s00190-005-0005-9.

J. L. Chen, C. R. Wilson, and K.-W. Seo. Optimized smoothing of Gravity Recovery and Climate Experiment (GRACE) time-variable gravity observations. *J. Geophys. Res. (Solid Earth)*, 111:6408–+, June 2006a. doi: 10.1029/2005JB004064.

J. L. Chen, C. R. Wilson, and B. D. Tapley. Satellite gravity measurements confirm accelerated melting of Greenland Ice Sheet. *Science*, 313:1958–1960, September 2006b. doi: 10.1126/science.1129007.

J. L. Chen, C. R. Wilson, J. S. Famiglietti, and M. Rodell. Attenuation effect on seasonal basin-scale water storage changes from GRACE time-variable gravity. *Journal of Geodesy*, 81:237–245, April 2007a. doi: 10.1007/s00190-006-0104-2.

J. L. Chen, C. R. Wilson, B. D. Tapley, and D. Blankenship. Antarctic regional ice loss rates from GRACE. *Earth and Planetary Science Letters*, 2007b. doi: 10.1016/j.epsl.2007.10.057. in press.

J. L. Chen, C. R. Wilson, B. D. Tapley, D. D. Blankenship, and E. R. Ivins. Patagonia Icefield melting observed by Gravity Recovery and Climate Experiment (GRACE). *Geophys. Res. Lett.*, 34:22501–+, November 2007c. doi: 10.1029/2007GL031871.

M. Cheng and B. D. Tapley. Variations in the Earth's oblateness during the past 28 years. *J. Geophys. Res.*, 109:9402–+, September 2004. doi: 10.1029/2004JB003028.

J. A. Church and N. J. White. A 20th century acceleration in global sea-level rise. *Geophys. Res. Lett.*, 33:1602–+, January 2006. doi: 10.1029/2005GL024826.

P. J. Clarke, D. A. Lavallée, G. Blewitt, T. M. van Dam, and J. M. Wahr. Effect of gravitational consistency and mass conservation on seasonal surface mass loading models. *Geophys. Res. Lett.*, 32:8306–+, April 2005. doi: 10.1029/2005GL022441.

O. L. Colombo. Notes on the mapping of the gravity field using satellite data. In *Mathematical and Numerical Techniques in Physical Geodesy*, pages 261–+, 1986.

J.-F. Crétaux, L. Soudarin, F.J.M. Davidson, M.-C. Gennero, M. Bergé-Nguyen, and A. Cazenave. Seasonal and interannual geocenter motion from SLR and DORIS measurements: Comparison with surface loading data. *J. Geophys. Res.*, 107(B12):2374, 2002. doi: 10.1029/2002JB001820.

S. D. Desai. Observing the pole tide with satellite altimetry. *J. Geophys. Res. (Oceans)*, 107:7–1, November 2002. doi: 10.1029/2001JC001224.

R. Dietrich, A. Rülke, and M. Scheinert. Present-day vertical crustal deformations in West Greenland from repeated GPS observations. *Geophysical Journal International*, 163:865–874, December 2005. doi: 10.1111/j.1365-246X.2005.02766.x.

H. Dobslaw and M. Thomas. Simulation and observation of global ocean mass anomalies. *J. Geophys. Res. (Oceans)*, 112:5040–+, May 2007. doi: 10.1029/2006JC004035.

D. Dong, J.O. Dickey, Y. Chao, and M.K. Cheng. Geocenter variations caused by atmosphere, ocean and surface ground water. *Geophys. Res. Lett.*, 24(15):L1867, 1997.

D. Dong, P. Fang, Y. Bock, M. K. Cheng, and S. Miyazaki. Anatomy of apparent seasonal variations from GPS-derived site position time series. *J. Geophys. Res. (Solid Earth)*, 107:2075–+, April 2002. doi: 10.1029/2001JB000573.

D. Dong, T. Yunck, and M. Heflin. Origin of the International Terrestrial Reference Frame. *J. Geophys. Res. (Solid Earth)*, 108:2200–+, April 2003. doi: 10.1029/2002JB002035.

J.P. Donnelly, P. Cleary, P. Newby, and R. Ettinger. Coupling instrumental and geological records of sea-level change: Evidence from southern New England of an increase in the rate of sea-level rise in the late 19th century. *Geophysical Research Letters*, 31(5):L05203+, March 2004. doi: 10.1029/2003GL018933.

B.C. Douglas, M.S. Kearney, and S.P. Leatherman, editors. *Sea level rise: History and consequences*. Academic Press, New York., 2001.

R.J. Eanes, S. Kar, S.V. Bettadpur, and M.M. Watkins. Low-frequency geocenter motion determined from SLR tracking. *EOS, Trans. Am. geophys. Un., Fall Meeting Suppl.*, F146, 1997. abstract.

M. C. Eble and F. I. Gonzalez. Deep-ocean bottom pressure measurements in the northeast Pacific. *Journal of Atmospheric and Oceanic Technology*, 8:221–233, April 1991. doi: 10.1175/1520-0426(1991)008.

G. Ekström, M. Nettles, and V. C. Tsai. Seasonality and increasing frequency of Greenland glacial earthquakes. *Science*, 311:1756–1758, March 2006. doi: 10.1126/science.1122112.

J. Ettema, M. R. van den Broeke, E. van Meijgaard, W. J. van de Berg, J. L. Bamber, J. E. Box, and R. C. Bales. Higher surface mass balance of the Greenland ice sheet revealed by high-resolution climate modeling. *Geophys. Res. Lett.*, 36: 12501–+, June 2009. doi: 10.1029/2009GL038110.

M. Fang and B.H. Hager. Postglacial sea level: energy method. *Global and Planetary Change*, 20:125–156(32), 1999. doi: 10.1016/S0921-8181(98)00067-8.

W.E. Farrell and J.A. Clark. On postglacial sea level. *Geophys. J. R. astr. Soc.*, 46:647–667, 1976.

R. Ferland, J. Kouba, and D. Hutchison. Analysis methodology and recent results of the IGS network combination. *Earth, Planets, and Space*, 52:953–957, November 2000.

X. Fettweis. Reconstruction of the 1979-2006 Greenland ice sheet surface mass balance using the regional climate model MAR. *The Cryosphere Discuss.*, 1: 123–168, 2007.

F. Flechtner. AOD1B product description document for product releases 01 to 04. Technical Report GRACE 327-750, rev. 3.1, Potsdam, Germany, 2007.

F. Flechtner. GFZ level-2 processing standards document for level-2 product release 0004. Technical Report GRACE 327-743, GFZ, Potsdam, Germany, 2007.

I. Fukumori, R. Raghunath, and L.-L. Fu. Nature of global large-scale sea level variability in relation to atmospheric forcing: A modeling study. *J. Geophys. Res.*, 103:5493–5512, March 1998. doi: 10.1029/97JC02907.

I. Fukumori, R. Raghunath, L.-L. Fu, and Y. Chao. Assimilation of TOPEX/Poseidon altimeter data into a global ocean circulation model: How good are the results? *J. Geophys. Res.*, 104:25647–25666, November 1999. doi: 10.1029/1999JC900193.

A.E. Gill. *Atmosphere-Ocean Dynamics*. International Geophysics Series. Academic Press, 1982.

G. Golub and W. Kahan. Calculating the singular values and pseudo-inverse of a matrix. *J. Soc. Indust. Appl. Math.: Ser. B, Numer. Anal.*, 2:205–224, 1965.

J. Gould, D. Roemmich, S. Wijffels, H. Freeland, M. Ignaszewsky, X. Jianping, S. Pouliquen, Y. Desaubies, U. Send, K. Radhakrishnan, K. Takeuchi, K. Kim, M. Danchenkov, P. Sutton, B. King, B. Owens, and S. Riser. Argo Ppofiling floats bring new era of in situ ocean observations. *EOS Transactions*, 85:185–190, May 2004. doi: 10.1029/2004EO190002.

S.-C. Han, C. K. Shum, and K. Matsumoto. GRACE observations of M_2 and S_2 ocean tides underneath the Filchner-Ronne and Larsen ice shelves, Antarctica. *Geophys. Res. Lett.*, 32:20311–+, October 2005. doi: 10.1029/2005GL024296.

E. Hanna and J. Cappelen. Recent climate of southern Greenland. *Weather*, 57: 320–328, September 2002.

E. Hanna, P. Huybrechts, K. Steffen, J. Cappelen, R. Huff, C. Shuman, T. Irvine-Fynn, S. Wise, and M. Griffiths. Increased runoff from melt from the Greenland Ice Sheet: a response to global warming. *J. Climate*, (2):331–341, 2008.

E. Hanna, J. Cappelen, X. Fettweis, P. Huybrechts, A. Luckman, and M. H. Ribergaard. Hydrologic response of the Greenland ice sheet: the role of oceanographic warming. *Hydrological Processes*, 23:7–30, January 2009. doi: 10.1002/hyp.7090.

W. A. Heiskanen and H. Moritz. *Physical geodesy*. San Francisco, W. H. Freeman [1967], 1967.

M. M. Helsen, M. R. van den Broeke, R. S. van de Wal, W. van de Berg, E. van Meijgaard, C. H. Davis, Y. Li, and I. Goodwin. Elevation changes in Antarctica mainly determined by accumulation variability. *Science*, 320:1626, 2008. doi: 10.1126/science.1153894.

D. Holland, R. Thomas, B. de Young, M. Ribergaard, and B. Lyberth. Acceleration of Jakobshavn Isbrae triggered by warm subsurface ocean waters. *Nature Geosci*, 1(10):659–664, October 2008. doi: http://dx.doi.org/10.1038/ngeo316.

M. Horwath and R. Dietrich. Errors of regional mass variations inferred from GRACE monthly solutions. *Geophys. Res. Lett.*, 33:L7502, April 2006. doi: 10.1029/2005GL025550.

I. M. Howat, I. Joughin, M. Fahnestock, B. E. Smith, and T. A. Scambos. Synchronous retreat and acceleration of southeast Greenland outlet glaciers 2000-06: ice dynamics and coupling to climate. *J. Glaciol.*, 54(187):646–660, 2008a.

I. M. Howat, B. E. Smith, I. Joughin, and T. A. Scambos. Rates of southeast Greenland ice volume loss from combined ICESat and ASTER observations. *Geophys. Res. Lett.*, 35:17505–+, September 2008b. doi: 10.1029/ 2008GL034496.

M. Ishii, M. Kimoto, K. Sakamoto, and S.I. Iwasaki. Steric sea level changes estimated from historical ocean subsurface temperature and salinity analyses. *J. Oceanogr.*, 62(2):155–170, 2006.

E. R. Ivins and D. Wolf. Glacial isostatic adjustment: New developments from advanced observing systems and modeling. *Journal of Geodynamics*, 46:69–77, October 2008. doi: 10.1016/j.jog.2008.06.002.

T. S. James and E. R. Ivins. Global geodetic signatures of the Antarctic ice sheet. *J. Geophys. Res.*, 102:605–634, January 1997. doi: 10.1029/96JB02855.

C. Jekeli. Alternative methods to smooth the Earth's gravity field. Technical Report Report 327, Department of Geodetic Science and Surveying, Ohio State University, December 1981.

S. Jevrejeva, J. C. Moore, A. Grinsted, and P. L. Woodworth. Recent global sea level acceleration started over 200 years ago? *Geophys. Res. Lett.*, 35:8715–+, April 2008. doi: 10.1029/2008GL033611.

O. M. Johannessen, K. Khvorostovsky, M. W. Miles, and L. P. Bobylev. Recent ice-sheet growth in the interior of Greenland. *Science*, 310:1013–1016, November 2005. doi: 10.1126/science.1115356.

I. Joughin, W. Abdalati, and M Fahnestock. Large fluctuations in speed on Greenlands Jakobshavn Isbræ glacier. *Nature*, 432(7017):608–610, 2004.

T. Kanzow, F. Flechtner, A. Chave, R. Schmidt, P. Schwintzer, and U. Send. Seasonal variation of ocean bottom pressure derived from Gravity Recovery and Climate Experiment (GRACE): Local validation and global patterns. *J. Geophys. Res. (Oceans)*, 110:C9001, September 2005. doi: 10.1029/2004JC002772.

W. M. Kaula. *Theory of satellite geodesy. Applications of satellites to geodesy.* Waltham, Mass.: Blaisdell, 1966, 1966.

W.S. Kessler. Observations of long rossby waves in the northern tropical. *J. Geophysic. Res.*, 95:51835217, 1990.

M. King, P. Moore, P. Clarke, and D. Lavallée. Choice of optimal averaging radii for temporal GRACE gravity solutions, a comparison with GPS and satellite altimetry. *Geophysical Journal International*, 166:1–11, July 2006. doi: 10.1111/j.1365-246X.2006.03017.x.

R. Klees, E. A. Zapreeva, H. C. Winsemius, and H. H. G. Savenije. The bias in GRACE estimates of continental water storage variations. *Hydrology and Earth System Sciences*, 11:1227–1241, May 2007.

R. Klees, E. A. Revtova, B. C. Gunter, P. Ditmar, E. Oudman, H. C. Winsemius, and H. H. G. Savenije. The design of an optimal filter for monthly GRACE gravity models. *Geophysical Journal International*, 175:417–432, November 2008. doi: 10.1111/j.1365-246X.2008.03922.x.

P. Knudsen. Ocean Tides in GRACE Monthly Averaged Gravity Fields. *Space Science Reviews*, 108:261–270, July 2003. doi: 10.1023/A:1026215124036.

W. Krabill, E. Hanna, P. Huybrechts, W. Abdalati, J. Cappelen, B. Csatho, E. Frederick, S. Manizade, C. Martin, J. Sonntag, R. Swift, R. Thomas, and J. Yungel. Greenland ice sheet: Increased coastal thinning. *Geophys. Res. Lett.*, 31:24402–+, December 2004. doi: 10.1029/2004GL021533.

J. Kusche. Approximate decorrelation and non-isotropic smoothing of time-variable GRACE-type gravity field models. *Journal of Geodesy*, pages 80–+, February 2007. doi: 10.1007/s00190-007-0143-3.

J. Kusche and E. J. O. Schrama. Surface mass redistribution inversion from global GPS deformation and Gravity Recovery and Climate Experiment (GRACE) gravity data. *J. Geophys. Res. (Solid Earth)*, 110:9409–+, September 2005. doi: 10.1029/2004JB003556.

K. Lambeck, F. Antonioli, A. Purcell, and S. Silenzi. Sea-level change along the Italian coast for the past 10,000yr. *Quaternary Science Reviews*, 23:1567–1598, July 2004a. doi: 10.1016/j.quascirev.2004.02.009.

K. Lambeck, M. Anzidei, F. Antonioli, A. Benini, and A. Esposito. Sea level in Roman time in the Central Mediterranean and implications for recent change. *"Earth and Planetary Science Letters"*, 224(3-4):563 – 575, 2004b. doi: 10.1016/j.epsl.2004.05.031.

D. A. Lavallée, T. van Dam, G. Blewitt, and P. J. Clarke. Geocenter motions from GPS: A unified observation model. *J. Geophys. Res. (Solid Earth)*, 111: B5405, May 2006. doi: 10.1029/2005JB003784.

D. A. Lavallée, P. Moore, E. J. Petrie, M. A. King, P. J. Clarke, and D. Booker. Can we measure geocenter motion accurately? *AGU Fall Meeting Abstracts*, pages B694+, December 2008.

J.-M. Lemoine, S. Bruinsma, S. Loyer, R. Biancale, J.-C Marty, F. Perosanz, and G. Balmino. Temporal gravity field models inferred from GRACE data. *J. Adv. Space*, 2007. doi: 10.10116/j.asr.2007.03062.

E. W. Leuliette and L. Miller. Closing the sea level rise budget with altimetry, Argo, and GRACE. *Geophys. Res. Lett.*, 36:4608–+, February 2009. doi: 10.1029/2008GL036010.

E.W. Leuliette, R.S. Nerem, and G.T. Mitchum. Calibration of TOPEX/Poseidon and Jason altimeter data to construct a continuous record of mean sea Level change. *Mar. Geod.*, 27:79–94, 2004.

S. Levitus, J. Antonov, and T. Boyer. Warming of the world ocean, 1955-2003. *Geophys. Res. Lett.*, 32:2604–+, January 2005. doi: 10.1029/2004GL021592.

X. Liu. *Global gravity field recovery from satellite-to-satellite tracking data with the acceleration approach*. PhD. thesis, Netherlands Geodectic Commission, Publication on Geodesy 68, TU Delft, Delft, The Netherlands, 2008.

R. A. Locarnini, A. V. Mishonov, J. I. Antonov, T. P. Boyer, and H. E. Garcia. *World Ocean Atlas 2005, Volume 1: Temperature.* U.S. Government Printing Office, Washington, D.C., 2006.

A. Lombard, D. Garcia, G. Ramillien, A. Cazenave, R. Biancale, J. M. Lemoine, F. Flechtner, R. Schmidt, and M. Ishii. Estimation of steric sea level variations from combined GRACE and Jason-1 data. *Earth and Planetary Science Letters*, 254:194–202, February 2007. doi: 10.1016/j.epsl.2006.11.035.

E. N. Lorenz. Empirical orthogonal functions and statistical weather prediction. Sci. Rep. No. 1, M.I.T. Cambridge, MA, 1956.

A. Luckman, T. Murray, R. de Lange, and E. Hanna. Rapid and synchronous ice-dynamic changes in East Greenland. *Geophys. Res. Lett.*, 33:3503–+, February 2006. doi: 10.1029/2005GL025428.

S. B. Luthcke, H. J. Zwally, W. Abdalati, D. D. Rowlands, R. D. Ray, R. S. Nerem, F. G. Lemoine, J. J. McCarthy, and D. S. Chinn. Recent Greenland ice mass loss by drainage system from satellite gravity observations. *Science*, 314:1286–1289, December 2006. doi: 10.1126/Science.1130776.

F. Lyard, F. Lefèvre, T. Letellier, and O. Francis. Modelling the global ocean tides: modern insights from FES2004. *Ocean Dynamics*, 56:394–415, December 2006. doi: 10.1007/s10236-006-0086-x.

S. J. Mason and L. Goddard. Probabilistic precipitation anomalies associated with ENSO. *Bulletin of the American Meteorological Society*, 82:619–638, April 2001. doi: 10.1175/1520-0477(2001)082.

Y. Masumoto and G Meyers. Forced rossby waves in the southern tropical indian ocean. *J. Geophys. Res.*, 103(C12):27589–27602, 1998.

P. C. D. Milly and A. B. Shmakin. Global modeling of land water and energy balances. part I: The land dynamics (LaD) model. *Journal of Hydrometeorology*, 3(3):283–299, 2002.

G.A. Milne and J.X. Mitrovica. Postglacial sea-level change on a rotating earth. *Geophys. J. Int.*, 133:1–19, 1998.

J. X. Mitrovica and W. R. Peltier. On postglacial geoid subsidence over the equatorial oceans. *J. Geophys. Res.*, 96:20053–+, November 1991.

J. X. Mitrovica, M. E. Tamisiea, J. L. Davis, and G. A. Milne. Recent mass balance of polar ice sheets inferred from patterns of global sea-level change. *Nature*, 409:1026–1029, February 2001.

P. Moore and M. A. King. Antarctic ice mass balance estimates from GRACE: Tidal aliasing effects. *J. Geophys. Res. (Earth Surface)*, 113:2005–+, April 2008. doi: 10.1029/2007JF000871.

P. Moore and J. Wang. Geocentre variation from laser tracking of LAGEOS1/2 and loading data. *Advances in Space Research*, 31:1927–1933, April 2003. doi: 10.1016/S0273-1177(03)00170-4.

A. Morimoto, K. Yoshimoto, and T. Yanagi. Circulations and eddies over the South China Sea derived from TOPEX/Poseidon altimetry. *J. Oceanogr.*, 56: 331–344, 2000.

T. L. Mote. Greenland surface melt trends 1973-2007: Evidence of a large increase in 2007. *Geophys. Res. Lett.*, 34:22507–+, November 2007. doi: 10.1029/2007GL031976.

M. Naeije, E. Doornbos, L. Mathers, R. Scharroo, E. Schrama, and P Visser. Radar Altimeter Database System: Exploitation and extension (RADSxx). Technical Report Final Rep. NUSP-2 02-06, Space Res. Organ. Neth., Utrecht, Netherlands, 2002.

G. R. North, T. L. Bell, R. F. Cahalan, and F. J. Moeng. Sampling errors in the estimation of empirical orthogonal functions. *Monthly Weather Review*, 110: 699–+, 1982. doi: 10.1175/1520-0493(1982)110.

M. L. Parry, O. F. Canziani, J. P. Palutikof, P. J. van der Linden, and C. E. Hanson, editors. *IPCC Fourth assessment report: Working group II report "Impacts, Adaptation and Vulnerability"*. Cambridge University Press, 2007.

A. Paulson, S. Zhong, and J. Wahr. Inference of mantle viscosity from GRACE and relative sea level data. *Geophysical Journal International*, 171:497–508, November 2007. doi: 10.1111/j.1365-246X.2007.03556.x.

K. Pearson. On lines and planes of closest fit to systems of points in space. *Philosophical Magazine*, 2:559–572, 1901.

W. R. Peltier. Global glacial isostasy and the surface of the Ice-Age Earth: The ICE-5G (VM2) model and GRACE. *Annual Review of Earth and Planetary Sciences*, 32:111–149, May 2004. doi: 10.1146/annurev.earth.32.082503.144359.

R. M. Ponte. A preliminary model study of the large-scale seasonal cycle in bottom pressure over the global ocean. *J. Geophys. Res.*, 104:1289–1300, 1999. doi: 10.1029/1998JC900028.

P. Prandi, A. Cazenave, and M. Becker. Is coastal mean sea level rising faster than the global mean? A comparison between tide gauges and satellite altimetry over 1993-2007. *Geophys. Res. Lett.*, 36:5602–+, March 2009. doi: 10.1029/2008GL036564.

R. W. Preisendorfer. *Principal Component Analysis in Meteorology and Oceanography*. Elsevier, Seattle, 1988.

W. H. Press, S. A. Teukolsky, W. T. Vetterling, and B. P. Flannery. *Numerical recipes in FORTRAN. The art of scientific computing*. Cambridge: University Press, —c1992, 2nd ed., 1992.

G. Ramillien, A. Lombard, A. Cazenave, E. R. Ivins, M. Llubes, F. Remy, and R. Biancale. Interannual variations of the mass balance of the Antarctica and Greenland ice sheets from GRACE. *Global and Planetary Change*, 53:198–208, September 2006. doi: 10.1016/j.gloplacha.2006.06.003.

G. Ramillien, S. S. Bouhours, S., Cazenave Lombard, A., F. A., Flechtner, and R. Schmidt. Land water storage contribution to sea level from GRACE geoid data over 2003-2006. *Global and Planetary Change*, 2007. doi: 10.1016/j. gloplacha.2007.04.002.

E. Rangelova, W. van der Wal, A. Braun, M. G. Sideris, and P. Wu. Analysis of Gravity Recovery and Climate Experiment time-variable mass redistribution signals over North America by means of principal component analysis. *J. Geophys. Res. (Earth Surface)*, 112:3002–+, July 2007. doi: 10.1029/2006JF000615.

R. D. Ray and S. B. Luthcke. Tide model errors and GRACE gravimetry: towards a more realistic assessment. *Geophysical Journal International*, 167:1055–1059, December 2006. doi: 10.1111/j.1365-246X.2006.03229.x.

C. Reigber, R. Schmidt, F. Flechtner, R. König, U. Meyer, K.-H. Neumayer, P. Schwintzer, and S. Y. Zhu. An Earth gravity field model complete to degree and order 150 from GRACE: EIGEN-GRACE02S. *Journal of Geodynamics*, 39:1–10, January 2005. doi: 10.1016/j.jog.2004.07.001.

R. Rietbroek, P. LeGrand, B. Wouters, J.-M. Lemoine, G. Ramillien, and C. W. Hughes. Comparison of in situ bottom pressure data with GRACE gravimetry in the Crozet-Kerguelen region. *Geophys. Res. Lett.*, 33:L21601, November 2006. doi: 10.1029/2006GL027452.

E. Rignot and P. Kanagaratnam. Changes in the velocity structure of the Greenland ice sheet. *Science*, 311:986–990, February 2006. doi: 10.1126/science. 1121381.

E. Rignot and R. H. Thomas. Mass Balance of polar ice sheets. *Science*, 297: 1502–1506, August 2002. doi: 10.1126/science.1073888.

E. Rignot, J. Bamber, M. van den Broeke, C. Davis, Y. Li, W. van de Berg, and E. van Meijgaard. Recent antarctic ice mass loss from radar interferometry and regional climate modelling. *Nature Geosci.*, 1:106 – 110, 2008a. doi: 10.1038/ ngeo102.

E. Rignot, J. E. Box, E. Burgess, and E. Hanna. Mass balance of the Greenland ice sheet from 1958 to 2007. *Geophys. Res. Lett.*, 35:20502–+, October 2008b. doi: 10.1029/2008GL035417.

M. Rodell and P. R. Houser. Updating a land surface model with MODIS-derived snow cover. *Journal of Hydrometeorology*, 5:1064–+, 2004. doi: 10.1175/JHM-395.1.

M. Rodell, P. R. Houser, U. Jambor, J. Gottschalck, K. Mitchell, C.-J. Meng, K. Arsenault, B. Cosgrove, J. Radakovich, M. Bosilovich, J. K. Entin, J. P. Walker, D. Lohmann, and D. Toll. The Global Land Data Assimilation System. *Bulletin of the American Meteorological Society, vol. 85, Issue 3, pp.381-394*, 85:381–394, March 2004.

C. F. Ropelewski and M. S. Halpert. Quantifying Southern Oscillation-precipitation relationships. *Journal of Climate*, 9:1043–1059, May 1996. doi: 10.1175/1520-0442(1996)009.

D. D. Rowlands, S. B. Luthcke, S. M. Klosko, F. G. R. Lemoine, D. S. Chinn, J. J. McCarthy, C. M. Cox, and O. B. Anderson. Resolving mass flux at high spatial and temporal resolution using GRACE intersatellite measurements. *Geophys. Res. Lett.*, 32:4310–+, February 2005. doi: 10.1029/2004GL021908.

R. Sabadini and B. Vermeersen. *Global dynamics of the Earth: Applications of normal mode relaxation theory to solid-Earth geophysics.* Global Dynamics of the Earth: Applications of Normal Mode Relaxation Theory to Solid-Earth Geophysics by Roberto Sabadini and Bert Vermeersen. Published by Kluwer Academic Publishers, Dordrecht, the Netherlands, 2004. ISBN 1-4020-2135-6, 2004.

N. H. Saji, B. N. Goswami, P. N. Vinayachandran, and T. Yamagata. A dipole mode in the tropical Indian Ocean. *Nature*, 401:360–363, September 1999.

R Scharroo, J Lillibridge, W Smith, and E Schrama. Cross-calibration and long-term monitoring of the microwave radiometers of ERS, TOPEX, GFO, Jason and Envisat. *Marine Geodesy*, pages 279–298, 2004. doi: 10.1080/01490410490465265.

R. Schmidt, S. Petrovic, A. Güntner, F. Barthelmes, J. Wünsch, and J. Kusche. Periodic components of water storage changes from GRACE and global hydrology models. *J. Geophys. Res. (Solid Earth)*, 113:8419–+, August 2008. doi: 10.1029/2007JB005363.

E. J. O. Schrama and R. D. Ray. A preliminary tidal analysis of TOPEX/POSEIDON altimetry. *J. Geophys. Res.*, 99:24799–24808, December 1994. doi: 10.1029/94JC01432.

E. J. O. Schrama and P. N. A. M. Visser. Accuracy assessment of the monthly GRACE geoids based upon a simulation. *Journal of Geodesy*, 81:67–80, January 2007. doi: 10.1007/s00190-006-0085-1.

E. J. O.. Schrama and B. Wouters. Surface mass loading estimates from GRACE and GPS. In *IAG GGEO2008 proceedings, Chania Crete*, 2008.

E. J. O. Schrama, B. Wouters, and D. A. Lavallée. Signal and noise in Gravity Recovery and Climate Experiment (GRACE) observed surface mass variations. *J. Geophys. Res. (Solid Earth)*, 112:8407–+, August 2007. doi: 10.1029/2006JB004882.

B. E. Schutz, H. J. Zwally, C. A. Shuman, D. Hancock, and J. P. DiMarzio. Overview of the ICESat Mission. *Geophys. Res. Lett.*, 32:21–+, November 2005. doi: 10.1029/2005GL024009.

G. Seeber. *Satellite geodesy : foundations, methods, and applications.* Berlin ; New York : W. de Gruyter, 1993.

A.B. Shmakin, P.C. D.Mill, and K. A. Dunne. Global modeling of land water and energy balances. part III: Interannual variability. *Journal of Hydrometeorology*, 3(3):311–321, 2003.

D. C. Slobbe, P. Ditmar, and R. C. Lindenbergh. Estimating the rates of mass change, ice volume change and snow volume change in Greenland from ICESat and GRACE data. *Geophysical Journal International*, 176:95–106, January 2009. doi: 10.1111/j.1365-246X.2008.03978.x.

N. Sneeuw. Global spherical harmonic analysis by least-squares and numerical quadrature methods in historical perspective. *Geophysical Journal International*, 118:707–716, September 1994. doi: 10.1111/j.1365-246X.1994.tb03995.x.

S. Solomon, D. Qin, M. Manning, Z. Chen, M. Marquis, K. B. Averyt, M. Tignor, and H. L. Miller, editors. *Climate Change 2007 - The Physical Science Basis: Working Group I Contribution to the Fourth Assessment Report of the IPCC.* Cambridge University Press, Cambridge, UK and New York, NY, USA, September 2007. ISBN 0521880092.

L. A. Stearns and G. S. Hamilton. Rapid volume loss from two East Greenland outlet glaciers quantified using repeat stereo satellite imagery. *Geophys. Res. Lett.*, 34:5503–+, March 2007. doi: 10.1029/2006GL028982.

S. Swenson and J. Wahr. Methods for inferring regional surface-mass anomalies from gravity recovery and climate experiment (GRACE) measurements of time-variable gravity. *J. Geophys. Res.*, 107(B9):219, 2002. doi: 10.1029/2001JB000576.

S. Swenson and J. Wahr. Post-processing removal of correlated errors in GRACE data. *Geophys. Res. Lett.*, 33:L8402, April 2006. doi: 10.1029/2005GL025285.

S. Swenson, D. Chambers, and J. Wahr. Estimating geocenter variations from a combination of GRACE and ocean model output. *J. Geophys. Res.*, 113: 8410–+, August 2008. doi: 10.1029/2007JB005338.

J. J. Sylvester. On the reduction of a bilinear quantic of the n th order to the form of a sum of n products by a double orthogonal substitution. *Messenger of Mathematics*, 19:42–46, 1889.

M. E. Tamisiea, J. X. Mitrovica, and J. L. Davis. GRACE gravity data constrain ancient ice geometries and continental dynamics over Laurentia. *Science*, 316: 881–, May 2007. doi: 10.1126/Science.1137157.

B. Tapley, J. Ries, S. Bettadpur, D. Chambers, M. Cheng, F. Condi, B. Gunter, Z. Kang, P. Nagel, R. Pastor, T. Pekker, S. Poole, and F. Wang. GGM02 An improved Earth gravity field model from GRACE. *Journal of Geodesy*, 79: 467–478, November 2005. doi: 10.1007/s00190-005-0480-z.

B.D. Tapley, S. Bettadpur, J.C. Ries, P.F. Thompson, and M.M. Watkins. GRACE measurements of mass variability in the earth system. *Science*, 305, 2004a.

B.D. Tapley, S. Bettadpur, M. Watkins, and C. Reigber. The gravity recovery and climate experiment: Mission overview and early results. *Geophys. Res. Lett.*, 31:L09607, 2004b. doi: 10.1029/2004GL019920.

M. Tedesco. A new record in 2007 for melting in Greenland. *EOS Transactions*, 88:383–383, September 2007. doi: 10.1029/2007EO390003.

M. Tedesco, M. Serreze, and X. Fettweis. Diagnosing the extreme surface melt event over southwestern greenland in 2007. *The Cryosphere*, 2(2):159–166, 2008.

M. Thomas. *Ocean induced variations of Earths rotation - Results from a simultaneous model of global circulation and tides*. PhD thesis, University of Hamburg, Germany, 2002.

M. Thomas, J. Sündermann, and E. Maier-Reimer. Consideration of ocean tides in an OGCM and impacts on subseasonal to decadal polar motion excitation. *Geophys. Res. Lett.*, 28:L2457, June 2001. doi: 10.1029/2000GL012234.

R. Thomas, E. Frederick, W. Krabill, S. Manizade, and C. Martin. Progressive increase in ice loss from Greenland. *Geophys. Res. Lett.*, 33:10503–+, May 2006. doi: 10.1029/2006GL026075.

R. Thomas, C. Davis, E. Frederick, W. Krabill, Y. Li, S. Manizade, and C. Martin. A comparison of Greenland ice-sheet volume changes derived from altimetry measurements. *Journal of Glaciology*, 54(185):203–212, March 2008. ISSN 0022-1430. doi: http://dx.doi.org/10.3189/002214308784886225.

P. Tregoning, K. Lambeck, and G. Ramillien. GRACE estimates of sea surface height anomalies in the Gulf of Carpentaria, Australia. *Earth and Planetary Science Letters*, 271:241–244, July 2008. doi: 10.1016/j.epsl.2008.04.018.

K. E. Trenberth. The definition of El Niño. *Bulletin of the American Meteorological Society*, 78:2771–2777, December 1997. doi: 10.1175/1520-0477(1997)078.

A. M. Tushingham and W. R. Peltier. Ice-3g - A new global model of late Pleistocene deglaciation based upon geophysical predictions of post-glacial relative sea level change. *J. Geophys. Res.*, 96:4497–4523, March 1991. doi: 10.1029/90JB01583.

UNESCO. Tenth report of the joint panel on oceanographic tables and standards. Technical Report 36, UNESCO, Paris, France, 1981.

T. van Dam, J. Wahr, and D. Lavallée. A comparison of annual vertical crustal displacements from GPS and Gravity Recovery and Climate Experiment (GRACE) over Europe. *J. Geophys. Res. (Solid Earth)*, 1112:B03404, March 2007. doi: 10.1029/2006JB004335.

M. van den Broeke, J. Bamber, J. Ettema, E. Rignot, E. Schrama, W.J. van de Berg, E. van Meijgaard, I. Velicogna, and B. Wouters. Partitioning Recent Greenland Mass Loss. *Science*, 326(5955):984–986, 2009. doi: 10.1126/science.1178176. URL http://dx.doi.org/10.1126/science.1178176.

E. Van Meijgaard, W.J. van de Berg, F. Bosveld, B. van den Hurk, G. Lenderink, P. Siebesma, and B. Van Uft. The KNMI regional atmospheric climate model, version 2.1. Technical Report Technical Report 302, KNMI, PO Box 201, 3730 AE De Bilt, The Netherlands., 2008.

I. Velicogna and J. Wahr. Measurements of time-variable gravity show mass loss in antarctica. *Science*, 311:1754–1756, March 2006a. doi: 10.1126/Science.1123785.

I. Velicogna and J. Wahr. Acceleration of Greenland ice mass loss in spring 2004. *Nature*, 443:329–331, September 2006b. doi: 10.1038/nature05168.

S. V. Vinogradov, R. M. Ponte, P. Heimbach, and C. Wunsch. The mean seasonal cycle in sea level estimated from a data-constrained general circulation model. *J. Geophys. Res. (Oceans)*, 113:3032–+, March 2008. doi: 10.1029/2007JC004496.

J. Wahr, M. Molenaar, and F. Bryan. Time variability of the earth's gravity field: Hydrological and oceanic effects and their possible detection using GRACE. *J. Geophys. Res. (Solid Earth)*, 103(B12):30305–30229, 1998.

J. Wahr, S. Swenson, and I. Velicogna. Accuracy of GRACE mass estimates. *Geophys. Res. Lett.*, 33:6401–+, March 2006. doi: 10.1029/2005GL025305.

L. Wake, G. Milne, and E. Leuliette. 20th Century sea-level change along the eastern US: Unravelling the contributions from steric changes, Greenland ice sheet mass balance and Late Pleistocene glacial loading. *Earth and Planetary Science Letters*, 250:572–580, October 2006. doi: 10.1016/j.epsl.2006.08.006.

M. Watkins and D.-N. Yuan. JPL level-2 processing standards document for level-2 product release 04. Technical Report GRACE 327-744, JPL, Pasadena, CA, USA, 2007.

J. K. Willis, J. M. Lyman, G. C. Johnson, and J. Gilson. Correction to "Recent cooling of the upper ocean". *Geophys. Res. Lett.*, 34:16601–+, August 2007. doi: 10.1029/2007GL030323.

J. K. Willis, D. P. Chambers, and R. S. Nerem. Assessing the globally averaged sea level budget on seasonal to interannual timescales. *J. Geophys. Res.*, 2008. doi: 10.1029/2007JC004517. in press.

H. C. Winsemius, H. H. G. Savenije, A. M. J. Gerrits, E. A. Zapreeva, and R. Klees. Comparison of two model approaches in the Zambezi river basin with regard to model reliability and identifiability. *Hydrology and Earth System Sciences*, 10:339–352, May 2006a.

H. C. Winsemius, H. H. G. Savenije, N. C. van de Giesen, B. J. J. M. van den Hurk, E. A. Zapreeva, and R. Klees. Assessment of Gravity Recovery and Climate Experiment (GRACE) temporal signature over the upper Zambezi. *Water Resources Research*, 42:12201–+, December 2006b. doi: 10.1029/2006WR005192.

G. R. Wood. The bisection method in higher dimensions. *Math. Program.*, 55(3): 319–337, 1992. ISSN 0025-5610. doi: 10.1007/BF01581205.

R.S. Woodward. On the form of and position of mean sea level. *US Geol. Surv. Bull.*, 48:87–170, 1888.

B. Wouters. Identification and quantification of sea level rise contributors. Master's thesis, Faculty of Aerospace Engineering, Delft University of Technology, 2004. (unpublished).

B. Wouters and E. J. O. Schrama. Improved accuracy of GRACE gravity solutions through empirical orthogonal function filtering of spherical harmonics. *Geophys. Res. Lett.*, 34:23711–+, December 2007. doi: 10.1029/2007GL032098.

B. Wouters, D. Chambers, and E.J.O. Schrama. GRACE observes small-scale mass loss in Greenland. *Geophys. Res. Lett.*, 35:20501–+, October 2008. doi: 10.1029/2008GL034816.

X. Wu, M. B. Heflin, E. R. Ivins, and I. Fukumori. Seasonal and interannual global surface mass variations from multisatellite geodetic data. *J. Geophys. Res. (Solid Earth)*, 111:9401–+, September 2006. doi: 10.1029/2005JB004100.

C. Wunsch. The long-period tides. *Reviews of Geophysics*, 5:447–475, 1967. doi: 10.1029/RG005i004p00447.

V. Zlotnicki, J. Wahr, I. Fukumori, and Y. Song. Antarctic circumpolar current transport variability during 200305 from GRACE. *J. Phys. Oceanogr.*, 37(2): 230–244, 2007.

H. J. Zwally, M. B. Giovinetto, J. Li, H. J. Cornejo, Beckley. M. A., A. C. Brenner, J. L. Saba, and S. Yi. Mass changes of the Greenland and Antarctic ice sheets and shelves and contributions to sea-level rise: 1992–2002. *J. Glaciol*, 51(175): 509–527, 2005.

Curriculum Vitae

Bert Wouters was born in Leuven (Belgium) on May 6, 1980. After attending secondary school at the Vrije Sint-Lambertusschool in Westerlo, he enrolled at the Faculty of Aerospace Engineering of the Technical University of Delft in 1998. After moving to Austria for one year in 2001 to study at the Technical University of Vienna, he started his master at the department of Astrodynamics and Satellite Systems of the TU Delft, which he completed in 2004 cum laude. Part of his M.Sc. thesis research was carried out at the Center for Space Research of the University of Austin at Texas in the United States.

In 2005, he took on a PhD. position at the same department under the supervision of Prof. B.A.C. Ambrosius, dr. E.J.O. Schrama and dr. L.L.A. Vermeersen. Again, part of the work was done at the Center for Space Research in Austin, TX, in cooperation with Dr. D.P. Chambers. From July 2009 on, Bert Wouters will work at the Royal Netherlands Meteorological Institute (KNMI) as a postdoctoral researcher.